

Martin-Luther-Universität Halle-Wittenberg

Studies on the ferroelectric field effect in perovskite oxide heterostructures

Dissertation

zur Erlangung des
Doktorgrades der Naturwissenschaften (Dr. rer. nat.)

der Naturwissenschaftlichen Fakultät II - Chemie und Physik

vorgelegt

von Herrn Dipl.-Phys. Daniele Preziosi

geboren am 27.08.1983 in Avellino (Italien)

Gutachter/in:

1. Prof. Dr. Dietrich Hesse
2. Prof. Dr. Kathrin Dörr
3. Prof. Dr. Ho Hyung Lee

Halle (Saale), 16 April 2015

List of Abbreviations	iii
1 Introduction	1
2 Materials and methods	3
2.1 Strontium-doped lanthanum manganite $\text{La}_{1-x}\text{Sr}_x\text{MnO}_3$	3
2.1.1 Exchange mechanisms in LSMO	6
2.1.2 Properties of thin films of LSMO	7
2.1.3 Crystal structure of the LSMO ($x=0.175$)	8
2.2 Lead zirconate titanate $\text{PbZr}_x\text{Ti}_{1-x}\text{O}_3$	9
2.3 Basics of x-ray absorption spectroscopy	11
2.3.1 X-ray linear dichroism	13
2.3.2 X-ray magnetic circular dichroism	15
2.3.3 Sum rules	15
2.4 Magnetic properties	18
2.4.1 Shape anisotropy	19
2.4.2 Magnetocrystalline anisotropy	19
2.4.3 Stoner-Wohlfarth model	20
2.5 Ferroelectric field effect: an example of charge-mediated magnetoelectric coupling	21
3 Experimental setup	24
3.1 Pulsed laser deposition	24
3.2 X-ray diffraction	25
3.3 Atomic force microscopy	27
3.4 Ferroelectric switching and hysteresis loop measurements	29
3.5 Magnetotransport measurements	31
3.6 Experimental details of the Deimos beamline at Soleil	32
4 Results on oxide growth and physical characterizations	34
4.1 Substrate preparation	34
4.1.1 Strontium titanate SrTiO_3 (STO)	35
4.1.2 Lanthanum aluminate LaAlO_3 (LAO)	36
4.1.3 Lanthanum strontium aluminum tantalate $(\text{La,Sr})(\text{Al,Ta})\text{O}_3$ (LSAT)	37

4.2	Growth and physical properties of LSMO($x=0.175$) thin films	38
4.2.1	Crystallographic and morphology properties on different substrates . . .	38
4.2.2	Functional properties: magnetotransport and magnetic characteriza- tions of LSMO thin films	41
4.3	Growth and characterization of PZT films	46
4.3.1	Structural, morphological and ferroelectric switching properties	46
4.3.2	Oxide electrodes for PZT films	49
4.4	Magnetic properties of PZT/LSMO/STO heterostructures	51
4.5	Conclusion	53
5	Magnetotransport and magnetic characterization of ferroelectric field effect devices (FeFEDs)	54
5.1	Engineering of the FeFEDs for magnetotransport and magnetic studies	55
5.2	P-dependent in-situ SQUID measurements	58
5.3	Magnetotransport studies of the FeFEDs	60
5.3.1	FeFED on STO	60
5.3.2	FeFED on LSAT	68
5.3.3	FeFED on LAO	71
5.4	Anisotropic magnetoresistance study of FeFEDs on STO	73
5.5	Magnetotransport measurements of LSMO/PZT/LSMO/STO heterostructures .	78
5.6	Conclusion	81
6	Soft x-ray absorption spectroscopy characterization of ferroelectric field ef- fect devices	82
6.1	Theoretical and practical guide to get (semi)quantitative information from XLD and XMCD spectra	82
6.2	XLD measurements on the LSMO/PZT/LSMO/STO FeFED	84
6.2.1	Atomic multiplet calculations	90
6.2.2	XAS at the O K-edge	94
6.3	XMCD measurements for the LSMO/PZT/LSMO/STO FeFED	96
6.4	Conclusion	98
7	Conclusions	100
	References	I
	Curriculum vitæ et studiorum	VII
	Acknowledgement	X
	Eidesstattliche Erklärung	XII

List of Abbreviations

- AFM** Atomic force microscopy
- AMR** Anisotropic magnetoresistance
- CMR** Colossal magnetoresistance
- DE** Double exchange
- DOS** Density of states
- EDX** Energy dispersive x-ray analysis
- E** Electric field
- E_F** Fermi level
- FeFED** Ferroelectric field effect device
- FM–I** Ferromagnetic insulator
- FM–M** Ferromagnetic metal
- FWHM** Full-width-half-maximum
- H** Magnetic field
- J** Current density
- JT** Jahn-Teller
- LAO** Lanthanum Aluminate LaAlO_3
- LSAT** Lanthanum strontium aluminum tantalate $(\text{La,Sr})(\text{Al,Ta})\text{O}_3$

- LSMO** Lanthanum strontium manganite $\text{La}_{1-x}\text{Sr}_x\text{MnO}_3$
- M** Magnetization
- p** X-ray polarization
- P** Ferroelectric polarization
- PPMS** Physical property measurements system
- PUND** Positive-up negative-down
- PZT** Lead zirconate titanate $\text{PbZr}_{0.2}\text{Ti}_{0.8}\text{O}_3$
- rms** root-mean-square
- RSM** Reciprocal space mapping
- SQUID** Superconducting quantum interference device
- SCM** Strongly correlated material
- SOC** Spin-orbit coupling
- STO** Strontium titanate SrTiO_3
- T_C** Ferromagnetic Curie temperature
- TEM** Transmission electron microscopy
- T_{IM}** Insulator-to-metal transition temperature
- TMO** Transition metal oxide
- u.c.** Unit cell
- XAS** X-ray absorption spectroscopy
- XLD** X-ray linear dichroism
- XMCD** X-ray magnetic circular dichroism
- XRD** X-ray diffraction

*Non si smette di pedalare quando si invecchia,
si invecchia quando si smette di pedalare.
Anonymous*

*You don't leave off to cycle because you are getting older,
you get older when you stop to ride your bike.
English Translation by myself*

Over the past few years researchers in material science have been focusing their studies on oxides with special attention on the transition metal oxides (TMOs) [1]. The latter exhibit fascinating properties such as high- T_c superconductivity, insulator-to-metal transitions, colossal magnetoresistance (CMR) and anisotropic magnetoresistance (AMR). As a result, a large bibliography can be found which is especially linked to the fundamental physics, and to the application perspectives offered by those aforementioned phenomena. Though simplicity has always been an obsession for physicists that are passionate about a certain interpretation of phenomena in nature, in the field of the TMOs, physics become more intriguing, and, in this case, possible interpretations are rather far from being simple. For instance, the universal classification of materials related to their transport properties into metallic, semiconductor and insulator, turns out to be not any longer valid when it is applied to TMOs. As a result, words like *complex* break into the scientific discussion, and new paradigms are necessary in order to account for the electronic correlations on which the complexity of the oxides is mainly based. Those strong correlations are the result of the interplay between several degrees of freedom such as charge, spin and orbital order that, all together, represent the fingerprint of the $3d$ electrons. In addition, the nowadays technological advances concerning the growth of high-quality oxide heterostructures, allow one to consider a further extra degree of freedom that is based on the presence of a well-defined interface. Interestingly, different electronic and magnetic features can be designed *ad hoc* with a suitable engineering process of the oxide stack. As a result, emergent phenomena can be obtained at the interface of artificial heterostructures made of TMOs [2], [3], [4], [5]. It was stated that "the interface is the device"ⁱ. Indeed, modern electronics take advantage from the properties exhibited at the interface between two different semiconductor materials. Since the miniaturization of the semiconductor technology will soon reach the physical limit, new routes are explored in order to improve the scaling down procedure. In this framework, heterostructures constituted by oxide materials represent a viable opportunity, and an always larger scientific community is devoting its efforts towards this directionⁱⁱ. The relatively short electric field screening length in TMOs can be 10 times lower than the one characterizing a standard semiconductor, hence, enabling a reliable further scaling down step of field effect transistors [6]. Moreover, the outstanding possibility to couple the electric and the magnetic order parameters at the interface of two different oxide materials represents one of the potential routes to realize a magnetoelectrically coupled system. Accordingly, since TMOs are usually characterized by a large number of competing electronic ground states, a high sensitivity to external stimuli such as electric and/or magnetic fields is easily

ⁱThis famous phrase was coined by the Nobel laureate Herbert Kroemer.

ⁱⁱAn example is given by the European project entitled IFOX (Interfacing Oxides) with grant agreement number NMP3-LA-2010-246102. This project has also sponsored the work presented in this Thesis.

obtained. As a result, the magnetic and (magneto)transport properties of a TMO can be tuned and/or controlled by an external electric field in well engineered field effect devices.

In this Thesis a study on the modulation of the (magneto)transport and magnetic properties of a ferroelectrically gated ultrathin TMO layer, i.e. the strontium doped lanthanum manganite ($\text{La}_{0.825}\text{Sr}_{0.175}\text{MnO}_3$, $\text{LSMO}(x=0.175)$) suitably patterned in a Hall bar geometry, is presented. In what is known as a ferroelectric field effect approach, the modulation of the (magneto)transport properties of the $\text{LSMO}(x=0.175)$ layer, revealed by magnetoresistance, Hall effect and AMR measurements, has been achieved upon the reversal of the ferroelectric polarization direction. Moreover, a proper study of the magnetic properties of the $\text{LSMO}(x=0.175)$ was possible thanks to an *in-situ* switching of the ferroelectric polarization. Additionally, x-ray linear dichroism at the Mn $L_{2,3}$ -edges and O K -edge were used to obtain information regarding the energetic scale of the Mn $3d$ orbitals upon the reversal of the ferroelectric polarization direction. The subsequent chapters are organized in the following way:

Chapter 2 gives a brief introduction of the functional and physical properties related to the oxide materials employed to build the ferroelectric field effect devices, i.e. $\text{LSMO}(x=0.175)$ that was used as "sensitive" material, as already mentioned before, and $\text{PbZr}_{0.2}\text{Ti}_{0.8}\text{O}_3$ (PZT) as ferroelectric oxide. Two sections of this chapter are also devoted to a brief introduction of the physics explaining the x-ray absorption effect and to the several types of magnetic anisotropy exhibited by magnetic materials, respectively. In the last section an overview on the possible ways to obtain a measurable field effect in layered composite oxide systems is presented. Both oxide materials were grown *in-situ* in epitaxial Hall bar patterned heterostructures by using pulsed laser deposition, and characterized by x-ray diffraction techniques which are introduced in Chapter 3. Here, also the other experimental systems, utilized for the (magneto)transport and ferroelectric measurements, are introduced. Chapter 4 includes an overview of the structural and morphological characterizations undertaken on the $\text{LSMO}(x=0.175)$ and PZT films and $\text{LSMO}(x=0.175)$ /PZT heterostructures. A study of the transport properties of the $\text{LSMO}(x=0.175)$ thin films, as a function of the thickness and different strain states, is also discussed. Moreover, a complete section is dedicated to the optimization of the growth process of the PZT films along with a consistent ferroelectric characterization. The ferroelectric field effect modulation of the (magneto)transport and magnetic properties of an ultrathin layer of $\text{LSMO}(x=0.175)$ is presented in Chapter 5. A key result is discussed along with the (out-of-plane) AMR measurements, where an electrostatic modulation of the surface magnetic anisotropy of the gated $\text{LSMO}(x=0.175)$ ultrathin film is proposed. In Chapter 6 the results collected at the beam-line Deimos of the synchrotron radiation facility of Soleil in Paris, are discussed. XMCD spectra acquired at the Mn L_{2-3} -edges demonstrated a clear electrostatic modulation of the magnetic moment. Additionally, atomic multiplet simulations of the two XLD spectra acquired as a function of the polarization direction rendered a plausible anisotropy in the Mn $3d_{e_g}$ orbitals occupancy as a function of the ferroelectric polarization direction. Finally, in Chapter 7 the conclusions of this work are presented along with an outlook onto new routes opening up new possibilities in the ferroelectric field effect approach of CMR oxides.

*On fait la science avec des faits comme une maison avec des pierres;
mais une accumulation de faits n'est pas plus une science qu'un tas de pierres n'est une maison.
Henri Poincaré, La science et l'hypothèse*

*Science is built up of facts, as a house is built of stones;
but an accumulation of facts is no more a science than a heap of stones is a house.
English translation by J. Larmor*

In this chapter a phenomenological basis on the general physical properties of the perovskites $\text{La}_{1-x}\text{Sr}_x\text{MnO}_3$ and $\text{PbZr}_x\text{Ti}_{1-x}\text{O}_3$ is briefly introduced. In this respect the following sections cannot be at all exhaustive since, regarding for example the $\text{La}_{1-x}\text{Sr}_x\text{MnO}_3$, a large bibliography can be found. This is the result of an intense research activity stimulated by the exhibited complexity of the manganite system. A wide overview of the several mechanisms characterizing the $\text{La}_{1-x}\text{Sr}_x\text{MnO}_3$, either as bulk or in thin film form, is offered by detailed reviews, for example, see Refs. [7], [8], [9], [10] and [11], to which the following sections will mainly refer to. Additionally, a short introduction of a particular synchrotron x-ray technique will be presented, followed by an overview regarding the various competing energetic terms accompanying the onset of ferromagnetism in magnetic material. Finally, the state of the art regarding the ferroelectric field effect in oxides will be introduced.

2.1 Strontium-doped lanthanum manganite $\text{La}_{1-x}\text{Sr}_x\text{MnO}_3$

Over the past few decades, strongly correlated materials (SCMs) have been attracting a lot of interest because of their appealing electronic properties. The discovery of the unusually large change of the resistivity ρ under an external magnetic field H , known as colossal magnetoresistanceⁱ (CMR) [12], has been a milestone in material science. Also the so-called anisotropic magnetoresistance (AMR) effect is very important from both the fundamental and application point of view. Indeed, relevant information regarding the system can be accessed [13]. In this case the variation of the resistivity is strictly related to the relative orientation between the external magnetic field H , and the current density J . The fingerprint of SCMs [8] is the interplay between charge, spin, lattice and orbital ordering, which in turn leads, for some of them, to a remarkable sensitivity of the system to external stimuli [14]. Since the seminal studies carried out by Jonker and van Santen [15], one of the most studied SCMs is the perovskite strontium-doped lanthanum manganite, i.e. $\text{La}_{1-x}\text{Sr}_x\text{MnO}_3$ (LSMO) with x being the level of doping. Figure 2.1a shows the ideal cubic perovskite crystal structure (space group $\text{Pm}\bar{3}\text{m}$) of the formula ABO_3 . The large cations A sit at the corners of the cubic cell and the small B cations are situated at the center surrounded by 6 anions O (usually oxygens) forming the BO_6 octahedra. The O anions are located in the middle of each face of the cube, and the angles B-O-B being all 180° imply all equal B-O distances. In order to account for the unavoidable distortions that characterize the real crystal structure of many perovskite oxides, Goldschmidtⁱⁱ introduced the

ⁱUsually the formula $[\rho(H=0) - \rho(H)]/\rho(H)$ quantitatively describes the magnetoresistance effect.

ⁱⁱHere the assumption that the atoms form a purely ionic chemical bond is considered.

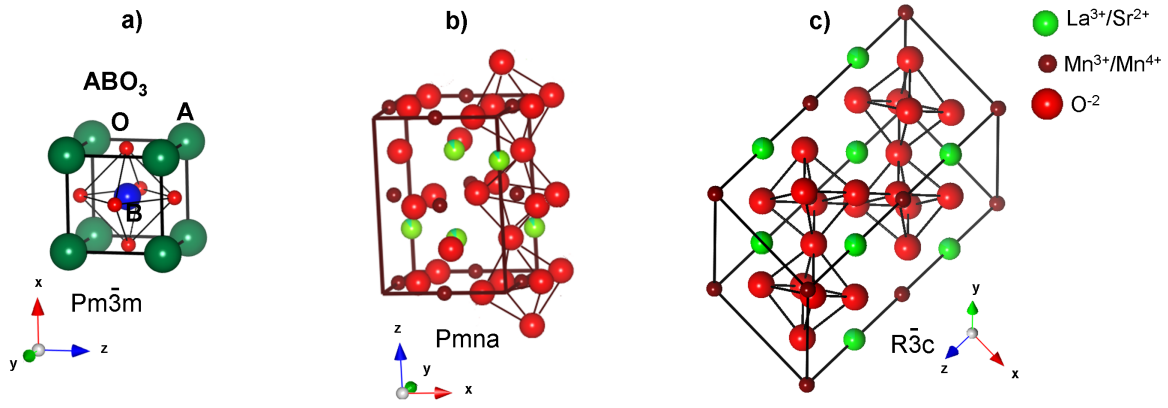


Figure 2.1: a) Ideal cubic perovskite unit cell. Ionic representation of the LSMO unit cell in the b) orthorhombic and c) rhombohedral structures. The rotation of the BO_6 octahedra is shown as well.

so-called tolerance factor t , defined from the ionic radii of the cations forming the perovskite crystal structure [16] as follows:

$$t = \frac{\langle r_A \rangle - \langle r_O \rangle}{\sqrt{2}(\langle r_B \rangle + \langle r_O \rangle)},$$

with $\langle r_A \rangle$, $\langle r_B \rangle$ and $\langle r_O \rangle$ being the averaged ionic radii of the A-site, B-site and oxygen ions, respectively. When the relation $0.9 < t < 1$ is encountered then the perovskite unit cell is stable. In the case of LSMO, the La^{3+} and Sr^{2+} cations share the corners of the pseudo-cubic perovskite structure, and the Mn ion exhibiting a mixed valence state (i.e. Mn^{3+} and Mn^{4+} , depending upon the chosen level of doping x) is at the center surrounded by six oxygens O^{2-} , hence, forming a MnO_6 octahedron. As a result, the different Sr-content modifies t , and the crystal structure may become different from the cubic one. Correspondingly, the MnO_6 octahedra rotate in order to accommodate the misfit in the ionic sizes induced by the presence of the additional Sr ions. The octahedron rotation is described through three angles which are calculated around each crystallographic direction of the cubic system ($[100]$, $[010]$ and $[001]$), indicated as Glazer angles [17]. In this respect, Figures 2.1b,c show the two typical structural distortions from the cubic one of the LSMO, i.e. the orthorhombic (space group Pmna) and rhombohedral (space group $\text{R}\bar{3}\text{c}$) phases, respectively. In this respect, upon the variation of x and/or temperature the two crystal structures can be stabilized [18], as shown by the structural phase diagram of Figure 2.2a. The modification of t drives an alteration of the Mn-O-Mn bond angles which, in turn, affect the hopping integrals between the Mn ions with a change of the Mn $3d$ band as well. As a result, different electronic correlations emerge in the system as a function of x that give rise to a manifold of ground states, usually summarized in a complex and rich electronic phase diagram. In this respect, Figure 2.2b shows the bulk phase diagram of the LSMO as a function of x . Accordingly, LSMO exhibits the low-temperature spin-canted antiferromagnetic insulating phase (AFM-CN.I) for $x < 0.1$. In this range of doping the crystal structure is orthorhombic, of which in Figure 2.2a the lattice parameter values as a function of x are also reported. With increasing hole doping, a ferromagnetic insulating (FM-I) phase is realized ($x < 0.175$) followed by a ferromagnetic metallic (FM-M) one ($x \geq 0.175$). Interestingly, at the value of $x = 0.175$, the crystal structure of the LSMO changes from orthorhombic to rhombohedral [20]. The Curie temperature T_C increases with x and reaches the maximum value of ~ 370 K around $x = 0.3$. The transition between the two FM-I and FM-M phases is very intriguing and still not fully understood [8]. Precisely, the double exchange mechanism [21] (see below) qualitatively explains only the FM-M phase and, for the more localized

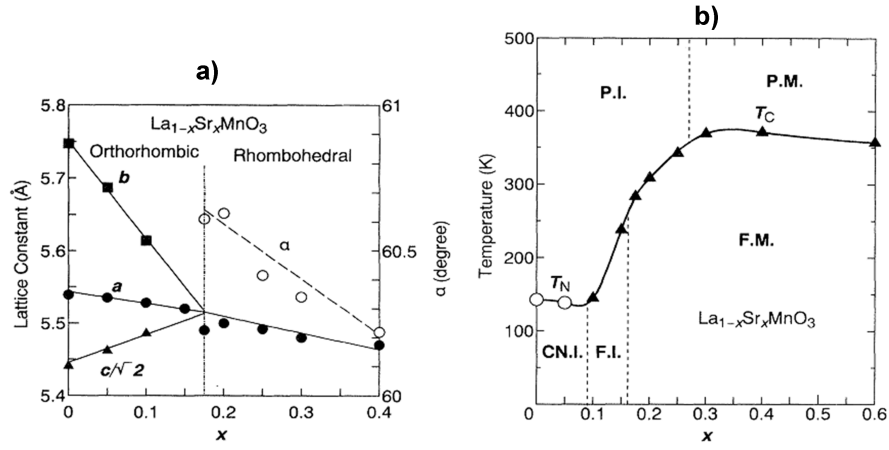


Figure 2.2: a) Structural phase and b) Electronic diagrams of $\text{La}_{1-x}\text{Sr}_x\text{MnO}_3$. Copied from Ref. [19].

electrons of the FM-I phase, the ferromagnetic interaction might be mediated through a percolative process of the local spins.

Interestingly, the distortions of the ideal cubic structure are induced also by a modification

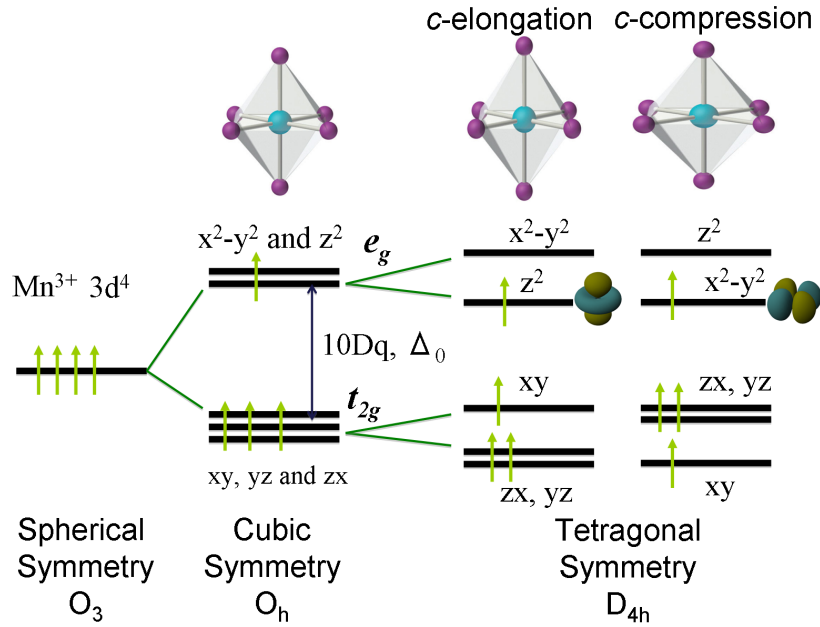


Figure 2.3: Crystal field splitting effects on the five-fold degenerate $3d$ orbitals of a Mn^{3+} ion for cubic (O_h) and tetragonal (D_{4h}) symmetries.

of the hierarchy in the energy levels related to the Mn^{3+} ions through the Jahn-Teller (JT) effect [22]. Several studies pointed out that, especially for small values of x , the JT effect is predominantly important for the magnetic as well as transport properties of the LSMO [23]. Figure 2.3 shows the effects of the crystal field splitting and tetragonal distortions induced on the energy scale regarding the $3d$ orbitals of a Mn^{3+} ion. Precisely, in an octahedral environment (i.e. MnO_6) the potential generated by the neighbouring oxygen ions (crystal field) splits the fivefold degenerate Mn^{3+} $3d$ orbitals into two distinct representations of t_{2g} and e_g symmetry [24]. The three-fold degenerate t_{2g} orbitals point between the ligands, and therefore their interaction with the octahedral ligands is smaller, i.e. xy , xy and yz in cartesian notations. Contrarily, the two-fold degenerate e_g states are formed by orbitals that point towards

the position of the ligands, i.e. $x^2 - y^2$ and z^2 in the cartesian notation, and they interact more strongly (electrostatically as well as covalently) with the ligands. The energy separation between the t_{2g} and e_g levels is indicated by $10Dq$ (or Δ_0)ⁱⁱⁱ. The t_{2g} and e_g levels further split up when a tetragonal symmetry is considered. Moreover, depending upon the direction of the JT distortion, relatively to the two e_g levels, a different order in the energy scale is obtained. Precisely, when the ligand octahedron is c -elongated, the z^2 orbitals become energetically favorable with respect to the $x^2 - y^2$ ones. On the other hand, in the case of a c -compression, the situation reverses completely, as schematically represented in Fig. 2.3. The several centers of JT distortions can also interact between each other and, consequentially, an orbital order can be obtained. In this case, the JT-induced structural distortions give rise to so-called lattice polarons [25], which mainly act localizing the e_g electrons. In this respect, especially at low temperatures and, for small values of x , the energy to pay in order to de-localize one electron of the Mn^{3+} ion is extremely high, and localization effects characterize the transport properties of the LSMO, hence, stabilizing insulating phases, either locally or at long range. Moreover, an ordered pattern of occupied and un-occupied e_g orbitals, along the several crystallographic directions, drives also the different magnetic properties of the LSMO usually categorized as magnetic modes indicated in literature with the following capital letters: A, B, C, E, CE and G (more information is in Ref. [26]). For example the orbital order related to LSMO($x=0$) is an A-type orbital system where the ordering of the Mn spins is FM in-plane and AFM out-of-plane [27]. Moreover, orbital order can be accompanied by charge ordering as well. In this respect, charge ordering is most likely obtainable for half doped LSMO with an equal concentration of Mn^{3+} and Mn^{4+} ions. The study regarding this possibility has been triggered by the potential capability of the system to develop a ferroelectric order [28].

2.1.1 Exchange mechanisms in LSMO

The magnetic properties of LSMO emerge mainly from the spin configuration related to the Mn ions. Precisely, according to Hund's first rule, the Mn^{3+} ion showing a $3d^4 t_{2g}^3 e_g^1$ electronic configuration, reveals $S=2$ with S being the total spin angular momentum. On the other hand, the Mn^{4+} ion showing a $3d^3 t_{2g}^3 e_g^0$ electronic configuration is characterized by $S=3/2$. As a result, neglecting the small orbital contribution,^{iv} their magnetic moments are $4 \mu_B$ and $3 \mu_B$, respectively. The quantity μ_B expresses the elementary magnetic dipole moment related to the orbital motion of an electron around the nucleus of the atom, i.e. the Bohr magneton. Since the exchange interactions are mediated by the oxygen ions lying between two Mn ions, the related magnetic properties of the LSMO are well explained in terms of superexchange interaction^v. Anderson showed that this kind of interaction favours an antiferromagnetic order between the Mn^{3+} ions [30]. Actually, the sign of the superexchange interactions is determined together with the orbital order, as already highlighted in the previous section, hence, a complex spin-orbital coupled state can be envisaged. In this respect, the Goodenough-Kanamori-Anderson rules [26] dictate how the local Mn spins can orient with respect to the related $3d$ orbital orientation in order to give the different magnetic modes already listed in the previous section. Additionally, the magnetic nature of the insulator-to-metal transition of the LSMO is qualitatively explained through the double-exchange (DE) mechanism [21]. The exchange interaction is always mediated by the oxygen ion between the Mn^{3+} and Mn^{4+} ions. The concentration of the latter is strictly related to the level of doping characterizing the LSMO and it increases when x increases as well. The electrons that occupy the t_{2g} levels ($S=3/2$) are strongly localized and do not participate in the transport process, which, on the other hand, is mainly depending upon

ⁱⁱⁱUsually values of $\Delta_0 \sim 1.5$ eV are encountered in the literature.

^{iv}Usually for $3d$ metal transition ions the orbital angular momentum is quenched [29].

^vThe Mn ions are sufficiently far apart as to have no magnetically ordered states that a direct Heisenberg interaction could explain.

the properties of the e_g electrons. In this respect, the intrinsic mixed valence state nature of the LSMO allows the e_g electrons to hop from one site to the other when their kinetic energy T is higher than U , i.e. the Hubbard energy that two electrons have to pay in order to share the same electronic level. In this framework, Zener showed that a simultaneous transfer of an electron from the O^{2-} to the Mn^{4+} and from the Mn^{3+} to again the O^{2-} ions is allowed when the ion configurations $Mn^{4+}-O^{2-}-Mn^{3+}$ and $Mn^{3+}-O^{2-}-Mn^{4+}$ are degenerate. The latter possibility is encountered when the core-spins ($S=3/2$) of the Mn ions are parallel. As a result, DE is always ferromagnetic and, for Mn-O-Mn bond angles lower than 180° and/or for non-parallel core-spin alignment, a decrease of the LSMO conductivity is obtained. In this respect, a relation between transport and ferromagnetism was also proposed by Zener. Precisely, it turned out that the relation $\sigma = (xe^2/ah)(T_C T)$ confirmed the available experimental data. Accordingly x is the doping level, a the Mn-Mn distance and T_C the Curie temperature of the LSMO. The concept of the DE mechanism has been also generalized by Anderson and Hasegawa [31]. As a result, the hopping procedure of the e_g electrons depends upon the angle θ between the core-spin moments of the t_{2g} electrons: $\varepsilon_t = -\varepsilon_0 \cos(\theta/2)$, ε_t being the energy associate to the hopping procedure. Hence, when the core-spin moments are aligned, i.e. $\theta=0$, the gain in energy is maximum and the system becomes more conductive than the case in which $\theta=\pi$. In this respect, Figure 2.4 shows a schematic view of the DE mechanism where, in the case of

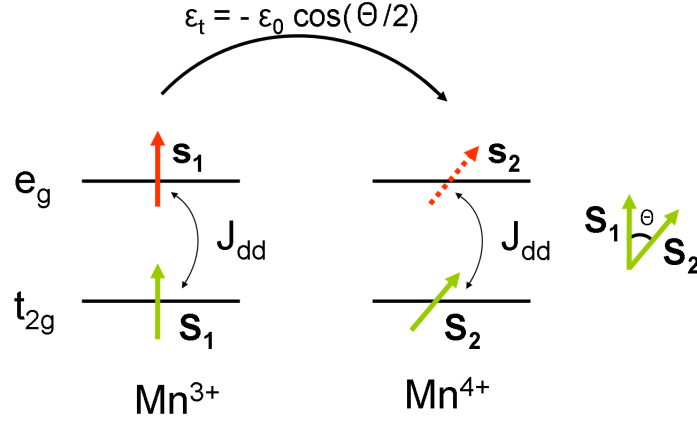


Figure 2.4: Schematic view of the DE mechanism. The green S_1 and S_2 vectors indicate the core-spin moments and the red $s_{1/2}$ vector indicates the spin associated to the hopping e_g electron.

infinitely large intra-atomic exchange integral coupling (i.e. Hund coupling J_{dd}), the hopping between adjacent e_g levels happens only in the case that the spin s_1 (indicated by the red arrow) will couple with the spin S_2 . The motion is extremely advantageous when a FM alignment (i.e. $\theta=0$ and, hence, $\varepsilon_t = -\varepsilon_0$) of the core-spin moments S_1 and S_2 is realized.

2.1.2 Properties of thin films of LSMO

As already discussed in the previous sections, JT and DE effects depend upon the Mn-O length and the Mn-O-Mn bond angle, respectively. When thin films of LSMO are considered, the use of different substrates can induce different lattice mismatches, which in turn, modifying the geometrical features of the crystal structure, induce changes on the physical properties of the LSMO itself. Generally the following formulas

$$\delta^{in} = \frac{a_{sub}(b_{sub}) - a_{film}}{a_{sub}} \quad \text{and} \quad \delta^{out} = \frac{a_{sub} - c_{film}}{a_{sub}},$$

indicate the lattice mismatch δ between the in-plane lattice parameter of the substrate, i.e. $a_{sub}(b_{sub})$, and the in-plane and out-of-plane lattice parameters of the film, i.e. a_{film} and c_{film} , respectively. Precisely, δ^{in} leads to an in-plane strain, i.e. $\epsilon_x(\epsilon_y)$, that in case of a pseudo-cubic approximation can be isotropic: $\epsilon_x = \epsilon_y$. On the other hand, δ^{out} sets an out-of-plane strain ϵ_z that is linked, according to continuum elasticity theory, to the in-plane strain through the Poisson ratio (ν) of the material that undergoes the strain, i.e. $\epsilon_z = -2\nu/(1-\nu) \cdot \epsilon_x$ [32]. Misfit strains are capable to heavily modify the properties of oxides as discussed in [33]. Regarding LSMO, indeed, magnetoresistance, magnetization and related Curie temperature values [24, 34], orbital order [35, 36] and transport properties [37], can be varied inducing different misfit strain states. Regarding the variation of the orbital ordering, Figure 2.3 can be very helpful for a basic understanding. Indeed, in the case of a positive in-plane lattice mismatch (hence the substrate is capable to induce an in-plane tensile strain of the LSMO crystal structure with $c_{film} < a_{film}$), a possible preferential occupancy of the in-plane $x^2 - y^2 e_g$ orbitals can be realized. The latter possibility is highlighted in Fig. 2.3 as a *c*-compression state. On the other hand, when an in-plane negative lattice mismatch is accomplished (hence the substrate is capable to induce an in-plane compressive strain of the LSMO crystal structure with $c_{film} > a_{film}$), a preferential occupancy of the out-of-plane $z^2 e_g$ orbitals is obtained (see *c*-elongation state in Fig. 2.3). Obviously the strain-induced anisotropy of the orbital occupancy affects also the magnetic properties of the LSMO. Accordingly, the superexchange interactions are modified since the electrons occupy different spatially oriented orbitals, hence, the DE mechanism is modified and different magnetic properties can be obtained as pointed out by Konishi and co-workers [35]. The effect of the misfit strain is capable to alter also the growth of the LSMO and phase separation can occur, which is capable to induce inhomogeneities at the film surface [38].

When thin films are studied, another important parameter that needs to be considered is the thickness value. In this respect, for thin enough films (usually several nm) a *dead layer* (which changes upon the used substrate), can be obtained which is characteristic of a worsening of both the magnetic and transport properties of the LSMO (actually of the oxide materials in general). As shown by Valencia and co-workers [39] by a synchrotron radiation spectroscopic technique, the breaking of the inversion symmetry experienced by very thin layers of LSMO drives a preferential occupation of the out-of-plane $z^2 e_g$ orbitals. For extremely thin layers of LSMO, where, hence, the interfacial states become very important, the aforementioned orbital reconstruction explains the worsening of the in-plane resistivity and of the magnetic properties, as already introduced in terms of the *dead layer* effect for very thin layers of LSMO.

Finally it is rather obvious that both thickness values and misfit strain states can be used to properly control the functional properties of the LSMO.

2.1.3 Crystal structure of the LSMO($x = 0.175$)

As already discussed in the previous section, LSMO undergoes a structural transition between the orthorhombic and rhombohedral crystal structures at $x = 0.175$. Interestingly, the rhombohedral phase which occurs at relatively high x values, prevents the occurring of static JT distortions of the MnO_6 octahedra, and better conduction properties are obtained than the ones evaluated for the orthorhombic phase. Indeed, as has already been discussed in the previous section, possible localization effects induced by the cooperative JT distortions are more likely obtained for lightly doped LSMO. The structural transition occurring at $x = 0.175$ is not so sharp as highlighted in Fig. 2.2a. Indeed, as a result of an accurate neutron diffraction characterization [40], undertaken on powder samples of LSMO grown with $x \leq 0.175$, the identification of an additional orthorhombic phase, indicated as O^* to be distinguished from the

standard one O' , was proposed. In this respect, Figure 2.5 shows the summarized results of the

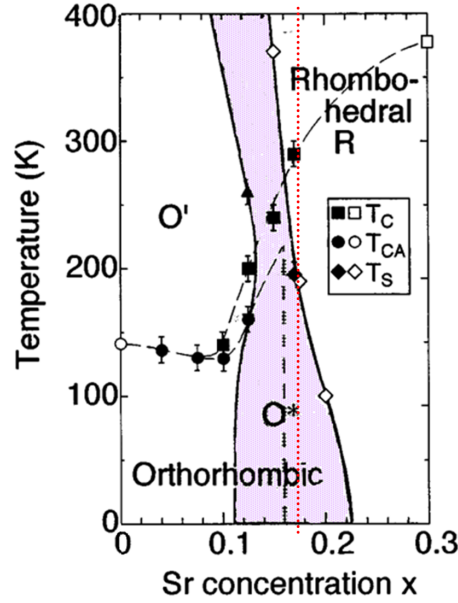


Figure 2.5: Structural phase diagram of LSMO for $x \leq 0.3$. The orthorhombic O^* is highlighted in the purple-colored area. The dotted red line gives a help for the eyes regarding the level of doping of $x = 0.175$. Graph adapted from [40].

mentioned study, where the O^* orthorhombic phase is highlighted in the purple-colored area. The O^* phase acts as a "structural bridge" between the two main stable crystal structures. Precisely, the O' phase is orthorhombic and the related lattice parameters obey to the following relation: $b/\sqrt{2} < c < a$. On the other hand, the O^* phase is more close to a pseudo-cubic phase with $b/\sqrt{2} \sim c \sim a$ with all the Mn-O bond lengths equal to ~ 0.2 nm. The orthorhombic parameters can be expressed in terms of the cubic lattice through the following simple relations: $a_{orth} \sim a_c \cdot \sqrt{2}$; $c_{orth} \sim a_c \cdot \sqrt{2}$ and $b_{orth} \sim 2 \cdot a_c$. Hence, it emerges that the LSMO with $x = 0.175$ exhibits a pseudo-cubic unit cell with $a_{pc} = 0.391$ nm since from Ref. [40] it emerges that $a_{orth} \sim 0.553$ nm. Additionally, at the temperature $T_s = 195$ K, a rhombohedral to O^* structural phase transition is observed (see dotted red line in Fig. 2.5). The latter is also observed as an anomaly in the curve that describes the temperature dependence of the resistivity at $\sim T_s = 190$ K [19].

2.2 Lead zirconate titanate $PbZr_xTi_{1-x}O_3$

The most widely studied oxide ferroelectric materials [41] are the ones that show a perovskite structure ABO_3 (see Fig.2.1a). Below T_C , a structural transition from the ideal cubic towards a lower-symmetry phase is a result of an off-center movement of the B cations with respect to the oxygen octahedra. As a result, the spontaneous polarization P emerges as a summation of the several electric dipole moments created by that off-centering process^{vi}. From the symmetry point of view, ferroelectric materials show a space-inversion symmetry breaking. However, the latter is a necessary but not sufficient condition on the base of which a material can be categorized as ferroelectric. Indeed, additionally, P has to be switchable between two stable states of opposite polarization direction by applying an external electric field.

Lead zirconate titanate, $PbZr_xTi_{1-x}O_3$, is a very well known ferroelectric perovskite oxide. As a result of the progress, nowadays, ceramic lead zirconate titanate is used as a non-volatile

^{vi}The origin of ferroelectricity is not only related to the appearing of a cation/anion off-centering, but geometric constraints or spin, charge and orbital degrees of freedom can play a vital role as well [42].

and high-density memory element and, indeed, it takes place in the large-scale production of the memory boards of the Sony Playstation (4Mb FRAM Samsung). Figure 2.6 shows the structural phase diagram related to the PbZrO_3 - PbTiO_3 solid solution system [43]. On increasing the percentage amount of PbTiO_3 , the ferroelectric oxide undergoes a structural phase transition from the ferroelectric rhombohedral (polarization directed along $[111]_R$), to the high-temperature tetragonal phase (polarization directed along $[001]_T$). Additionally, at $x=0.52$ a morphotropic phase boundary separates the two aforementioned structures [44]. In this Thesis, ceramic targets (Pi-Kem Ltd) of $\text{PbZr}_{0.2}\text{Ti}_{0.8}\text{O}_3$ (PZT), were used to grow all the ferroelectric oxide thin films. At that composition (see red dotted line in Fig. 2.6), the exhibited

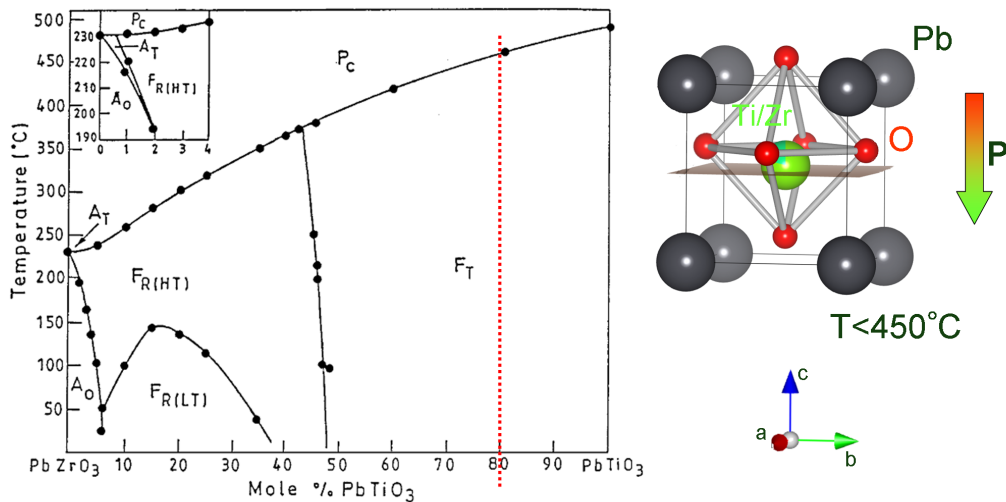


Figure 2.6: Structural phase diagram related to the PbZrO_3 - PbTiO_3 solid solution system copied from [43]. The dotted red line indicates the composition used for the PZT films grown in this Thesis. The related tetragonal perovskite unit cell along with the relative displacements between cations and anions are shown as well.

tetragonal crystal structure (space group $P4mm$), shows for room temperature the following lattice parameters: $a_T = b_T = 0.395$ nm and $c_T = 0.415$ nm. The ferroelectric properties of the PZT are due to the relative off-centering of the central cations Zr/Ti with respect to the oxygen octahedra, as schematically depicted in Figure 2.6, where the downward arrow indicates the ferroelectric polarization P . Accordingly, it has been pointed out by Jia and co-workers [45] through a transmission electron microscope technique based on a negative spherical-aberration imaging (NCSI) technique, that the cations (Zr/Ti) and anions (O) of the PZT perovskite unit cell move in the same direction of the tetragonality relative to the Pb ions. As a result, the ferroelectric polarization occurs, since the anions show a higher vertical displacement than the cations.

PZT thin films exhibit a lowering of the P saturation and paraelectric-to-ferroelectric transition temperature values as the overall thickness is decreased. However, in literature it is possible to find both theoretical [46] and experimental [47] proofs that the intrinsic polar properties of perovskite ferroelectric oxides are independent from size effects. Precisely, synchrotron x-ray studies performed on the free surface of 3 unit cells (u.c.) thick PbTiO_3 films demonstrated that a possibility to retain the ferroelectric properties is realized. Actually, in the reality the things are more complex, since metallic electrodes that are capable to generate the necessary amount of charges in order to screen/compensate the depolarizing field are missing. Hence the effect of the depolarizing field is to create a minimum thickness value below which the ferroelectric properties of the oxide completely disappear. Moreover, Lee and co-workers [48] have shown that the relative displacements between cations and anions of a PZT thin film are

practically insensible to the strain induced by a suitable substrate. The spontaneously occurring displacements in the PZT are already much larger than in the case of the ferroelectric BaTiO₃, where on the other hand, indeed, an effective improvement of the polarization magnitude can be obtained by strain. In the case of PZT, as shown by Vrejoiu and co-workers, [49] the possibility to get high polar ferroelectric dipoles is mainly given by defect-free PZT thin films, hence, a good optimization of the PZT growth parameters needs to be achieved in order to get saturation polarization values of about 100 μCcm^{-2} .

2.3 Basics of x-ray absorption spectroscopy

X-ray absorption spectroscopy (XAS) is an extremely powerful, element-sensitive technique that provides information related to the unoccupied density of states of the specific element investigated. Precisely, when a material is irradiated by x-rays, core electrons are excited into an empty state just above the Fermi level. Nowadays, mainly synchrotron radiation is used as a tunable and intense x-ray source. XAS spectra are obtained varying the energy of the incident monochromatic radiation in the specific range where the transitions of core electrons to the excited states need to be studied. In the case of soft x-rays the energy generally is ranging from ~ 20 eV to ~ 2000 eV. The absorption process is usually described quantum mechanically, by using Fermi's golden rule. The latter states that the transition of a system from an initial state i to a final state f , has a probability P to take place, in formula:

$$P_{i \rightarrow f} = \frac{2\pi}{\hbar} |\langle f | T | i \rangle|^2 \delta_{E_f - E_i - \hbar\nu}.$$

T indicates the x-ray absorption transition operator (including all possible transitions) and the delta function accounts for the energy conservation. In order to explicitly calculate T in particular situations, the Hamiltonian describing the interaction of x-rays with electrons i.e. H_{int} , needs to be considered. In this respect, in the framework of perturbation theory as the first term of the series development, it is written: $H_{int} = (e/mc) \vec{p} \cdot \vec{A}$, where $\vec{A} = A_0 \cos(kx - \omega t) \hat{e}_p$ (with \hat{e}_p being the unitary vector related to the polarization p of the incoming x-rays), and \vec{p} represents the vector field and the moment operator of an electron, respectively. By re-writing the cosine function of \vec{A} as an exponential function, i.e. $2\cos(kx - \omega t) = [e^{i(kx - \omega t)} + e^{-i(kx - \omega t)}]$, and by keeping only the related absorbing term ($e^{-i\omega t}$), the well-known dipole approximation form for the transition operator T is obtained: $T_1 \approx \sum_p \hat{e}_p \cdot \vec{p}$. It follows that, in the dipole approximation, the selection rules (see below) allow XAS transitions if the relations $\Delta L = \pm 1$ and $\Delta S = 0$ are respected, L and S being the angular and spin momentum quantum numbers, respectively. As a result, only transitions between atomic levels for which the related orbital moments differ by one are allowed (i.e. $s \rightarrow p$, $p \rightarrow s$, $p \rightarrow d$, etc.). On the other hand, for quadrupole transitions (i.e. $(\hat{e}_p \cdot \vec{p})(\vec{k} \cdot \vec{r})$) which are obtained by considering the second term in the perturbation theory applied to H_{int} , the relation $\Delta L = \pm 2$ has to be respected between initial and final states (i.e. $s \rightarrow d$, $p \rightarrow f$, etc.)

Generally, the absorption process is detected in transmission mode where the incoming photon intensity is measured before and after the sample. Nevertheless, for soft x-rays usually the absorption is obtained using the different decay mechanisms of the created core-hole. As a result, yield (electron or photon) measurements offer an alternative to the transmission mode experiments which are based on two different detection methods: total electron yield (TEY) and total fluorescence yield (TFY). The excited system subsequently returns to the ground state principally by following either an Auger decay process or by emitting a photon (fluorescence) [50]. In the soft x-rays region the Auger process dominates the decay (99% of probability). Therefore, one possibility to measure a signal that is proportional to the XAS signal, is given by the

total electron yield mode. In this case, all the electrons that escape the sample (of course from the region exposed to the x-rays), irrespective of their relative energy, are detected. As a result, the sample is positively charged and, if suitably grounded, a flow of current is generated to re-establish the neutrality. The current, measured by a picoammeter, is proportional to the XAS signal. Due to the finite mean free path of the electrons, the TEY detection mode is mainly a surface sensitive technique. The effective thickness explored is approximately ranging from 3 to 10 nm [51]. On the other hand, the TFY method detects the photons that are emitted after a core-hole is neutralized by a transition of an electron from a higher energy lying shell (usually on a femtosecond time scale). The amount of fluorescence decay increases with energy and, without entering into details, for example, the $3d$ transition metals show strong fluorescence at the K -edge and mainly Auger decay at all the other edges [52]. The advantage to use the TFY detection mode (in comparison to the TEY one), is mainly related to the higher sensitivity to the bulk. Indeed, the mean free path of the photons show the same order of magnitude as the incoming x-rays (~ 60 nm at 2000 eV), which excludes any surface effect. However, as a drawback, saturations and self-absorption effects are the cause of signals that are not proportional to the XAS characteristics. As a result, the XAS spectral shape is modified in a very complicated manner and the related interpretation is difficult to be accomplished.

The XAS spectra described in this Thesis were obtained using the TEY technique at the Mn $L_{2,3}$ -edges, i.e. the $2p \rightarrow 3d$ transition, and at the O K -edge, i.e. the $1s \rightarrow 2p$ transition. Generally, the electronic properties of several materials are studied making a net distinction between localized and itinerant electrons, and two different models are successfully employed to analyze the respective experimental results [53]. As a result, in order to successfully explain the XAS process the interaction between the electrons and the core-hole created after the $2p \rightarrow 3d$ transition needs to be properly considered in any theoretical model to reproduce the observed spectrum. As a consequence of this strong local interaction, the final state in the XAS process, is successfully described through the $2p3d$ multiplets theory which correctly describes the correlated electronic states in partly filled atomic shells and consequently the shape of the XAS spectra.

Below, few elements regarding the atomic theory are presented. The main focus will be given to the usual nomenclature used in order to be able to clearly read the subsequent sections. For more detailed information, the reader can refer to the textbook written by Fuggle [54].

By following the Russel-Saunders (LS) coupling scheme, the electronic configuration of each atom or ion with partially filled shells is named *term* and denoted spectroscopically as ^{2S+1}L , where S and L define the spin and orbital moments, respectively. The orbital moments, $L = 0, 1, 2, 3, \dots, etc.$, are usually indicated with the letters $s, p, d, f, \dots, etc.$ An LS state is degenerate $(2L + 1)(2S + 1)$ times and, by including the spin-orbital coupling ($\sim \vec{L} \cdot \vec{S}$), the degeneracy is partially lifted giving $2J + 1$ energy levels, where $\vec{J} = \vec{L} + \vec{S}$ is the total orbital moment. Each level is characterized by a total orbital moment ranging as $|L - S| \leq J \leq |L + S|$. The *term* related to the final collection of all levels is denoted as $^{2S+1}L_J$, where the quantity $2S + 1$ is called the spin multiplicity of the *term*. As a result, *terms* with different spin multiplicity form a multiplet originating from a single configuration. Experimentally, a multiplet effect can be visible in XAS depending on the core levels' lifetime broadenings. To give some examples, for an ion characterized by the electronic configuration $2p^5$, with $L = 1$, $S = 1/2$, and $J = 1/2, 3/2$ (since the spin-orbital coupling is important in this case), the *terms* are $^2P_{1/2}$ and $^2P_{3/2}$. In a XAS experiment where the energy of the x-rays is chosen to excite $2p$ core-electrons of a transition metal element, the previous introduced *terms* represent the L_2 and L_3 peaks commonly observed in the XAS spectrum. Indeed, the XAS process excites a $2p$ core-electron into the first empty $3d$ level, and in a general form, the transition can be described as follows: $2p^6 d^n \rightarrow 2p^5 d^{n+1}$. Specifically considering the Mn ions, they will absorb part of the incoming x-rays at the energy

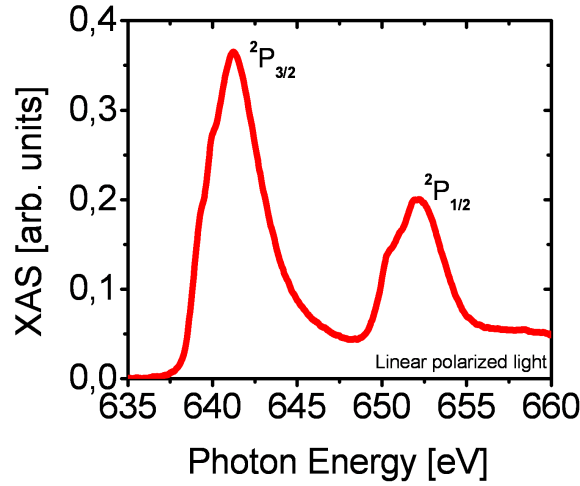


Figure 2.7: Example of a XAS spectrum obtained in TEY mode detection at the Mn $L_{2,3}$ -edges for a PZT/LSMO/STO bilayer. Both layers were grown with 5 nm thickness each.

of ~ 640 eV so that a sharp rise in the absorption will be observed (absorption edge). The binding energy of the excited $2p$ core level determines the energy at which the absorption edge is observed. As an example, Figure 2.7 shows the XAS spectrum obtained at the Mn $L_{2,3}$ -edges of a 5 nm thick LSMO film capped by a 5 nm PZT layer on an STO substrate. The spectrum is composed by two main peaks separated by an energy gap which is close to the spin-orbit coupling exhibited by the electrons in the $2p$ core-levels. They correspond to the ${}^2P_{3/2}$ and ${}^2P_{1/2}$ terms. The relative intensities of the two peaks is also ruled by the spin-orbit coupling, and the following formula is usually used to get quantitative information:

$$\frac{I_{L+1/2}}{I_{L-1/2}} = \frac{L+1}{L}$$

In the case of $L=1$ (p levels) we obtain that the relative intensities of the ${}^2P_{3/2}$ and ${}^2P_{1/2}$ levels have to respect the proportion 2:1 (as roughly obtained for the XAS spectrum shown in Fig. 2.7). The relatively smooth background observed at energies higher than ~ 655 eV is explained through the contribution of transitions, although much weaker, of the form $2p \rightarrow 4s$.

2.3.1 X-ray linear dichroism

Linear dichroism in the x-ray absorption (XLD) at the L -edge gives information regarding the spatial occupancy of the distinct orbitals that are investigated. A well-known example is given by the results obtained studying manganite compounds [55]. The XLD spectrum is calculated from the difference between the XAS spectra acquired with two different linear polarizations, p , of the incident radiation, i.e. parallel (p_{ab}) and perpendicular (p_c) to the sample plane, respectively. As a result, if I_{ab} represents the XAS intensity measured with the light polarized parallel to the sample plane, and I_c is the XAS intensity measured with the light polarized perpendicular to the sample plane, then the difference $I_{ab} - I_c$ gives a direct information on the empty $3d$ orbitals. Precisely, a positive (negative) $I_{ab} - I_c$ value is representative of a preferred out-of-plane (in-plane) orbital occupancy of the available electrons. Hence, regarding the electronic configuration of the LSMO, the anisotropic orbital occupancy of the two e_g levels can be studied. Accordingly, the calculated area of the XLD spectrum, which is on average positive (negative) indicates a preference of the out-of-plane z^2 (in-plane $x^2 - y^2$) orbitals. Figure 2.8 offers a schematic view of the XLD process related to the possible $3d$ orbital occupancy.

Moreover, it has also been proven by XLD, that for thin films of $\text{La}_{0.7}\text{Sr}_{0.3}\text{MnO}_3$, tensile strain

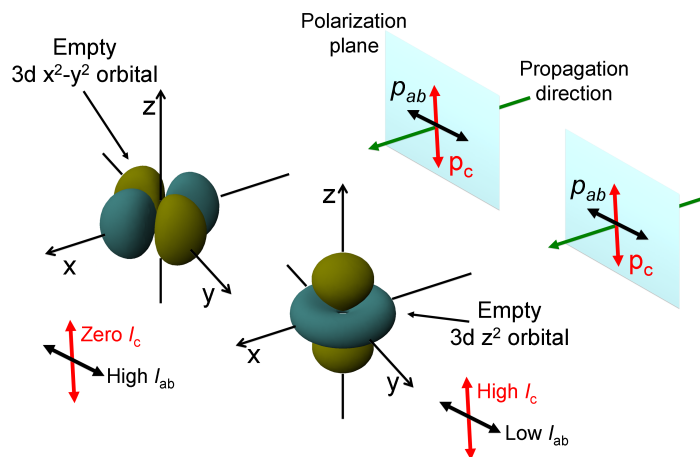


Figure 2.8: Schematic view of the XLD process. A preferential $3d x^2 - y^2$ orbital occupancy is obtained when I_c is larger than I_{ab} ; vice versa, a preferential $3d z^2$ orbital occupancy is obtained when I_{ab} is larger than I_c .

favors a preferential occupancy of the $3d x^2 - y^2$ orbitals and, vice-versa, compressive strain favors a preferential occupancy of the $3d z^2$ orbitals [56], [57]. As an example of XLD spectra,

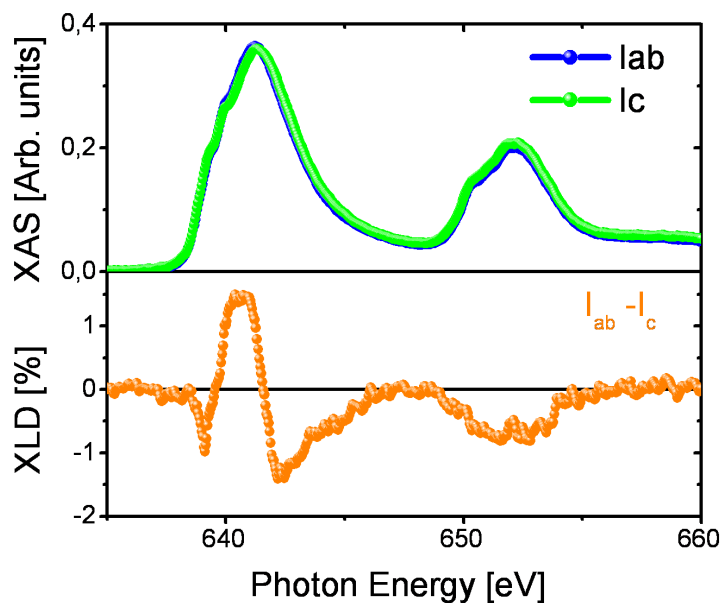


Figure 2.9: (Upper part) Polarization-dependent Mn $L_{2,3}$ -edges XAS spectra obtained for a 8 nm thick LSMO film grown on top of a PZT film 100 nm thick. The spectra were acquired in a grazing incidence geometry (x-ray beam at $\sim 30^\circ$ from the sample normal) at the temperature of 300 K. (Lower part) Calculated XLD spectrum, i.e. $I_{ab} - I_c$.

Figure 2.9 displays the light polarization dependent XAS Mn $L_{2,3}$ -edges spectra (upper part) together with the calculated linear dichroism $I_{ab} - I_c$ (lower part). The XAS spectra were acquired at 300 K for a LSMO film 8 nm thick grown on top of a 100 nm thick PZT layer. By applying the sum rule to the obtained XLD spectrum, as will be more clear later, in this case a preferential $3d_{x^2-y^2}$ orbital occupancy can be concluded.

2.3.2 X-ray magnetic circular dichroism

X-ray magnetic circular dichroism (XMCD) uses the polarization properties of the x-rays to extract information regarding the magnetic properties of the material investigated. Precisely, the XMCD is the difference between the XAS spectra of a ferromagnetic material acquired with left and right circularly polarized light, *CL* and *CR*, respectively. The inset of Figure 2.10 clarifies the geometry convention adopted for the light polarization. A photon carries an intrinsic angular momentum, $j = 1$, that is always parallel to the direction of motion. Regarding the absorption process, j is referred to as photon helicity or photon spin angular moment, and the terms "spin-up" and "spin-down" are used to define the polarization state of the photons. Accordingly, $m_j = +1$ and $m_j = -1$ indicate *CL* (parallel to the motion direction) and *CR* (antiparallel to the motion direction) polarized photons, respectively. As a result, the XMCD is a powerful element-selective magnetometry technique [58]. Moreover, the spin and orbital contribution, to the total magnetic moment, can be completely separated due to the XMCD sum rules (see later) [59].

In order to successfully describe the XMCD process, the main consideration to be done concerns the absorption of circularly polarized x-ray photons which leads to a spin polarization of the photoelectrons due to the spin-orbit coupling [60]. Moreover, according to the selection rules imposed by the electric dipole transitions of the XAS process (i.e. $\Delta S = 0$), spin-up (spin-down) photoelectrons from the $2p$ core levels can only be excited into spin-up (spin-down) $3d$ states. Since the ${}^2P_{1/2}$ and ${}^2P_{3/2}$ levels have opposite spin-orbit coupling, the spin polarization will be opposite at the two different L_3 and L_2 edges, respectively. By considering the Stoner model for magnetic materials, which postulates the presence of two subbands unevenly filled by spin-up and spin-down electrons (see upper part of Fig. 2.10a), the $3d$ band acts as a spin (orbital) moment "detector". Precisely, using the spin configuration sketched in Fig. 2.10a, due to the higher number of unoccupied spin-up states, at the L_3 -edge (dark yellow area) the XAS intensity is higher for *CL* photons than the one obtained with *CR* photons. Due to the opposite spin-orbital coupling (i.e. $L - S$) exhibited at the L_2 -edge, the situation completely reverses, i.e. the measured XAS intensity is higher with *CR* polarized photons. The latter circumstance is schematically reproduced in Figure 2.10a, through the thick arrows. The relevant success of the XMCD technique is mainly related to sum rules which provide the magnitude of the spin and orbital momentum separately. Indeed, referring to the lower part of Figure 2.10a,b, the difference of the XAS spectra obtained with *CL* and *CR* photons (i.e. $CR - CL$) gives two peaks, i.e. A (L_3 -edge) and B (L_2 -edge), respectively. As already highlighted before, the ${}^2P_{3/2}$ and ${}^2P_{1/2}$ levels have opposite spin-orbit coupling and, consequently, A and B have opposite sign as well. The A and B intensities and their differences are quantitatively related, by sum rules, to the number of $3d$ holes and the magnitude of the spin and orbital magnetic moments. Accordingly, the sum rules, $A - 2B$ and $A + B$, link the XMCD intensity to the spin moment and the orbital moment of the $3d$ band, see Fig. 2.10a and Fig. 2.10b, respectively. As a result, Figure 2.11 shows a typical example of an XMCD spectrum calculated at the Mn $L_{2,3}$ -edges for a 5 nm thick LSMO film covered by an equally thick PZT layer. The XAS spectra were acquired at the temperature of 4 K with an applied magnetic field of 2 T along the x-ray propagation direction.

2.3.3 Sum rules

As already highlighted before, the sum rules are very important when quantitative information needs to be discussed. In Ref. [61] it has been shown that the x-ray linear dichroism integral D_L

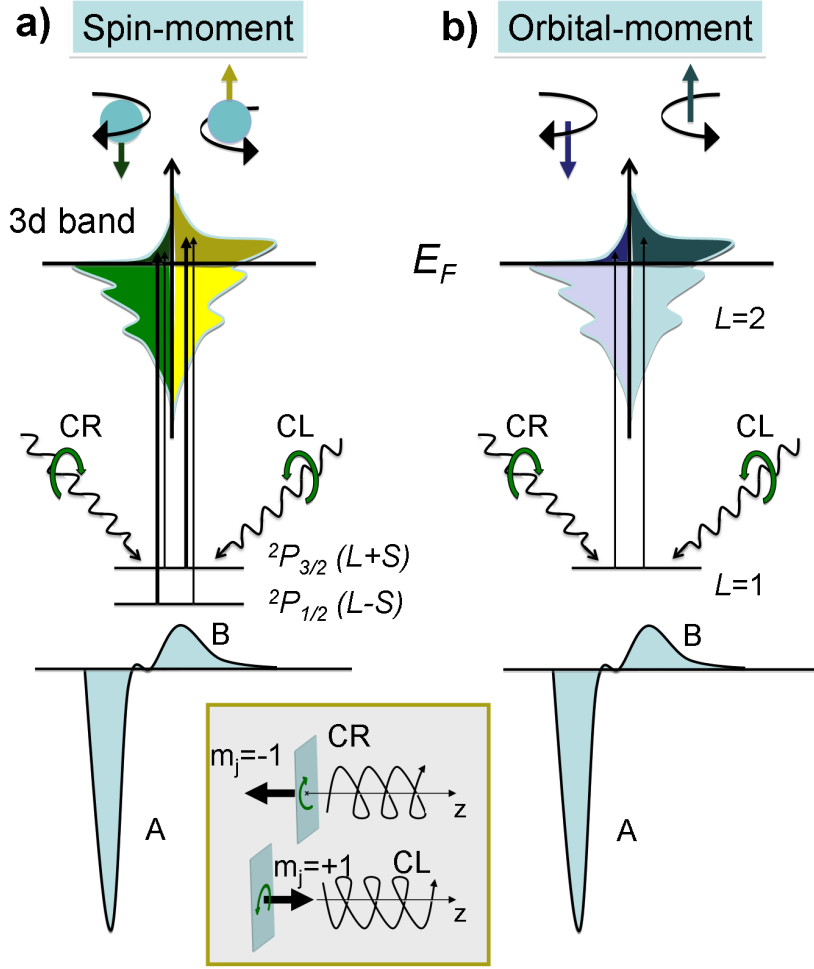


Figure 2.10: (Upper part) One electron picture of the XMCD process from which the spin-moment (a) and the orbital-moment (b) of the magnetic material can be obtained. The 3d band is split into spin-up and spin-down subbands (Stoner model). The absorption process of CL photons mainly excites spin-up electrons (${}^2P_{3/2}$) and, vice versa, the absorption of CR photons excites spin-down electrons (${}^2P_{1/2}$). (Lower part) Dichroic difference of the XAS spectra acquired with CL and CR photons, respectively. By using the sum rules it is possible to obtain the spin-moment and the orbital-moment contribution to the total magnetic moment of the material. More information are in the text. Scheme re-adapted from [58]. (Inset) Adopted geometry convention for the x-ray circularly (CR and CL) polarized light.

is related to the expectation value of the angular momentum operator L , through the following relation:

$$D_L = \frac{\int_{L_3+L_2} (I_{ab} - I_c) dE}{\int_{L_3+L_2} (2I_{ab} + I_c) dE} = \frac{\langle Q_{zz} \rangle}{h(2L-1)L} = \frac{\langle \sum_i [3L_z^2 - L(L+1)]_i \rangle}{2h(2L-1)L}. \quad (2.1)$$

As already stated above, I_{ab} and I_c represent the XAS intensity measured with light polarized parallel and perpendicular to the sample plane, respectively. $\langle Q_{zz} \rangle$ is the expectation value of the quadrupole moment relative to the local charge around the absorbing Mn atoms. Generally from the symmetry point of view, $\langle Q_{zz} \rangle \neq 0$ in all cases where the probed system has a symmetry lower than cubic. $h = 2(2L+1) - n$ represents the number of holes in the final 3d states with n electrons and L_z is the projected angular momentum along the z -axis. Through simple algebra steps, it is possible to determine the relation between D_L and the anisotropic occupancy of the 3d orbitals, considering the values of h , L and of L_z for each orbital. Finally, by considering the atomic multiplet approach as valid and an equal occupation of the in-plane and out-of-plane t_{2g}

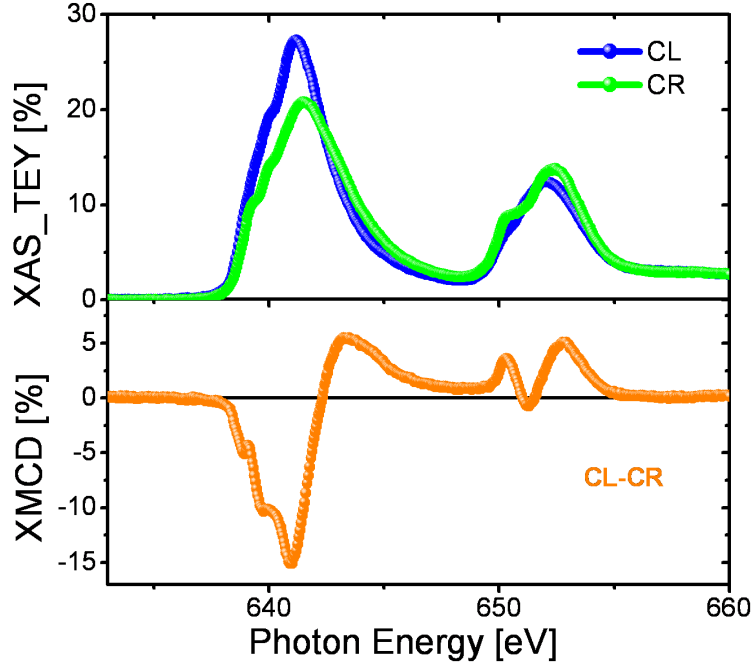


Figure 2.11: (Upper panel) XAS spectra (*CR* and *CL* polarized light) acquired at the Mn $L_{2,3}$ -edges at the temperature of 4 K for a PZT/LSMO/STO bilayer. Applied magnetic field of 2 T along the x-ray propagation direction. (Lower panel) The difference of the two XAS spectra gives the XMCD spectrum.

orbitals, the sum rule for the linear dichroism can be simply expressed through the following relation:

$$D_L = \frac{h_{x^2-y^2} - h_{z^2}}{12}. \quad (2.2)$$

This sum rule is valid only in the case that the magnetic (spin) contribution to the XLD is completely absent.

Regarding the XMCD spectrum obtained at the Mn $L_{2,3}$ -edges, two sum rules (already partially introduced in the previous section) are capable to unambiguously determine the orbital (m_{orb}) and effective spin (m_{spin}^{eff}) contributions to the total magnetic moment [62], which are expressed through the following formulae (in units of $\mu_B/u.c.$):

$$m_{orb} = -\frac{4}{3} \frac{\int_{L_3+L_2} (I_{CR} - I_{CL}) dE}{\int_{L_3+L_2} (I_{CR} + I_{CL}) dE} h = -\frac{4}{3} \frac{q}{r} h,$$

$$m_{spin}^{eff} = \frac{6 \int_{L_3} (I_{CR} - I_{CL}) dE - 4 \int_{L_3+L_2} (I_{CR} - I_{CL}) dE}{\int_{L_3+L_2} (I_{CR} + I_{CL}) dE} h = \frac{6p - 4q}{r} h =$$

$$= 2\langle S_z \rangle + 7\langle T_z \rangle. \quad (2.3)$$

Here I_{CR} and I_{CL} stand for the XAS spectra obtained with *CR* and *CL* polarized light, respectively; and h represents the number of holes in the $3d$ states. The quantities p , q and r just indicate the listed integrals in the left hand side of the equations. Moreover, $\langle T_z \rangle$ is the expectation value of the spin quadrupole coupling operator and $\langle S_z \rangle$ is the wanted spin moment. The magnitude of $\langle T_z \rangle$ plays an important role in the application of the sum rule to the analysis of the experimental spectra. Usually, the option to consider it equal to zero is followed (if not accessible from a different experiment). As a result, the impossibility to easily define it becomes

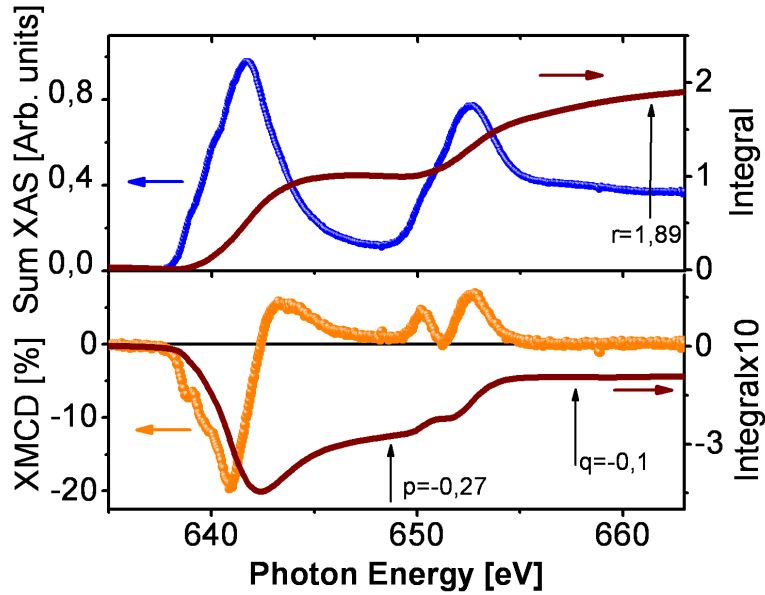


Figure 2.12: Example of the application of the sum rules for XAS spectra acquired with *CR* and *CL* polarized radiation at the Mn $L_{2,3}$ -edges. In a) the sum spectrum is shown (blue dots), i.e. $(I_{CR} + I_{CL})$; integration over the energy in correspondence to the two L_3 and L_2 peaks gives (purple solid line) a value of $r=1.89$. In b) the XMCD spectrum is shown (orange dots), i.e. $(I_{CR} - I_{CL})$. Here the two black arrows indicate the results of the integration over the energy (purple solid line), obtained considering only the first peak L_3 and both peaks with the relative values of $p=-0.27$ and $q=-0.1$, respectively.

a source of error in the sum rule regarding the determination of the spin magnetic moment. Figure 2.12 shows, as an example, the definition of the quantities p , q and r . Precisely, in Fig. 2.12a the sum of the two spectra acquired with *CR* and *CL* polarized light is shown, with related integration (purple line), and the value r is indicated as well. Moreover, in Fig. 2.12b the XMCD spectrum is shown with the related integration (purple line); in this case the values of p and q are indicated as well.

2.4 Magnetic properties

The ground state of a magnetic material is the result of a competition between several energetic terms. In general, the Zeeman energy term aligns the magnetization M along the direction of the applied magnetic field H , i.e. $E_{Zeeman} = -\vec{H} \cdot \vec{M}$. Additionally, the exchange interaction energy term describes the long-range magnetic order related to the interaction between the several magnetic moments of spin S of the ferromagnetic ions, i.e. $E_{ex} = -\sum_{i \neq j} J_{ij} \vec{S}_i \cdot \vec{S}_j$, where J_{ij} indicates the exchange constant between two different spins. Precisely, for a positive (negative) J_{ij} sign the spins align in a parallel (anti-parallel) way and a ferromagnetic (anti-ferromagnetic) order is obtained. Another energetic term that is also very important to be considered is the one stemming from the magnetic anisotropy. The latter simply means that the magnetic properties of the material are strictly related to the direction along which the measurement is performed. Examples of a directional dependence of the magnetic properties are given by the magnetocrystalline anisotropy term (E_{mc}), to minimize the spin-orbital coupling, and the shape anisotropy term (E_{shape}) to minimize the magnetostatic energy. It is important to highlight that the aforementioned energetic terms characterize the Hamiltonian of the magnetic material differently if the latter is studied in bulk or thin film form. The following sub-sections are mainly based on the book "Introduction to magnetic materials" written by Cullity and Graham [63].

2.4.1 Shape anisotropy

The shape of the sample represents a source of magnetic anisotropy. Precisely, the concept of shape anisotropy is mainly based on magnetostatic considerations. When the magnetization (or at least one of its components) of a thin film is lying along the out-of-plane direction (i.e. c -axis), the magnetic dipoles so oriented give rise to a demagnetizing field $H_d = N_d M$, where N_d is the demagnetizing coefficient. H_d acts to reduce M along the c -axis and, hence, a higher H value is required to completely orient M along the reduced dimension of the sample. However, keeping the discussion rather general, the magnetic shape anisotropy energy term for a sample shaped as a prolate spheroid is expressed as follows:

$$E_{shape} = \frac{1}{2}N_c M^2 + \frac{1}{2}(N_a - N_c)M^2 \sin^2 \theta, \quad (2.4)$$

where N_c and N_a represent the demagnetizing coefficients along the two semi-major c and semi-minor a axes, respectively. Equation 2.4 shows an angle-dependent term similar to a material characterized by a uniaxial contribution term of the magnetic anisotropy (see later). As a result, for a thin film the magnetic shape anisotropy constant becomes:

$$K_{shape} = -\frac{1}{2}N_c M^2, \text{ since } N_c \gg N_a. \quad (2.5)$$

2.4.2 Magnetocrystalline anisotropy

Regarding $3d$ materials like the case of LSMO, the magnetocrystalline anisotropy energy term E_{mc} originates from the crystalline field (see Fig. 2.3) and spin-orbit coupling (SOC). Precisely, the oxygen octahedra act through the generated crystal field potential, lifting the degeneracy of the Mn $3d$ electronic levels, and as a result the orbital magnetic moments of the surrounded transition metal ions are quenched. Accordingly, the orbitals akin to the Mn ions are strongly fixed to the lattice and only by using very high magnetic field (several Tesla) their spatial orientation can be altered. When an external magnetic field tries to rotate M , since the orbitals are spatially unchanged, the spin system is successfully oriented when the SOC energy is suitably exceeded. As a consequence, E_{mc} favours the alignment of magnetization along particular directions or planes, called easy axes or planes. The high energy direction (or plane) is a hard axis (or plane). Depending upon the particular crystal structure of the magnetic material the magnetocrystalline anisotropy energy term can be expanded phenomenologically as follows:

$$E_{mc} = K_0 + K_1(\alpha_1^2 \alpha_2^2 + \alpha_2^2 \alpha_3^2 + \alpha_1^2 \alpha_3^2) + K_2(\alpha_1^2 \alpha_2^2 \alpha_3^2) + \dots \text{cubic structure} \quad (2.6)$$

$$E_{mc} = K_0 + K_1 \sin^2 \theta + K_2 \sin^4 \theta + \dots \text{hexagonal structure} \quad (2.7)$$

where K_0, K_1, K_2, \dots are constants of the material. Moreover, $\alpha_{1,2,3}$ are the direction cosines related to the \vec{M} direction with respect to the cubic crystal structure, and θ is the angle between \vec{M} and the c -axis of the hexagonal crystal structure. Usually K_2 is so small that it can be neglected and, hence, the higher terms are practically never considered. In this respect, materials that exhibit a cubic crystal structure are characterized by a biaxial anisotropy when considered in the form of thin films, i.e. the two easy axes are in the plane. Hence, it can be written: $E_{mc} = K_0 + (K_1/4) \sin^2 2\theta$. Interestingly, if H is applied in the plane of such a thin film and E_{mc} is measured, a four-fold symmetry curve is obtained. On the other hand, considering a material with a hexagonal crystal structure, on the first order E_{mc} is characterized by a uniaxial contribution term, i.e. $E_{mc} = K_u \sin^2 \theta$, and a two-fold symmetry curve is measured. In the case of a LSMO thin film the JT distortions lower the symmetry with respect to the cubic perovskite, hence, a uniaxial contribution is expected for the magnetocrystalline anisotropy term.

Additionally, due to the breaking of symmetry experienced by the surface atoms, the concept of surface magnetic anisotropy has also been considered. Precisely, Néel [64] introduced a new anisotropy constant K_s strictly related to the surface or interface properties of the system. Nowadays due to the possibility to grow high-quality ferromagnetic thin films, the concept of magnetic surface anisotropy has been also generalized, and the magnetocrystalline anisotropy term can be expressed as a function of the film thickness value d through the following formula:

$$E_{mc} = K_{eff}(t) \sin^2 \theta, \quad \text{where } K_{eff}(t) = K_{bulk} + 2\frac{K_s}{d}. \quad (2.8)$$

Usually, the K_{bulk} and K_s terms favor an in-plane and out-of-plane preferential orientation of \vec{M} , respectively.

As a conclusion of this small section it is important to introduce the concept of the anisotropy field H_a , which is related to the aforementioned anisotropy constants. Precisely, by considering a uniaxial contribution to the magnetocrystalline anisotropy, the following relation is valid:

$$H_a = \frac{2K_1}{M_s} \quad (2.9)$$

where M_s represents the saturation magnetization value. Accordingly, H_a is the minimum magnetic field necessary to rotate \vec{M} into the direction perpendicular to the easy axis.

2.4.3 Stoner-Wohlfarth model

Ferromagnetic and ferroelectric materials exhibit domains and domain walls. Hence, following the same arguments valid for ferroelectrics, it is possible to argue that the magnetization process takes place allowing the magnetic domains to nucleate, with subsequent domain wall motion. However, Stoner and Wohlfarth [65] offered a (rather) straightforward way to describe the hysteretic behaviour of ferromagnetic materials. The model provides a simple picture based on which \vec{M} does not change its magnitude, but in the attempt to follow the externally applied \vec{H} , rotates in order to minimize the potential energy. Moreover, the model has been developed for a magnetic material exhibiting a uniaxial anisotropy contribution. Accordingly, with reference to Figure 2.13 the energy of the system can be written as follows:

$$E = K_u \sin^2 \phi - \mu_0 M H \cos(\phi - \theta), \quad (2.10)$$

where K_u is the uniaxial anisotropy coefficient and μ_0 is the magnetic permeability of free space. \vec{M} (\vec{H}) makes an angle ϕ (θ) with the hard axis of the material, as sketched in Fig. 2.13. By minimizing the energy of the system with respect to ϕ , the most energetically favorable direction of \vec{M} with respect to \vec{H} is found. At zero field, the anisotropy contribution term plays the main role, and \vec{M} is oriented along the easy axis. On the other hand, for a sufficiently high value of H , i.e. $> 2K_u/M$, \vec{M} is oriented along the hard axis direction. Interestingly, for materials where the uniaxial anisotropy contribution stems mainly from the shape anisotropy, the minimum magnetic field necessary to orient \vec{M} along the hard axis, hence, the anisotropy field is: $\vec{H}_a = \mu_0 \vec{M}$.

In this Thesis this model has been used because it offered a possibility to explain the results obtained from the anisotropic magnetoresistance measurements (see Section 5.5). Indeed, the inherent simplicity of the model, where the reversal of \vec{M} is treated in terms of rotations, allowed a better understanding of the aforementioned measurements.

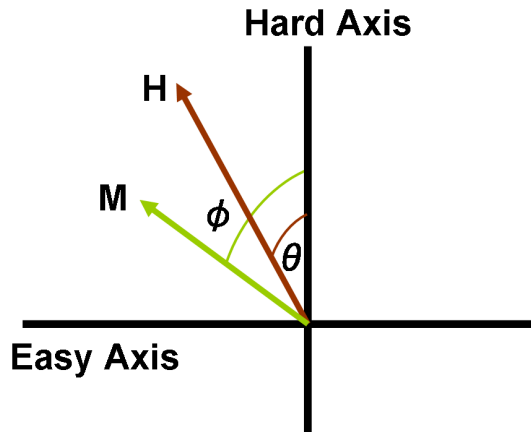


Figure 2.13: Schematic view of the \vec{M} rotation, with an externally applied \vec{H} , in the picture of the Stoner-Wohlfarth model.

2.5 Ferroelectric field effect: an example of charge-mediated magnetoelectric coupling

The ongoing research in the field of oxide materials^{vii} is mainly focused on the possibility to exploit alternative routes towards the development of new systems exhibiting the outstanding magnetoelectric coupling [66]. Following the Landau approach, the expansion of the free energy density of a material at a fixed temperature value in a magnetic H and electric E fields, considered up to the quadratic order, results in a linear magnetoelectric coupling term, i.e. $\sum_{ij} = \alpha_{ij} E_i H_j$ ^{viii}. In single-phase multiferroic materials which are characterized by a simultaneous time-reversal and space-inversion symmetry breaking (reliable examples are materials like Cr_2O_3 [67], BiFeO_3 [68] and BiMnO_3 [69]), the smallness of the magnetoelectric coefficients re-addressed the efforts of the scientific community towards composite-type multiferroic heterostructures [70]. In the latter case the expansion of the free energy density related to each material not necessarily shows a linear magnetoelectric coupling term. As a result, the effective interaction between the two ferroic order parameters originates at the interface between the two different oxides which are basically characterized, separately, by a magnetic and (ferro)electric order. Along this direction, several oxide combinations and geometries [71] have been investigated with the aim to exploit all the possible responsiveness of the ferroic materials to external stimuli such as strain and/or charge. Figure 2.14, taken from [70], should offer a clear idea of the different multiferroic structures so far investigated, along with the type of mechanisms used to drive the coupling between the magnetic and electric order parameters. As an example, one possibility to obtain a relevant magnetoelectric coupling is directly related to the product property between the elastic components of the materials chosen [72, 73]. Precisely, a magnetostrictive material is embedded in a piezoelectric (ferroelectric) matrix and, upon the application of an external electric field as a result of the converse piezoelectric effect, a stress is transferred to the magnetostrictive material, which in turn, undergoes a modification of the magnetic anisotropy properties, for example the variation of the easy axis direction can be pursued. Another promising approach is given by layered (possibly patterned) heterostructures which take advantage of the magnetic sensitivity of a strongly correlated material to a charge modulation, that is induced at the interface with a ferroelectric material upon the reversal of the

^{vii} Along this direction also the possibility to grow oxide films and heterostructures in a highly controlled way is very important.

^{viii} α_{ij} represents the magnetoelectric tensor which describes the onset of an electric (magnetic) polarization induced by the application of a magnetic (electric) field.

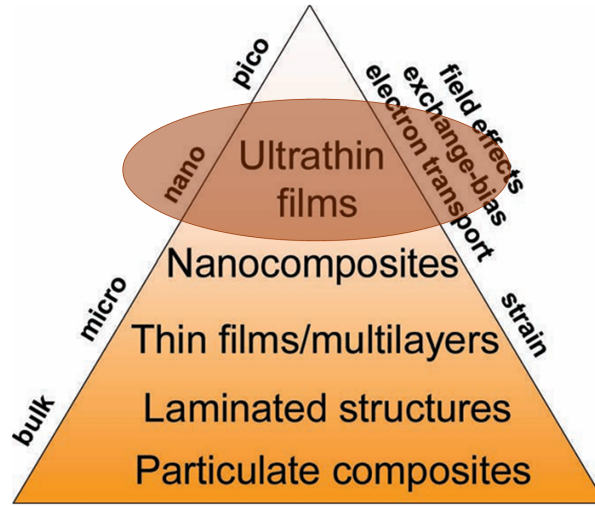


Figure 2.14: Scheme regarding the several possibilities to exploit the magnetoelectric coupling in different structures along with the suggested coupling mechanism. The shaded area indicates the type of structure used in this Thesis. Image from [70].

polarization direction (the shaded area in Fig. 2.14 indicates this possibility). In this respect, the magnetic and/or transport properties of an LSMO ultrathin film can be altered by an accumulation and/or depletion of carriers at the interface with a ferroelectric material. Precisely, the aforementioned interfacial charge modulation is realized in the LSMO in order to screen the electric field generated by the ferroelectric polarization charges, hence, ferroelectric/LSMO heterostructures represent a type of composite multiferroic system [74]. In this respect, the magnetoelectric coupling is a charge-driven effect which is triggered by a field-effect process. Accordingly, at the interface of the two different ferroic oxides, screening effects become extremely important. Moreover, due to the high carrier concentration of the LSMO (common values range between 10^{20} to 10^{22} carriers \cdot cm^{-3}), a relatively high modulation of the carriers is obtained considering a thin film of LSMO which is gated by a rather thick PZT layer that, hence, ensures a high ferroelectric polarization value. In the semiclassical approach of the screening effect usually known as Thomas-Fermi theory (see p. 340 of [75]), the characteristic distance beyond which the external electric field^{ix} is completely screened, i.e. the electrostatic screening length λ_{TF} , should be comparable with the overall thickness of the LSMO in order to achieve a measurable effect. Usually λ_{TF} is expressed as follow:

$$\lambda_{TF} = [\pi^{-1} e^2 g(E_F)]^{-1/2}, \quad (2.11)$$

where $g(E_F)$ represents the density of states at the Fermi level E_F of the LSMO. In literature λ_{TF} values, ranging in the interval $0.3 \div 1$ nm are encountered. Hence, ultrathin layers of LSMO are necessary to measure a relevant magnetoelectric effect.

The ferroelectric field effect can be used from the fundamental point of view, in the attempt to discriminate among the several degrees of freedom that regulate the features of SCMs. Field effect experiments can be very promising, since only the carrier concentration can be dynamically varied without altering the level of disorder as, on the other hand, it is realized in the case of chemical substitutions [76]. Indeed, the latter approach is irreversible and, by considering the tolerance factor, the crystalline structure can be also modified. Moreover, the ferroelectric field effect on superconducting materials revealed the possibility to electrostatically modulate the temperature related to the onset of the superconductive state by several Kelvin in epitaxial

^{ix}It is extremely important to stress the fact that here E is generated by the polarization charges of the ferroelectric material. The effect of the carrier accumulation and/or depletion on the LSMO magnetic and/or transport properties endures also when the external applied voltage, necessary to switch the ferroelectric polarization, is removed.

heterostructures [77].

The ferroelectric field effect can be very promising also for non-volatile memory devices where the information is stored as polarization direction, and it is accessed by reading the resistance state of the gated LSMO (which is used also as bottom electrode of the entire memory device). Interestingly, the ferroelectric field effect is amenable to a reading procedure that doesn't destroy the information and, as a result, a decrease of the size characterizing the memory device can be boosted with a possibility to reach new limits in the scaling-down process. However, as pointed out by Hoffman and co-workers [78], the short retention time experienced by PZT ferroelectric thin films (21 days in case of their investigated devices) of course becomes detrimental for LSMO/PZT ferroelectric field-effect devices which would not be rightly suitable for non-volatile memories. Defects with the associated trap levels and depolarizing fields represent the main drawbacks of the ferroelectric oxides, and more work is required to be done in order to overcome the aforementioned problems.

The changes of the interfacial carrier density are responsible for an alteration of the Mn valence state at the $\text{La}_{0.8}\text{Sr}_{0.2}\text{MnO}_3/\text{PZT}$ interface, as reported by Vaz and co-workers in [79], where also a possible modification of the interfacial spin configuration was proposed to account for the relatively large modulation of the magnetization magnitude [80]. Indeed, the possibility that the accumulation and/or depletion of the holes(electrons) can give rise to a magnetic reconstruction at the manganite/ferroelectric interface has been theoretically studied by Burton and Tsymbal in [81] and by Dong and co-workers in [82] through density functional theory (DFT) calculations. Also a microscopic model has been put forward by Dagotto and co-workers [83], where interfacial magnetic phase transitions are observed by modulating the electronic charge density at the system interface. Additionally, displacements of interfacial atoms, triggered by polar distortions [84, 85], can alter the overlapping of the $3d$ Mn orbitals at the ferromagnetic/ferroelectric interface, hence, affecting the interface magnetization. The proposed interface bonding mechanism was introduced specifically for Fe/BaTiO_3 multilayers [86], but Rondinelli and co-workers pointed out in [87] that the mechanism can be rather general and independent of the details regarding the particular interfacial bonding. Moreover, phase separation or phase co-existence [11] could also give a plausible explanation of the field effect experiments on manganites. In this respect transport and magnetic properties are described through percolation paths which may be suitably tuned by the accumulation and depletion of holes [88].

It is worth to notice that the intriguing electronic correlations exhibited by manganites (due to the interplay between charge, spin and orbital degree of freedom) preclude the possibility to clearly indentify and discriminate between cause and effect regarding the microscopic origin of the mechanism driving the changes of the transport and magnetic features in a field effect experiment.

*Per quanto bella e attraente possa essere una teoria,
c'è sempre un giudice supremo che ne decide le sorti: l'esperimento.*
Antonio Masiero

*As much as beautiful and attractive may be a theory,
there is always a supreme arbiter that decides its fate: the experiment.*
English Translation by myself

The aim of this chapter focuses on the different experimental techniques that were employed to obtain the necessary information regarding the structural, morphological and magnetotransport properties of all the single layers and heterostructures of LSMO and PZT grown in this Thesis. All the oxide thin films were grown by pulsed laser deposition and, accordingly, in the first section a brief introduction related to this deposition technique will be presented. Then as further step, the technique of x-ray diffraction related to the structural characterization will be explained. The surface morphology characterization accomplished by an atomic force microscope will be the subject of the third part of this chapter. The instrument that was used for the characterization of the ferroelectric switching properties will be introduced as well, along with a different custom set-up. Finally, the magnetotransport characterization accomplished through the physical properties measurement system (PPMS, Quantum Design) will be also briefly introduced followed by a description of the Soleil beamline where a synchrotron experiment was performed.

3.1 Pulsed laser deposition

Pulsed laser deposition (PLD) represents one of the most used physical vapor deposition techniques for oxides [89], where a high-energy pulsed laser ⁱ ablates a ceramic target and forms a vapor-plume as schematically shown in Figure 3.1. The PLD is nowadays supporting the research activity of big companies, since it represents the most straightforward technique to deposit oxide materials with a perfect stoichiometric transfer from the target onto a peculiar substrate. On the other hand a drawback is the small deposition area related to the effective focused area of the laser spot and, hence, of the generated plume that limits its use mostly to research purposes.

Simply, as a result of the ablation process the (in part highly ionized) particles, ejected from the target (typical diameter 2 inches), show a certain kinetic velocity depending upon the energy of the laser and the oxygen (O₂) partial pressure present in the chamber. The latter is connected to a suitable vacuum pump system (a base pressure of $\sim 10^{-7}$ mbar was realized in the PLD used in this Thesis). Additionally, the O₂ partial pressure is regulated by dedicated gas inlet circuits and pressure gauge. Once the plume is generated, a certain amount of particles condenses onto the substrate which is kept at a fixed distance from the target (~ 6 cm) and at a certain temperature. In order to optimize the growth of each oxide, parameters such as fluence (defined as the ratio between the energy and the area of the laser pulse, usually expresses in mJ cm^{-2}), O₂

ⁱA KrF excimer laser (Lambda Physik LPX300) was employed for all the deposition experiments in this Thesis. Wavelength and pulse duration were 248 nm and 30 ns, respectively.

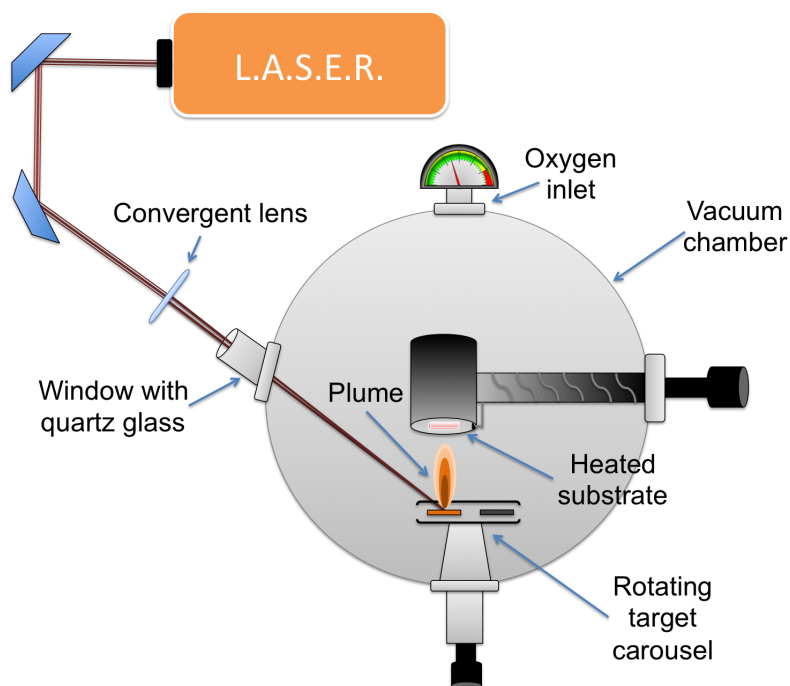


Figure 3.1: Schematic view of the pulsed laser deposition chamber. The relevant parts are indicated in the picture.

pressure background, temperature of the substrate and repetition rate (frequency related to the pulsed ablation) were systematically changed. Moreover, in order to obtain a rather uniform ablation of the ceramic target the carousel, where it is lodged, is subjected to an appropriate eccentric rotation.

3.2 X-ray diffraction

X-ray diffraction (XRD) is mainly based on Bragg's law and, hence, on the concept that solids exhibit a periodic arrangement of their constituents [90]. Precisely, the atoms that obey certain symmetry relations (space group) form planes which, in turn, give rise to the elastic scattering of the incoming x-rays. Each family of planes can be identifiedⁱⁱ by means of integers h , k and l known as the Miller indices [75]. Accordingly, a/h , b/k and c/l specify the points of intersection of the planes with the unit cell edges with a , b and c being the related lattice parameters. As a result, Bragg's law can be generally written as follows:

$$\lambda = 2d_{hkl} \sin \theta_{hkl}, \text{ with}^{\text{iii}} \lambda = 0.15406 \text{ nm} \quad (3.1)$$

where θ_{hkl} and d_{hkl} are the angle of incidence and the interplanar distance of the (hkl) lattice planes, respectively. As an example, for a cubic crystal structure the interplanar distance d between $\{hkl\}$ ^{iv} lattice planes is $d = a/(h^2 + k^2 + l^2)^{1/2}$, where a is the lattice parameter of the cubic unit cell.

In this Thesis a Philips PANalytical XPert XRD system was employed for all the structural characterizations of the samples. The instrument was operated in the Bragg-Brentano geometry where the divergent and diffracted beams exhibit the same focal distance from the sample.

ⁱⁱThis is more easily done in the Laue formalism where Bragg's law becomes $\Delta\mathbf{K} = \mathbf{K} - \mathbf{K}_0 = \mathbf{G} = h\mathbf{s}_x + k\mathbf{s}_y + l\mathbf{s}_z$, where \mathbf{K} and \mathbf{K}_0 are the diffracted and incoming wavevectors, respectively. \mathbf{G} is a reciprocal lattice vector, $\mathbf{s}_{x,y,z}$ being the unit vectors of the reciprocal space.

ⁱⁱⁱWavelength related to the Cu $K\alpha$ radiation.

^{iv}Here curly brackets indicate both negative and positive choice for the Miller indices and interchanges between h, k and l .

In the simplest configuration, the x-ray source is fixed, while the sample holder and the detector can be rotated by an angle θ and 2θ , respectively. Additionally, independent rotations of the sample holder are also possible which are indicated as ω , ψ and ϕ angles in Figure 3.2a. The divergence slit has the main function to control the aperture of the incoming x-ray beam and a Cu $K\beta$ filter was also used to cut the correspondent narrow peak from the x-ray radiation. Indeed, the latter is generated by the copper anode of an x-ray tube, where the accelerated electrons also eject the Bremsstrahlung.

Studies on the orientation of thin films grown on different substrates were performed through θ - 2θ scans. The experimental set-up of a θ - 2θ scan can be understood considering once more Fig. 3.2a. The sample is positioned at the center of the instrument and the incoming x-ray beam hits the sample surface with an incidence angle θ . At the 2θ angle the detector monitors the scattered radiation. While the scan is performed, the angles θ and 2θ are continuously varied in such way that the angle at which the detector collects the scattered radiation is always the double of the incident one. The quantity measured throughout the scan is the number of counts that at each 2θ angle the diffracted radiation induces in the scintillator/detector. The obtained spectra are usually given in the Intensity(Number of Counts)- 2θ representation. Interestingly, in a θ - 2θ scan the scattering vector \mathbf{G} is always parallel to \mathbf{s}_z (already defined in the footnote ii). Accordingly, the upper part of Figure 3.2b shows a graphical definition of the scattering vector \mathbf{G} . Due to this geometrical constraint only those lattice planes (hkl) that are oriented parallel to the sample plane can contribute to the Bragg diffraction.

Rocking curve measurements or ω -scans were necessary for the characterization of the degree of mosaicity of the thin films. The experimental set-up is realized by fixing the angular position of the detector at the value 2θ related to the family of crystallographic planes $\{hkl\}$ needed to be investigated and varying ω around the angle of incidence (i.e. θ). As a result, a peak is obtained which is narrower, the more the family of planes is perfectly aligned. Since, this measurement provides information on the alignment of the crystallographic planes of the family in question through the full-width-at-half-maximum (FWHM) of the measured peak, relevant information on the growth of the film along the direction perpendicular to the investigated family of lattice planes is obtained. The FWHM parameter is also affected by the angular resolution of the instrument itself. However, in general, values of FWHM less than 0.1° are required for a small degree of mosaicity.

Reciprocal space mappings were also performed for some of the samples grown in this Thesis for lattice relaxation studies. The idea of the reciprocal space mapping measurements relies on the possibility to measure differently accessible points of the reciprocal space as, for example, the one indicated by the \mathbf{S} scattering vector in the upper part of Figure 3.2b. Here, the dotted red arrows indicate the incidence and diffracted vectors that satisfy the symmetry requirement of Bragg's diffraction, i.e. $\mathbf{G} \parallel \mathbf{s}_z$. Hence, to access the non-symmetric point of the K -space it is necessary to modify the incidence angle in order to move \mathbf{S} in the \mathbf{G} position (the ω angle can be calculated with an appropriate program, i.e. CaRIne Crystallography 4.0), and looking for the scattered beam moving the detector in the new 2θ angle position. Accordingly, the latter is calculated relatively to the new family of lattice planes which is not anymore parallel to the sample surface (see, for example, the lower part of Fig. 3.2b where the (103) plane is indicated). Afterwards, the measured \mathbf{S} scattering vector can be decomposed into its components along \mathbf{s}_x (\mathbf{s}_y) and \mathbf{s}_z , and information about the in-plane and out-of-plane lattice parameters of the film can be obtained. Accordingly, the following formulae are used:

$$\begin{aligned} a(b) &= \frac{\lambda}{2 \sin \theta \sin(\theta - \omega)} \cdot h(k); \\ c &= \frac{\lambda}{2 \sin \theta \cos(\theta - \omega)} \cdot l. \end{aligned} \quad (3.2)$$

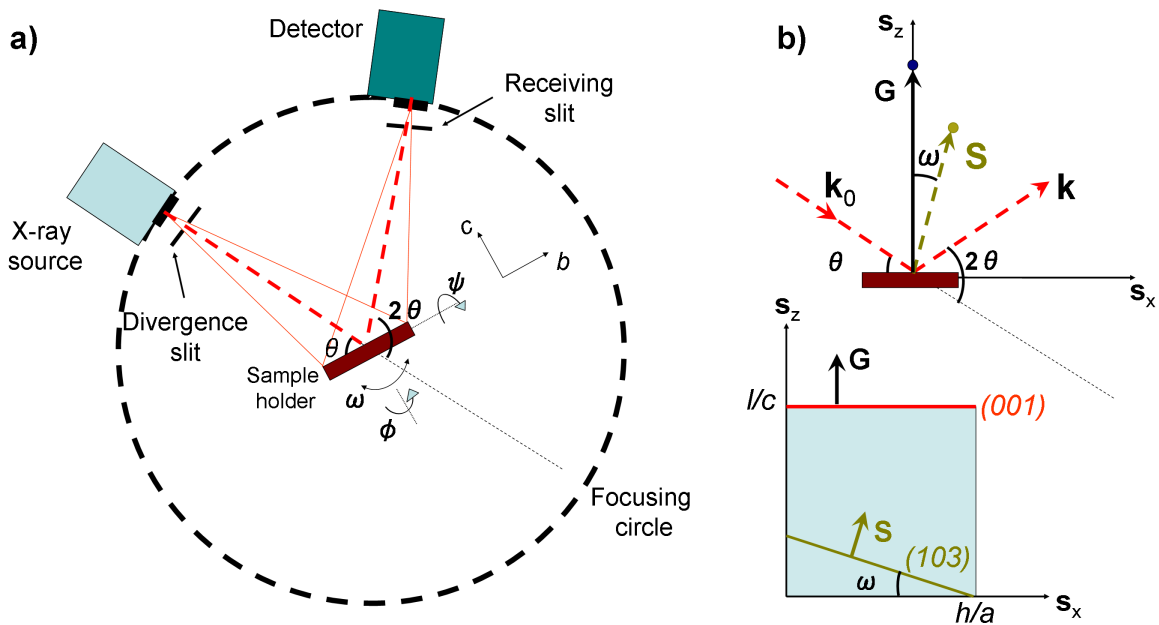


Figure 3.2: a) Schematic view of the Bragg-Brentano geometry. Additionally, the angular movements related to the sample holder are highlighted as well. b) Scheme representing in the upper part the symmetric condition for a Bragg diffraction (see red dotted arrows). Moreover, also the non-symmetric point **S** of the K -space (see dark green dotted arrow) is figured, which corresponds to the family plane (103). In the lower part, the latter is represented along with the angle ω between the two planes (001) and (103).

Experimentally, a reciprocal space mapping measurement can be carried out by combining 2θ scans and ω -steps. Precisely, ω is fixed for every angular step, which defines the accuracy of the measurement itself, while a 2θ scan is performed. As a result, a 2D map of the reciprocal space is obtained where the distribution of the diffraction intensity gives important structural information regarding the investigated samples. Indeed, the relative position of the measured reciprocal space points between the film and substrate depend upon the relaxation state of the film. Accordingly, for a completely strained film the reciprocal space points, corresponding to a general family plane (hkl), are perfectly in line with the ones related to the substrate for both symmetric and non-symmetric diffraction spots.

3.3 Atomic force microscopy

Atomic force microscopy (AFM) can be considered as a spin-off of scanning tunnelling microscopy (STM). In 1986 Binnig and Smith [91] proposed the STM as a method to measure forces as small as 10^{-18} N. Nowadays with AFM it is possible to investigate surfaces of insulators^v on an atomic scale. In this Thesis the AFM technique was mainly used for morphology studies of all the prepared samples and, here, the basic concepts concerning the operation principle will be introduced. Precisely, a Dimension 3000 AFM microscope from VEECO was employed. The instrument, operating in air, was isolated from acoustic and vibrational noise through a standard acoustic enclosure and active damping table, respectively.

Figure 3.3a offers a schematic view of the experimental set-up of an atomic force microscope. Basically the main part of the latter is represented by a cantilever (usually made of silicon) at the end of which the probing tip (force sensor) is suitably mounted. Metallic or insulator materials, depending upon the required use, can be used to cover the tip. The latter

^vIn the case of STM the investigated material has to exhibit a non-zero conductance value. Hence the STM technique is applicable only to metallic and/or semiconductor materials.

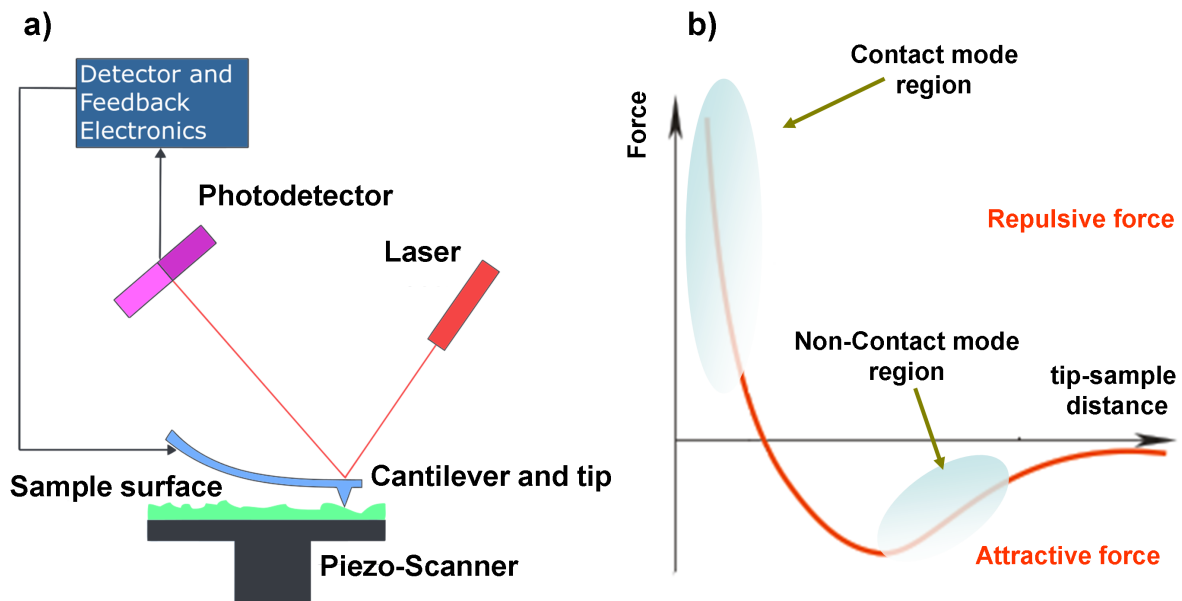


Figure 3.3: a) Schema offering a basic view of the working principle of a atomic force microscope. Image adapted from wikipedia. b) Force versus tip-sample distance graph. The non-contact and contact working area are highlighted. Image from the NT-MDT website.

exhibits in average curvature of a ~ 50 nm nanometers that ensure a lateral resolution of less than 10 nm. The tip represents the force sensor which experiences the Van der Waals force from the atoms forming the sample surface (see Fig. 3.3b). The latter is scanned in a predefined micrometer-sized area moving the sample suitably lodged on an accurate piezo-scanner. Generally speaking, the tip-sample interactions vary during scanning, since the tip-sample distance is modulated by the morphology features of the investigated sample. As a consequence of the variation of the inter-atomic force of the tip-sample system, the laser beam, diffracted from the cantilever, falls on one of the quadrant of the 4-quadrants photodetector. As a result, the obtained voltage signal is used as a feedback to keep the tip-sample interaction constant during scanning. The feedback signal is recorded for each investigated (x,y) point and turned into a color-contrast image, where each color exhibits a linear relationship with the "sensed" surface height. As a result, a map of the morphology of the scanned area is obtained.

Relatively to the Van der Waals force-distance graph depicted in Fig.3.3b, the operating mode of an AFM system can be varied from non-contact to contact mode depending upon the particular tip-sample distance. Precisely, in the non-contact mode, few tens of Angstroms from the surface are enough, so that the tip responds to an attractive Van der Waals force. Additionally, in the non-contact mode the cantilever is forced to oscillate near its resonant frequency (~ 30 KHz). The tip-sample force interaction during scanning alters the effective spring constant of the cantilever, thereby changing its resonant frequency, phase, and oscillation amplitude. These changes are detected using an internal lock-in amplifier. Hence, the feedback loop adjusts the tip-sample distance in order to keep the amplitude of the cantilever oscillation constant during scanning. In the contact mode region the tip is subjected to a repulsive Van der Waals force that bends the cantilever at a fixed value usually addressed as set-point. In this case the feedback signal, given by the variation of the repulsive force experienced by the tip-sample system, acts in such a way as to keep the set-point value constant. Hence, in contact mode the deflection of the cantilver is kept constant during the scan. As in the case of the non-contact mode, the feedback signal renders a color-contrast image of the investigated sample surface. In this Thesis all the AFM images were acquired in non-contact mode.

3.4 Ferroelectric switching and hysteresis loop measurements

One of the key measurements related to ferroelectric materials is the recording of the P - V hysteresis loop, since it proves that P can be reversed between two stable states upon the application of a suitable voltage pulse V . The charge Q to the spanned area A ratio, i.e. Q/A , represents a textbook definition of P . Experimentally, the latter can be switched when the ferroelectric material is suitably embedded in a type of device structure where the voltage pulses are applied between a bottom and top electrode (usually the parallel-plate capacitor geometry is used). As a result, since the polarization charges (of different polarity at the two metallic contact interfaces) reverse upon the application of a voltage pulse, the induced screening charges at the top/bottom electrode also reverse and, hence, a current peak I is measured. Correspondingly, the dynamic current-voltage characteristics, i.e. I - V , are measured in order to, eventually, calculate P through the following general formula valid for a parallel-plate capacitor geometry:

$$P = \frac{1}{A} \int I_{ferr}(t) dt + \frac{\sigma}{d} \int V(t) dt, \quad (3.3)$$

where A , σ and d represent the top electrode area, the electrical conductivity and the thickness of the ferroelectric material, respectively. The first term on the right hand side of equation 3.3 represents the ferroelectric contribution to the overall current peak, i.e. I_{ferr} , and on the contrary, the second term represents the contribution stemming from the dielectric conduction of the parallel-plate capacitor system (bottom-electrode/ferroelectric/top-electrode), i.e. the so-called leakage current. Here, precisely, $V(t)$ is the time variation of the applied voltage pulse.

In this Thesis the possibility to switch the ferroelectric polarization of the PZT thin films was

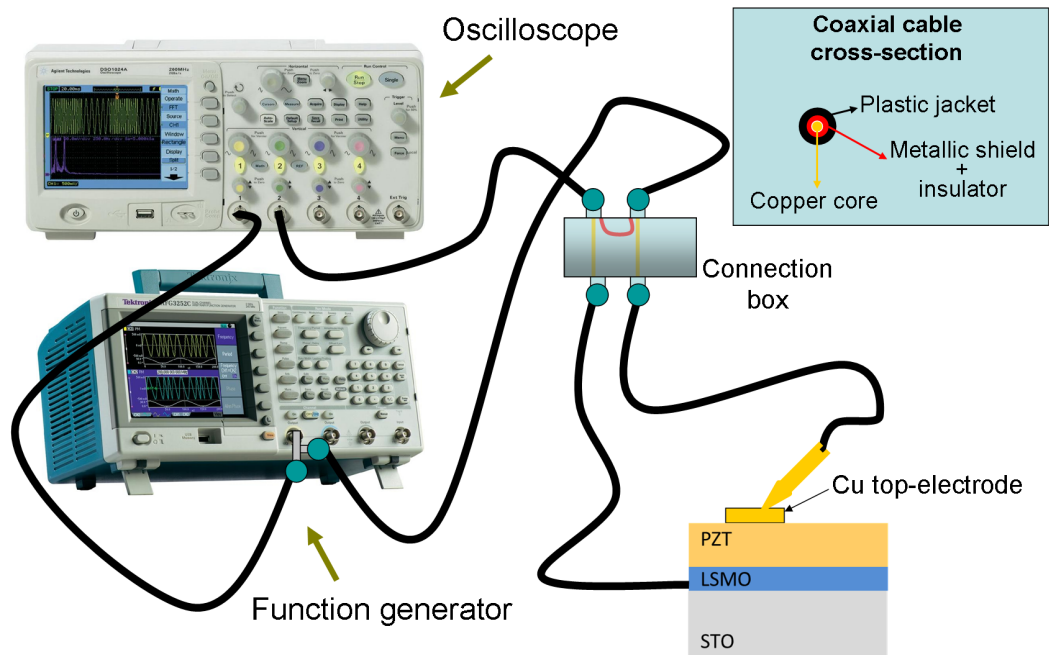


Figure 3.4: Custom made ferroelectric system. The inset shows a cross-section related to the coaxial cables employed for all the connections.

accomplished following two different experimental methods. In the first case a commercial test apparatus by aixACCT systems GmbH, i.e. the TF Analyzer 2000 measurement system, was employed. In the second case a custom set-up consisting of an oscilloscope connected to a function generator was used to send a so-called positive-up negative-down (PUND) signal [92]

to the sample to investigate. Precisely, the Tektronix AFG3102 function generator and the Agilent Technologies DSO1024A oscilloscope were connected to the parallel-plate capacitor as schematically shown in Figure 3.4. Accordingly, the PUND waveform is sent from the function generator to the top electrode of the device and, parallel, to the oscilloscope as a trigger signal. The bottom electrode of the device is connected to the oscilloscope for the reading procedure. The ferroelectric current peak is "detected" by the oscilloscope through a suitable internal resistor, hence, the voltage pulses displayed in the oscilloscope can be eventually converted into the ferroelectric switching current pulses for the P calculation, as required by formula 3.3. All the connections were made by using coaxial cables of which a cross-section view is offered in the inset of Fig. 3.4. In this respect, it is worth to notice that the metallic shields of the two coaxial cables, usually connected to the ground, are connected together in the connection box in order to improve the signal-to-noise ratio. Moreover, Figure 3.5 shows the typical sequence of five voltage pulses as a function of the time which defines a PUND waveform. Accordingly,

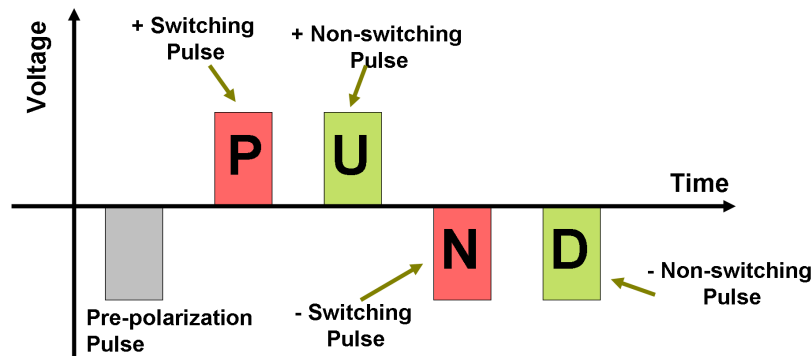


Figure 3.5: Typical voltage pulse sequence defining a PUND waveform.

the first peak pre-sets the polarization state of the sample. The second peak P then polarizes the sample *positively* and from the third peak U , assuming a good retention time,^{vi} information regarding only the leakage contribution is accessed. The subtraction (i.e. $P-U$) of the two measured pulses gives the real ferroelectric switching current from which, eventually, the polarization value for the positive voltage pulse can be calculated. The same discussion is simply repeated for the next two negative pulses, i.e. N and D . In this case the ferroelectric characterization related to the negative voltage pulse is obtained. As a result, PUND measurements give the possibility to measure only the switchable ferroelectric contribution of the device, and all the other intrinsic contributions are completely excluded.

Regarding the TF Analyzer apparatus the $I-V$ loops were automatically converted into $P-V$ ($P-E$) loops since the TF Analyzer 2000 Hysteresis Software V2.1 provided the possibility to insert the values of the top electrode area and the thickness of the ferroelectric thin film. A suitable probe station was used to ensure a proper contact between the measurement system and the sample. As already highlighted before, the measurement of an $I-V$ loop requires a time-dependent voltage pulse applied to the sample while recording the current. The pulse is cycled from a negative value to a positive one and in this case the switching current pulse, produced by the change of the polarization charges ΔP , depends on the switching time Δt , i.e. $I = \Delta P / \Delta t$. As a result the switching current peak is larger for a faster switching voltage pulse. The TF Analyzer measures the $I-V$ loops with the so-called dynamic hysteresis measurement (DHM). The voltage excitation signal is schematically depicted in Figure 3.6 in the case of a triangular pulse^{vii} [93]. Precisely, four bipolar triangular pulses of frequency ν ^{viii} are applied

^{vi}At least not less than the space between two different pulses.

^{vii}Usually triangular pulses are favoured to the square pulses since, in the first case, a high rise time of the peak is avoided.

^{viii}Typical range from 1 Hz to 2 kHz.

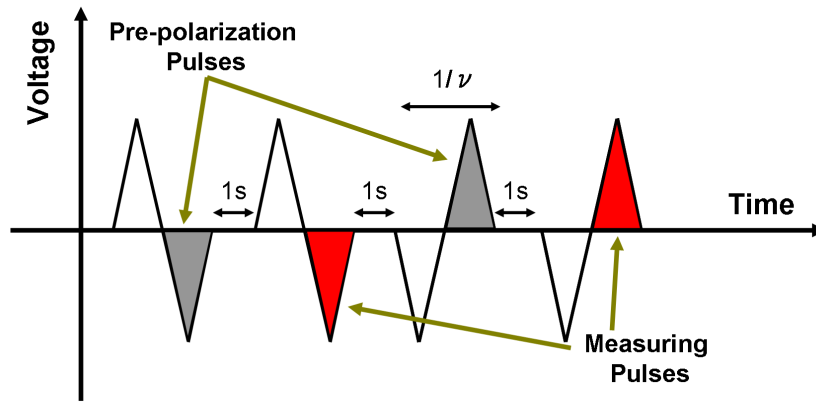


Figure 3.6: Typical voltage pulse sequence used by the TF Analyzer apparatus. The shaded gray pulses account for the pre-polarization of the sample while in red the measuring pulses are represented.

with a delay time of 1 s between each other. The first and third bipolar pulse are necessary to pre-polarize the sample into the negative and positive state, respectively. Hence, the second and fourth pulse are used to effectively measure the switching current pulses, and the I - V loop is calculated from the combination of the currents measured in the corresponding voltage pulses.

The copper/gold top-electrodes^{ix} were made by thermally evaporating the metallic material source in a vacuum chamber (typical base pressure of 10^{-6} mbar) through a shadow mask. The tungsten evaporation boat, hosting the source to evaporate, was heated through the Joule effect and brought to a temperature higher than the characteristic melting temperature of the metallic material. The boat-sample distance was always fixed around 20 cm, and the evaporation process was controlled by a quartz balance in order to evaporate top electrodes of a certain thickness value. Accordingly, large attention was given to accurately positionate the center of gravity related to the sample-balance system on the same vertical line passing from the center of the evaporation point on the underneath boat.

3.5 Magnetotransport measurements

All the magnetotransport measurements that will be presented in the following chapters were performed by using a physical property measurement system (PPMS) of Quantum Design Co. The samples were mounted on standard resistive bridge (pucks) supplied by Quantum Design Co. Figure 3.7 shows one of the typically used resistive bridges where the sample was contacted with simple copper wires. The latter were soldered to the appropriate labelled pads. Conductive silver paste G3303B supplied by Plano GmbH was also used to allow a proper contact between the aforementioned copper wires and the sample itself. The PPMS is basically a cryostat where the temperature can be varied from 2 K to 400 K and, additionally, a magnetic field, ranging from -9 T to +9 T, can be applied in- and out-of-plane with respect to the sample surface [94]. The PPMS offered also the possibility to use a special rotator platform to mount the sample; in this case the temperature measurement is done just on the sample holder and not on the bottom of the cryostat like for the other type of measurements. The allowed angles of rotation range from -10° to $+370^\circ$, for the standard rotator motor. The motorized steps are in 0.0532° increments, and the maximum rate of rotation is 10° per second. All the measurements were acquired by using the provided software, i.e. PPMS MultiVu. The latter served as a single interface to the PPMS through the Model 6000 PPMS Controller. However, in special

^{ix}Typical area used in this Thesis is $60 \times 60 \mu\text{m}^2$.

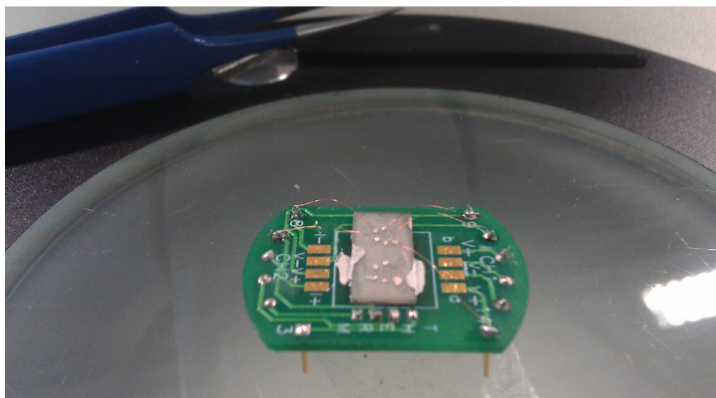


Figure 3.7: Typical resistive bridge supplied from Quantum Design Co. for the rotator circuit board.

cases, the latter was by-passed to allow measurements through external instruments because the Controller was not ensuring the necessary resolution for the measurement. Precisely, the resolution is defined by three different specified limits for current, power and voltage. Accordingly, all the limits were exceeded in case of samples exhibiting a high resistance state and, as a result, the related measurement was rather questionable. To overcome this problem the resistance $R = V/I$ was measured by employing a DC/AC Current Source 6221 and a Nanovoltmeter 2182A both from Keithley Instruments Inc., in order to send a certain current amplitude I to the sample and measure the related voltage drop V , respectively. In this case the measurement was performed controlling in a remote mode the aforementioned instruments by using already existing custom-made programs^x.

3.6 Experimental details of the Deimos beamline at Soleil

The Deimos (Dichroism Experimental Installation for Magneto-Optical Spectroscopy) beamline is dedicated to soft x-ray dichroic measurements at SOLEIL (Source Optimisée de Lumière à Énergie Intermédiaire du LURE) of Paris, France [95]. The Deimos beamline is an Apple-II undulator producing x-ray in a $350 \div 2500$ eV energy range with variable polarizations (circular and linear). The x-ray spot size can be as small as $80 \times 80 \mu\text{m}^2$ and the absorption measurements can be performed, at the same time, in TEY and TFY mode. Nevertheless, at the time of the measurements shown here, the detector for the TFY mode was not working properly and for this reason all the XAS spectra were acquired by measuring only the total electron yield (TEY) current as a function of the x-ray photon energy. The end-station of the beamline consists of two interconnected ultrahigh vacuum (UHV) chambers used on request, for sample preparations and/or sample characterizations (i.e. scanning tunnel microscopy), which are coupled to the cryo-magnet chamber where the samples are suitably loaded, through a load-lock module connected to a clean atmosphere glove box (see Fig. 3.8). The cryomagnet chamber (internal pressure of $\sim 10^{-10}$ mbar) is provided with a superconducting coil capable to supply a magnetic field of 7 T parallel to the x-ray beam, and of 2 T perpendicular to it. Moreover, the sample temperature can be varied between 1.5 and 350 K. The polarization plane is perpendicular to the direction of the x-ray beam, which hits the sample with an incident angle of $\sim 30^\circ$. As a consequence of the sample holder geometry, for a vertically polarized incoming beam (LV), the electric field (E) vector of the light is oriented perpendicular to the z -axis of the device (light polarized in-plane with respect to the sample, p_{ab}), whereas the E -vector of horizontally polarized (LH) light is oriented nearly parallel to the z -axis (light polarized nearly

^xThe programs were written by Prof. Marin Alexe and Dr. Ignasi Fina by using TestPoint and LabWindows softwares, respectively.

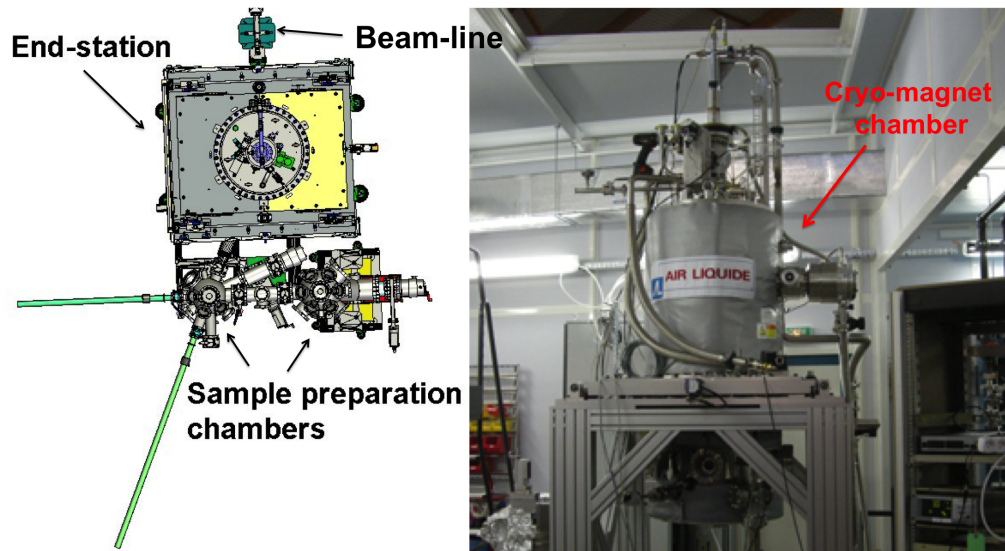


Figure 3.8: Left: Schematic view of the cryomagnet chamber as described in the text. Right: Related photo taken from the Deimos beamline website.

completely out-of-plane with respect to the sample, p_c), (see, for example, Fig. 6.2a in Chapter 6).

*Ci sono soltanto due conclusioni:
se il risultato conferma le ipotesi, allora hai appena fatto una misura;
se il risultato è contrario alle ipotesi, allora hai fatto una scoperta.*
Enrico Fermi

*There are only two consequences:
if the experimental result confirms the theory, you have just done a measurement;
if the experimental result is inconsistent with the theory, then you have done a discovery.*
English translation by myself.

Results on oxide growth and physical characterizations

The aim of the following chapter is to describe the growth and characterization of high-quality thin films of LSMO and PZT. Achieving the stoichiometry control of both the oxygen content and the cation ratio is decisive for the quality of the oxide materials. Moreover, the success of the ferroelectric field effect experiments depends on the possibility to handle ultrathin layers of LSMO but also on the challenge to grow both oxide materials as multilayers with very sharp and plane interfaces. It is of common knowledge that transport and magnetic properties of LSMO thin films can be tailored not only by inducing different epitaxial strain [35] but also by allowing different growth modes [96]. As a result, the morphology becomes a key point especially when the LSMO thin film is grown starting from the PZT layer and not from the usual atomically flat single terminated substrate surface. Accordingly, not only the ferroelectric properties of the PZT thin films are of paramount importance but also their morphology represents a key point, especially when a layer-by-layer growth mode of the subsequent LSMO layer is aimed at. The results obtained from transport, (micro)structural, ferroelectric and magnetic characterizations shown in the following sections, gave valuable feedbacks to optimize the majority of the growth parameters for both oxide materials. As already mentioned in the previous chapter, all the LSMO and PZT single layers and heterostructures were grown by PLD, and a PPMS was used for the (magneto)transport measurements. Additionally, the measurements of the ferroelectric properties of the PZT thin films studied mostly in the parallel plate capacitor geometry, as shown here, were performed by the commercial apparatus TF Analyzer. Finally, the magnetic investigations of both LSMO and LSMO/PZT heterostructures were accomplishedⁱ by a magnetic property measurement system (MPMS) of Quantum Design Co.

4.1 Substrate preparation

In general nucleation and growth of thin films depends on the morphology of the substrate surface such as steps or chemical segregations being present. Accordingly, all the substrates need some treatments before being employed as template for the growth experiments. Here the way is discussed in which atomically flat surfaces and/or single chemical terminations can be obtained. Along this direction, the choice of the substrate represents the first main step for the growth of an epitaxial thin film. Several substrates are present on the market and the selection has to be done allowing a reasonable comparison of the chemical and structural properties with the material to grow. In this Thesis substrates provided by *CrysTec GmbH* have been

ⁱAll the magnetic characterizations presented in this Chapter were performed by external collaborators. Thanks are given to Martin Wahler at the Martin-Luther University Halle-Wittenberg, Germany.

mainly used. Among the most common substrates, strontium titanium oxide SrTiO_3 (miscut ranging from 0.08° to 0.11°), lanthanum aluminum oxide LaAlO_3 and lanthanum strontium aluminum tantalum oxide $(\text{LaAlO}_3)_{0.3}(\text{Sr}_2\text{AlTaO}_6)_{0.7}$ have been the ones used for the growth experiments.

4.1.1 Strontium titanate SrTiO_3 (STO)

STO has a cubic perovskite unit cell with the lattice parameter $a = 0.3905 \text{ nm}$. Figure 4.1a shows a schematic view of the unit cell. Accordingly, the STO can be considered as a stack of neutral SrO and TiO_2 planes. The substrates as received from the company show always a rather rough surface with both chemical terminations. A coherent and fully epitaxial growth of oxide materials can be successfully achieved when substrates with very smooth and (preferentially) single-terminated surfaces are used. For this reason the nowadays standard Kawasaki [97] procedure involving etching and annealing steps, was used for the treatment of the STO substrates. Since etching can be chemically selective, an atomically flat single

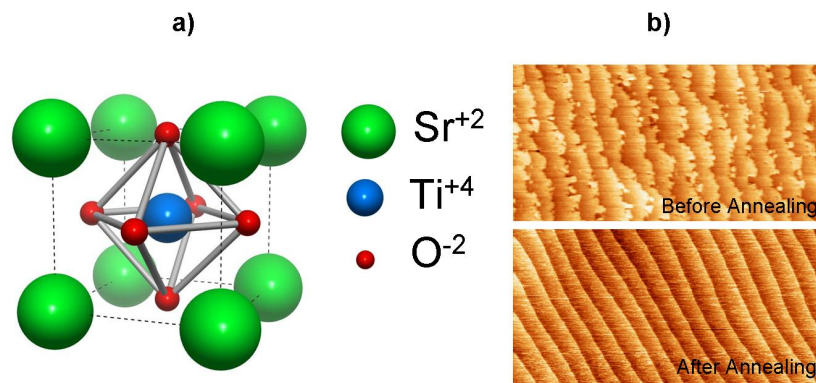


Figure 4.1: a) Schematic view of the STO perovskite unit cell. b) Atomic force microscopy images ($4 \times 2 \mu\text{m}^2$) of STO substrates demonstrating the morphology improvement due to the annealing procedure.

TiO_2 -terminated STO surface is obtained, and with the successive annealing procedure a well ordered terrace-step like structure (characteristic of substrates with miscut) is realized. Specifically the substrates as received were rinsed in deionized water for 3 minutes and quickly etched in a 1:30 aqueous solution of NH_4F -buffered HF. In order to limit the time of action of the etching solution to the chosen range (15 seconds), the substrates were again dipped into deionized water for a few seconds and then dried by pure N_2 gas. As final step the substrates were annealed in air at the temperature of 950°C for two hours. The etching solution acts in order to eliminate the natural SrO termination on top of the STO surface, and the annealing procedure to reconstruct a well ordered terrace-step like structure. The latter was demonstrated by performing atomic force microscopy (AFM) images before and after the annealing procedure, see for example Figure 4.1b. First, just after the etching process, the step edges are not very well defined, but no Sr islands are present on the substrate surface (upper part of Figure 4.1b). The annealing procedure on the other hand induced a surface reconstruction yielding a perfect vicinal surface exhibiting steps with a very defined edge and with a single unit cell height of $\sim 0.4 \text{ nm}$ (lower part of Figure 4.1b).

4.1.2 Lanthanum aluminate LaAlO_3 (LAO)

LAO single crystals have a rhombohedral unit cell [98], but for sake of simplicity the pseudocubic notation is used. As a result, the LAO crystal structure is represented by a cubic distorted-perovskite structure with lattice parameters $a_{pc}^{LAO} = 0.3786$ nm and $\alpha = \beta = \gamma = 90.066^\circ$. Figure 4.2 shows a schematic view of the rhombohedral crystal structure (black dotted line) where also two distinct distorted-perovskite pseudocubic unit cells are highlighted (orange dotted line). In the pseudocubic representation it is easy to recognize that also for the LAO substrates two

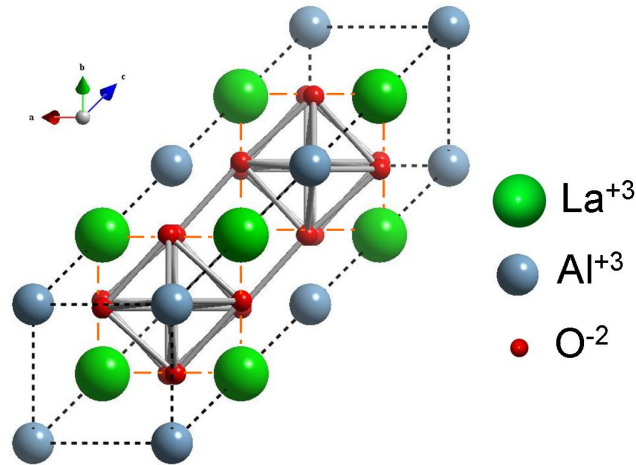


Figure 4.2: Schematic view of the LAO rhombohedral crystal structure. Highlighted are also two distinct perovskite cubic unit cells with lattice parameter of $a_{pc} = 0.3786$ nm.

different chemical terminations are possible. As a result, like for the STO substrates, it seems to be the case that etching and annealing treatments are required to achieve the desirable smooth single terminated surfaces. Nevertheless it has been demonstrated that only by means of an annealing procedure single terminated atomically flat surfaces can be obtained [99]. Precisely an AlO_2 -terminated LAO substrate can be obtained by only an annealing procedure. In this regard the annealing time is a key parameter that can be modified accordingly to optimize the morphology. Indeed Figure 4.3 shows the morphology of the same LAO substrate, cut in two pieces, each of which has undergone a different annealing procedure. Figure 4.3a shows the morphology of an LAO(001) substrate annealed for 2 hours at 1000°C . Although the terrace step-like structure is quite well defined, the surface of each single terrace is not flat. Indeed the scan line profile shown in Figure 4.3b demonstrates that surface pores are present. Increasing the annealing time to 10 hours, the pores (darker contrast in the previous AFM image) completely disappear, and as shown in Figure 4.3c, an atomically flat surface can be achieved. Annealing experiments carried out for 10 hours gave the possibility to the surface atoms to occupy the positions where they are expected to have the lowest energy. Moreover, from the phase image Fig. 4.3d of the AFM image shown in Fig. 4.3c, due to a uniform contrast color a single chemical termination can be envisaged. The procedure of plane flattening (not shown here), performed using the free software WSxM (WIndows Scanning $x = \text{Force, Tunneling, Near Optical, ... Microscope}$), revealed in average steps of single unit cell height, i.e. 0.378 nm, as expected from the pseudocubic notation.

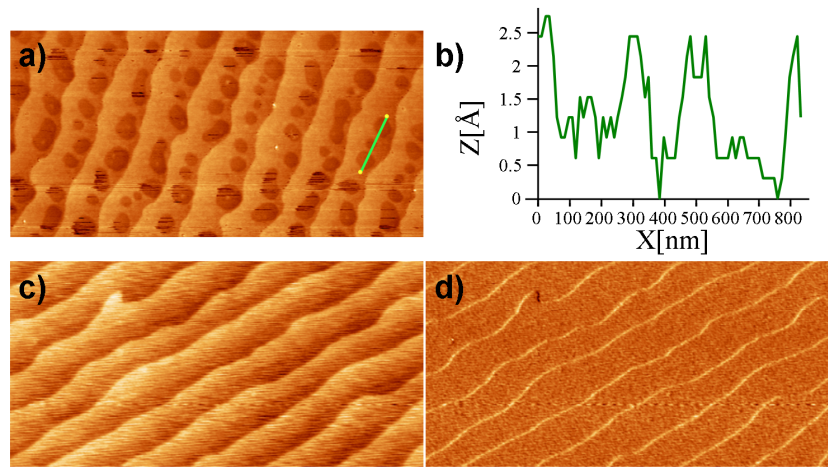


Figure 4.3: a) AFM image of a LAO substrate annealed for 2 hours at 1000 °C. The related scan line profile (b) clearly shows a step-edge surface characterized by the presence of pores on the terraces. c) AFM image of a LAO substrate annealed for 10 hours at 1000 °C demonstrating a surface completely flat with the related phase image (d) showing a single color contrast characteristic of single-terminated surfaces. All the AFM images are $4 \times 2 \mu\text{m}^2$.

4.1.3 Lanthanum strontium aluminum tantalate $(\text{La,Sr})(\text{Al,Ta})\text{O}_3$ (LSAT)

LSAT single crystals belong to the family of mixed perovskites $(\text{AA}')(\text{BB}')\text{O}_3$, crystallographically defined in the space group $\text{Pn}\bar{3}\text{m}$ with lattice parameter $a = 0.7720 \text{ nm}$. Figure 4.4 shows the unit cell where the mixed occupancy of each cation site is visualized using balls of same color. The as-received LSAT(001) substrates show double terminations like in the case of the

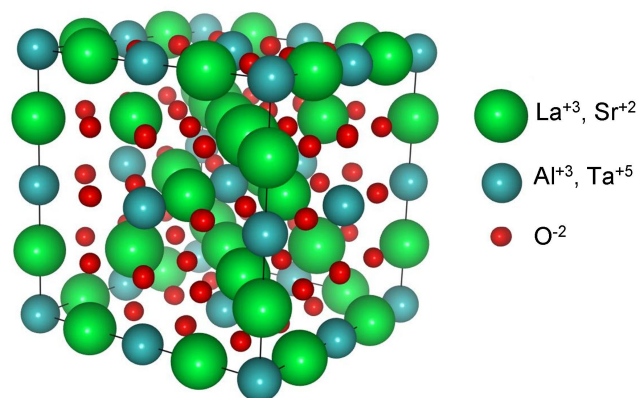


Figure 4.4: Schematic view of the LSAT mixed-perovskite unit cell.

other substrates. In order to achieve the formation of steps with unit-cell height, preferentially *A*-site terminated, a special annealing procedure, as outlined in a recent work [100], has been followed. Specifically the annealing procedure has to take place in a controlled lanthanum pressure in order to keep the ratio between the *A* type cations at the substrate surface acceptable. To obtain a sufficiently high lanthanum vapor pressure during the annealing, one LAO substrate was positioned on top of the LSAT single crystal in the form of a bridge. As a result, all the LSAT substrates were annealed using the LAO-bridge setup at the temperature of 1200 °C for two hours. The result of this procedure is depicted in Figure 4.5, where the topography image (left) and the related phase image (right) are shown. The terrace-step morphology is successfully recovered without any SrO segregation. Some sinks are nevertheless present in

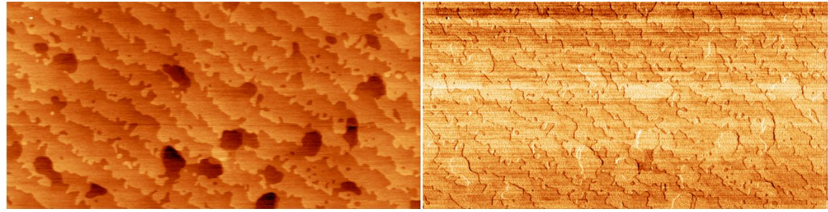


Figure 4.5: Atomic force microscopy images ($4 \times 2 \mu\text{m}^2$) of an LSAT substrate after annealing in a controlled lanthanum atmosphere. Surface profile (left) and related phase image (right) demonstrate a step-terrace structure and the complete absence of two different chemical terminations.

the morphology. The measured step height of $\sim 0.384 \text{ nm}$ is comparable with half the c -axis lattice constant value of LSAT.

4.2 Growth and physical properties of LSMO($x = 0.175$) thin films

The interesting functional properties exhibited by the perovskite LSMO have been extensively investigated through recent few years and partially reviewed in Ref. [101]. In this respect, a massive number of reports can be found in the literature covering quite consistently the entire range of doping x . Nevertheless, the particular compositional doping used in this Thesis, i.e. $x = 0.175$, is rather poorly explored, especially for thin films. Considering the electronic phase diagram of bulk LSMO (shown in Fig. 2.2b), as already briefly discussed in the chapter 2.1, a transition between the metallic and the insulating phases, with a T_C of $\sim 280 \text{ K}$, is exhibited at the nominal level of doping of $x = 0.175$. Moreover, the latter peculiar transition at that specific doping level is also accompanied by a structural transition, as already illustrated in Fig. 2.5. LSMO thin films grown with a nominal level of doping lying just at the border between two or more electronic ground states should be characterized by an increased sensitivity to external stimuli (such as the ferroelectrically induced electric field). This assumption here motivated the choice to study LSMO thin films with $x = 0.175$. As already highlighted by Ahn and co-workers in [102], when strongly correlated oxides are used as sensitive material in prototypical ferroelectric field effect devices (FeFEDs), due to the relatively high carrier concentration (order of $10^{21} \text{ charge cm}^{-3}$) to which corresponds a screening length of a few Angstroms (as obtained in the framework of the Thomas-Fermi model, see formula 3.1), ultrathin layers are indispensable to have a measurable field effect. Consequentially several growth experiments were necessary to study the (magneto)transport properties of the LSMO thin films exhibiting different misfit strain and thickness values. The data obtained in this direction are shown in this section along with the structural and the morphological characterizations as well. Moreover, also a magnetic characterization will be introduced. For sake of simplicity hereafter in this Thesis the acronym LSMO will indicate only thin films grown with $x = 0.175$.

4.2.1 Crystallographic and morphology properties on different substrates

The growth of LSMO thin films was optimized onto STO(001) single crystal substrates, tuning the deposition temperature and the oxygen background pressure in the PLD chamber. As a result of several growth experiments, values of 600°C and 0.20 mbar turned out to be the best choice for the deposition temperature and for the O_2 background pressure, respectively. The laser fluence has been fixed around the value of 0.4 mJ/cm^2 , taking into consideration the possibility to have a well-confined plume with boundaries at two-thirds of the substrate-target distance. Moreover, all the samples were slowly cooled down to room temperature in an O_2 background atmosphere of 100 mbar . The root-mean-square (rms) surface roughnesses of all

the LSMO thin films grown, determined by AFM, was less than 0.2 nm. As already discussed previously, the bulk LSMO is lying just at the border of a structural transition, i.e. between the O^* orthorhombic towards the rhombohedral crystal structure as x is increased. However, when thin films are considered, the structural/electronic phase diagrams undergo relevant modifications due to the presence of external parameters such as strain, possible oxygen vacancies and thickness value. For this reason, from the structural point of view and mainly for sake

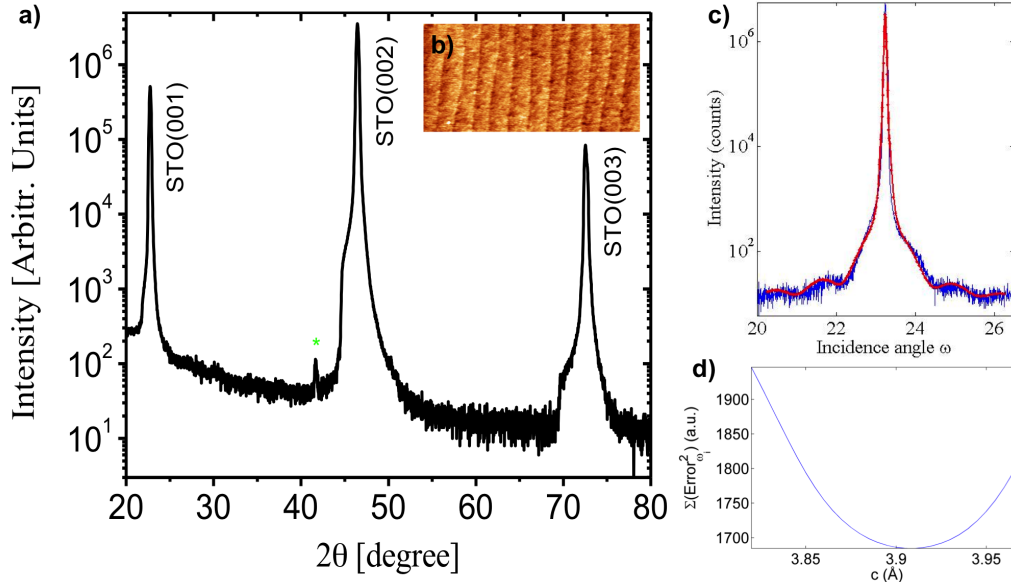


Figure 4.6: a) θ - 2θ XRD pattern of a 50 nm thick LSMO film grown on top of a STO(001) single crystal substrate. The LSMO peaks completely overlap the STO ones. In b) the related AFM image ($4 \times 2 \mu\text{m}^2$) reveals a completely smooth surface free of precipitates with a rms surface roughness of 0.19 nm. c) θ - 2θ XRD measurement (blue curve) acquired for a 5 nm thick LSMO film around the (002) reflection of the STO. The red curve indicates the result of the fitting procedure. From the minimum of the root-mean-square deviation curve (d), the value of (0.391 ± 0.001) nm for the LSMO out-of-plane lattice parameter is estimated.

of simplicity, the pseudo-cubic notation is commonly employed. Indeed, basically repeating what has been already explained in section 2.1, thin films of $\text{La}_{1-x}\text{Sr}_x\text{MnO}_3$ show a slightly distorted perovskite unit cell that can be further distorted depending upon the choice of an appropriate substrate. Specifically, as the effect of a different accommodation of the misfit strain, distinct JT distortions, along with appropriate oxygen octahedral rotations, can emerge which in turn affect the transport and the magnetic properties of the manganite system [35]. According to Ref. [19] the pseudo-cubic lattice constant of the bulk $\text{La}_{1-x}\text{Sr}_x\text{MnO}_3$ compound ranges between $a_{pc} = 0.391$ nm at the level of doping $x = 0.15$, to $a_{pc} = 0.388$ nm at $x = 0.3$. Moreover, as already introduced in section 2.1 it emerges that the LSMO in the O^* orthorhombic structural phase is actually more close to a (pseudo)cubic unit cell with $a = 0.391$ nm. Interestingly, Figure 4.6a shows the XRD pattern obtained from a 50 nm thick LSMO film grown onto a STO substrate. Only the peaks corresponding to the latter can be easily distinguished. The overall absence of other peaks (not considering the one indicated by the green asterisk since it corresponds to a spectral line of the copper x-ray source) demonstrates, primarily, a fully epitaxial growth of the LSMO thin film on top of the STO, and next, a very low (practically absent) mismatch between the LSMO and the substrate in-plane lattice parameters. In order to get a better insight of the latter result, a XRD θ - 2θ scan was acquired for a ultrathin (i.e. 5 nm) layer of LSMO which is shown in Figure 4.6c, along with the result of a fitting procedure described in Ref. [103] (see, for example, the red curve). Accordingly, from the fitting procedure an out-of-plane lattice parameter identical to the in-plane parameter of the STO(001) was obtained.

Precisely, the red solid curve in Fig. 4.6c shows the result of a fully dynamical simulation obtained using as fixed parameter the value of 5 nm for the LSMO thickness which was the result of a transmission electron microscopy (TEM) technique investigation. The satisfactory match between the measured oscillations around the (002) peak of the STO and the fitting curve occurs when the out-of-plane lattice parameter of the pseudo-cubic structure of the LSMO is precisely $a_{pc}^{LSMO} = (0.391 \pm 0.001)$ nm (see the rms deviation curve in Fig. 4.6d). As a result, it can be claimed that the LSMO grows as a real (pseudo)cube onto a STO(001) single crystal with a lattice parameter value as obtained from the fitting procedure. Moreover, this result is further substantiated by the morphology characterization undertaken for the same 5 nm thick LSMO film. In this respect, Figure 4.7a shows the related AFM image where the atomically flat surface, characterized by the complete absence of islands, demonstrates firstly a proper optimization of the deposition parameters and, secondly, the cube-on-cube growth. Indeed, as a result of the flattening procedure which is shown in Figure 4.7b, the related cross-sectional profile, which is further shown in Figure 4.7c, proves an averaged step height of ~ 0.4 nm, that confirms the previous crystallographic result. Accordingly, from a cube-on-cube growth mode the step height value should correspond to the out-of-plane lattice parameter of the crystal structure related to the thin film. Additionally, also LAO and LSAT single crystals were used

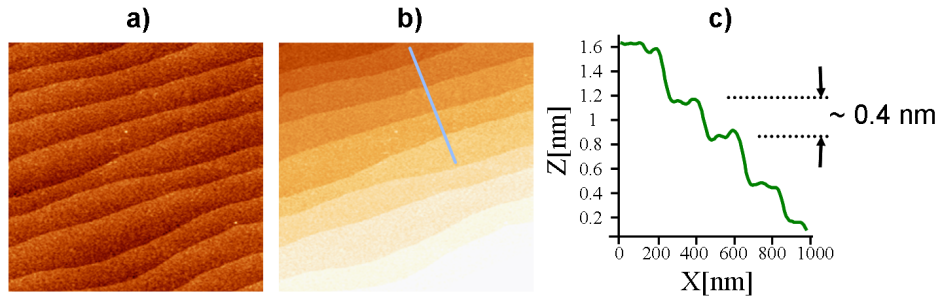


Figure 4.7: a) Topography image ($2 \times 2 \mu m^2$) of a 5 nm thick LSMO film grown onto a STO(001) single crystal. b) Flattened image with related scan-line profile (c) from which a step height of ~ 0.4 nm is obtained.

as substrates for the LSMO growth. Considering the previous calculated lattice parameter value for the LSMO, i.e. $a_{pc}^{LSMO} = (0.391 \pm 0.001)$ nm, a compressive strain state is expected in both cases of growth onto the two aforementioned substrates. Interestingly, the growth experiments were carried out using the same optimized PLD parameters as for the STO substrates. Figures 4.8a,c show the XRD patterns obtained from a 25 nm thick LSMO film grown on top of LAO and LSAT single crystals, respectively. The growth is epitaxial and no spurious phases are present. By analyzing the diffraction patterns, the two out-of-plane pseudo-cubic lattice parameters of $c_{pc} = (0.402 \pm 0.001)$ nm and of $c_{pc} = (0.392 \pm 0.001)$ nm are calculated for the LSMO grown onto LAO and LSAT single crystals, respectively. Cube-on-cube growth is also demonstrated. Indeed, Figures 4.8b,d show the topography images characterized by an atomically flat surface with a step-terrace structure. Reciprocal space mapping (RSM) measurements acquired at room temperature around the (103) reflection of the LSMO grown onto LAO and LSAT substrates (see Figures 4.8e,f respectively), reveal a completely strained LSMO film in both cases. Indeed the peaks corresponding to the LSMO layers, that are 5 nm thick on the LAO substrate and 25 nm on the LSAT substrate, are perfectly aligned to the corresponding substrate peak (the vertical dotted line represents a guide to the eyes). Considering the lattice parameter values of the pseudo-cubic unit cell of the LAO and LSAT substrates (*viz.* $a_{pc}^{LAO} = 0.378$ nm and $a_{pc}^{LSAT} = 0.386$ nm), an in-plane compressive strain state of -3.44% and of -1.30% can be calculated for the LSMO layers, respectively.

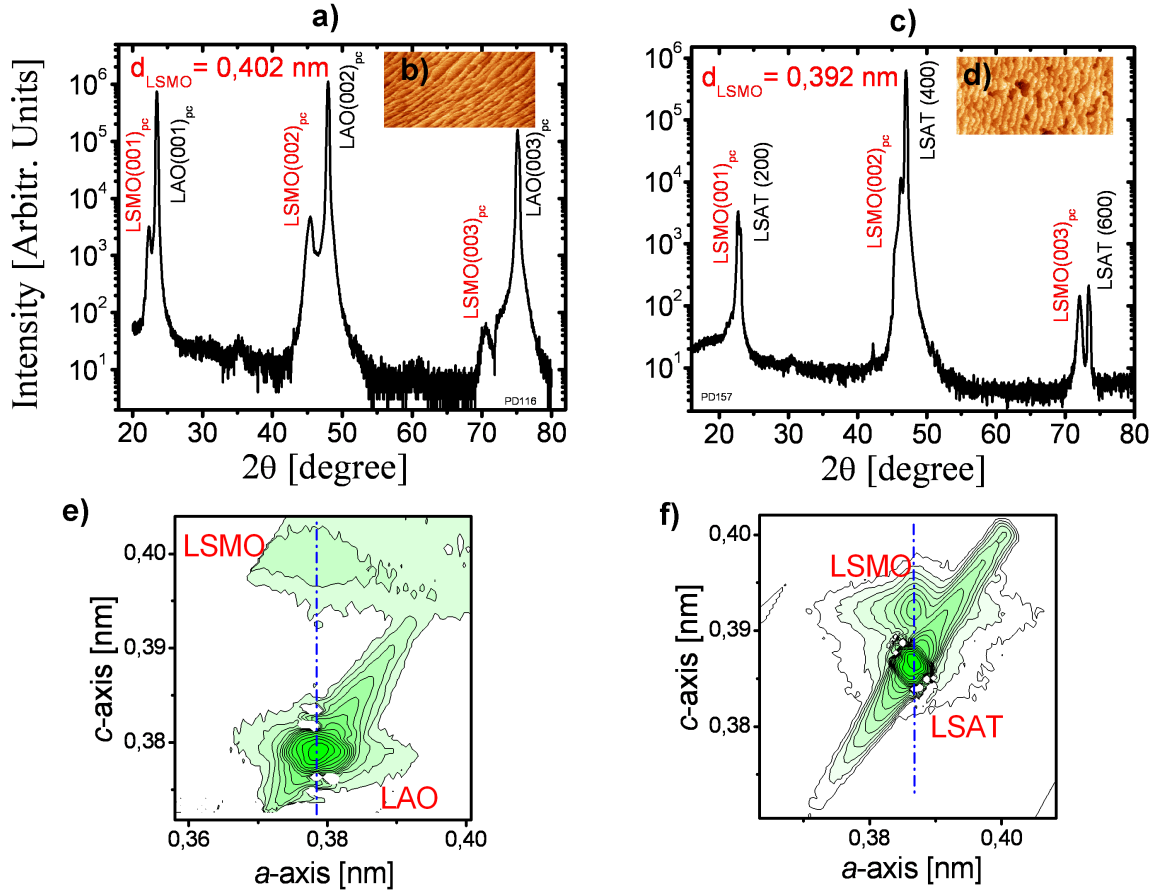


Figure 4.8: a) θ - 2θ XRD pattern of a 25 nm thick LSMO film grown on LAO single crystal. b) The related topography image ($4 \times 2 \mu\text{m}^2$) with a calculated RSM surface roughness of 0.18 nm. c) θ - 2θ XRD pattern of a 25 nm thick LSMO film grown on top of a LSAT single crystal. d) The related topography image ($4 \times 2 \mu\text{m}^2$) with a calculated RSM surface roughness of 0.21 nm. e) Reciprocal space map of a 5 nm thick LSMO film around the (103)_{pc} family plane of the LAO substrate. f) Reciprocal space map of a 25 nm thick LSMO film around the (103) family plane of the LSAT substrate. In both cases the LSMO is completely strained.

4.2.2 Functional properties: magnetotransport and magnetic characterizations of LSMO thin films

As already pointed out before, an important step during the characterization of the LSMO thin films, in particular for a successful achievement of the ferroelectric field effect experiments, is the study of the magnetic and transport properties. In this respect a short discussion regarding the observed variations of the functional properties exhibited by LSMO thin films grown on different substrates and using different oxygen partial pressure (i.e. P_{O_2}) is given here. The transport measurements were performed mainly using the Van der Pauw technique [104]. Hence, the edges of the (5×5) mm^2 samples were contacted by copper wires using silver paste as the optical microscope image shows in the upper part of Figure 4.9 where also a schematic representation of the two Van der Pauw configurations used for the measurement of the sheet resistance and Hall coefficient are sketched. Source-meter and volt-meter are indicated by A and V labels, respectively. Moreover, in the lower part of Figure 4.9 also a Hall bar (HB) geometry is schematically shown along with the two possible configurations for the measurements of the longitudinal and transversal resistance, i.e. R_{xx} and R_{xy} , respectively. Irrespective of the measurement set-up used for the (magneto)transport characterization of the LSMO thin films, a constant current I is injected and the voltage drop is monitored as a function of the

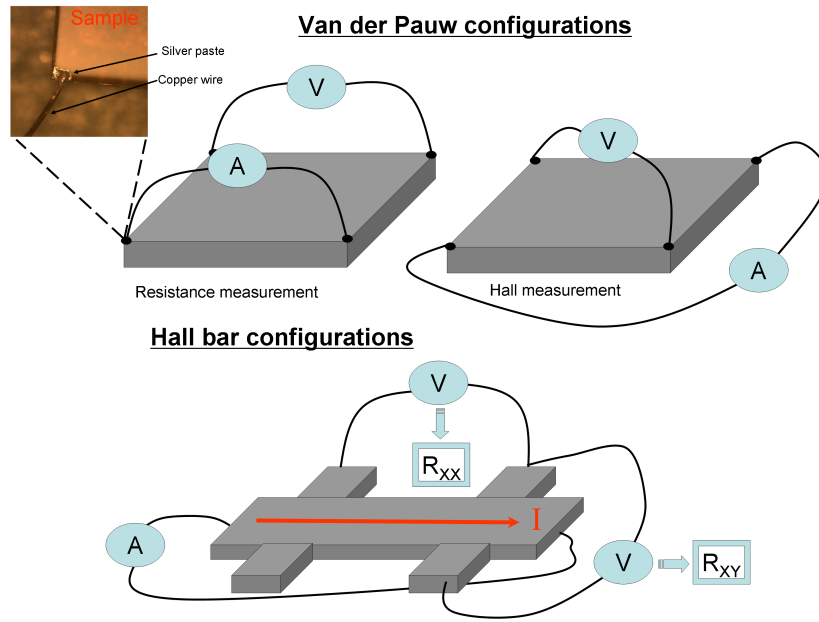


Figure 4.9: (Upper part) Scheme of the Van der Pauw technique. The two configurations for resistance and Hall coefficient measurements are schematically reproduced. An optical microscope image represents an example of sample's contact. (Lower part) Schematic representation of the Hall bar set-up employed for the measurement of R_{xx} and R_{xy} .

temperature and/or magnetic field. As a result, in Figure 4.10a (4.10b), resistivity $\rho(T)$ and magnetization $M(T)$ curves are shown, as a function of the temperature for a 50 nm thick LSMO film, grown on top of a STO(001) single crystal with $P_{O_2} = 0.15$ mbar ($P_{O_2} = 0.2$ mbar). The related AFM images are shown in the insets of the two graphs as well. The acquired $\rho(T)$ curves show the typical temperature dependence of the perovskite manganite [19]. An insulating (in the sense of $d\rho/dT < 0$) behavior is observed at high temperature and a metallic ($d\rho/dT > 0$) behavior is characteristic of the low temperature region. At the temperature T_{IM} , the insulator-to-metal transition is found (see black dotted lines in both graphs of Fig. 4.10). Due to the magnetoresistance effect, the transition is practically suppressed when an external magnetic field H is applied along one particular crystalline direction, and the overall resistivity decreases. The latter effect is properly displayed in the two graphs of Figure 4.10, where the two red $\rho(T)$ curves were acquired with an external magnetic field of 5 T applied along the out-of-plane direction. The DE mechanism qualitatively accounts for the magnetic nature of the insulator-to-metal transition, and the experimental proof is given in both graphs of Figure 4.10. Specifically, highlighted by the vertical dotted line is the expected correspondence between the LSMO insulator-to-metal transition, and the onset of the magnetization: T_{IM} and T_C almost overlap. Indeed, when the LSMO becomes ferromagnetic for temperature values lower than T_C , the observed metallic behavior can be qualitatively ascribed to the DE model as introduced in section 2.1.1. The influence of P_{O_2} on the transport properties of the LSMO is obvious. An increase of the P_{O_2} value, from 0.15 mbar to the value of 0.2 mbar, improves the metallicity of the LSMO. Indeed the overall resistivity value is lowered when the deposition is carried out with 0.2 mbar: the measured residual resistivity at 20 K is equal to 0.5 m Ω cm to compare with the higher value obtained at 0.15 mbar, i.e. ~ 3 m Ω cm. Moreover, T_P is shifted to a higher temperature, from 301 K obtained with a value of $P_{O_2} = 0.15$ mbar to 311 K for $P_{O_2} = 0.2$ mbar. The same trend is also experienced by the $M(T)$ curves: a higher T_C and a higher magnetization saturation are exhibited by the film grown with $P_{O_2} = 0.2$ mbar. Specifically, the relation $M(0.2 \text{ mbar}) > M(0.15 \text{ mbar})$ is obtained. It is clear that the P_{O_2} value influences the functional properties of the LSMO thin films. The role played by the oxygen va-

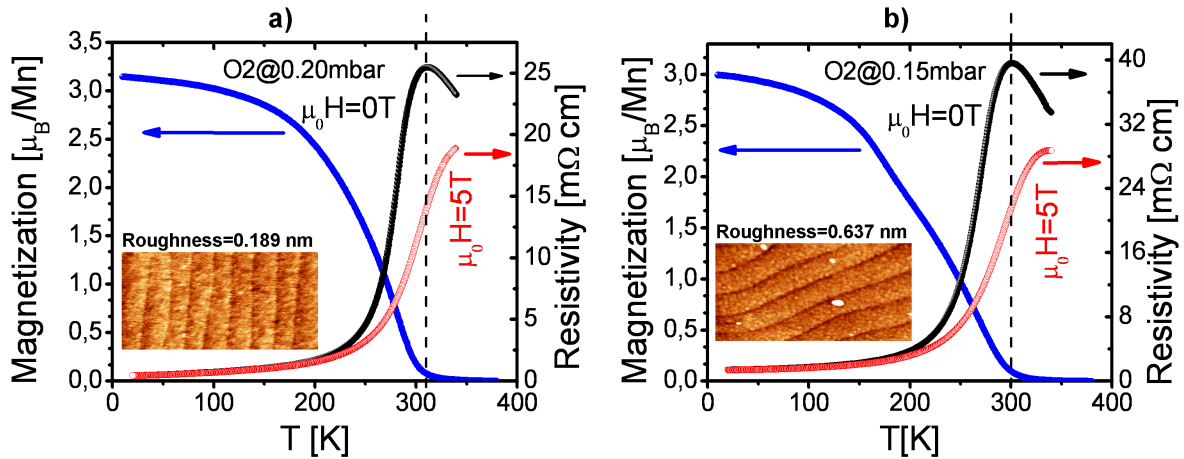


Figure 4.10: Resistivity and magnetization curves as a function of the temperature acquired for two 50 nm thick LSMO layers grown on top of STO(001) single crystals. Two different P_{O_2} of (a) 0.2 mbar and (b) 0.15 mbar were employed. For the transport measurements H was applied along the out-of-plane [001] direction of the sample. The magnetization was acquired with $\mu_0 H = 0.1$ T applied along the [110] direction (diagonal of the sample). The vertical dotted lines represent a guide to the eyes, and they highlight the correspondence between T_{IM} and T_C . Atomic force microscope images ($3 \times 1.5 \mu m^2$) are shown in the insets.

cancies is a rather common approach for a plausible explanation of the observed trends. Indeed in Ref. [105] similar results have been shown. Here, the possible presence of oxygen vacancies was considered as the main cause of the worsening of the transport and magnetic properties of the studied manganite thin films. However, it has also been demonstrated in Ref. [106] that an increase of T_{IM} and T_C can be obtained in a completely opposite situation, *viz.* lowering the P_{O_2} background value. In this case the key point to consider regards the optimization of the correct transfer of the stoichiometry from the target to the substrate. In this respect, the insets of each graph of Figure 4.10 showing the AFM images of the two LSMO films, clearly show that some precipitates are observed in the case of the LSMO grown with $P_{O_2} = 0.15$ mbar. Those precipitates are the consequence of an improper control of the cation stoichiometry in the ablation process as reported in Ref. [107]. Along with the presence of precipitates, the step-terrace structure of the vicinal substrate is nevertheless recovered, and the presence of the small islands demonstrates a too high kinetic energy of the ad-atoms. Indeed the latter can be decreased, increasing the oxygen pressure, and a very smooth surface, free of precipitates (see AFM image in Fig. 4.10a), can be obtained. On the other hand, the decrease of the kinetic energy of the ad-atoms can be achieved upon a proper tuning of the laser fluence, for instance. However, the decision to keep the value of $P_{O_2} = 0.2$ mbar was taken since the growth of the subsequent ferroelectric oxide layer can be better achieved and controlled at relatively high oxygen pressure values.

Important information regarding the transport properties (*i.e.* type, number and mobility of the charge carriers), can be accessed performing Hall effect measurements. Figure 4.11a shows the field dependence of the Hall resistance ρ_{Hall} , acquired for a 22 nm thick LSMO film at various temperatures. Asamitsu and co-worker studied [108] the Hall effect for single crystals of $La_{1-x}Sr_xMnO_3$ at several x . Interestingly, a good agreement with the Hall data acquired for thin films is found. Some of the LSMO films were patterned photo-lithographically in a Hall bar geometry characterized by a 200 μm long and 100 μm wide channel. The transverse resistivity ρ_{xy} , of the Hall bar configuration, was measured sweeping the external applied magnetic field H from negative to positive values. In this way the even contribution in H of the longitudinal resistivity ρ_{xx} , due to possible misalignment effects of the Hall bar leads, was completely removed as explained in Ref. [109]. Hence, ρ_{Hall} was obtained by averaging

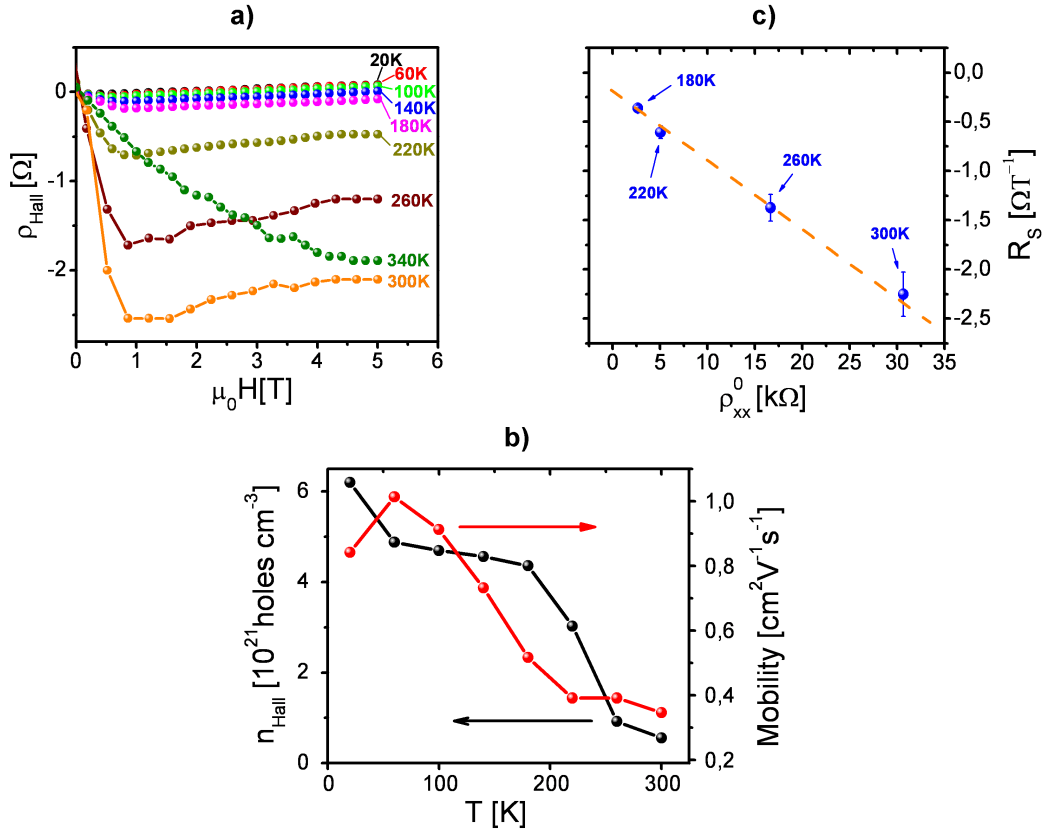


Figure 4.11: a) Hall resistance ρ_{Hall} curves acquired for a 22 nm thick LSMO film versus H at temperatures from 20 K to 340 K. b) Calculated Hall charge density (n_{Hall}) and mobility (μ_{Hall}) as a function of the temperature. c) Intercept of the ρ_{Hall} curves at zero field from the linear part at high field versus ρ_{xx}^0 .

the value of ρ_{xy} acquired at opposite H , precisely: $2\rho_{Hall} = [\rho_{xy}(+H) - \rho_{xy}(-H)]$. Since the LSMO is ferromagnetic an anomalous Hall effect is expected, as observed in ferromagnetic metals [110]. Indeed for temperatures well below T_C (~ 300 K) the ρ_{Hall} curves follow the phenomenological equation:

$$\rho_{Hall} = R_O B + \mu_0 R_S M,$$

where $B = \mu_0 H + \mu_0(1 - N)M$ is the magnetic induction, R_O and R_S represent the ordinary and the anomalous Hall coefficients, respectively. The demagnetization factor N due to the used geometry (thin film) is almost one ($N \sim 1$), so that the small deviation in B from $\mu_0 H$ can be neglected. For temperatures above 180 K, the ρ_{Hall} curves undergo a relevant decrease with H , reaching the minimum at $H \sim 1$ T (anomalous Hall effect) and then they rise linearly for higher field values (ordinary Hall effect). The sharp drop in ρ_{Hall} almost vanishes for temperatures below 180 K demonstrating a characteristic temperature dependence for R_S . The theory, by which the anomalous contribution to the Hall effect originates from an asymmetric scattering of the charge carriers at the localized magnetic ions [111], is commonly accepted. Moreover, it has been well established that the relation $R_S(T) \propto \rho_{xx}(T)^n$ is valid also for oxide materials [108]. The exponent n depends on the type of the scattering mechanism involved in the transport: $n = 1$ for skew scattering and $n = 2$ for side jump scattering [110].

Through a linear fit in the high-field region ($H > 1$ T) of the measured ρ_{Hall} curves, the ordinary Hall coefficient R_O , and the anomalous Hall coefficient R_S (intercept at zero field) can be calculated. M can be considered a constant since at high field it is saturated. Assuming as valid the relation $n_{Hall} = 1/eR_O$ which has been obtained for a single-band material [29], the Hall charge carrier density can be easily calculated as well. Figure 4.11b shows the temper-

ature dependence of n_{Hall} (black line) together with the calculated Hall mobility (red curve) $\mu_{Hall} = R_O/\rho_{xx}^0$, where ρ_{xx}^0 is the longitudinal resistance measured at zero magnetic field. Both n_{Hall} and μ_{Hall} smoothly increase as the temperature is decreased. A relatively high value of 10^{21} holes \cdot cm $^{-3}$ for the Hall charge density, and a relatively small value ~ 1 cm 2 V $^{-1}$ s $^{-1}$ for the mobility were measured. This demonstrates that the LSMO thin films behave like a bad metal where the charge carriers are holes (positive slope of ρ_{Hall}). Furthermore, plotting the $R_S(T)$ coefficient against the corresponding $\rho_{xx}^0(T)$ values in the region of high temperature values (i.e. from 300 K down to 180 K), a relevant information about the anomalous Hall effect can be inferred as well. Figure 4.11c shows the temperature dependence of the R_S coefficients versus the zero-field longitudinal resistance ρ_{xx}^0 for a 22 nm thick LSMO film. A linear relationship between ρ_{xx}^0 and R_S can be argued (see, for example, the dotted blue line in Fig. 4.11c). Since $n \sim 1$, a skew scattering, arising from the spin-orbit coupling between the magnetic moment and the charge carrier, may be suggested. Indeed in a material, where the DE mechanism is proved to determine the transport below T_C , the magnetic scattering or the spin-disorder scattering is expected to be the main scattering process in the system, as already observed in Ref. [108].

In the framework of the Thomas-Fermi model [102] a screening length, i.e. the distance over which external applied electric fields are screened in the material, of only a few Angstroms is obtained considering the concentration of holes measured at room temperature of $\sim 10^{21}$ cm $^{-3}$. This means that, as already highlighted before, in order to have a measurable modulation of the (magneto)transport properties of the LSMO through a field effect approach, ultrathin films need to be considered. Accordingly, a systematic study regarding the thickness dependence of the LSMO transport properties was performed in order to determine the minimum thickness at which an insulator-to-metal transition was still observed. Figure 4.12a shows the transport

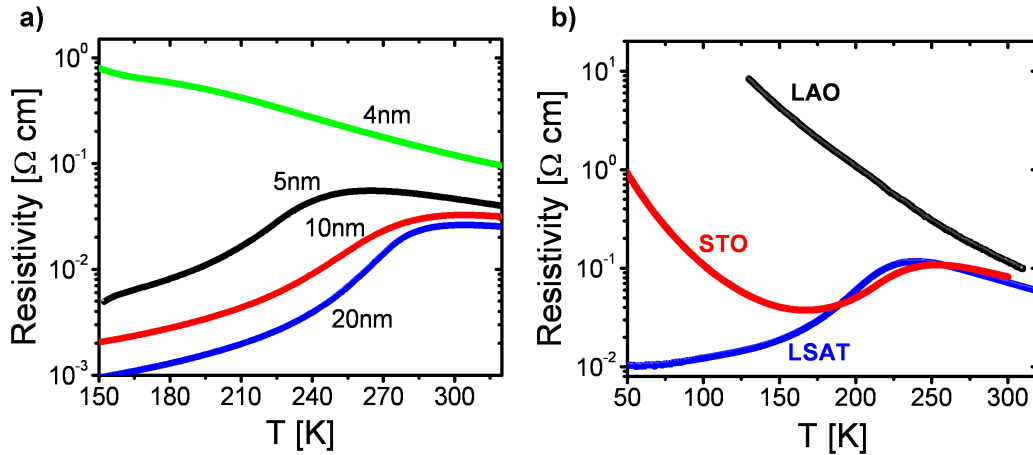


Figure 4.12: a) Temperature dependence of the resistivity acquired for unpatterned LSMO layers of various thicknesses grown on top of STO single crystals. b) Temperature dependence of the resistivity acquired for 5 nm thick LSMO films grown on STO, LAO and LSAT single crystals, respectively.

measurements on a series of LSMO thin films of various thicknesses grown onto STO single crystals. It is worth to note that LSMO films grown with thicknesses higher than 4 nm exhibit the characteristic insulator-to-metal transition as described before. Upon the decrease of the thickness, a concomitant lowering of T_{IM} is experienced as well, and for the nominal thickness value of 4 nm no transition is found anymore. This feature is commonly addressed invoking the presence of a *dead layer*. Ultrathin layers (≤ 4 nm in this case) of LSMO show a complete insulating behavior, and a proper understanding of the physics involved in this mechanism is still missing. Regarding the ferroelectric field effect experiments, described in the next section 5.3,

the minimum thickness value of 5 nm (still characterized by an insulator-to-metal transition) was chosen for all the PZT/LSMO heterostructures investigated. Moreover, relevant information regarding the transport properties were obtained exploring the role of the strain induced by using different substrates as well. Specifically, 5 nm thick LSMO films were grown onto STO, LAO and LSAT single crystals, and the transport measurements are shown in Figure 4.12b. The LSMO film grown on top of the STO shows the already discussed insulator-to-metal transition at ~ 250 K and it undergoes a second transition at ~ 150 K, and below an insulating behavior is recovered. This result is obtained only for 5 nm thick LSMO films demonstrating that the thickness is in general an important parameter for the transport properties of oxides grown in the form of thin films. Actually this observed upturn is the fingerprint of $La_{1-x}Sr_xMnO_3$ single crystals with $x = 0.15$ [19], demonstrating to some extent that a decrease of the thickness value of LSMO films implies a possible recovery of the typical physical properties of the low-doping level region. The LSMO bulk electronic phase diagram indeed shows, at doping levels lower than $x = 0.175$, an insulating electronic ground state. Moreover, as already reported in Ref. [36], the transport properties of manganites are heavily depending on the electronic anisotropy arising from the different orbital occupation of the Mn $3d e_g$ levels. Specifically, compressive and tensile strains induce an elongation and a compression of the MnO_6 octahedra, respectively. As a result, the z^2 or the $(x^2 - y^2)$ orbital state are lowered in energy for compressive and tensile strain states, respectively. Accordingly, insulating and conducting behaviors are triggered in the former and in the latter case, respectively. Indeed when a 5 nm thick LSMO film is grown on an LAO single crystal, the transport properties show a completely insulating behavior for the entire temperature range investigated, because of the compressive strain. Considering as pseudo-cubic lattice parameter for the LSMO film the one obtained on STO, i.e. $a_{pc}^{LSMO} = 0.391$ nm, a compressive in-plane strain $\epsilon_x = \epsilon_y$ of almost -3% and -1% are obtained on LAO and LSAT substrates, respectively. Although the LSMO exhibits a compressive strain when grown on LSAT single crystals, the transport properties show a clear metallic behavior even at low temperatures. Indeed in Figure 4.12b the upturn in the temperature dependence of the resistivity is not anymore observed for the LSMO grown on LSAT single crystals. That most probable might be ascribed to the fact that on LSAT the LSMO *dead layer* thickness is lower than one experienced onto STO and LAO substrates.

4.3 Growth and characterization of PZT films

PZT is the ferroelectric material chosen as dielectric gate for the ferroelectric field effect device. Structural, morphological and ferroelectric properties of PZT films were investigated. These properties are relevant in order to obtain good switching properties (low leakage, high polarization and very good retention), combined with a morphology that in principle should allow a layer-by-layer growth of the subsequent LSMO layer. Part of the results collected during the entire optimization and characterization procedure are shown here.

4.3.1 Structural, morphological and ferroelectric switching properties

The growth of epitaxial ferroelectric PZT layers was carried out mainly by using STO(001) single crystals as substrates, buffered with a 5 nm thick LSMO film. It is needless to mention that in order to allow the PZT polarization reversal, the presence of a bottom electrode is mandatory. The growth optimization was achieved mainly by varying parameters such as substrate temperature and laser repetition rate. Throughout the entire set of deposition experiments, the laser fluence and the oxygen pressure were kept constant at the values of 0.4 mJ/cm^2 and of 0.28 mbar, respectively. The latter growth parameters were already optimized in a previous

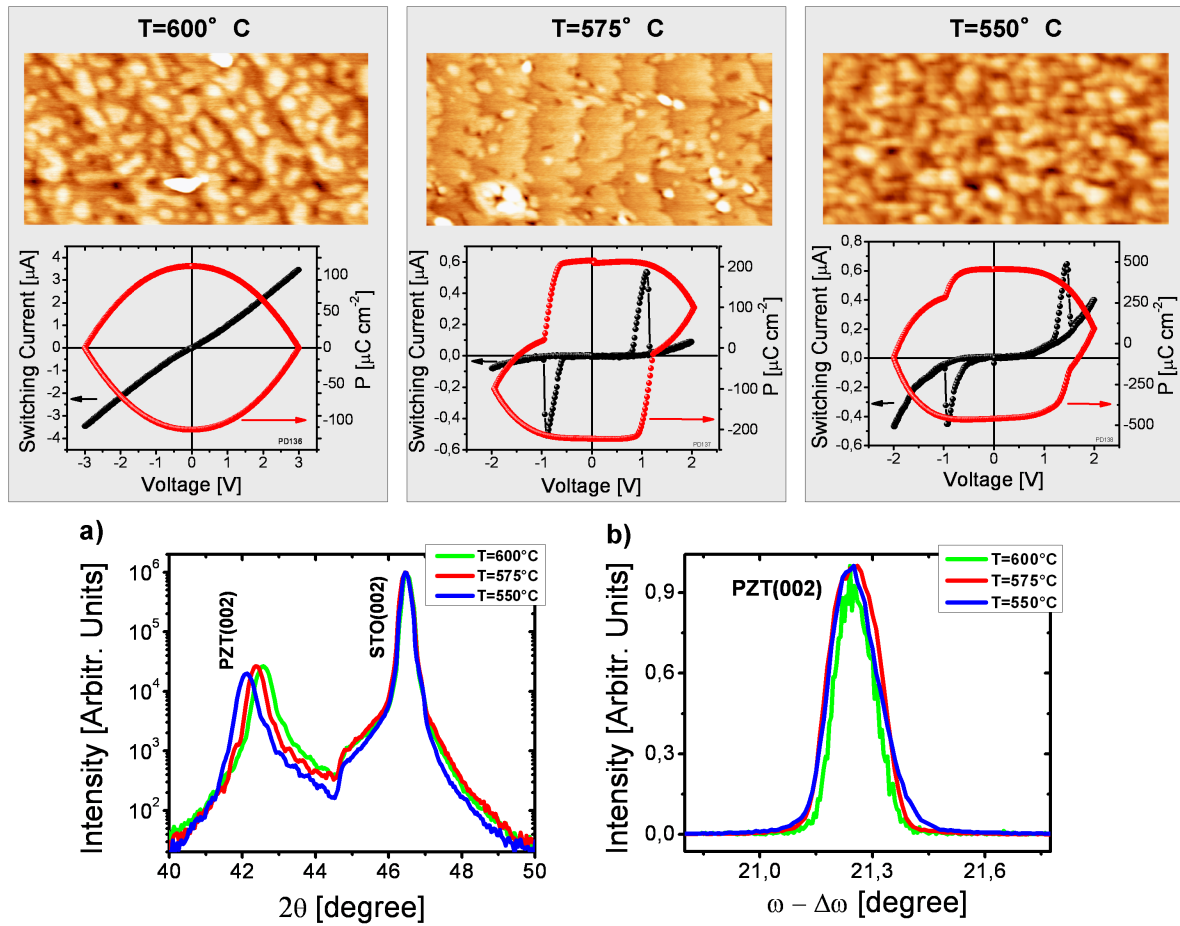


Figure 4.13: (Upper part) AFM images ($0.5 \times 1 \mu\text{m}^2$) and hysteresis loops along with dynamical current-voltage characteristics of three Cu/PZT/LSMO/STO capacitors grown at various temperatures. Each loop was acquired at 1 Hz. Top electrode area was $60 \times 60 \mu\text{m}^2$. (Lower part) a) $\theta - 2\theta$ scans of 30 nm thick PZT films grown at three different temperatures show a c -axis elongation of the tetragonal crystal structure as the temperature is decreased. b) ω -scans taken around the (002) PZT reflection show the same degree of crystallinity for all three ferroelectric films. Gaussian fits of the rocking curves (not shown) gave a value for FWHM of $\sim 0.12^\circ$.

work. Figure 4.13 shows morphological, ferroelectric switching and structural characterizations of 30 nm thick PZT films grown at several temperatures with the repetition rate fixed at 5 Hz. Copper top electrodes of $60 \times 60 \mu\text{m}^2$ area were evaporated *ex-situ* on PZT, in order to have a well-defined parallel-plate capacitor geometry. From the upper part of Figure 4.13 the best combination of morphology and ferroelectric properties is given by the PZT films grown at a temperature of 575°C . The step-terrace structure resembles the original vicinal STO surface and typical ferroelectric switching, corresponding to a high value of the remanent polarization of $\sim 100 \mu\text{C cm}^{-2}$ (calculated after the subtraction of the contribution given by the leakage current) is obtained. The structural properties of all PZT films displayed an intrinsic temperature dependence. Indeed in Figure 4.13a, θ - 2θ scans show a clear shift of the (002) PZT peak position towards lower angle values as the temperature is decreased. Accordingly, the tetragonal distortion becomes more pronounced: from $c_{\text{PZT}} = 0.426 \text{ nm}$ calculated at 600°C to $c_{\text{PZT}} = 0.430 \text{ nm}$ obtained at 550° . Moreover, rocking curves shown in Figure 4.13b (centered at the same ω value to be easily comparable) demonstrate that the degree of crystallinity is constant for all growth temperatures. Through a Gaussian fit (not shown in the plot) a FWHM value of $\sim 0.12^\circ$ is obtained for all three samples. Usually thin films with a good level of crystallinity are characterized by FWHM values less than 0.1° . Further growth experiments

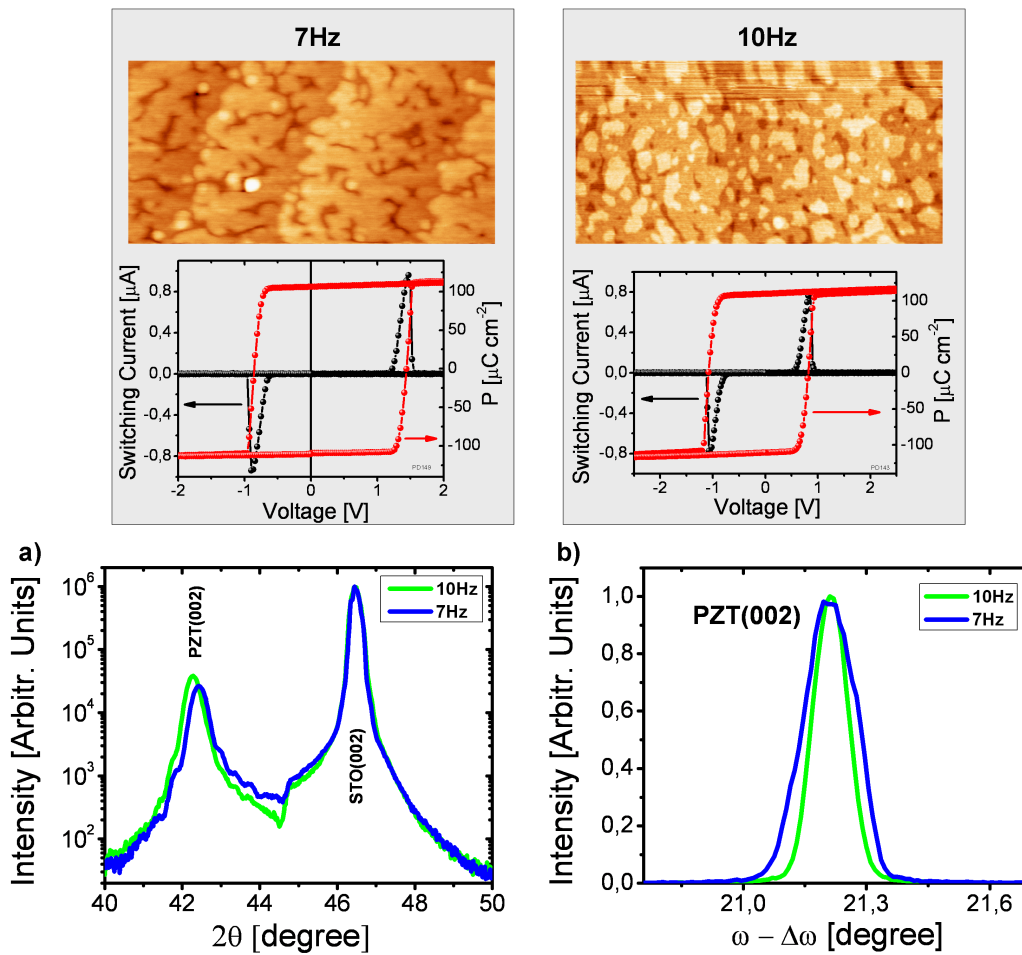


Figure 4.14: (Upper part) AFM images ($0.5 \times 1 \mu\text{m}^2$) and hysteresis loops along with the dynamical current-voltage characteristics of two Cu/PZT/LSMO/STO capacitors grown at 575°C with a repetition rate of 7 and 10 Hz. Each loop was acquired at 1 Hz. Top electrode area was $60 \times 60 \mu\text{m}^2$. (Lower part) a) θ - 2θ scans of 30 nm thick PZT films grown at two different repetition rates show a c -axis elongation of the tetragonal unit cell as the repetition rate is increased. b) ω -scans taken around the (002) PZT reflection show a higher degree of crystallinity when the repetition rate of 10 Hz is used. A FWHM of $\sim 0.08^\circ$ is the value obtained by a Gaussian fit of the rocking curve (not shown).

were required, and the influence of the laser repetition rate was studied. Figure 4.14 shows the morphology, ferroelectric switching and structural characterizations of 30 nm thick PZT films grown at a temperature of 575°C by using two different repetition rates, i.e. 7 and 10 Hz. A higher repetition rate improves the morphology of the PZT films and also the ferroelectric switching properties (calculated polarization value higher than $100 \mu\text{C cm}^{-2}$). In this case the best combination can be considered the one of the film grown at 10 Hz where PZT films show better morphology and an imprint-free switching with lower coercive voltage. Figure 4.14a shows the θ - 2θ scan of the film grown at 10 Hz and an out-of-plane lattice parameter equal to $c_{\text{PZT}} = 0.429 \text{ nm}$ is obtained. Moreover, the very small FWHM value ($\sim 0.08^\circ$) obtained from the rocking curve depicted in Fig. 4.14b demonstrates a higher degree of crystallinity than previously reported. The same c_{PZT} value obtained in this case was also observed for the PZT film grown at a temperature of 550°C . Figure 4.15 shows a high resolution TEM image taken on the PZT/LSMO/STO sample grown at this high repetition rate along with a RSM taken around the asymmetric reflection (103). A coherent growth of both oxide materials with a plane and sharp interface is demonstrated (see Fig. 4.15a). This is an important point to highlight since a robust ferroelectric field effect is highly depending on the quality of the oxide interface. Moreover,

the RSM shows a completely strained film as expected for the relatively low thickness value of 30 nm.

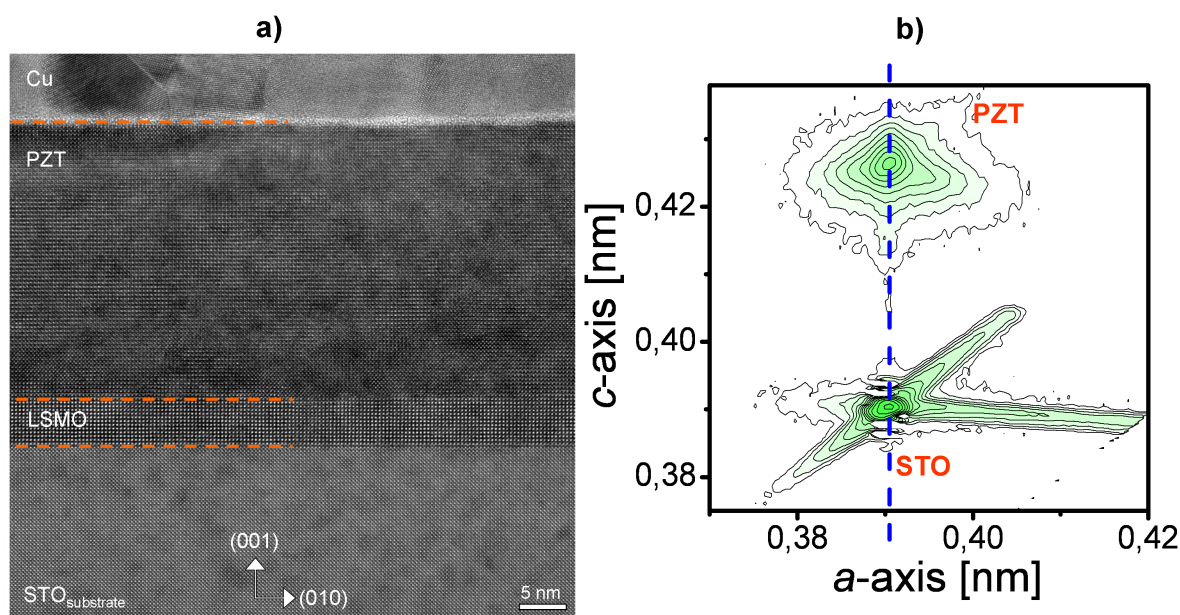


Figure 4.15: a) High resolution TEM image of a 5 nm thick LSMO film used as bottom electrode for a ferroelectric capacitor in the parallel plate geometry. The interface with the PZT (30 nm was the thickness) is sharp and plane and no dislocations are present. b) RSM taken around the asymmetric reflection (103). A fully strained PZT film is observed.

4.3.2 Oxide electrodes for PZT films

The ferroelectric switching properties are not only depending on the intrinsic quality of the ferroelectric oxide. The nature of the metal contact is of paramount importance for the magnitude of the leakage current measured between top and bottom electrode in a typical switching experiment. Indeed in Ref. [112] it has been demonstrated that Cu top electrodes, forming a better rectifying contact than other metallic materials such as Pt or Au, represent the best choice for epitaxial PZT films. The choice to use Cu top electrodes to investigate the ferroelectric properties of the PZT thin films, is thus justified. Moreover, in this Thesis the additional possibility to switch the ferroelectric polarization of a PZT layer by using LSMO electrodes was considered as well. Figure 4.16 shows the (micro)structural characterizations of a LSMO/PZT/LSMO/STO heterostructure characterized by thickness values of 5, 30 and 8 nm for the bottom LSMO, PZT and top LSMO layers, respectively. As a result, the θ - 2θ scan shown in Fig. 4.16a exhibits only peaks belonging to the (001) family plane demonstrating a single c -domain state of the PZT layer. From the peak positions an out-of-plane lattice parameter of 0.429 nm can be calculated. Moreover, from the rocking curve acquired around the (002) PZT reflection and depicted in Figure 4.16b, the evident broadening of the PZT peaks is also demonstrated (i.e. FWHM of $\sim 0.2^\circ$). The latter can be attributed to a small presence of a -domains. Actually from the reciprocal space map, shown in Figure 4.16c, the PZT film embedded in the two LSMO layers is completely strained or, at least, the related RSM features are very similar to the ones obtained for the PZT/LSMO/STO bilayer (see Fig. 4.15b) which was characterized by a very small value of the FWHM parameter. Hence, a -domains should be absent. To get more information the bilayer was investigated also by TEM, and Figure 4.16d shows the obtained result. Though sharp and plane interfaces are easily recognizable, demonstrating a coherent growth of the top LSMO layer as well, the presence of extended defects

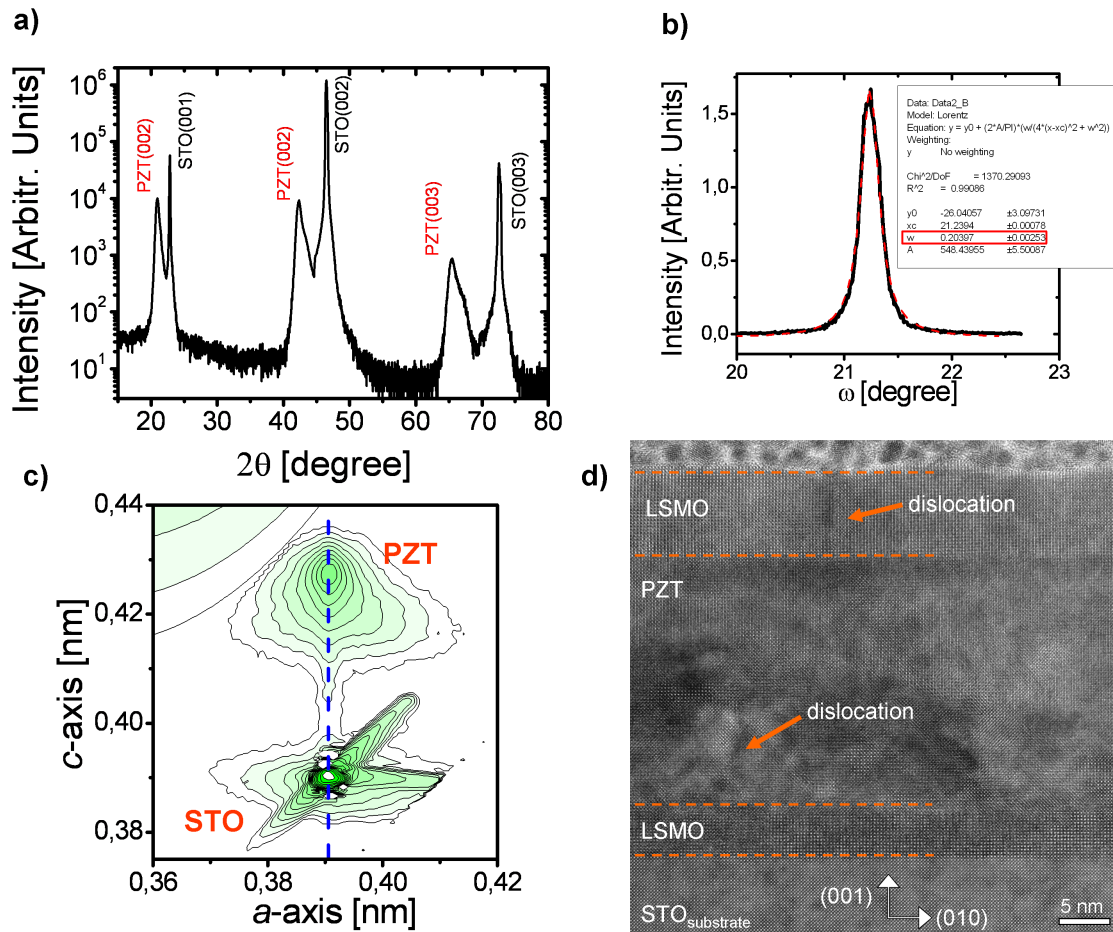


Figure 4.16: a) θ - 2θ scan of a LSMO/PZT/LSMO/STO heterostructure. b) Rocking curve of the (002) PZT reflection with a calculated FWHM parameter of $\sim 0.2^\circ$. (c) RSM acquired around the (013) asymmetric reflection. d) TEM image showing plane and sharp interfaces with some dislocations in the PZT and the top LSMO layers (orange arrows).

in the PZT film (see arrow in the TEM image) clarifies the very large value obtained for the FWHM parameter. The extra time needed to grow the top LSMO layer most probably altered the density of the extended defects and generated a broadening of the PZT peaks. Regarding the top LSMO layer a dramatic change of the morphology and the transport properties can be envisaged as well. In this respect, Figure 4.17b shows the surface morphology of the top LSMO layer characterized by a massive presence of grains. The rms roughness of the surface also largely increased, i.e. ~ 0.9 nm. From the line profile analysis of the AFM image the depth of the valley between two grains is about one-third of the overall LSMO thickness. As already highlighted before, the morphology of manganite thin films is an important parameter for the transport properties. Figure 4.17a shows the temperature dependence of the top LSMO resistance and, indeed, a completely insulating behavior is found on the entire range of temperature investigated. Since the resistance of the top LSMO layer was very high at low temperatures, a Keithley 6517B Electrometer (two-probe method) was necessary to use.

However, aside from these last results the improvement of the ferroelectric switching properties of a PZT thin film sandwiched between two LSMO layers by annealing was pursued. In Figure 4.18a the schematic view of the Cu/LSMO/PZT/LSMO/STO capacitor structure is shown. The top LSMO layer was chemically etched after the evaporation of the metallic Cu contacts. All the switching experiments were performed at 100 Hz. In Figures 4.18b,c the measured current-voltage characteristics for the capacitor in the as-obtained state and after an

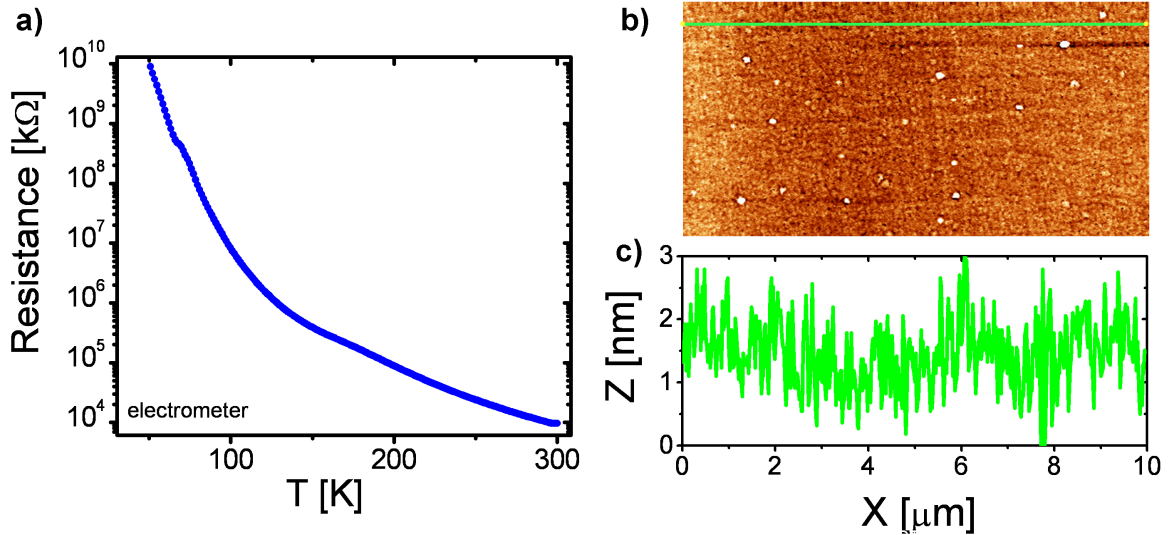


Figure 4.17: a) Insulating behavior of an 8 nm thick LSMO film grown on top of a PZT layer. b) AFM image ($10 \times 5 \mu\text{m}^2$) displaying the poor morphology with the related line profile scan (c) demonstrating the high rms roughness of ~ 0.9 nm.

ex-situ annealing procedure (300°C for 1 hour) are shown, respectively. First, a lower polarization value of $\sim 80 \mu\text{C}/\text{cm}^2$ is measured, (a value of $\sim 100 \mu\text{C}/\text{cm}^2$ was obtained when the metallic Cu top electrodes were evaporated directly on top of the free PZT surface), and further, a large imprint suppressed the possibility to have a switchable system with two stable polarization states. The measured asymmetry in the hysteresis loop was still present after the *ex-situ* annealing procedure, demonstrating that the oxygen content might not play a role in the explanation of the observed features. Indeed, a completely different result was obtained decreasing the cooling rate of the heterostructures from $15^\circ\text{C}/\text{min}$ to $5^\circ\text{C}/\text{min}$. Figure 4.18d shows a completely imprint-free hysteresis loop. A clear understanding of the imprint in ferroelectric capacitors is still missing. Nevertheless, from the presented results it can be easily evidenced that a careful control of the cooling rate is very important since the thermal stress of each single oxide might play the relevant role for the polarization pinning of the PZT layer.

4.4 Magnetic properties of PZT/LSMO/STO heterostructures

As already pointed out before, the goal of the ferroelectric field-effect experiments is given by the possibility to tune the magnetic properties of LSMO thin films by switching the PZT polarization. For this reason, the magnetic characterization of simple LSMO/PZT bilayers was necessary in order to gain information from the magnetic properties of the system as well. Accordingly, here, the magnetic properties of a PZT/LSMO/STO heterostructure, characterized by thickness values of 5 and 150 nm for the LSMO and PZT layers, respectively, are discussed. The different measurements performed gave information on the magnetic anisotropy of the heterostructure. Precisely, the easy axis direction was determined, i.e. the crystallographic direction that is energetically favorable for the alignment of the Mn magnetic moments. Generally, in the case of thin films, the magnetization is expected to lie always in the plane of the film. In this respect, shape anisotropy and demagnetizing field energies play the main role. Figure 4.19a shows the hysteresis loops obtained at 10 K, with H applied along the in-plane [100] and [110] crystallographic directions. The diamagnetic contribution of the substrate was subtracted from the linear fit made from the magnetization curve acquired up to 5 T. The

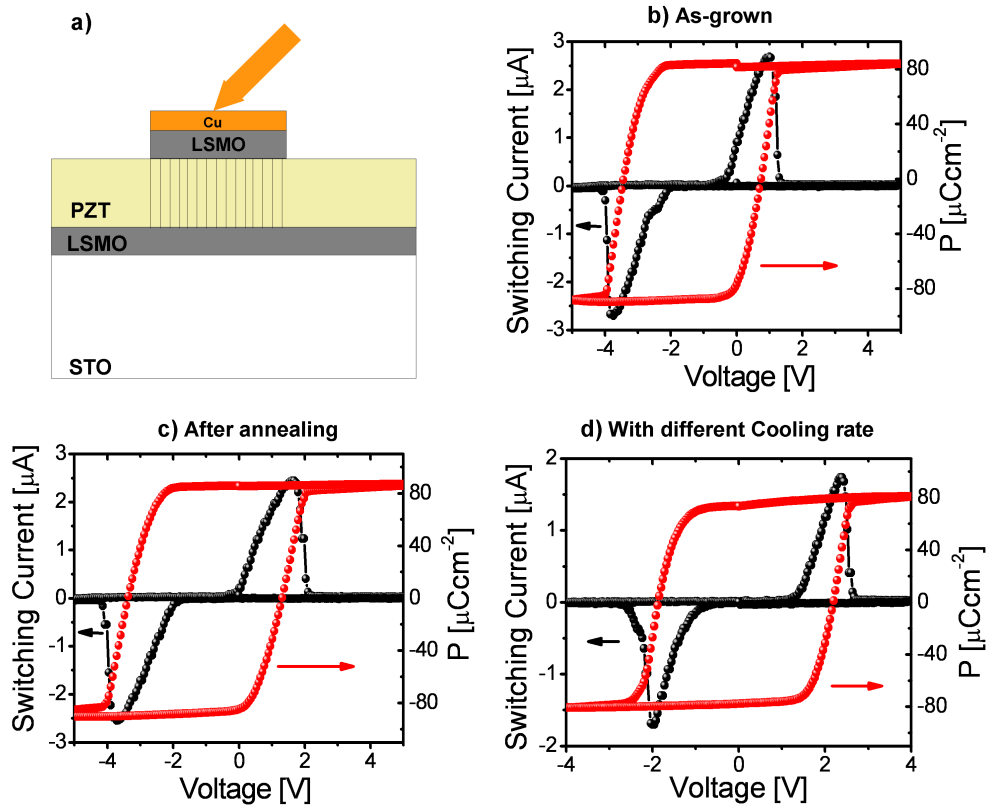


Figure 4.18: a) Schematic view of the Cu/LSMO/PZT/LSMO/STO capacitor. b), c) Hysteresis loops and dynamical current-voltage characteristics of the capacitor in the as-obtained state and after the annealing procedure, respectively. d) Imprint-free hysteresis loop after a decrease of the cooling rate.

saturation magnetization is reached for an applied field of ~ 0.5 T for both directions and is equal to $\sim 2.3 \mu_B/Mn$. The remnant magnetization value measured along the [100] direction is significantly smaller than the one measured along the [110] direction. This result has been already observed for other LSMO doping levels [113]. As a result, the [100] and [110] directions represent the hard and easy axis, respectively. A difference of $\sim 0.7 \mu_B/Mn$ between the two different orientations is obtained. μ_B is the Bohr magneton. Also the coercivity fields are slightly different between the two different orientations, ± 44 mT and ± 30 mT for [100] and [110] directions, respectively. The temperature dependence of the magnetization, acquired at two different magnetic fields and along the two different directions, are presented in Figures 4.19b,c. The measurements were performed in the field-cooling (FC) mode, i.e. a constant applied magnetic field was switched on at 400 K, and the temperature dependence of the magnetization was recorded on cooling down the heterostructure to 4 K. Figure 4.19b shows the results obtained for the small field of 2 mT applied along the hard and the easy axis, respectively. Along the direction [110] the magnetization value almost reaches the saturation, i.e. $\sim 2.3 \mu_B/Mn$. A completely different scenario is obtained when the field is oriented along the [100] direction. In this case, the magnetic moments are not capable to orient completely and the smaller magnetization saturation value of $\sim 1.4 \mu_B/Mn$ is recorded. This result confirms that the [110] direction represents the easy axis for the magnetization. The T_C of the heterostructure is ~ 265 K. On the other hand, Figure 4.19c shows the results obtained for the field of 0.5 T applied along the hard and easy axis, respectively. In this case the externally applied magnetic field is sufficient to saturate, in both directions, the magnetization value. Since each magnetic moment experiences a low exchange energy, due to the presence of a large applied magnetic

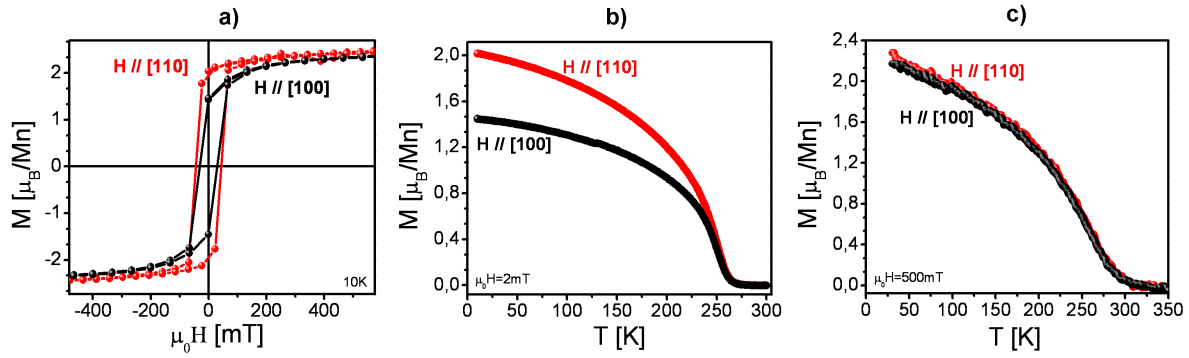


Figure 4.19: a) Magnetic hysteresis loops of a LSMO/PZT/STO heterostructure. LSMO and PZT thickness is 5 nm and 150 nm, respectively. Magnetic field applied in plane along the [100] and [110] directions. b),c) Magnetization curves as function of the temperature acquired applying a magnetic field of 2 mT and 500 mT along the easy axis (red curve) and hard axis (black curve), respectively.

field, the T_C value measured is shifted to a higher temperature region (~ 300 K). The saturation value of the magnetization along the two different orientations turned out to be the same, i.e. all the magnetic moments are aligned along the two different orientations.

4.5 Conclusion

Table 4.1 lists the optimized deposition parameters for both oxide materials used in this Thesis. A highly oxidizing atmosphere is the optimal growth condition for both oxides. Structural and TEM-based analysis revealed that highly epitaxial LSMO and PZT thin films were grown on different substrates. A coherent growth is achieved for the PZT/LSMO heterostructures, and morphological investigation showed smooth and atomically flat surfaces of both oxides. Moreover, (magneto)transport characterizations of bare LSMO films showed the typical insulator-to-metal transition, and thickness-dependent measurements demonstrated that for the chosen level of doping, i.e. $x = 0.175$, the latter is still observed for LSMO films with thickness values higher than 4 nm. The properties were completely different when the LSMO layers were grown on top of the PZT layer. In this latter situation LSMO shows a completely insulating behaviour also for a thickness value of ~ 5 nm. The relatively high resistance, as will be shown in the next chapter, hides the expected interfacial field effect and, hence, the modulation of the magnetic and (magneto)transport properties of the electrostatically gated LSMO layer. Different characterizations like dichroic x-ray absorption spectroscopy (see, for example, 6) were necessary to investigate the effective ferroelectric field effect on LSMO thin films grown on PZT in suitably patterned LSMO/PZT/LSMO/STO heterostructures.

Table 4.1: Deposition parameters

Oxides	Temperature [$^{\circ}\text{C}$]	P_{O_2} [mbar]	Fluence [J/cm^2]	Repetition Rate [Hz]	Cooling Rate [$^{\circ}\text{C}/\text{min}$]
LSMO	600	0.2	~ 0.4	1/2	5
PZT	575	0.28	~ 0.4	10	5

...*"the theory of metallic resistance abounds in mysteries"...*

Meaden, G.T.

"Conduction electron scattering and the resistance of the magnetic elements."

Cont. Phys.; vol. 12, No. 4, 313-337, (1971).

Magnetotransport and magnetic characterization of ferroelectric field effect devices (FeFEDs)

The following chapter focuses on the studies of (magneto)transport and magnetic properties of LSMO thin films as function of the PZT polarization (P) direction, undertaken on prototypical ferroelectric field effect devices (FeFEDs). To allow the study of the field effect only in correspondence to the switched area of the FeFEDs, a specific engineering process of the (top electrode)/PZT/LSMO heterostructures was necessary. In this respect, the efforts to obtain pre-patterned Hall bar masked substrates are discussed here as well. The LSMO ultrathin film of the FeFED accomplishes a two-fold function such as a sensitive material (channel) and a bottom electrode of the device itself. Experimentally, the majority of carriers in the LSMO layer are electrostatically accumulated/depleted at the LSMO/PZT interface upon the reversal of P . With reference to Figure 5.1 the meaning of accumulation and depletion states are here

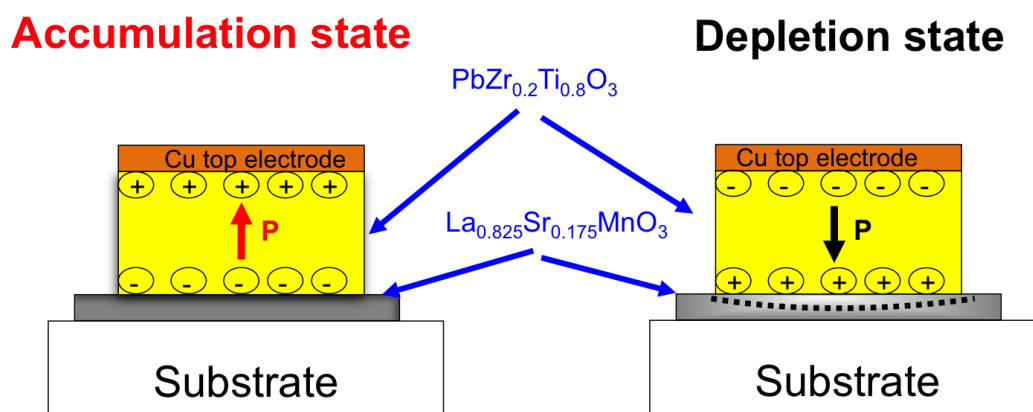


Figure 5.1: Schematic representation of a ferroelectric field effect device (FeFED). The accumulation (left) and depletion (right) states are represented.

introduced through the following argument. As already highlighted in the previous chapter the majority of carriers in the channel are holes. Correspondingly, upon the application of a negative voltage to the top electrode of the FeFED, P is switched as pointing upward and, consequently, the electric field generated by the negative polarization charges at the LSMO/PZT interface is screened by an accumulation of holes (see left side of Fig. 5.1). Regarding the opposite situation, i.e polarization pointing downward, a depletion of holes at the LSMO/PZT interface is realized (see right side of Fig. 5.1). As a result, a reversible P -control of the onset of the ferromagnetic order and the modulation of the temperature dependence of the re-

sistance $\rho(T)$, regarding the gated LSMO thin film is achieved. Moreover, also anisotropic magnetoresistance (AMR) measurements, as function of the P direction, are presented here. The magnetic field H was applied in a plane perpendicular to the current density J , and the obtained electrostatic modulation of the anisotropy field values H_a are explained introducing a possible modulation of the interfacial magnetic anisotropy of the gated LSMO layer.

5.1 Engineering of the FeFEDs for magnetotransport and magnetic studies

In order to unambiguously study the magnetotransport properties of the LSMO as a function of the P direction, a suitable measurement geometry has been considered, i.e. a Hall bar (HB) geometry. As a result, a feasible patterning of the heterostructures represents a procedure as complex as necessary. Accordingly, the "top-down" method is generally used. The latter is based on two different *modi operandi* which include dry or wet etching procedures. Linked to them are some drawbacks, such as the non-environment friendly character and the high probability of unwanted ion implantation for the wet and dry etching methods, respectively. For this reason, as pointed out by Banerjee *et al.* in [114], both aforementioned approaches can be completely avoided when a high temperature stable sacrificial oxide mask is suitably designed. Along this direction, almost all the FeFEDs studied in this Thesis were engineered using amorphous aluminum oxide (AlO_x)-masked substrates. As a result, an *in-situ* growth of the LSMO and PZT oxides in a pre-patterned HB geometry was possible. Accordingly, Figure

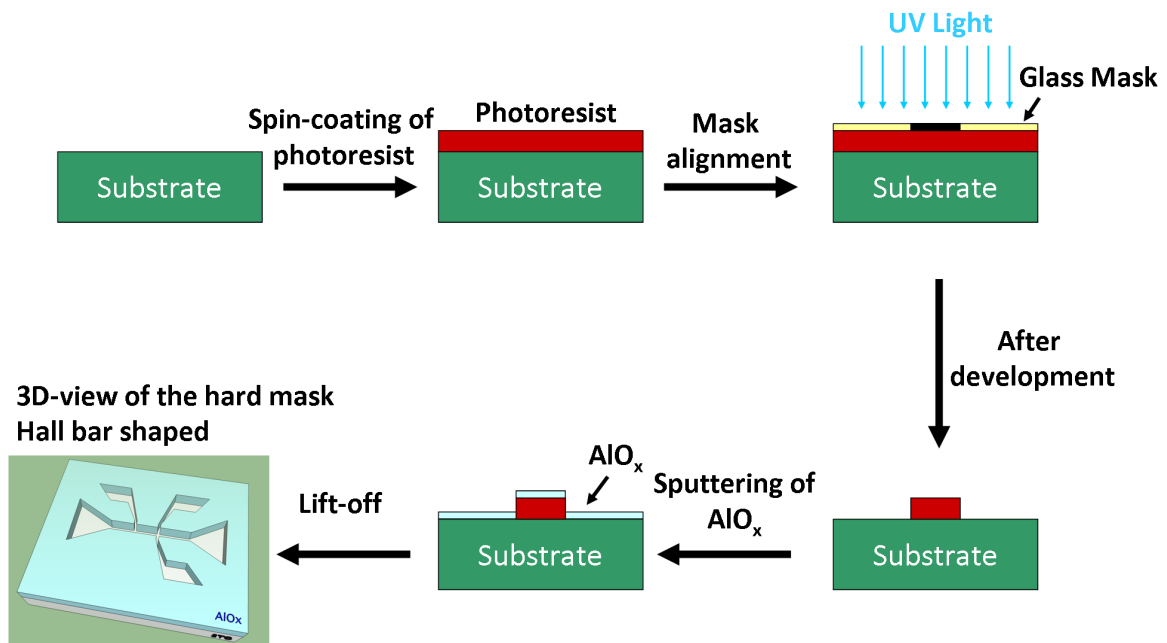


Figure 5.2: Schematic view of the several steps required to prepare the sacrificial AlO_x hard mask.

5.2 shows a schematic view of the several steps required to prepare the sacrificial AlO_x hard mask. First, a photolithographic process was necessary to pattern the HB geometryⁱ directly onto the different substrates. Thereafter, a very thick layer of AlO_x (~ 200 nm) was deposited by sputtering an aluminum target under 2.5 mbar of gas mixture (90%Ar/10% O_2). Henceforth,

ⁱThe photomask that was used to transfer the HB geometry onto the several substrates, was custom-designed by using the software Layout. Afterwards, the company Compugraphics Jena GmbH was charged for the realization of the quartz glass with an opaque chrome layer shaped as the wanted HB geometry.

a lift-off process performed using organic solvents provided substrates completely covered by an amorphous AlO_x layer appropriately patterned for the HB geometry. As a result, the epitax-

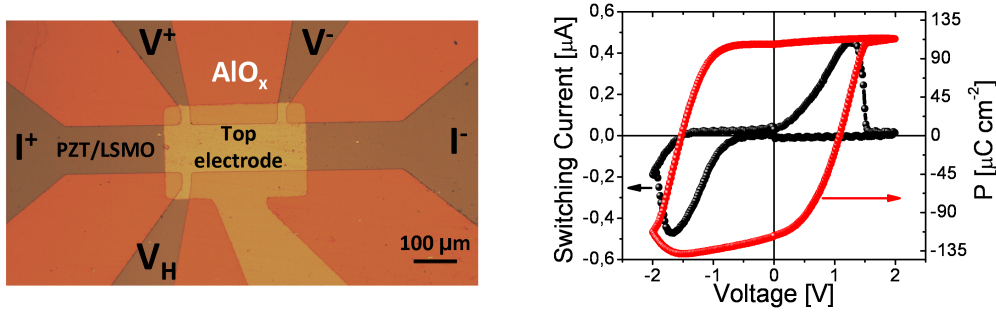


Figure 5.3: (Left side) Optical image of the FeFED after the evaporation of the copper top electrode. (Right side) Dynamical current-voltage characteristic with related calculated polarization hysteresis curve. A polarization value higher than $100 \mu\text{Ccm}^{-2}$ can be obtained for the FeFED grown on top of a STO single crystal with 5 and 170 nm thick LSMO and PZT layers, respectively.

ial growth of the LSMO and PZT oxides was achieved only in the region where the substrate was unmasked by the AlO_x layer. Subsequently, in order to allow the PZT polarization reversal only in the restricted area corresponding to the HB channel area, an appropriate copper top electrode was evaporated. Figure 5.3 shows the optical image of the FeFED after the evaporation of the top electrode (left side). I^+ , I^- and V^+ , V^- , V_H indicate the current and voltage pads of the HB geometry, respectively. Scratches were made manually with a diamond-coated tip through the PZT layer in order to contact the LSMO pads with simple copper wires by using silver paste. The $200 \mu\text{m}$ long and $100 \mu\text{m}$ wide area, delimited by the contact legs V^+ and V^- , corresponds to the channel of the HB geometry. The right side of Figure 5.3 shows the ferroelectric switching features of a FeFED grown onto an STO substrate with 5 and 170 nm thick LSMO and PZT layers, respectively. Successfully, a saturation polarization value of $\sim 100 \mu\text{Ccm}^{-2}$ was measured, as expected for high quality PZT films [49].

On the other hand, Figure 5.4a shows the schematic view of the device used for the *in-situ* P -dependent magnetometer experiments. In this respect, the magnetic characterization of the LSMO/PZT heterostructures was a challenging task, since it requires large-scale samples (several mm^2) and also the possibility to reverse the ferroelectric polarization without removal of the device from the SQUID. As a result, in order to study the influence of the P -reversal on the magnetic properties of the LSMO, capacitors exhibiting relatively large area were necessary. Accordingly, the improvement of the ferroelectric properties of the PZT was indispensable in order to reduce the leakage current and, hence, allow the switching of large area-capacitors. In this case, the PZT/LSMO/STO heterostructures were not patterned and after the PLD growth, by using a metallic shadow mask, nine gold top electrodes were evaporated on top of the $(3 \times 3) \text{mm}^2$ area sample. The area of each top electrode was measured through an optical microscope which in average turned out to be equal to $(0.64 \pm 0.01) \text{mm}^2$. As schematically shown in Fig. 5.4a, the top electrodes were contacted in parallel in groups of three (also in this case through simple copper wires and silver paste), in order to allow the simultaneous ferroelectric switching, keeping the underneath LSMO layer to ground, as sketched in the cross-section shown in Fig. 5.4a. As a result, Figure 5.4b shows the PUND voltage train pulse used to switch the polarization (see top section 3.4) of all the capacitors connected in parallel. An oscilloscope was used to acquire the dynamical voltage-time signal from the FeFED in response to the PUND. The calculated current (the internal resistance of the oscilloscope was equal to 50Ω) as a function of the time is displayed in Fig. 5.4b. Here it is possible to see the clear difference between the two current pulses I_{SW} and $I_{leakage}$, obtained during the P and U pulses, respectively. The larger value of the current obtained while applying the P pulse accounts for the ferro-

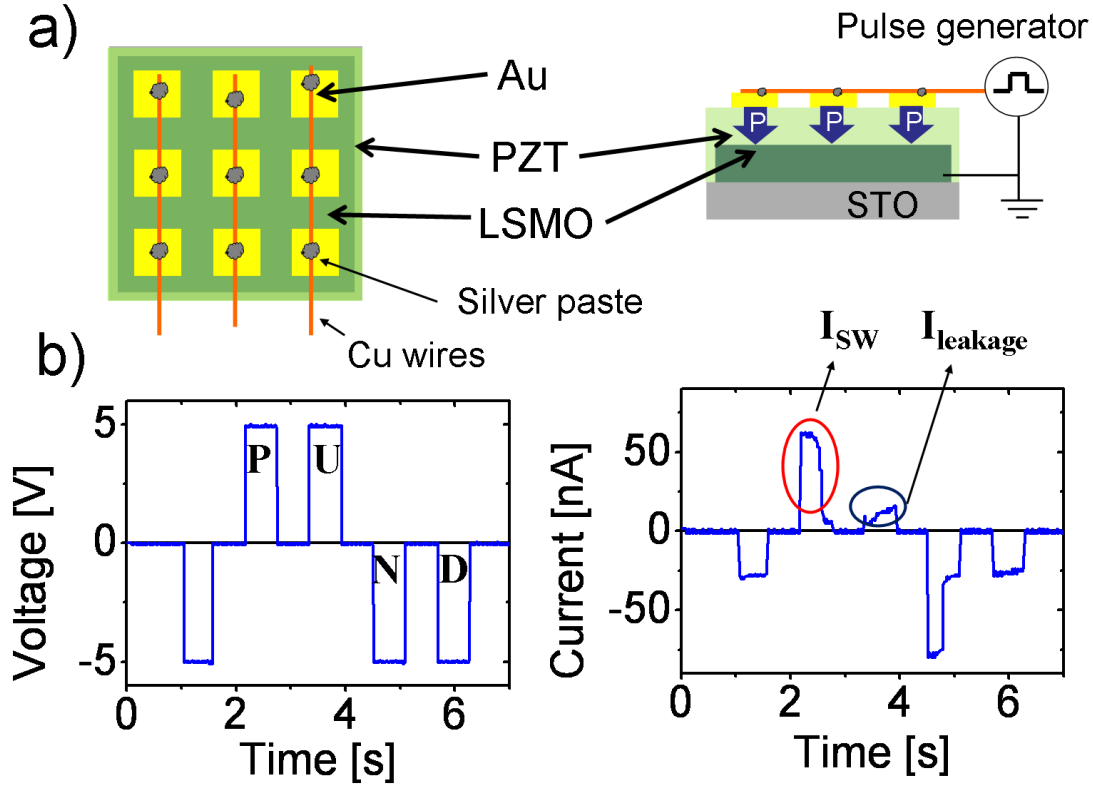


Figure 5.4: a) Schematic view of the FeFED for the *in-situ* SQUID measurements. The P switching was allowed only in correspondence of the 9 capacitors (see cross section view). b) Switching features of 3 capacitors connected in parallel. The PUND signal (left side) was sent to the FeFED by using a function generator and the switching current peaks (right side) were acquired by using an oscilloscope.

electric switching. The leakage current (due to the electronic transport across the capacitor) is obtained while applying the U pulse. Similar behavior can be inferred from the subsequent N and D pulses. Consequentially, by integration over time of the obtained free-leakage current peak (i.e. U(D)-P(N)), normalized to the total electrode area and averaged between both voltage polarities, a total amount of switchable polarization of $\sim 100 \mu\text{C}/\text{cm}^{-2}$ was obtained. Hence, after the successful confirmation of the proper switchability, the FeFED was mounted on a custom made copper rodⁱⁱ providing the necessary electrical connections. To account for the magnetic signal coming from the connection setup and from non-uniformities close to the FeFED, a background signal was acquired well above the T_C of the LSMO (i.e. 350 K), which was subtracted in the subsequent measurements at lower temperatures. The latter was possible since both diamagnetic and paramagnetic contributions are considered basically temperature independent (at least in the temperature range of interest).

Moreover, since the ferroelectric field effect is in principle an interface effect [115], the quality of the LSMO/PZT interface is an important issue which needs to be investigated. As a matter of fact, during the relatively high temperature growth of the oxides, interdiffusion of some more mobile elements (such as Pb in the case of PZT), could deteriorate the interface quality. For this reason the control of the layer-by-layer growth of the oxides is an important step along the direction of successful field effect experiments. In the previous chapter the plane and sharp LSMO/PZT interface has been already shown. Here, in order to confirm (at least within the experimental errors) the absence of interdiffusion effects, energy dispersive x-ray analysis

ⁱⁱThanks are given to Francis Bern of Leipzig University.

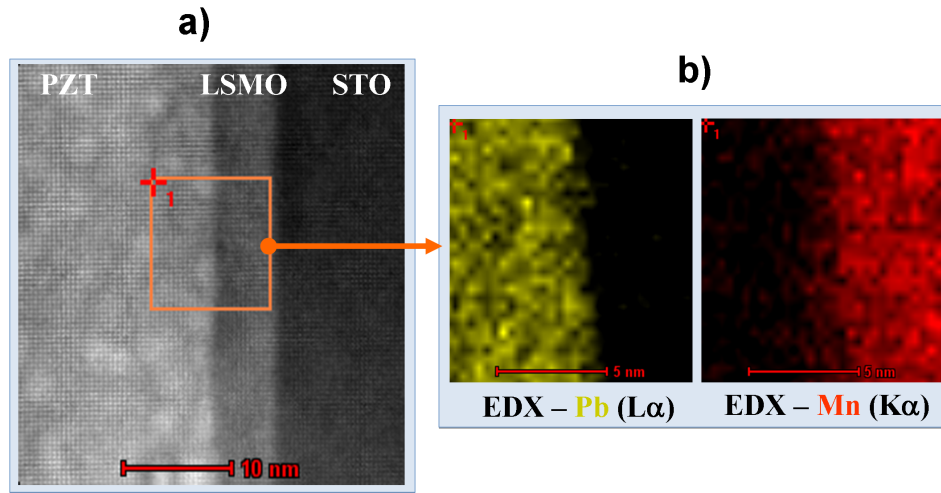


Figure 5.5: In a) the HAADF/STEM characterization of the PZT/LSMO/STO heterostructure is shown. The two figures in b) show the two-dimensional Mn and Pb elemental distributions at the crossing PZT/LSMO interface area (indicated in a) by the red square) measured by EDX.

(EDX) measurements are shown as well. The latter were performed by using a scanning transmission electron microscopeⁱⁱⁱ recording the x-ray intensity, in a cross section of the sample, along a line across the sample interface and calculating the spatial distribution of the selected elements (Mn and Pb in this case) with an accuracy of a few percent. Figure 5.5 shows the EDX measurement results. Figure 5.5a shows a high angle annular dark field (HAADF) scanning transmission electron microscopy (STEM) image of a PZT/LSMO/STO system and Fig. 5.5b shows the two-dimensional Mn and Pb spatial element distributions at the PZT/LSMO interface area (indicated by the red square) measured by EDX. For the semi-quantitative analysis the Mn- $K\alpha$ and the Pb- $L\alpha$ x-ray peaks were used. Due to the abrupt color gradient in the Fig. 5.5b, the two-dimensional EDX map demonstrated the absence of a Pb diffusion from the PZT into the underneath LSMO thin film.

5.2 P-dependent in-situ SQUID measurements

Magnetization measurements were carried out in a Superconducting Quantum Interference Device (SQUID, Quantum Design MPMS-7) in DC mode with a custom made sample holder equipped with copper wires to allow the *in-situ* P-switching. Moreover, all the copper contact parts were properly organized in order to extend uniformly along the whole sample region, and the measurements were performed by orienting the externally applied magnetic field along the [100] STO orientation (in-plane geometry). Upon the application of a +5 V (-5 V) pulse the PZT polarization was switched to point downward (upward), in order to induce the depletion (accumulation) state (see cross-section in Fig. 5.4a). Figure 5.6 shows the *in-situ* P-dependent magnetometer experiments of a FeFED characterized by 5 and 100 nm thick LSMO and PZT layers, respectively. First, the device was switched into accumulation (-5 V voltage pulse) at the temperature of 300 K, and then the magnetization M was acquired as a function of the temperature until $T = 4$ K (see solid red dots in Fig. 5.6a). Afterwards, P was switched, again at 300 K, pointing downward, i.e. the depletion state was achieved (+5 V voltage pulse). Correspondingly, M was measured in the same temperature range (see solid black dots in Fig. 5.6a). As a result, a clear modulation of T_C and M upon the ferroelectric switching is obtained.

ⁱⁱⁱThanks are given to Dr. Eckhard Pippel for the EDX measurements.

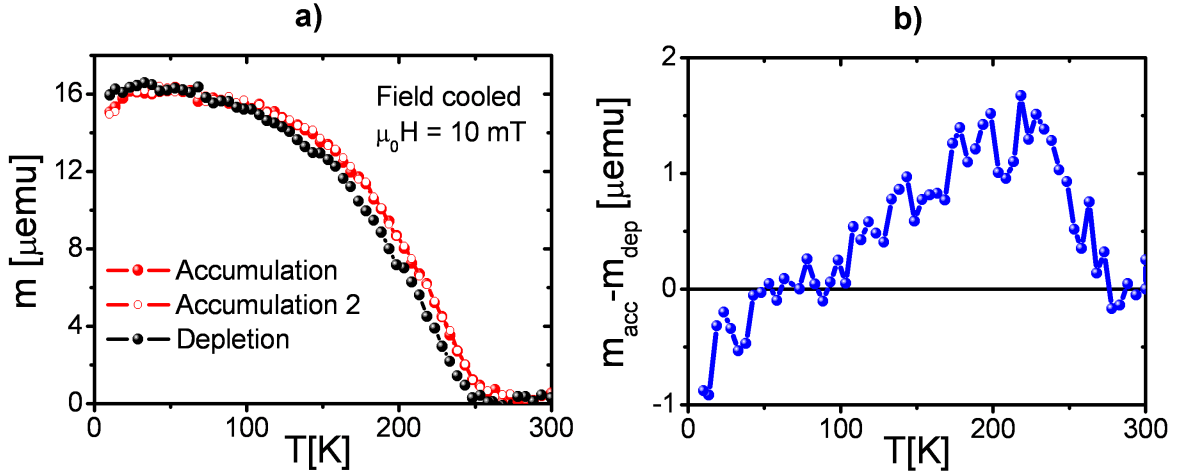


Figure 5.6: a) Temperature dependence of the magnetization for both polarization states acquired in field cooling with $H=10$ mT. The result is completely reproducible. b) Calculated difference of the magnetization values measured in accumulation and depletion states, respectively.

The latter result is in complete agreement with previous reports [80] and [116], for LSMO thin films of a different Sr-content (i.e. $x' = 0.2$). In order to verify the reproducibility of the SQUID measurements, the device was switched back into accumulation, and as visualized in Figure 5.6a both measurements in accumulation (see red open and solid dots) match perfectly. By a close inspection of the magnetization curves a T_C shift of ~ 11 K is obtained, from ~ 249 K to ~ 260 K, switching the device from the depletion to the accumulation state. Those temperature values were estimated from a linear extrapolation to zero magnetization near the critical region, as explained in Ref. [80]. This result is in complete agreement with a genuine charge-driven effect: the higher T_C value for the hole accumulation is considered to be consistent with the trend reported by the electronic bulk phase diagram [11] of $\text{La}_{1-x}\text{Sr}_x\text{MnO}_3$ in the ferromagnetic phase, where T_C increases with Sr-content. For the temperature range $100 < T < 250$ K, the measured value of M in accumulation is higher than that measured in depletion, since the magnetic state, in accumulation, starts at higher T_C than in depletion. The crossover related to the temperature behavior observed at ~ 50 K is not very distinct, but, nevertheless, it can still be explained in the framework of the charge modulation. Indeed, in the case of manganite, M varies with Sr-content, x , as $(4-x)\mu_B/\text{Mn}$. As a result, in depletion an increase of M is obtained with respect to the accumulation state. The latter trend is highlighted in Figure 5.6b, where the calculated difference as a function of the temperature is shown regarding the magnetization values measured in accumulation and depletion. As a result, this difference is mainly positive (M in accumulation higher than in depletion) from 300 K until ~ 50 K where the trend fully changes sign. The maximum is obtained at almost 230 K with a magnetization modulation of $\sim 1.5 \mu\text{emu}$ at which, by using the LSMO thickness of 5 nm, a variation of total magnetic moment between accumulation and depletion of $0.34 \mu_B/\text{Mn}$ is calculated. By considering the bulk phase diagram of manganite, a change of $0.34 \mu_B/\text{Mn}$ in magnetic moment should be accompanied by the same magnitude change in x . Since the nominal value of the measured LSMO is $x=0.175$, it can be easily argued that the change in magnetic moment cannot be simply accounted for by band-filling effects. The possibility that an accumulation of holes is capable to create an antiferromagnetic (AFM) spin re-arrangement at the LSMO($x=0.2$)/PZT interface could account for the observed large discrepancy, as proposed by Vaz and co-workers in Ref. [79]. In spite of the reliability linked to the previous plausible explanation of the mea-

sured M modulation, it is clear that the magnetic properties of a 5 nm thick LSMO film grown onto a STO substrate can be successfully controlled by P -reversal.

5.3 Magnetotransport studies of the FeFEDs

The general properties of the perovskite hole-doped manganite $\text{La}_{1-x}\text{Sr}_x\text{MnO}_3$, with a particular attention regarding the high sensitivity to external stimuli such as magnetic and electric fields, have been already introduced in the section 2.1 of this Thesis. Accordingly, colossal magnetoresistance (CMR) and anisotropic magnetoresistance (AMR) effects are widely studied especially for their appealing technological relevance. Prototypical FeFEDs offer the possibility to exploit the aforementioned properties to obtain intriguing modulations. In this section, the results obtained from the (magneto)transport characterization of the FeFEDs grown onto STO, LSAT and LAO single crystals are shown. The P -switching of the FeFEDs was accomplished by using the same setup employed for the *in-situ* SQUID magnetometer measurements. Precisely, by applying a square pulse of +3 V (-3 V) of magnitude and with a period of 50 ms, between the top electrode (see Fig. 5.3) and the LSMO (which, hence, was connected to the ground), the FeFED was set into the depletion (accumulation) state. All the switching experiments were performed at $T = 300$ K while the FeFED was mounted on the special holder of the PPMS^{iv}, which was employed for the (magneto)transport measurements.

5.3.1 FeFED on STO

Figure 5.7a shows the reversible effects of the P -switching regarding the resistivity of the gated LSMO as a function of the temperature, $\rho(T)$. It is worth to notice that the latter exhibits, for both P states, the typical temperature dependence of the bare 5 nm thick LSMO film, which has been already presented in the section 4.2.2. Here, the ferroelectric field effect produces an overall shift of the resistivity curves measured in the depletion (ρ^{depl}) and accumulation (ρ^{acc}) states of the FeFED. Interestingly the ρ^{depl} to ρ^{acc} ratio turned out to be higher than 1.5 at room temperature, and, as the temperature decreases, a peak is observed with a maximum of nearly 3.5 at 200 K (see inset in Fig. 5.7a). In addition, the characteristic peak of the $\rho(T)$ curves which marks, at the temperature T_{IM} , the insulator-to-metal transition of the LSMO, is electrostatically modulated by ~ 20 K (from ~ 230 to ~ 250 K, switching the FeFED from the depletion to the accumulation state, respectively). Moreover, as the temperature is further decreased, the characteristic metallic behavior (i.e. $\partial\rho/\partial T > 0$) vanishes for both P states, while the LSMO is still ferromagnetic (see Fig. 5.6a). The less itinerant character of the conduction electrons is due, most probably, to localization effects [117] where the random impurity (Sr-substitution) or the electron-lattice interaction (i.e. effect of the lattice polaron already introduced in section 2.1) might play the main role. As already highlighted in section 2.1.3 a structural phase transition (i.e. from R to O^* phase) is expected at this doping level upon the decrease of the temperature [40], and the observed upturn in the resistivity curves can be the result of that structural transition at the particular thickness value of 5 nm as well. The localized carriers may mediate the ferromagnetic interaction between the neighboring Mn ions and, as a result, the ferromagnetic phase occurs in a percolative fashion. Indeed, as already highlighted previously, the bulk LSMO is on the borderline between the insulating and metallic phases, which, hence, are in close competition, and the localization effects can be also the consequence of possible phase separations in the system. (It is important to note also that the LSMO thickness value is slightly above the electrical dead layer thickness, as already described in section 2.1.3). By a close inspection of the $\rho(T)$ curves, it is also clear that the

^{iv}In the PPMS the sample environment is kept at a low pressure state of ~ 10 mbar.

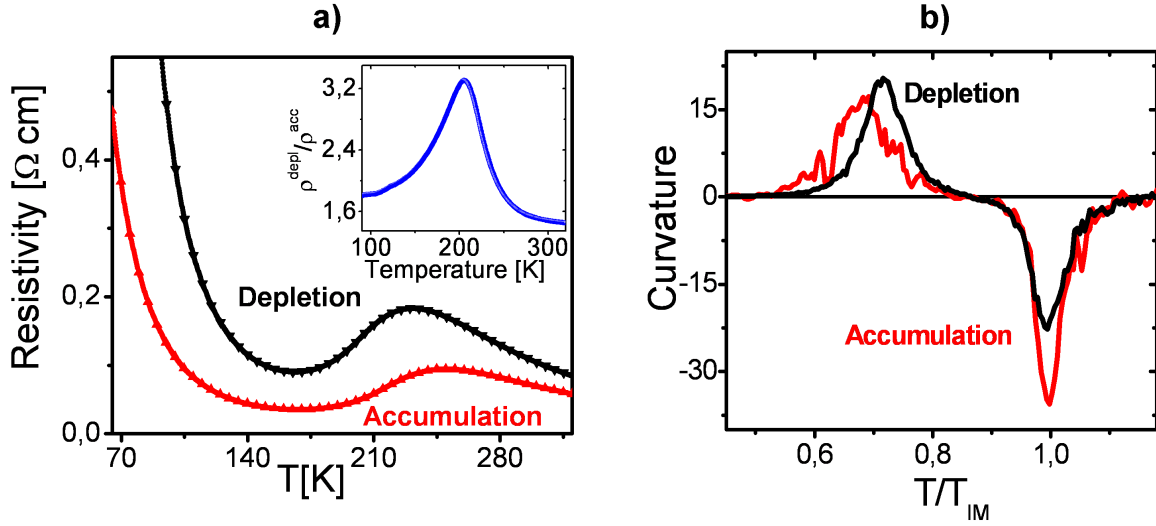


Figure 5.7: a) Temperature dependence of the resistivity for both polarization states of the FeFED grown on STO. The inset shows the ρ^{depl} to ρ^{acc} ratio. b) Curvature of the resistivity curves acquired in depletion and accumulation as a function of $\tilde{t} = T/T_{IM}$.

ferroelectric field effect affects the temperature at which the upturn is observed for the two P states. As a result, the geometric properties of the LSMO $\rho(T)$ curves are modulated by the ferroelectric field effect. In this respect, by defining $\tilde{t} = T/T_{IM}$ and $\tilde{\rho} = \rho(T)/\rho(T_{IM})$, the curvature $c(\tilde{t}) = \tilde{\rho}'/[1+(\tilde{\rho}'')^2]^{3/2}$ (where the prime denotes the derivative with respect to \tilde{t}), can be calculated. Figure 5.7b shows the results of the curvature calculation as a function of the reduced temperature \tilde{t} . It is easily noticed that, in correspondence to the magnetic phase transition (i.e. $\tilde{t} = 1$), between the depletion and accumulation state a variation of almost 50% is obtained for the curvature value. The latter result might justify that in accumulation the ferromagnetic phase transition is sharper than in depletion, hence the resistivity peak (that marks that transition) is less broad in accumulation. On the other side, regarding the peaks related to the upturn of the resistivity, the amplitudes of the curvature (see peaks around $\tilde{t} = 0.7$ in Fig. 5.7b) are rather comparable between the accumulation and depletion states. It is clearly observed that in depletion the possible localization effects come into picture at a higher temperature than in accumulation. By considering the fact that this upturn of the resistivity is obtained, at this nominal level of doping (i.e. $x = 0.175$), only for 5 nm thick LSMO films, the previous finding can be simply explained considering that the effects of the dead layer become more pronounced in depletion: the charge carriers available for the conduction are "subtracted" from the FeFED.

This charge-driven effect is also at the base of the observed modulation of T_{IM} , which can be directly linked, as expected from the DE mechanism, to the observed shift of T_C [19]. Precisely, from the electronic phase diagram of $\text{La}_{1-x}\text{Sr}_x\text{MnO}_3$ a decrease of the Curie temperature is observed correspondingly to a decrease of x . Summarizing, these findings demonstrate that the ferroelectric field effect is capable to tune the (magneto)transport properties of the LSMO in the same way in which the variation of the level of doping does. Hence, the highlighted trend of the transport properties of the FeFED can be macroscopically explained as a genuine charge-driven effect.

In order to get more information regarding the electronic behaviour of the FeFED, also Hall effect measurements at several temperatures were performed. Correspondingly, Figure 5.8

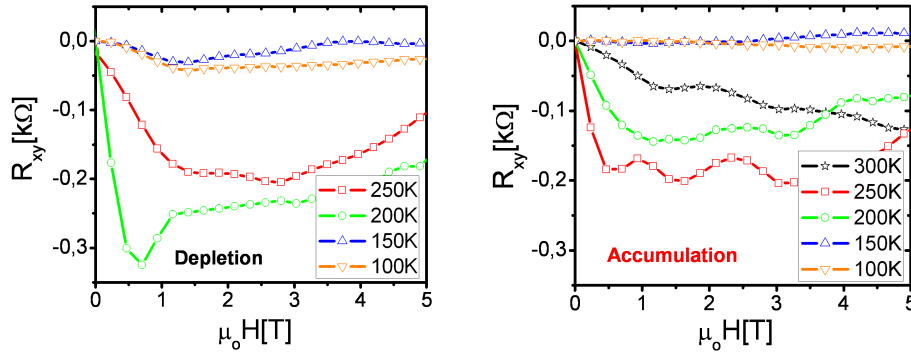


Figure 5.8: Hall resistance as a function of the externally applied magnetic field, calculated for the two opposite PZT polarization states of the FeFED grown onto STO single crystal, i.e. accumulation (right) and depletion (left).

shows the transverse resistance (R_{xy}) measurements^v as function of the externally applied H , for both depletion (left) and accumulation (right) states of the FeFED. The anomalous Hall effect is observed already at the temperature of 250 K for both P directions. The measured R_{xy} values are higher than the one measured for the bare 22 nm thick LSMO film. Precisely, as already reported in the previous chapter, values of few Ω for the R_{xy} quantity were obtained (see Fig. 4.11a). Here, regarding the FeFED, values of R_{xy} of the order of $k\Omega$ were measured. Those high resistance values are due, most probably, to the very small thickness of the LSMO film (i.e. 5 nm) and to an inadequate quality of the electrical contact which was ensured simply scratching the top PZT layer. Nevertheless, by using the same procedure already intro-

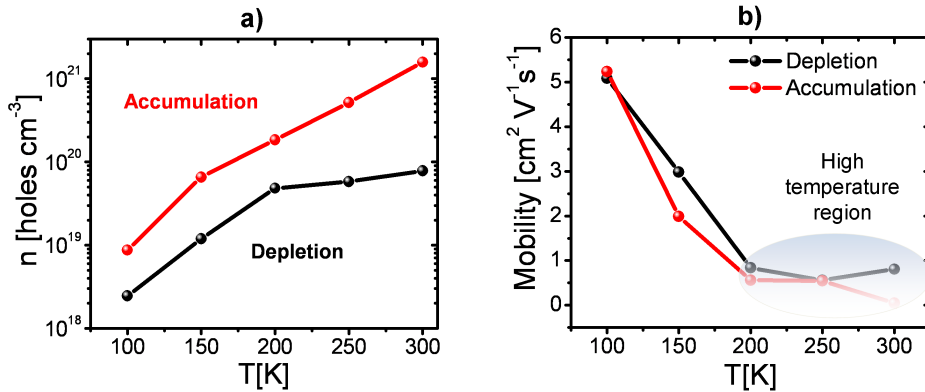


Figure 5.9: Hall charge carrier concentration (left) and Hall mobility (right) as a function of the temperature measured for both accumulation and depletion states of the FeFED grown on STO.

duced in the section 4.2.2, it was still possible to obtain a reliable linear fit of the R_{xy} curves at high magnetic field values. In this respect, Figure 5.9a shows the results of the fitting procedure. A ferroelectric field effect modulation of the (3D) Hall charge carrier concentration as a function of the temperature is clearly obtained for the investigated FeFED. Interestingly, the Hall charge carrier concentration obtained in accumulation is higher than in depletion, hence, demonstrating that the modulation of the physical properties related to the FeFED are due to a real charge-driven effect. Precisely, at 250 K, by employing the nominal value of 5 nm for the thickness of the LSMO for both P states, an effective carrier density of 0.03 and 0.004 carriers/u.c. is obtained for the accumulation and depletion state, respectively. The latter result

^vThe presented R_{xy} measurements are the result of a smoothing and interpolation procedure, since the unwanted rather low signal-to-noise ratio due to the high contact resistance of the FeFED was detrimental for the Hall measurement itself.

shows a complete mismatch with the expected nominal value of the carrier density as imposed by the chosen level of doping, i.e. 0.175 carriers/u.c. This can be explained following two different arguments. In the first case the Hall effect measurements are actually not reliable, since the ordinary Hall coefficient was difficult to determine because of either the effect of the large contact resistance or the large magnetoresistance measured even at low temperatures. Second, in the case that the Hall measurements and the subsequent analysis procedure can be considered certain, a possible non-homogenous distribution of the carriers across the channel area might induce the measurement of a very low carrier density. As a result, not all the available carriers seem to contribute to the transport. Moreover, different from what was measured for the 22 nm thick LSMO layer (see Fig. 4.11b), the temperature trend of the charge density of the FeFED is completely opposite (for both accumulation and depletion states). Precisely, for a 5 nm thick LSMO layer, which is just above the dead layer thickness (i.e. ~ 4 nm), the carrier density decreases as the temperature is decreased. The latter trend might be explained in the framework of the localization effects: The overall number of carriers available for the conduction decreases as the temperature is decreased, and a parallel increase of the resistivity is obtained.

From the Hall resistance measurements also the Hall mobility can be calculated. As a result, Figure 5.9b shows the Hall mobility of the FeFED for both accumulation and depletion states. In the high temperature region (i.e. 200–250 K), the Hall mobility practically does not depend on the temperature, hence, the main contribution to the transport is guaranteed by the charge carriers, which are characterized by an energy very close to the mobility edge^{vi} [118]. When the temperature is further decreased, an increase of the mobility values for both P directions is observed. Accordingly, the mobility increases up to $\sim 5 \text{ cm}^2 \text{ V}^{-1} \text{ s}^{-1}$. Although the temperature dependence of the Hall mobility would clearly describe the presence of a metallic state, the $\rho(T)$ curves of the FeFED exhibit the upturn as already shown before in Figure 5.7. As a result, the temperature dependence of the $\rho(T)$ curves can be explained assuming that the main contribution to the transport is basically given by the density of the charge carriers irrespective of the related mobility values. Indeed, from the Hall resistance measurements the charge carrier density of the FeFED deeply decreases as the temperature is decreased.

The presence of the reported upturn^{vii} of the $\rho(T)$ curves, below ~ 150 K, indicates that the DE picture does not hold anymore though the 5 nm thick gated LSMO layer still exhibits clear ferromagnetism. As a result, other electronic mechanisms need to be considered. In principle, the exact transport mechanism in ultrathin $\text{La}_{1-x}\text{Sr}_x\text{MnO}_3$ films is still an open question. As already reported for a low doping level of $\text{La}_{1-x}\text{Sr}_x\text{MnO}_3$ single crystals, the variable range hopping (VRH)^{viii} [117] dominates the conductivity in the ferromagnetic phase [119]. The VRH theory is based on the idea that charges are localized with a finite probability to jump (hopping mode) to another localized state. As a result, the temperature dependence of the resistivity is expressed through the following relation:

$$\rho = \rho_0 e^{(T_0/T)^{1/4}}, \quad \text{where } T_0 = \frac{\beta}{K_B N(E_F) a^3}. \quad (5.1)$$

Where $N(E_F)$, a and β are the density of states (DOS) at the Fermi level E_F , the radius of the localized states and a constant (nearly 20 [120]), respectively. Nevertheless, it is questionable whether the VRH theory can be applied to the lanthanum manganite oxide which is characterized by low values of mobility [121].^{ix} In this respect, Figure 5.10 shows the temperature

^{vi}The meaning of the mobility edge supposes the presence of disorder in the system and is strictly related to the presence of localized states. Precisely, the mobility edge defines the energy separation between localized and de-localized states.

^{vii}This is actually obtained, as expected from the bulk electronic phase diagram of $\text{La}_{1-x}\text{Sr}_x\text{MnO}_3$, for $x=0.15$ [19].

^{viii}Originally, the VRH theory was developed to explain electron transport in doped semiconductors where electrons are localized due to the effect of the doping. Hence, the VRH theory is strictly valid for materials that do not show good transport properties such as manganites.

^{ix}Actually this simple transposition is conventionally done by the oxide materials community.

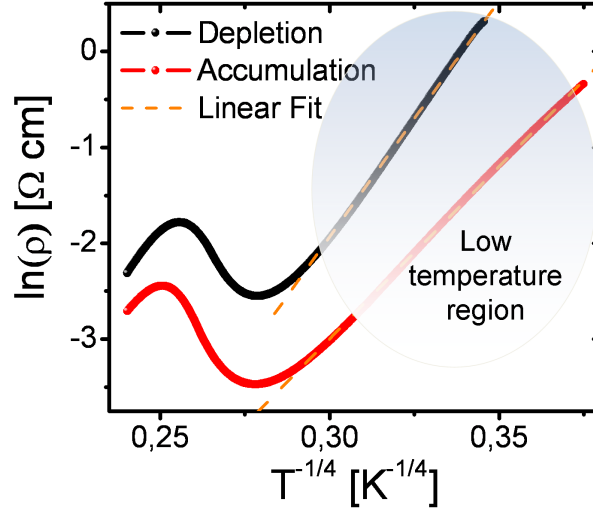


Figure 5.10: Temperature dependence of the FeFED resistivity in the Arrhenius, $\ln\rho-1/T^{1/4}$ representations for both accumulation and depletion states. In the highlighted low temperature region a linear fit (orange dashed lines) is successfully obtained.

dependence of the resistivity in the $\ln\rho-1/T^{1/4}$ representation. As a result, from the linear extrapolation of both $\rho(T)$ curves in the low temperature region, i.e. $\sim 120 \div \sim 50$ K, T_0 values of ${}^{1/4}\sqrt{(50.57 \pm 0.05)} \text{ K}$ and ${}^{1/4}\sqrt{(36.46 \pm 0.03)} \text{ K}$, are obtained for depletion and accumulation states, respectively. Interestingly, if the VRH theory can be considered valid^x, the ratio between the two T_0 values obtained in depletion and accumulation, i.e. T_0^{depl}/T_0^{acc} , is ~ 3.7 . Accordingly, if the ferroelectric field effect by a simple conjecture leaves unaffected the radius of the localized states, in accumulation an increase of the DOS at E_F is obtained. Hence, as a first result it can be simply claimed that in the aforementioned temperature region the FeFED in accumulation shows an overall decrease of the resistivity (when compared to the depletion case), due to an increase of the localized states available for the hopping mechanism.

On the other hand, regarding the resistivity properties above T_{IM} and, hence, in the paramagnetic phase, different mechanisms can account for the transport. Accordingly, the VRH theory can be still useful but also a pure thermally activated law can be used to fit the resistivity curves, i.e. $\rho = \rho_0 e^{(E_{act}/K_B T)}$, with E_{act} being the activation energy^{xi}. Additionally, also the law describing the hopping of small polarons^{xii} between localized states, i.e. $\rho = \sim T e^{(E_{act}/K_B T)}$ [122], can be used. In this respect, the previous procedure of processing the experimental results (linear fit of $\rho(T)$ displayed in Arrhenius plots) is not always univocal. Precisely, the temperature range in which the linear fit is performed is very important. For example, in the range from 320 to 270 K the resistivity covers a very limited range in both the accumulation and depletion states, and in the Arrhenius representation both T^{-1} (thermal activation) and $T^{-1/4}$ (VRH) dependences can be easily confused. It is clear that in this case the possibility to distinguish between several mechanisms is difficult, and in general, additional measurements are required. Nevertheless, several works, which are collected in the Salamon review article (see Ref. [123]), attribute the conduction mechanism of manganite thin films to hopping of small (Holstein) polarons in the paramagnetic phase. In this respect, the conduc-

^xIn principle, in order to effectively assume that the VRH is the dominant transport mechanism, also thermopower measurements need to be performed [118].

^{xi}Usually for a disordered system the activation energy is related to the possibility that the carriers can be thermally activated between the Fermi level and the mobility edge.

^{xii}Polarons, in a simplified view, can be considered as carriers that bring with them a local crystalline distortion.

tion is characterized by an activation energy E_{act} . As a matter of fact, the linear extrapolation performed in the temperature range of interest for the $\rho(T)$ curves of the FeFED suitably displayed in the Arrhenius $\ln\rho-1/T$ representation (not shown here) gave two different values for the activation energy. Precisely, values of (80.7 ± 0.5) meV and (99.6 ± 0.4) meV for accumulation and depletion, respectively, were obtained. The latter result demonstrates that the ferroelectric field effect is able to modulate not only the number of carriers that contribute to the transport, but also the related energy scale. As already widely discussed in this section, the transport mechanism in manganite thin films is not uniquely defined, and several models are necessary to account for different experimental evidences. Usually the scientific community is amenable to the simple physical concepts of doped semiconductor which, hence, are extended to the world of manganites. In this respect, the different activation energy values of the FeFED can be explained, accounting for a possible tuning of the relative position between the Fermi level and the mobility edge of the localized states.

As already shown in the previous chapter the transport properties of the LSMO strongly depend on the presence of a magnetic field. As expected, a large negative magnetoresistance (MR) is obtained. The latter was studied as a function of the P direction, with H applied along two different directions with respect to the FeFED normal. In this respect, Figure 5.11 shows the schematic view of the FeFED along with the two different aforementioned H orientations. Accordingly, the quantities ρ_{\perp}^{out} and ρ_{\perp}^{in} indicate the resistivity measured with H oriented out-

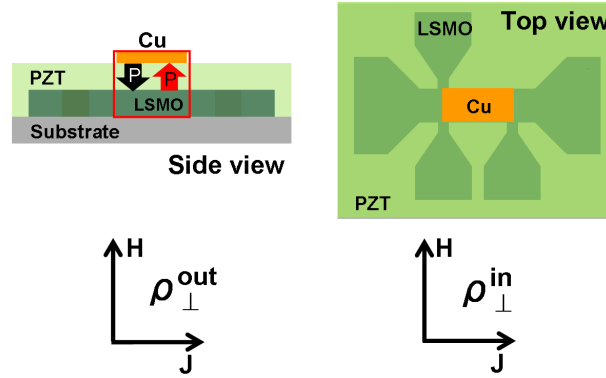


Figure 5.11: Definition of the quantities ρ_{\perp}^{out} and ρ_{\perp}^{in} with respect to the schematic view of the FeFED. (Left) H oriented out-of-plane (parallel to the FeFED normal), correspondingly ρ_{\perp}^{out} is defined. (Right) H oriented in-plane (parallel to the FeFED plane), correspondingly ρ_{\perp}^{in} is defined. The subscript \perp stands for H perpendicularly to the current density J .

of-plane and in-plane with respect to the FeFED, respectively. Moreover, the symbol used as subscript stands for H oriented at an angle of 90° with respect to the current density J . To quantify the MR effect, the quantities $MR^{in(out)} = 100 \cdot [\rho_{\perp}^{in(out)}(T) - \rho_{H=0}] / \rho_{H=0}$ were calculated for both accumulation and depletion states of the FeFED. Figure 5.12a,b shows the FeFED resistivity, under a magnetic field of 5 T applied in-plane and out-of-plane with respect to the FeFED plane, as a function of temperature for both depletion and accumulation states, respectively. It is worth to note that for both PZT polarization states, when the magnetic field is oriented out-of-plane, the expected decrease of the resistivity is less marked than when H is oriented in-plane. As a result, Figure 5.12c shows that the maximum of the MR^{in} signal is found at ~ 214 K for the depletion state and at ~ 248 K for the accumulation state. Precisely, the maximum in depletion is 64.5 % and decreases to 59.4 % in accumulation. The observed trend of the MR^{in} peak position confirms the effective modulation of the T_C of the FeFED. Moreover, the decrease of the MR^{in} maximum, switching the FeFED from depletion to accumulation, is also confirmed from several other studies where the level of doping in the system was modified statically (hence adopting different chemical doping [18]) and not electrostatically, like in this

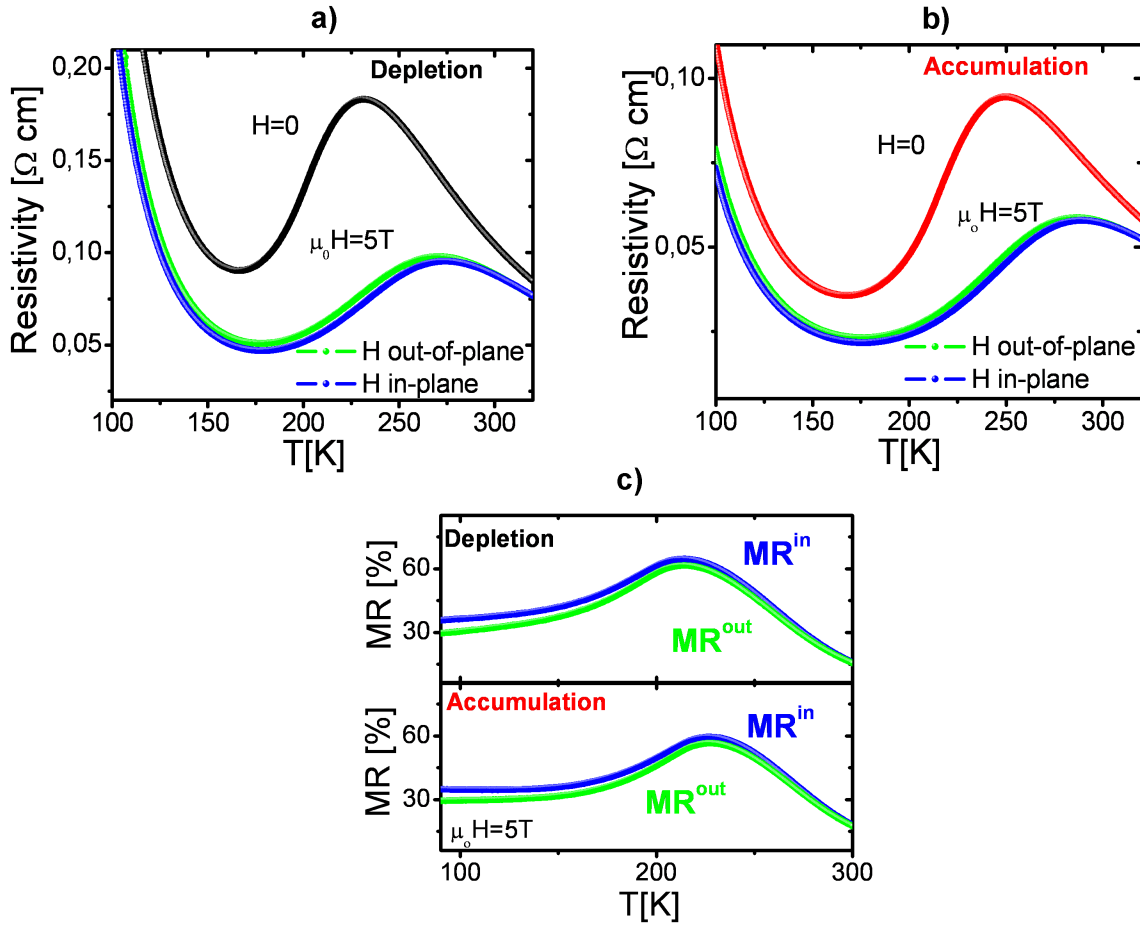


Figure 5.12: Temperature dependence of the resistivity related to the FeFED for (a) depletion and (b) accumulation states measured with an applied magnetic field of 5 T. c) Magnetoresistance data calculated for H oriented perpendicular (green) and parallel (blue) to the FeFED plane for the depletion and accumulation states.

case. This offers the possibility to completely discriminate the pure charge-driven effect (of the decrease of the MR peak in the LSMO upon the increase of the carrier concentration) from a possible disorder-driven effect. The same discussion applies to the MR^{out} signals. In this case, it is clearly observed that the peak magnitude decreases remarkably when H turns to be oriented out-of-plane. Specifically, the FeFED normal direction (c -axis) represents the hard axis for the field-dependent MR measurements. The small but distinct variation of the $\rho(T)$ curves by orienting H from the in-plane towards the out-of-plane direction demonstrates that the insulator-to-metal transition of the LSMO depends on the orientation of H . The observation of the appearing of a gap between MR^{in} and MR^{out} (similar to the modulation between $\rho_{\perp}^{\text{out}}$ and ρ_{\perp}^{in}) triggered further magnetotransport studies which will be presented in the next section.

Also isothermal MR measurements were carried out in order to completely characterize the FeFED from the magnetotransport point of view. In this way the relation between the magnetoresistive properties and the magnetization M of the FeFED can be studied as a function of the P direction as well. Figure 5.13 shows the isothermal magnetoresistance curves normalized at the $\rho_{H=0}$ value, as a function of the magnetic field acquired at several temperatures for ρ_{\perp}^{in} (see Fig. 5.13a) and $\rho_{\perp}^{\text{out}}$ (see Fig. 5.13b), respectively. Regarding the MR data acquired for H applied in-plane, an overall decrease of the resistivity for all the investigated temperatures is clearly observed at each value of the magnetic field. Precisely, at the temperatures of 300 K

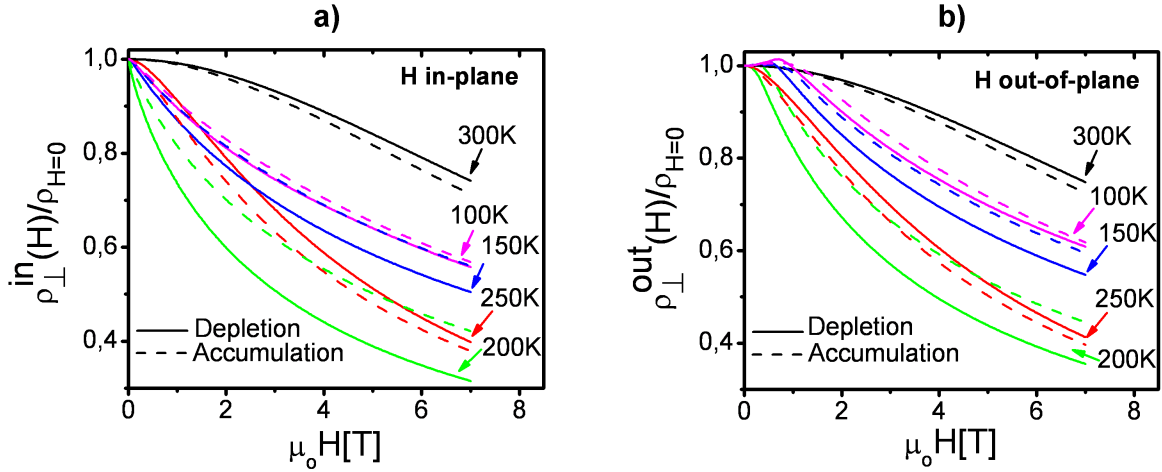


Figure 5.13: H -dependence of the MR properties of the FeFED acquired at several temperatures for the magnetic field applied (a) in-plane and (b) out-of-plane with respect to the FeFED plane.

and 250 K the MR magnitude is higher in accumulation than in depletion. As the temperature is further decreased, this trend completely reverses. The same trend is observed also in the case of H applied out-of-plane as it is possible to visualize in Fig. 5.13b. Here, the very important difference with respect to the MR curves acquired with H applied in-plane is related to the small upturn observed at low temperature and magnetic field values. As already shown in section 4.4, the magnetization of LSMO single layers (grown on top of STO substrates) is lying along the $[110]$ direction. The presence of the shape anisotropy favors the orientation of the magnetization in-plane [63]. Hence, when H is applied out-of-plane, the energy that the system gains aligning all the magnetic moments in-plane needs to be exceeded, and additionally also the demagnetizing field has to be considered. The latter is strictly related to the geometry of the sample under investigation. In general, when a thin film geometry is considered, the applied H is cancelled out by the out-of-plane component of the magnetization [124], i.e. $M_{\perp} = H/4\pi$. In this respect, as H keeps increasing from zero, the internal field is zero along the normal direction and M completely rotates out-of-plane when $H = 4\pi M$. During this rotation, M is constant, resulting in the observed upturn of the MR curves. For $H \geq 4\pi M$ the internal field is no longer zero, and the negative magnetoresistance is restored. As a result, in the case of the investigated FeFED, in order to completely orient M out-of-plane, a magnetic field higher than 1.5 T was necessary. By a close inspection of the MR curves depicted in Fig. 5.13b, it is clearly observed that the decrease of the MR curves (after the observed upturn), at a fixed temperature value, is measured at different magnetic fields for the accumulation and depletion states. In accumulation, in order to completely rotate M out-of-plane, a higher magnetic field is required, and the latter increases as the temperature is lowered. This trend is in complete agreement with the *in-situ* magnetic characterization (which was discussed in section 5.2), where in the temperature range of interest here, a higher value of M was measured in accumulation than the one obtained in depletion. Hence, it turns out easy to conclude that the magnetoresistance and magnetic characterizations are in complete agreement.

The ferroelectric field effect gave the possibility to study, in a relatively limited range, the effect of the charge density variation without adding any disorder due to chemical doping. The measured modulation of the T_{IM} , T_C and MR peaks well reproduces the results obtained with the static variation of the chemical doping. Hence, these results demonstrate that by tuning the carrier density of a strongly correlated material the related functional properties can be reversibly modulated, as already reported by Hong *et al.* in Ref. [76] for similar devices. Moreover,

from the attempts to gain some information regarding the transport mechanism of the gated LSMO, it turned out that the ferroelectric field effect is, most likely, capable to modulate the energy scale of the electronic levels that regulates the transport in the system. For example, in the paramagnetic phase, where the resistivity value is electrostatically modulated by more than 50 %, the believed polaronic hopping mechanism that follows a thermally activated law is characterized by different energy activation values between accumulation and depletion states. As a result, the intrinsic energy scale of the material, LSMO in this case, is affected and, hence, the "active" carriers (the ones that contribute to the transport) are modulated according to the boundary conditions fixed by the field effect.

5.3.2 FeFED on LSAT

Figure 5.14a shows the temperature dependence of the resistivity related to the FeFED grown onto an LSAT substrate, as a function of P . As in the case of the FeFED built onto STO, the 5 nm thick gated LSMO film grown onto LSAT exhibits the standard temperature dependence of the resistivity as already discussed before. An overall shift of the $\rho(T)$ curves is observed between accumulation and depletion. Also the upturn is still observed, and the temperature at which it takes place is modulated upon the P -switching: this temperature is ~ 70 K for the depletion state and ~ 20 K for the accumulation state. The latter values are lower than the ones reported before for the FeFED grown on top of a STO substrate. The ρ^{depl} to ρ^{acc} ratio turned

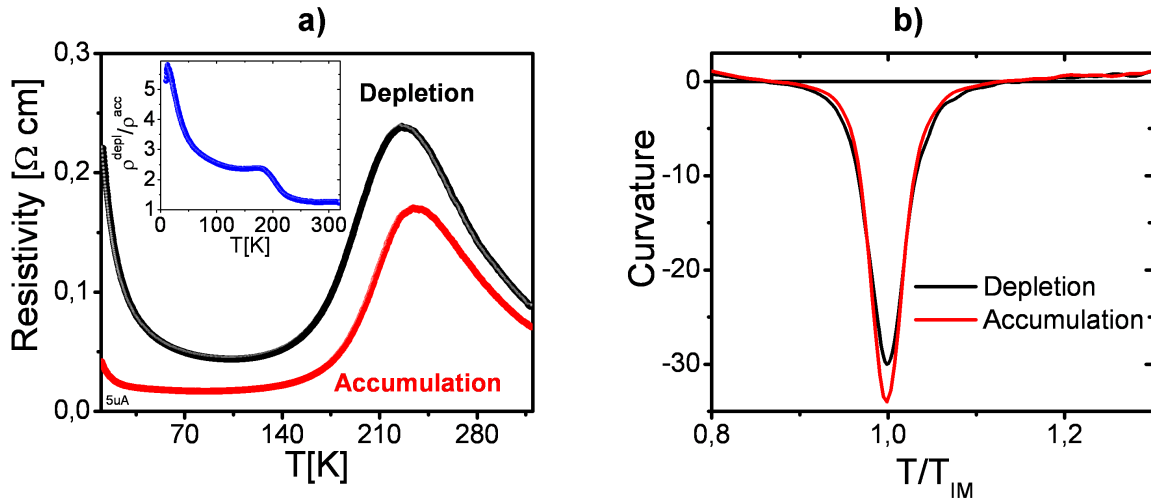


Figure 5.14: a) Temperature dependence of the resistivity related to the FeFED grown onto an LSAT substrate for both P states. The inset shows the ρ^{depl} to ρ^{acc} ratio. b) Curvature of the resistivity curves acquired in depletion and accumulation as a function of $\tilde{T}=T/T_{IM}$.

out to be ~ 1.5 at room temperature, and as the temperature is further decreased a rising maximum of nearly 6 is observed at ~ 20 K (see inset in Fig. 5.14a). Moreover, Figure 5.14b shows the curvature curves calculated for both accumulation and depletion states as a function of the reduced temperature \tilde{T} . Accordingly, like in the case of the FeFED on STO, the magnitude of the peak calculated in accumulation is larger than in depletion. As a result, the insulator-to-metal transition in accumulation is sharper than in depletion. Moreover, as expected, also the T_{IM} temperatures are modulated: from ~ 235 K in accumulation to ~ 226 K in depletion. The experienced shift in T_{IM} of ~ 9 K is lower than the one measured on the FeFED grown on STO, and interestingly, irrespective of the field effect modulation, the T_{IM} suffered an overall decrease. The latter translates (through the DE mechanism) to a decrease of T_C values of

the FeFED itself^{xiii}. Since the LSMO thin film grown onto an LSAT substrate experiences a compressive strain (as shown in the previous chapter), a worsening of the DE mechanism is expected as reported in [34]. Basically in thin films, only the in-plane interactions are important, and the control of the orbital ordering (i.e. overlapping of the e_g states) is important for the control of the magnetic exchange energy and, hence, of T_C . Indeed, the compressive strain state stabilizes a preferential occupancy of the $3d_{z^2}$ over the $3d_{x^2-y^2}$ orbitals [35], with obvious subsequent decrease of the in-plane exchange interaction energy.

Figure 5.15 shows the Hall resistance measured as a function of the magnetic field at several

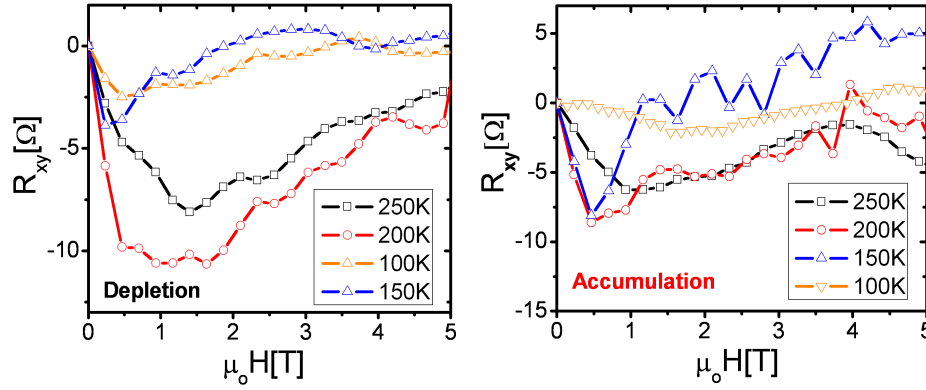


Figure 5.15: Hall resistance curves as a function of H calculated for the FeFED grown onto a LSAT single crystal for both accumulation (right) and depletion (left) states.

temperatures for accumulation and depletion. Also in this case the anomalous field effect is already observed at the temperature of 250 K and, in this case, the measured Hall resistance values are one order of magnitude lower than the ones obtained in the case of the FeFED grown on STO (see Fig. 5.8). Accordingly, below 250 K the normal Hall signal is saturated

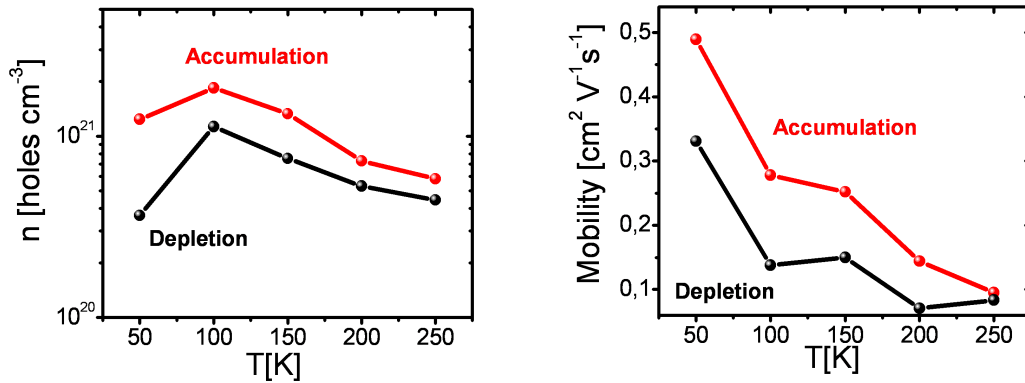


Figure 5.16: Hall charge carrier concentration (left) and Hall mobility (right) as function of the temperature measured for accumulation and depletion states of the FeFED grown onto a LSAT substrate.

and the calculation of the effective carrier density of the gated LSMO grown on an LSAT single crystal can be achieved. In this respect, Figure 5.16 shows the temperature dependence of the Hall charge density (left) and Hall mobility (right), for both accumulation and depletion states. Interestingly, also in this case the ferroelectric field effect modulates the overall Hall carrier concentration. Precisely, at 200 K carrier concentrations of $\sim 7 \cdot 10^{20} \text{ cm}^{-3}$ and

^{xiii}For LSMO/LSAT and PZT/LSMO/LSAT heterostructures no magnetic characterization have been undertaken.

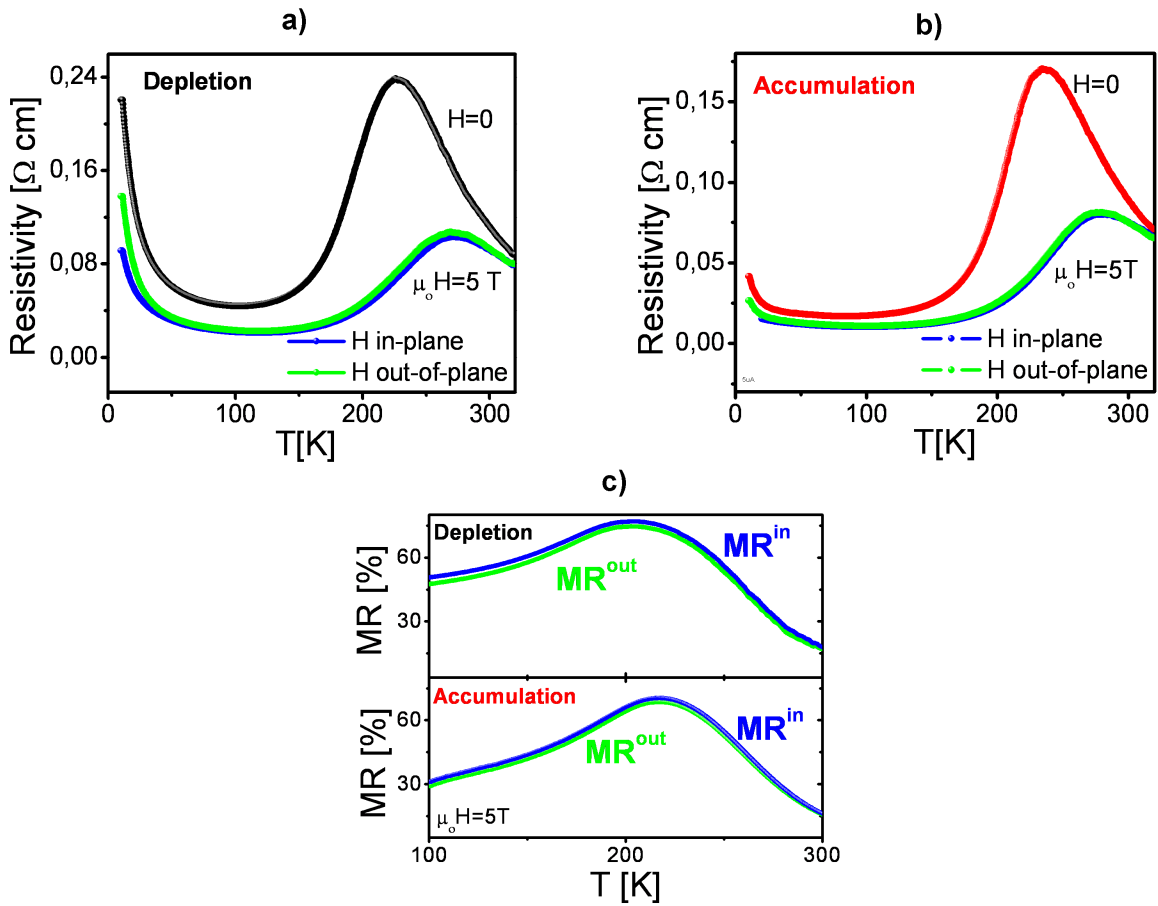


Figure 5.17: Temperature dependence of the resistivity related to the FeFED grown on LSAT for (a) depletion and (b) accumulation states measured with H of 5 T. c) Related magnetoresistance curves calculated for H applied out-of-plane (green curve) and in-plane (blue curve) with respect to the FeFED plane for depletion and accumulation states.

$\sim 5 \cdot 10^{20} \text{ cm}^{-3}$ in accumulation and depletion were measured which corresponds to 0.04 and 0.03 carriers/u.c., respectively. It is worth to notice that the overall value of the carrier concentration is one order of magnitude higher than the one measured on the FeFED grown onto a STO substrate but, however, still not comparable to the nominal expected value. Moreover, as the temperature is decreased, the Hall carrier concentration is smoothly increased. Actually, at 50 K a deep decrease of the latter is observed, most probably due to the same, aforementioned, localization effects that drive the upturn of the resistivity. Regarding the Hall mobility (graph shown on the right side of Fig. 5.16), also in this case the Hall mobility slowly goes towards zero as the temperature is increased. Moreover, in accumulation the Hall mobility is higher than in depletion, though the calculated values are very small if compared to the ones obtained from the FeFED grown on STO. The latter finding might be explained as a possible bending of the Mn-O-Mn bonds due to the compressive strain state exhibited by the LSMO grown onto the LSAT substrate. As a result, it might be concluded that, also in this case, the major contribution to the transport is given by the effective number of the carriers and not particularly by their related mobility value. Moreover, from the Arrhenius representation of the two $\rho(T)$ curves (not shown for sake of simplicity) it turned out that for $T \geq T_{IM}$ two different values for the activation energy are obtained also in this case. Precisely, values of $(83.6 \pm 0.2) \text{ meV}$ and $(70.6 \pm 0.3) \text{ meV}$ for depletion and accumulation are obtained, respectively. Hence, also for the FeFED engineered onto an LSAT single crystal, the modulation of the energy scale related to the different $3d$ electronic levels of the Mn ions seems to take place: the formation of small

polarons, which then contribute to the transport by hopping between several localized states, is obtained at different energy for the accumulation and depletion state.

As already reported in [125] by Jin *et al.*, the magnetoresistance properties of manganites exhibiting a lower T_C value are enhanced. In this respect, the magnetoresistance characterization of the FeFED, which is shown in Figure 5.17, confirms the aforementioned trend. Precisely, a value of $\sim 77\%$ (to compare with the value of $\sim 65\%$ measured in depletion for the FeFED grown on STO) is obtained for the amplitude of the MR^{in} peaks in the depletion state. In accumulation the maximum value of the MR decreases to the value of $\sim 71\%$. The trend observed for the shift of the temperature at which those maxima are measured and of the maximum amplitudes mimics the results obtained measuring the FeFED engineered onto STO (see Fig. 5.12c). Additionally, a rather small difference between the MR^{in} and MR^{out} signals is still present and, consequentially, the c -axis of the FeFED turned out to be the hard axis for the magnetoresistance measurements also for the FeFED grown onto an LSAT single crystal. As a result, these findings demonstrate that the ferroelectric field effect acts on the (magneto)transport properties in a rather general way, irrespective of the strain state exhibited by the manganite thin film.

5.3.3 FeFED on LAO

Figure 5.18 shows the resistivity as a function of temperature related to the FeFED grown onto an LAO single crystal. The resistivity exhibits an insulating behavior in the entire temperature range investigated (see Fig. 5.18a) for both accumulation and depletion states. As already reported in the literature, see for example [126], a dead layer thickness of ~ 15 nm is reported for a LSMO($x=0.3$) thin film grown onto an LAO single crystal. As a result, the

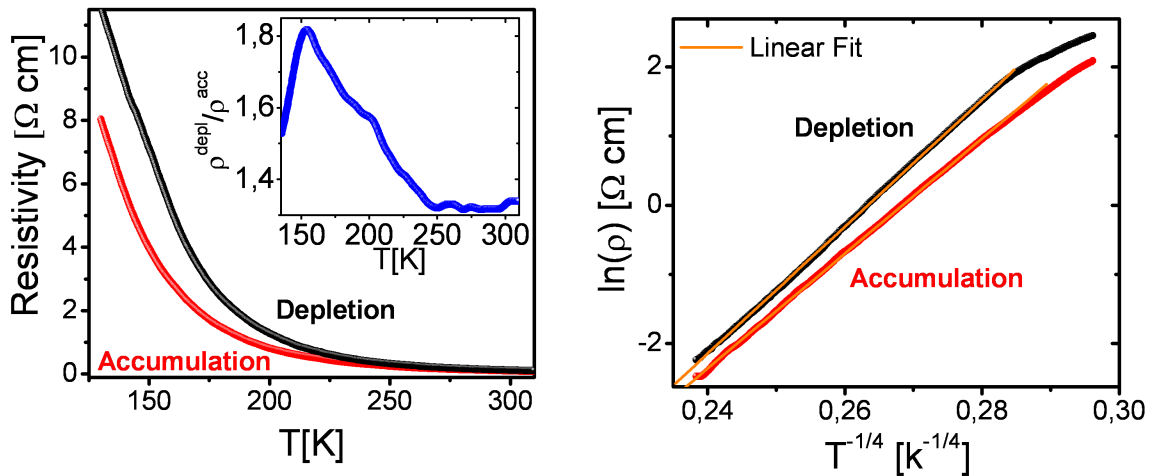


Figure 5.18: a) Temperature dependence of the resistivity related to the FeFED grown onto a LAO substrate for both P states. The inset shows the ρ^{depl} to ρ^{acc} ratio. b) Arrhenius $\ln\rho-1/T^{1/4}$ representation of both $\rho(T)$ curves.

thickness value of 5 nm was expected to be well below the dead layer thickness value, also for the LSMO composition used in this Thesis. Nevertheless, the ferroelectric field effect is capable to modulate the overall resistivity value. As a result, the ρ^{depl} to ρ^{acc} ratio turned out to be higher than 1.3 at room temperature, and as the temperature decreases, a rising maximum of nearly 2 is observed at ~ 150 K (see inset of Fig. 5.18a). Moreover, the $\ln\rho-1/T^{1/4}$ representation of both $\rho(T)$ curves displayed in Figure 5.18b shows that from 320 K until ~ 150 K the VRH hopping mechanism successfully describes the transport of the gated LSMO thin film. From the linear extrapolation performed in the aforementioned temperature range, T_0 values

of $^{1/4}\sqrt{(91.83 \pm 0.09)}$ K and $^{1/4}\sqrt{(83.42 \pm 0.05)}$ K are obtained for the depletion and accumulation states, respectively. The ratio T_0^{depl}/T_0^{acc} turned out to be equal to ~ 1.4 . Accordingly, in accumulation an increase of the DOS at E_F is obtained, though the relative modulation is less robust when compared with the FeFED grown on STO (*viz.* 3.7). The magnetoresistance characterization of the FeFED is shown in Figure 5.19. In this case the value of 0.5 T for the applied magnetic field was employed. The presence of the magnetic field decreases the overall

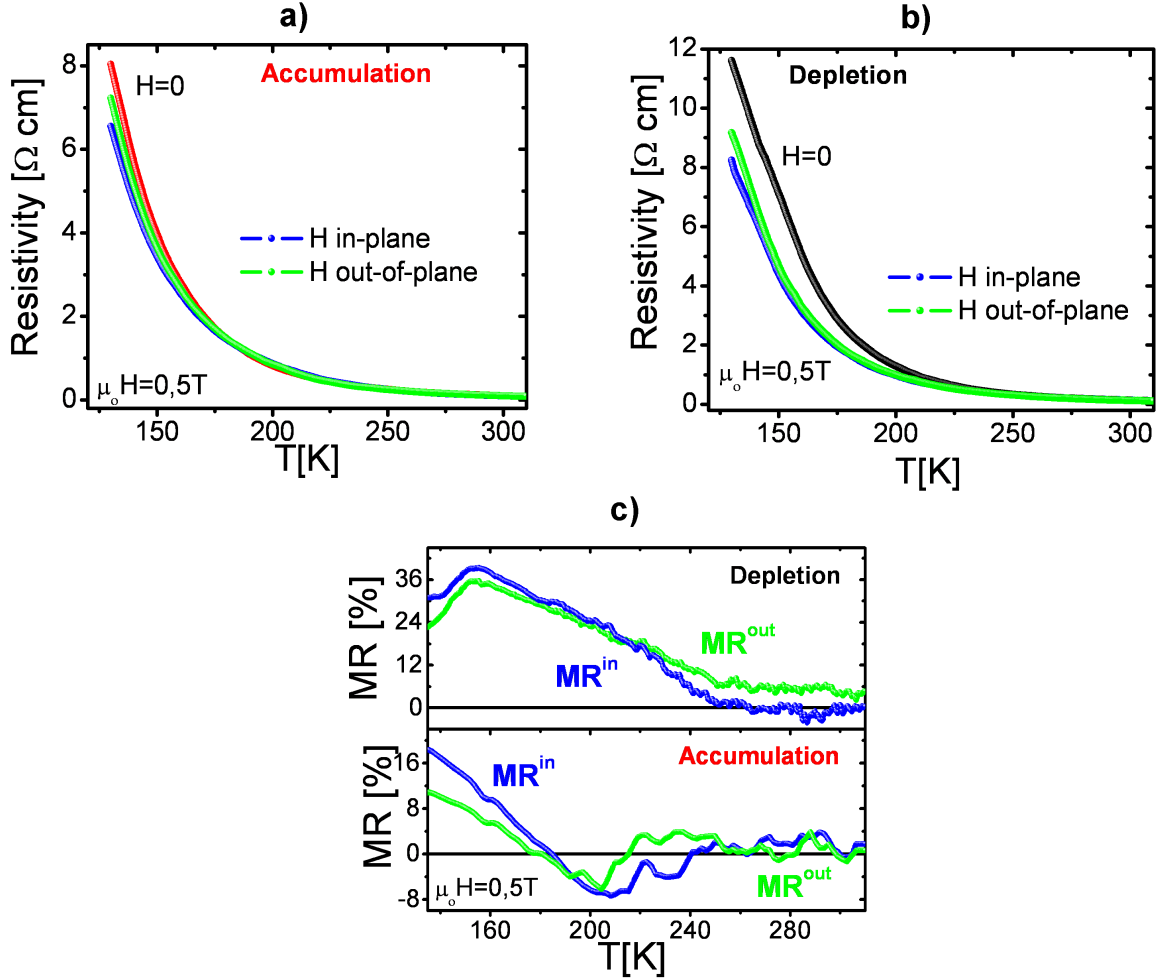


Figure 5.19: Temperature dependence of the resistivity related to the FeFED grown onto an LAO substrate for both (a) depletion and (b) accumulation states measured with an applied H of 0.5 T. c) Magnetoresistance data calculated with H oriented out-of-plane (green curve) and in-plane (blue curve) with respect to the FeFED plane for depletion and accumulation states.

value of the resistivity for both accumulation and depletion states, as shown in Figure 5.19a,b respectively. The effect is enhanced in the lower temperature region, and from Fig. 5.19c it can be easily envisaged that the MR magnitude is higher in depletion than in accumulation. Precisely, values of $\sim 40\%$ and $\sim 12\%$ are obtained at ~ 160 K for the depletion and accumulation state, respectively. Interestingly, regarding the MR calculated in the depletion state, a distinct difference of $\sim 6\%$ between MR^{out} and MR^{in} is obtained around room temperature, i.e. in the range of $310 \div 250$ K. As the temperature is further decreased the sign completely reverses and $MR^{out} < MR^{in}$, as experienced so far for all the reported results of the MR characterization of the FeFEDs grown onto STO and LSAT substrates. On the other hand, regarding the MR calculated in the accumulation, the aforementioned gap between MR^{out} and MR^{in} , observed

in a quite large interval around room temperature, is practically absent. The latter result might turn out interesting for application purposes where usually MR values of less than 1 % are commonly characterizing real devices. The large compressive strain exhibited by the LSMO thin film grown on top of the LAO (i.e. almost -3.3 %) triggers an overall occupancy of the Mn $3d z^2$ orbitals that, consequentially, enhances an out-of-plane DE mechanism.

5.4 Anisotropic magnetoresistance study of FeFEDs on STO

The anisotropic magnetoresistance (AMR) which was discovered by William Thompson [127], can reveal interesting magnetic properties, and the related microscopic mechanism is at the base of the most modern concept of spintronics. Experimentally, as already mentioned, AMR refers to the variation of the resistance that depends on the orientation of the magnetization M with respect to both the current density J and the crystal axes. In the manganite the underlying physics of the AMR mechanism is rather complicated to explain, due to the strong correlations exhibited by the system. In general, from the angular dependence of the AMR [128, 129], information on the spin-orbit coupling (SOC) [130] and the magneto-elastic coupling (Jahn-Teller distortions) [129] of the system can be obtained. Commonly, AMR measurements are performed rotating H within the plane of the system, hence, allowing H to rotate from the parallel to the perpendicular direction with respect to J . As a result, for sufficiently large applied

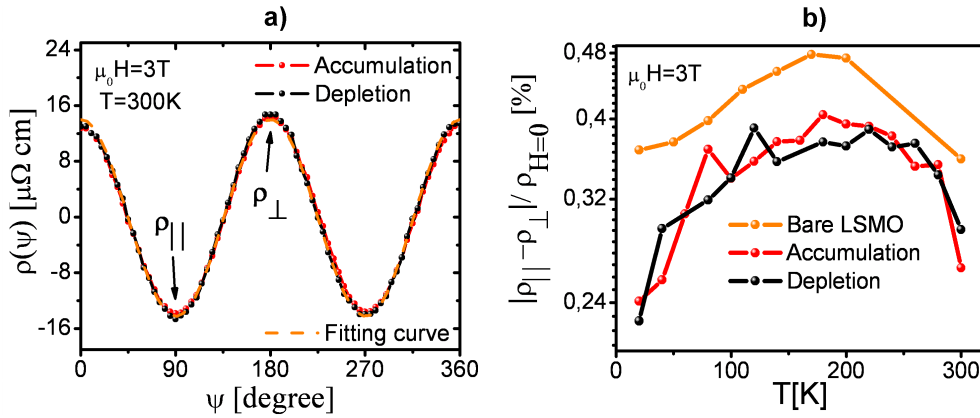


Figure 5.20: In-plane AMR characterization undertaken with H equal to 3 T for a FeFED and a bare 10 nm thick LSMO film grown onto a STO substrate. The same HB geometry was used for both samples. a) Angular dependence of the AMR resistivity at 300 K for the accumulation and depletion states. The orange dot line represents a fit done by using the $\cos^2(\psi)$ dependence. b) Temperature dependence of the normalized AMR ratio for accumulation, depletion and a bare 10 nm thick LSMO film.

fields^{xiv}, the AMR follows the well know [131] $\cos^2(\phi)$ dependence, where ϕ is the angle between M and J . Hong *et al.* in [76] reported that the electrostatically-induced charge carrier modulation of a LSMO($x=0.2$) ultrathin film is not capable to alter the normalized AMR ratio, i.e. $|\rho_{\parallel} - \rho_{\perp}| / \rho_{H=0}$, where ρ_{\parallel} and ρ_{\perp} indicate the resistance of the gated LSMO film measured for H oriented parallel and perpendicular to J , respectively. Interestingly, in this Thesis, the latter result was also confirmed for a FeFED engineered onto a STO substrate. In this respect, Figure 5.20 summarizes the results obtained from the AMR characterization of a 10 nm thick gated LSMO film performed with an applied H of 3 T. Figure 5.20a shows the angular dependence of the resistivity $\rho(\psi)$ acquired at 300 K for accumulation and depletion states. Here ψ represents the angle between J and H . For both P states the $\cos^2(\phi)$ angular

^{xiv}This requirement is necessary since M may not follow the direction of H .

dependence is obtained as demonstrated by the fitting curve shown by the orange dotted line in Fig. 5.20a. In this case $\psi \equiv \phi$ since at the value of 3 T, M completely follows (supposedly) H . It is worth to note that the amplitude of the AMR signal, i.e. $\rho_{\parallel} - \rho_{\perp}$, is not affected by the field effect. On the other hand, Figure 5.20b shows the temperature dependence for $|\rho_{\parallel} - \rho_{\perp}|/\rho_{H=0}$

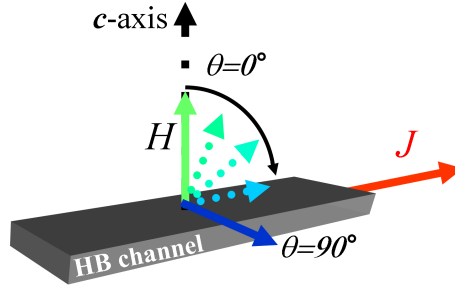


Figure 5.21: Schematic view of the H rotation with respect to the FeFED normal.

(*viz.* the normalized AMR ratio), calculated for the FeFED and for a bare 10 nm thick LSMO layer as well. The solid lines represent a guide for the eyes and, first, it can be easily noticed that the presence of the PZT decreases the magnitude of the normalized AMR ratio by $\sim 25\%$. Second, it is also clearly recognizable that the normalized AMR ratio curves collapse into each other for the accumulation and depletion states. Hence, it can be concluded that, regarding the used LSMO composition, the $|\rho_{\parallel} - \rho_{\perp}|/\rho_{H=0}$ quantity is independent from the carrier concentration modulation as well.

As already mentioned in the previous section, the observed modulation between MR^{out} and MR^{in} triggered a different type of AMR characterization. Completely new results are obtained by allowing the rotation of H in a plane always perpendicular to J , from the out-of-plane ($\theta = 0^\circ$) towards the in-plane ($\theta = 90^\circ$) direction with respect to the FeFED normal (out-of-plane AMR). In Figure 5.21 the adopted geometry for the out-of-plane AMR measurement is schematically sketched. In this case the information collected originates from the relative orientation between M and the crystal axes of the gated LSMO layer. As a result, Figure 5.22a shows the angular dependence of the resistivity $\rho(\theta)$, exhibiting a two-fold symmetry, measured at $T=180$ K with an applied H equal to 2 T, for accumulation and depletion states. In this case, the out-of-plane AMR investigation was undertaken for the same FeFED grown onto a STO substrate, and of which the magnetotransport results have been already shown and discussed in the section 5.3.1. Notably, the out-of-plane AMR amplitude is clearly influenced by the field effect. A key result of this Thesis is shown in Figure 5.22b where the temperature dependence of the normalized AMR ratio, i.e. $\Delta\rho_{AMR}/\rho_{H=0}$, with $\Delta\rho_{AMR}$ being the difference between ρ_{\perp}^{out} and ρ_{\perp}^{in} , has been already previously determined (see for example Fig. 5.11). The two curves almost overlap at high temperatures but for $T < \sim 220$ K, a clear splitting occurs and, precisely, a higher value in accumulation than in depletion is obtained. Remarkably, the latter electrostatically-induced modulation is only related to the out-of-plane AMR measurements. Therefore, to gain an insight into the aforementioned modulation, the measured $\rho(\theta)$ curves, all dominated by a uniaxial magnetic anisotropy contribution, were successfully described through the following formula:

$$\rho = \rho_0 + \Delta\rho_{AMR} \cos(2\phi),$$

where ϕ is the angle between M and the c -axis, and ρ_0 is a constant. Accordingly, the fit was performed (see the green and black solid lines in Figure 5.22a), by calculating $\phi(\theta)$ within the original Stoner-Wohlfarth model [65] (magnetization rotation), considering as magnetic hard axis (due to shape anisotropy) the FeFED normal (i.e. c -axis). As a result, from the fitting

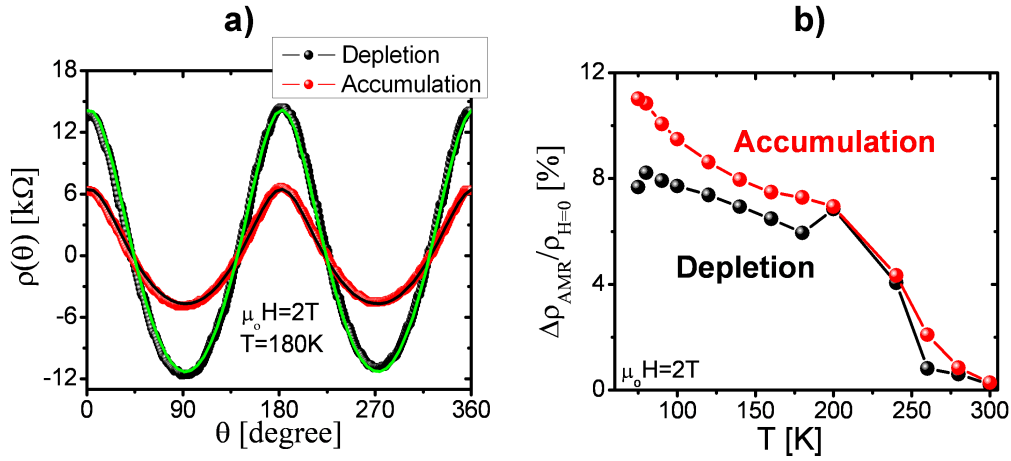


Figure 5.22: a) Angular dependence of the resistivity $\rho(\theta)$, exhibiting a two-fold symmetry acquired at the temperature of 180 K applying a constant magnetic field of 2 T for accumulation (red curve) and depletion (black curve) states. The solid lines represent a fit made by using the $\cos(2\phi)$ dependence, ϕ being the angle between the device normal and the magnetization. b) Temperature dependence of the normalized AMR ratio, i.e. $\Delta\rho_{AMR}/\rho_{H=0}$, for both P states.

procedure (where only the second order term was considered), the minimum magnetic field value necessary to rotate M out-of-plane, i.e. the anisotropy field H_a , was obtained. The latter can be expressed as $\mu_0 H_a = 2K_{tot}/M_s$, where K_{tot} and M_s are the total effective uniaxial anisotropy constant of the system and the saturated magnetization value, respectively. Regarding the magnetoresistance curves acquired as a function of the magnetic field (see Figure 5.13) it is important to show that at $H = 2$ T, the FeFED exhibits in both depletion and accumulation states a decreasing trend for $\rho_{\perp}^{out(in)}(T)$ which proves that M can be completely aligned out-of-plane and thus follows H for the entire range of temperatures investigated, as already reported in Ref. [124]. Subsequently, at the temperature of 180 K, H_a values of (0.47 ± 0.01)

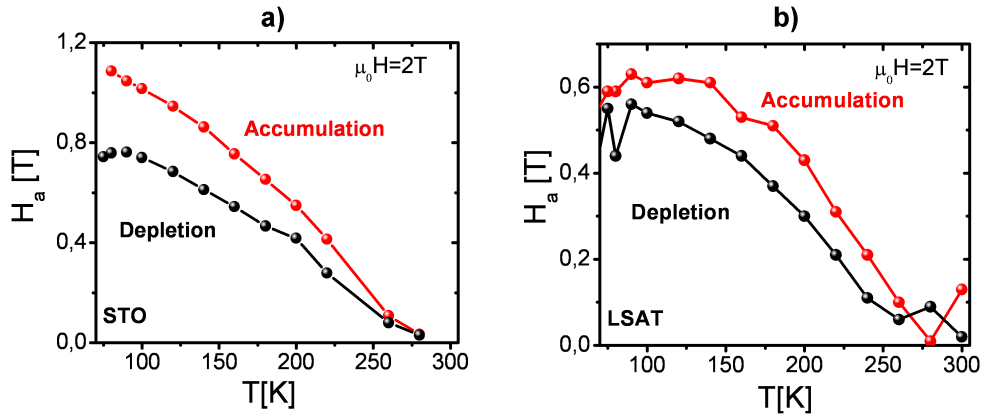


Figure 5.23: Temperature dependence of the anisotropy field values, i.e. H_a , calculated regarding the FeFEDs engineered onto a (a) STO and (b) an LSAT substrate for the accumulation and depletion states.

and (0.66 ± 0.01) T were calculated for the accumulation and depletion states, respectively. In Figure 5.23a the calculated H_a values are shown as a function of the temperature for the accumulation and depletion states. It is worth to notice that the temperature dependence of the H_a values mimics the one of the normalized AMR ratio, and it is observed that in the accumulation state a higher magnetic field is required to rotate M out-of-plane than in depletion. The aforementioned results demonstrate that the electrostatic coupling at the LSMO/PZT interface is capable to induce a variation of the magnetic anisotropy field as large as 40% at 180 K. More-

over, in order to get more information regarding the observed $\Delta\rho_{AMR}/\rho_{H=0}$ modulation and the different magnetic states (i.e. ferromagnetic and/or paramagnetic phases) of the FeFED, also out-of-plane AMR measurements at different H values were undertaken. Figure 5.24 summarizes the results of those measurements for two different temperatures. Precisely, Figure 5.24a (b) shows the magnetic field dependence of the normalized AMR ratio at the temperature of 200 K (300 K) for the accumulation and depletion states. At 200 K, just below the T_C value,

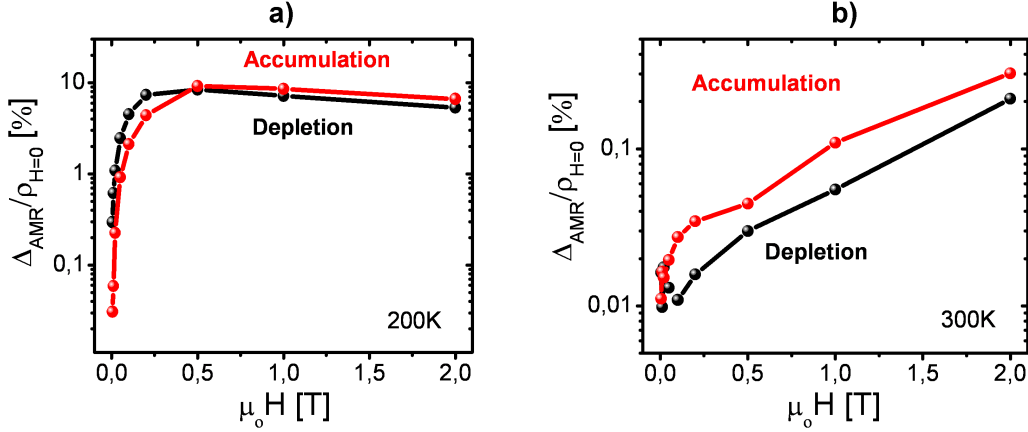


Figure 5.24: Field dependence of $\Delta\rho_{AMR}/\rho_{H=0}$ calculated at (a) 200 K and (b) 300 K for the accumulation and depletion states.

$\Delta\rho_{AMR}/\rho_{H=0}$ exhibits different values but practically the same field dependence is obtained for both accumulation and depletion states. Notably, for high magnetic field values, the normalized AMR ratio decreases. On the other hand, at 300 K, where the gated LSMO thin film is in the paramagnetic state, the latter is keeping increasing upon the increase of the applied field. However, also in this case the field dependence emerges to be the same for accumulation and depletion, together with a rather small modulation measured for the entire range of magnetic field values investigated. Interestingly, it can be claimed that the different magnetic states of the gated LSMO thin film are susceptible to alter the scaling law of the normalized AMR ratio as function of the field and, additionally, the ferroelectric field effect is capable to modulate the measured amplitude values.

As already shown before from the out-of-plane data analysis, information regarding the magnetic anisotropy of the PZT/LSMO system can be envisaged. Generally speaking, the magnetic anisotropy of a system consists of shape (magnetostatic), magnetocrystalline, magnetoelastic, and surface anisotropy terms [63]. Correspondingly to the investigated system, the present out-of-plane AMR measurements indicate that the observed two-fold symmetry of the $\rho(\theta)$ curves can be mainly attributed to the shape anisotropy term (which, in the case of thin films, favors an in-plane orientation of M). In this framework, it emerges that $K_{shape} = 0.5\mu_0 M_s^2$, where K_{shape} is the shape anisotropy constant and, consequently, it follows that $H_a = M_s/2$ (see Ref. [63]). As a result, the same relative percentage variation is expected for H_a and M_s upon the ferroelectric switching of the FeFED. However, as a matter of fact, it was measured (at 180 K) $\sim 30\%$ of variation for H_a (see Fig. 5.23a) and only $\sim 6\%$ for M_s (see Fig. 5.6a), on switching from the accumulation to the depletion state. Therefore, one would have to assume that another uniaxial anisotropy contribution term should be responsible for the relatively large variation of the H_a values. Since the ferroelectric field effect is mainly an interface effect [132], the extra K_s term is expected to originate from the broken symmetry that the Mn ions experience at the PZT/LSMO interface, i.e. the surface magnetic anisotropy term (Néel model [64]). Along this direction, the modulation of the H_a values can be argued to be a consequence of the alteration of the

energy scale related to the e_g levels of the interfacial Mn ions. Indeed, Kyuno and co-workers in Ref. [133] gave a theoretical prediction on the sensibility of the surface magnetic anisotropy of Ag/Fe and Au/Fe multilayers related to the $3d$ band filling of the Fe ions. Accordingly, the results obtained from the (magneto)transport characterization of the FeFEDs presented so far established an essential proof that the ferroelectric field effect is capable to electrostatically and reversibly modulate the valence state of the interfacial Mn ions. Interestingly, Chen and co-workers by using a transmission electron microscopy technique [134] were able to underline the dynamical modulation of the c/a ratio, related to the oxygen octahedra surrounding the Mn ions at the LSMO($x=0.2$)/ferroelectric interface, induced by depletion/accumulation states. Moreover, earlier reports [36] pointed out that substrate-induced strain effects, altering the c/a ratio of the MnO_6 octahedra, drive the lowering in energy of either the $3d z^2$ (i.e. compressive strain) or the $3d x^2 - y^2$ (tensile strain) orbitals which, subsequently, modify the magnetic properties of the system. All these arguments can be used to propose a valid model that qualitatively explains the observed modulation of the H_a values related to the FeFED grown on STO. The model should establish a link between the ferroelectrically induced displacements of the interfacial Mn and O ions of the LSMO and the Mn $3d$ orbital reconstruction (different overlapping and filling). Accordingly, such a model is based on the sketch shown in Figure 5.25,

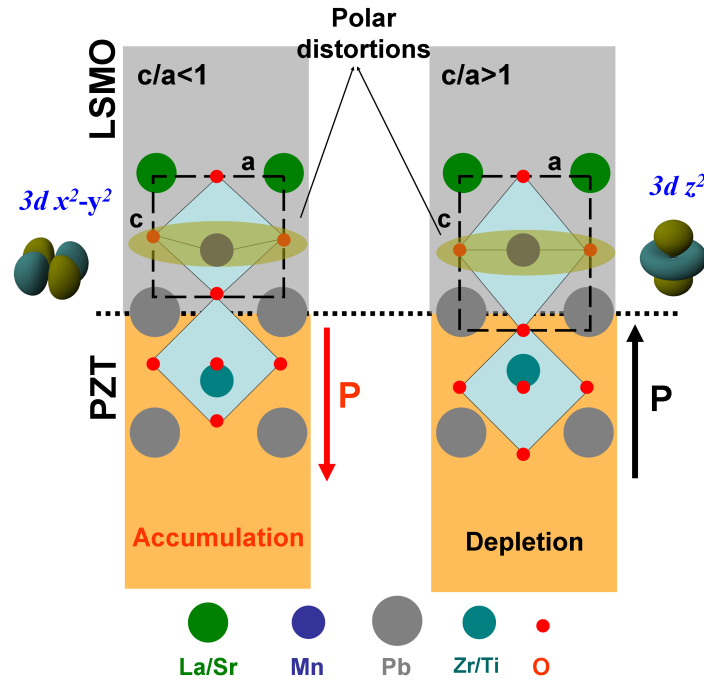


Figure 5.25: Model displaying the effect of the polarization charges on the interfacial LSMO unit cells. Related to the depletion (accumulation) state a decrease (increase) of the c/a ratio is proposed. Accordingly, a different hybridization energy and a strain-mediated effect allow a different interfacial orbital anisotropy. Schema re-adapted from Ref. [134]

where at the PZT/LSMO interface the depletion (accumulation) state increases (decreases) the c/a ratio, resulting in a preferential out-of-plane $3d z^2$ (in-plane $3d x^2 - y^2$) orbital occupancy. By applying this model to the results shown in Figure 5.23a, a qualitative explanation can be envisaged. Indeed, since in depletion the interfacial MnO_6 octahedra expand along the out-of-plane direction, a preferential occupancy of the $3d z^2$ orbitals is obtained. Consequently, the ferromagnetic coupling is enhanced along the out-of-plane direction [27] and the rotation of M is easier to take place. As a result, the expected H_a values are lower than the ones related to the accumulation state where, on the other hand, the out-of-plane shrinking of the MnO_6

octahedra triggers a preferential $3d x^2 - y^2$ orbital occupancy which favors a more *stable* in-plane orientation of M . As a result, the electrostatically-induced Mn $3d$ orbital reconstruction at the PZT/LSMO interface accounts for the observed modulation of the H_a values. In this respect, the PZT/LSMO interface was uniquely accessible since the rotation of H in a plane perpendicular to J , from the out-of-plane (hard axis for M) towards the in-plane (easy plane for M) direction, allowed to study the symmetry breaking experienced by the interfacial atoms. To further validate the proposed model, the out-of-plane AMR measurements were repeated for a FeFED grown onto an LSAT substrate. Accordingly, an extrinsic strain-induced out-of-plane elongation of the LSMO unit cell was obtained. As a result, since an overall occupancy of the out-of-plane $3d z^2$ orbitals is triggered, a decrease of the H_a values, as predicted by the model (superimposed to the ferroelectric field effect modulation) was expected. Accordingly, out-of-plane AMR measurements were performed also in this case with an applied H equal to 2 T and, in this respect, Figure 5.23b shows the calculated H_a values as a function of the temperature for the accumulation and depletion states. It is worth to notice that the H_a values, as expected, are remarkably decreased, compared to the ones obtained on the FeFED grown onto STO. Moreover, the modulation of the H_a values between the accumulation and depletion states is still observed, originating from the electrostatic alteration of the interfacial Mn $3d$ orbital occupancy. The observed variation of the surface magnetic anisotropy is directly linked to a feasible orbital reconstruction, electrostatically induced, that in turn can be responsible for a variation of the SOC at the PZT/LSMO interface. X-ray linear dichroism (XLD) combined with X-ray magnetic circular dichroism (XMCD) measurements, as a function of the PZT polarization directions, which are reported in the next following chapter, can elucidate the intrinsic mechanism of the proposed interfacial spin/orbital reconstruction inherent to the Mn ions.

5.5 Magnetotransport measurements of LSMO/PZT/LSMO/STO heterostructures

In this section the attempts to achieve a relevant ferroelectric field effect in heterostructures exhibiting the following stack of the oxide layers: LSMO/PZT/LSMO/STO, will be discussed. Along this direction, it is necessary to emphasize that the large efforts, devoted to the optimization of the morphology of the PZT film (partly presented in the previous chapter), were actually part of an "evolving" project. Specifically, the final goal of the present Thesis was to study the magnetotransport properties of an LSMO thin film sandwiched between two (switchable) ferroelectric layers. As a consequence, all the results shown so far represent the effective starting point necessary to engineer a more complex device. Actually, along this direction, two main problems one was faced with: First, the worsening of the transport properties of the LSMO thin film grown on top of the PZT layer (see for example Fig. 4.17) and, second, the low quality of the PZT ferroelectric properties mainly related to the poor retention time^{xv}. The latter might be linked to the several photolithographic steps necessary to obtain the complex device, most probably being mainly detrimental for the oxide interface quality and, hence, preventing a reliable field effect study of the transport properties of the LSMO. Precisely, in order to permit the switching of the PZT polarization, relatively to the channel area of the top LSMO patterned in the usual HB geometry, the bottom LSMO layer had to be patterned in an appropriate gate geometry as well. However, among several attempts only a LSMO/PZT/LSMO/STO heterostructure was obtained showing an acceptable retention time. As a result, Figure 5.26 shows

^{xv}The low retention time was monitored as follows: The externally applied voltage pulses, of the same polarity, were consequentially applied to the device at a fixed interval of time (i.e. 10 minutes). As a result, the extremely low retention time was demonstrated, since the current switching peaks were repeatedly observed at each applied voltage pulse.

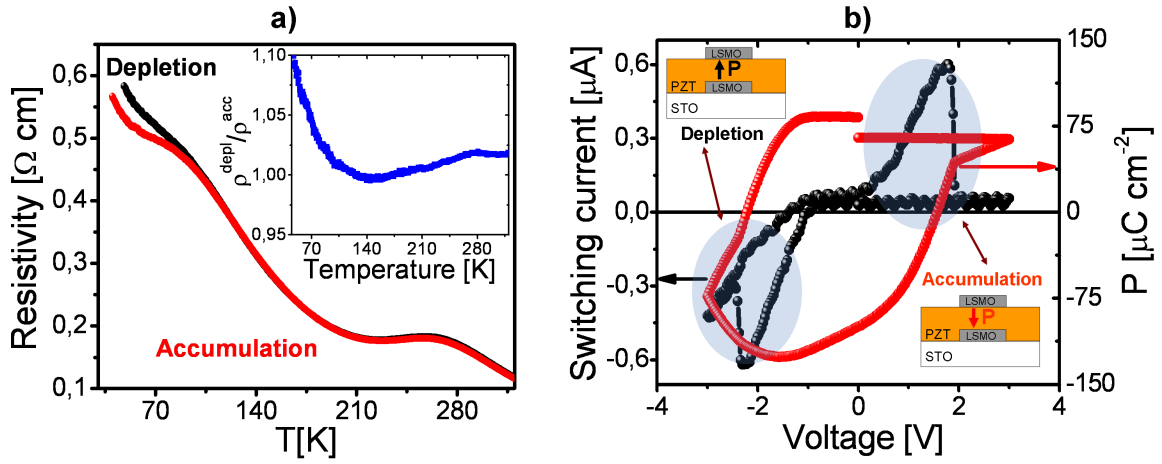


Figure 5.26: a) Temperature dependence of the resistivity of the LSMO/PZT/LSMO/STO heterostructure as function of the two P states. The related inset shows the ρ^{depl} to ρ^{acc} ratio. b) Ferroelectric switching features of the heterostructure.

the temperature dependence of the resistivity acquired for the aforementioned heterostructure, along with the ferroelectric switching properties. The latter were measured by using a TF Analyzer applying the voltage signal to the top LSMO layer while keeping the bottom one to the ground. The switching was performed at the controlled temperature of 300 K, as in the previous cases, with a frequency of 1 Hz. As a result, the dynamical current-voltage characteristic shown in Figure 5.26b exhibits a small value for the coercive voltage, i.e. around ± 2 V, and practically absent imprint features. Though at negative voltage values the leakage is not negligible, the ferroelectric switching peak is still observed. The depletion and accumulation states related to the investigated heterostructure are characterized by a PZT polarization direction as schematically shown in the two insets of Figure 5.26b. A relatively high polarization value of $\sim 75 \mu\text{C cm}^{-2}$ was measured for a thickness value of the PZT equal to 100 nm. On the other hand, the value of the thickness for the bottom and top LSMO layers was chosen to be 10 nm. Figure 5.26a shows the $\rho(T)$ curves of the heterostructure as a function of the two P directions. As a result, a completely insulating behavior is observed for both the accumulation and depletion states, concomitantly to a minor field effect modulation of the transport properties. Indeed, the ratio of ρ^{depl} to ρ^{acc} turned out to be barely one, except for temperatures lower than ~ 70 K, where a slightly distinguishable modulation between accumulation and depletion can be observed. Moreover, at the temperature of ~ 250 K, where the metal-to-insulator transition is expected to take place, a little kink is observed, but, as the temperature is further decreased, the insulating behavior became very stable and the resistivity keeps on increasing for both the accumulation and depletion states. As already highlighted in the previous chapter, the quality of the morphology of the LSMO is very important for the transport properties, which are worsened by the presence of grains. Figure 5.27 shows the morphological and structural characterization of the LSMO/PZT/LSMO/STO heterostructure. The AFM image related to the top LSMO layer shown in Fig. 5.27a indeed exhibits a very rough profile (see Fig. 5.27b), demonstrating that the LSMO cannot grow in a layer-by-layer mode as already presented in the previous chapter (see, for example, Fig. 4.17b). Moreover, the x-ray pattern acquired around the (002) STO reflection and shown in Fig. 5.27c, exhibits a quite broad full-relaxed (002) PZT peak characterized by a rocking curve with a FWHM parameter equal to $\sim 0.6^\circ$ (not shown here). As a result, the worsening of the transport properties related to the top LSMO layer might be due either to the poor morphology quality or to the possible presence of an increased electrically dead layer thickness.

Along this direction, in order to understand if a LSMO film with a thickness value below the

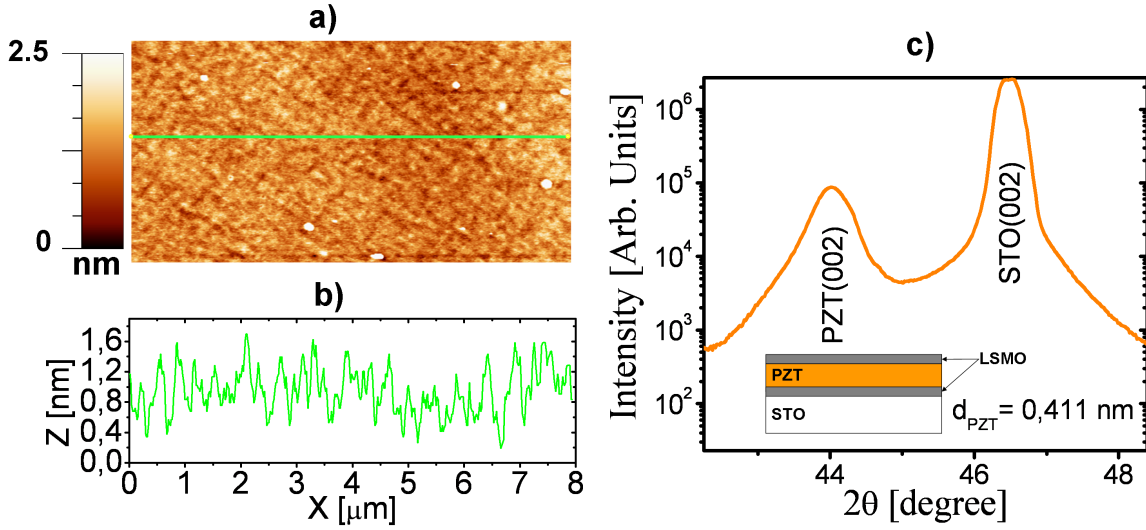


Figure 5.27: a) AFM image ($8 \times 4 \mu\text{m}^2$) of the top LSMO layer demonstrating the poor quality of the morphology. The green line represents the profile scan shown in (b). The calculated rms surface roughness is equal to ~ 0.385 nm. c) θ - 2θ scan around the (002) STO reflection.

dead layer (< 5 nm on STO), can undergo a modulation of the transport properties through the ferroelectric field effect, a FeFED with a 4 nm thick LSMO film was investigated as well. The latter was grown on top of a STO single crystal. As a result, Figure 5.28 shows the (magneto)transport characterization of a 4 nm thick LSMO gated by a 150 nm thick PZT layer as a function of both accumulation and depletion states. Interestingly, though the LSMO exhibits the expected insulating behavior (see Fig. 4.12), the ferroelectric field effect is capable to modulate the overall LSMO resistivity curves as shown in Fig. 5.28a. Accordingly, the ratio of ρ^{depl} to ρ^{acc} increases as the temperature is decreased, precisely, from the value of ~ 1.4 obtained at the temperature of 300 K, it reaches the maximum value of ~ 2.4 at 125 K (see inset in Fig. 5.28a). The magnetoresistance properties were also investigated, and it turned out that upon the application of a magnetic field of 5 T oriented along the FeFED normal (i.e. out-of-plane), the LSMO exhibits the standard decrease of the resistivity (see up and down-triangle curves in Fig. 5.28a). As a result, the MR^{out} as a function of temperature was calculated for both accumulation and depletion states and, interestingly, it emerges that the modulation of the position and magnitude of the MR peaks completely mimics the results obtained on the FeFED engineered with a 5 nm thick LSMO film. Precisely, a MR maximum of $\sim 46\%$ is found at the temperature of ~ 194 K in accumulation, and it increases to the value of $\sim 58\%$ at the temperature of ~ 180 K in depletion. The $\ln\rho - 1/T^{1/4}$ representation of both $\rho(T)$ curves (not shown here) shows that in the entire investigated temperature range (except the observed kink covering the values from ~ 200 K to ~ 160 K) the transport mechanism of the electrostatically gated LSMO can be described by a VRH hopping mechanism. From the usual linear extrapolation performed in the higher temperature range (i.e. $320 \div 200$ K), T_0 values of $^{1/4}\sqrt{(58.71 \pm 0.04)}$ and $^{1/4}\sqrt{(49.74 \pm 0.07)}$ K are obtained for the depletion and accumulation states, respectively. The related ratio, i.e. T_0^{depl}/T_0^{acc} , is equal to ~ 2 . As a result, also in this case, in accumulation an increase of the DOS at E_F is obtained, although the relative modulation is lower if compared with the FeFED grown with a 5 nm thick LSMO layer. Indeed, in the case of 5 nm thick LSMO the value of ~ 3.7 was calculated for the T_0^{depl}/T_0^{acc} ratio. Moreover, the ferroelectric field effect modulates the overall Hall carrier concentration. At 280 K, values of $\sim 2 \cdot 10^{20}$ and $\sim 6 \cdot 10^{19}$ holes/cm³ are measured in accumulation and depletion, respectively. It seems rather

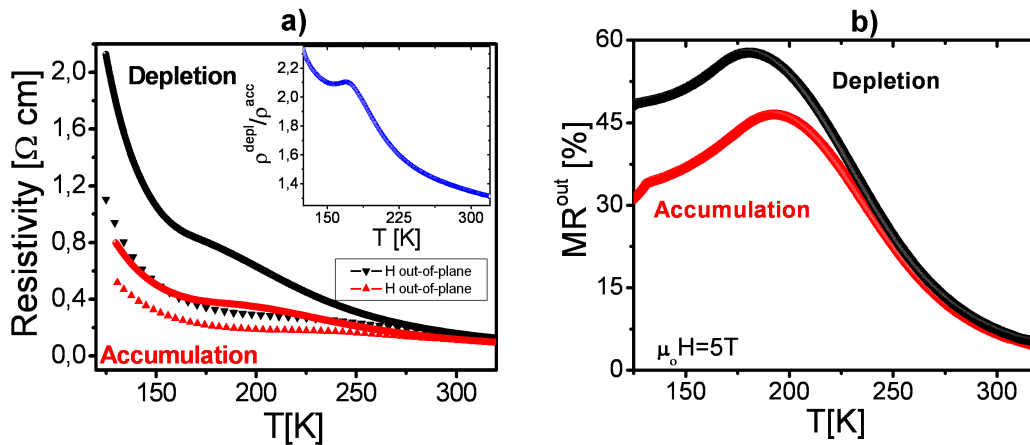


Figure 5.28: a) Temperature dependence of the resistivity acquired for a 4 nm thick LSMO film gated with a 150 nm thick PZT layer for both depletion and accumulation states. Up and down-triangle curves are obtained upon the application of a 5 T magnetic field along the FeFED normal. The related inset shows the ρ^{depl} to ρ^{acc} ratio. b) Magnetoresistance curves calculated for the accumulation and depletion states.

clear that even in the case of an electrically "dead" LSMO layer (directly grown onto a STO single crystal) the ferroelectric field effect is capable to modulate the related magnetotransport properties.

As a result the effectiveness of the dead layer seems not to be insensitive to the ferroelectric field effect modulation. Hence, for the LSMO thin film grown on top of the PZT layer it can be concluded that the driving factor for the observed poor modulation of the transport properties through the ferroelectric field effect might be attributed to the decrease of the quality either of the LSMO morphology or of the top LSMO/PZT interface^{xvi}.

5.6 Conclusion

In summary, the ferroelectric polarization is capable to significantly modulate the magnetic and (magneto)transport properties of a LSMO thin film upon switching a neighbouring PZT layer between its two remanent states. The overall trends observed for the T_C and T_{IM} temperatures are well explained in the framework of the DE mechanism. Attempts to understand the transport mechanism of the several FeFEDs investigated gave plausible reasons to believe that the ferroelectric field effect is capable to alter the energy scale related to the electronic states which, hence, plausibly affect the transport properties. A key result of this Thesis is obtained from the out-of-plane AMR measurements which demonstrated that the normalized AMR ratio can be electrostatically modulated. The normalized AMR ratio modulation was explained by re-adapting a model where polar distortions, induced by the ferroelectric instability of the PZT layer to the interfacial unit cells of the LSMO thin film, were explaining the AMR data collected from FeFEDs grown on STO and LSAT single crystals. In this respect, the interfacial magnetic anisotropy of the electrostatically gated LSMO layer has been put forward. Moreover, studies undertaken on suitably patterned LSMO/PZT/LSMO/STO heterostructures revealed the impossibility to obtain a reliable field effect of the top LSMO layer, where an improvement of the LSMO morphology is still required. Finally, the FeFED grown on a single crystal of LAO exhibited a relevant difference between the room temperature MR^{out} amplitude obtained in accumulation ($\sim 0\%$) and depletion ($\sim 6\%$). The latter might be considered an important result from the application point of view.

^{xvi}No TEM images were acquired for this type of heterostructure.

*In rebus quibuscumque difficilioribus non expectandum, ut qui simul, et serat,
et metat, sed praeparatione opus est, ut per gradus maturescant.*
BACON, *Serm. fidel, n. XLV*

*In all Negotiations of Difficulty, a Man may not look to sow and reap at once;
But must Prepare Business, and so Ripen it by Degrees.*
English Translation by Francis Bacon himself

Soft x-ray absorption spectroscopy characterization of ferroelectric field effect devices

Important information related, mainly, to the electronic structure of a strongly correlated material are given by x-ray absorption spectroscopy (XAS) measurements. By using particular fitting models and sum rules, also a quantitative picture of electronic and magnetic properties of the material under study can be obtained. The following chapter focuses on the spectroscopic results obtained by investigating the magnetic and electronic properties of suitably patterned LSMO/PZT/LSMO/STO heterostructures using the XAS technique with linearly and circularly polarized synchrotron radiation. X-ray magnetic circular dichroism (XMCD) and x-ray linear dichroism (XLD) at the Mn $L_{2,3}$ -edges were used to gain information regarding the magnetic moment and the interfacial orbital occupancy of the LSMO layer as a function of the P direction. XAS at the O K -edge was also acquired and demonstrated that an overall modulation of the hybridization level of the system was achieved as well with the P -switching. The XAS spectra were acquired at the Deimos beamline of the Soleil synchrotron radiation facility located in Paris (France). Interestingly, a satisfactory agreement between the experimental data and multiplet atomic calculations rendered a reliable electrostatical modulation of the interfacial orbital polarization of the LSMO layer.

6.1 Theoretical and practical guide to get (semi)quantitative information from XLD and XMCD spectra

As already discussed in section 2.3, the XAS spectra can be reproduced applying theoretical models which take into account the electronic properties of the specific element. Accordingly, single band or atomic multiplet models are used to describe delocalized and localized states, respectively. However, in the case of the TMOs (i.e. $\text{La}_{1-x}\text{Sr}_x\text{MnO}_3$) the situation cannot be delineated so sharply because of the intrinsic competition between localized and delocalized states. Nevertheless, XLD and XMCD spectra at the Mn $L_{2,3}$ -edges can be successfully explained by using atomic multiplet models, which nevertheless need to be modified to incorporate features regarding different symmetries, typically non-spherical, of the solid environment [135]. As a result, the coordination and local symmetry of the final and ground states become relevant. The most common symmetry effect in solids is the cubic ligand field. Accordingly, a cubic (undistorted octahedra around the transition metal), tetragonal (D_{4h} , JT-distorted octahedra) or lower symmetries need to be taken into account. Those symmetry effects have been already introduced in section 2.1 specifically to the perovskite structure of the LSMO (see, for example, Fig. 2.3). As a consequence of the previous symmetry considerations, the XAS spectra are the convolution of the multiplet structures at the L_3 - and L_2 -edges that reflect the spin-

orbital coupling of the $2p$ states, i.e. the ${}^2P_{3/2}$ and ${}^2P_{1/2}$ core-levels, combined with all the possible final $3d$ states which are accessible (by symmetry) to the excited electron. Moreover, those peaks, associated to the aforementioned multiplet structures, are also convoluted by a peculiar broadening associated to intrinsic and instrumental effects. The intrinsic broadening is related to the lifetimes of the core-hole and the excited final state. The broadening of core-hole lifetimes can be modeled by a Lorentzian function [54]. The broadening by the excited state lifetimes is more complicated. At the edge onset (where the lifetime of the excited state approaches infinity) the broadening is zero and increases with increasing energy. Nevertheless, the peak at the L_3 -edge is usually characterized by broadening values ranging in the interval $0.3\div 0.4$ eV for Mn compounds. This parameter is rather empirical, and can be estimated on the base of the spectral shape. On the other hand, the peak at the L_2 -edge exhibits a shorter lifetime. As a result, the broadening value is roughly two times higher than the one obtained at the L_3 -edge, and values of $0.6\div 0.7$ eV are usually used for Mn compounds. The instrumental broadening is easiest to simulate: it can be modeled by a Gaussian with a FWHM given by the instrument which is rarely below 0.1 eV [136]. Nevertheless, at the Deimos beamline of the Soleil synchrotron, the nominal resolution of the x-ray beam was 0.08 eV. The open-source CTM4XAS program¹ [137] was used for the atomic multiplet scattering splitting calculation of the XLD and XMCD spectra. Figure 6.1 shows an example of two simulated XLD spectra for

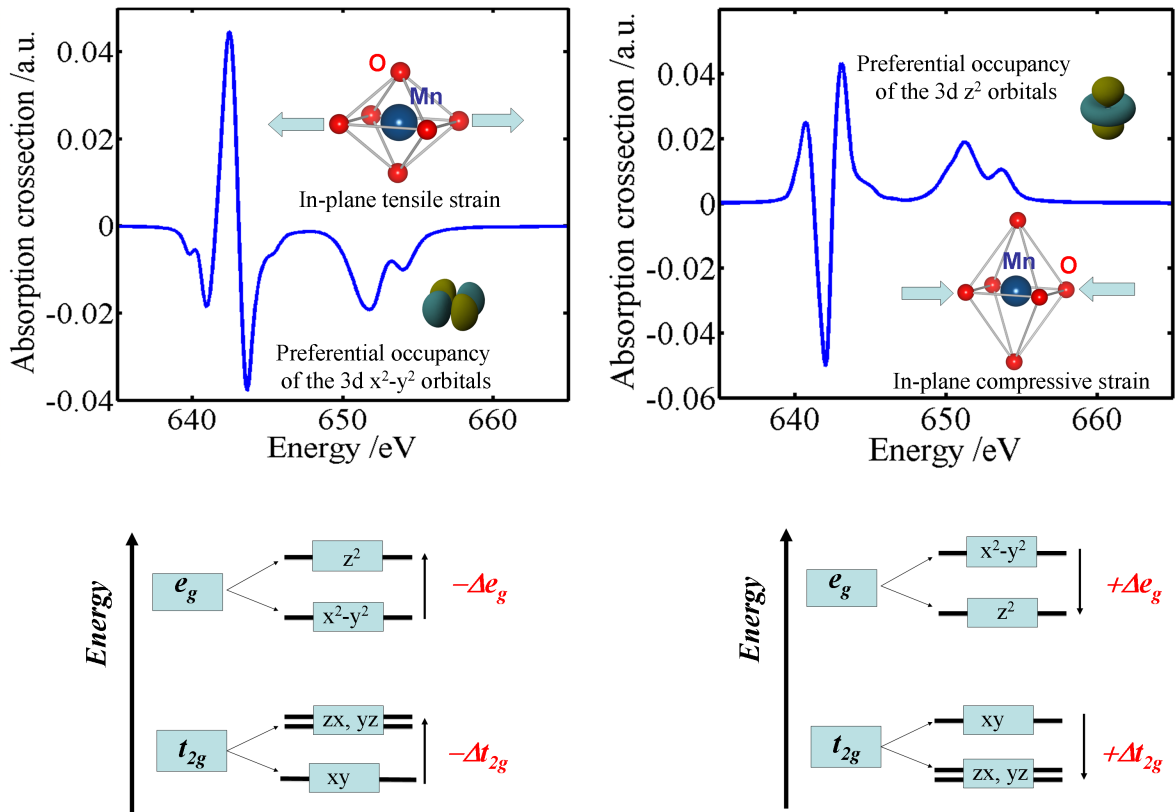


Figure 6.1: Calculated XLD spectra for the Mn $L_{2,3}$ -edges of a Mn^{3+} ion (D_{4h} symmetry). Used program parameters: $10Dq = 1.8$ eV, $\Delta t_{2g} = [xy - (xz, yz)] = \pm 0.9$ eV and $\Delta e_g = [(x^2 - y^2) - z^2] = \pm 0.2$ eV. (Left) The simulation for negative values of Δt_{2g} and Δe_g indicates a preferential in-plane orbital ($x^2 - y^2$) occupancy. The completely opposite situation, i.e. preferential out-of-plane orbital (z^2) occupancy, is found for positive values of the previous parameters (right).

the Mn $L_{2,3}$ -edges of a Mn^{3+} ion for both in-plane compressive and tensile strain states. The two insets represent a schematic view of the two typical Jahn-Teller distortions of the MnO_6

¹Another identical code is Missing developed by Prof. Claudia Dellera at the Politecnico of Milano.

octahedron. The XLD spectra were calculated by the atomic multiplet scattering theory implemented with the CTM4XAS code. Basically, the XLD spectra reflect the relative energy splitting of the e_g and t_{2g} levels, which is reported again in a more simple view in the lower part of Figure 6.1. In the case of an in-plane tensile (compressive) strain state the $3d x^2 - y^2$ (z^2) orbitals are lower in energy, and the XLD spectrum looks like the one depicted on the left side (right side) of Figure 6.1. Moreover, in many systems (like for the case of doped manganites) it is important to extend the crystal field multiplet theory with the inclusion of charge transfer effects [138] which complicate the description of the final state in the XAS process. Precisely, charge-transfer effects take into account the partial hybridization between the Mn $3d$ and O $2p$ orbitals. The simulated XLD spectra, shown before in Figure 6.1, were indeed calculated introducing also such kind of effect. Specifically, in the CTM4XAS software the charge-transfer effects are parametrized by the following constants: charge transfer gap Δ_{CT} , on site U_{dd} and intersite U_{pd} Coulomb repulsion. Typical values reported in literature for LaMnO_3 are $\Delta_{CT} = 3 \div 3.5$ eV, $U_{dd} = 5$ eV and $U_{pd} = 6.5$ eV [136]. As a result, when also charge-transfer effects are considered, the XLD spectra of manganites can be still simulated by multiplet scattering splitting theory. However, beyond any possible complex mechanism that needs to be considered to explain the shape of the XAS spectra, especially for the case of doped manganites, the overall information regarding the e_g orbital splitting and, hence, the related anisotropy in the occupancy can be gained from the analysis of XLD spectra.

Similar considerations are capable to describe also the XMCD spectra. Specifically, the atomic multiplet calculations successfully reproduce the experimental results, introducing the magnetic exchange interaction into the model. The latter splits the final states with different spin configurations, which give rise to a magnetic dichroism. Also the XMCD spectra are dependent on the Mn valence, and in general for ferromagnetic manganites cannot be completely reproduced without explicitly considering the presence of a mixing between the Mn^{4+} and Mn^{3+} ions. On the other hand, when the mixing effect is considered, combinations of atomic spectra obtained from ions in different electronic configurations can be dangerous, since not always strictly valid. As a result, the fitting procedure needs to be evaluated case-by-case.

6.2 XLD measurements on the LSMO/PZT/LSMO/STO FeFED

Several studies have shown that different surface symmetries [57] and substrate-induced strain effects [36] are capable to induce a different interfacial partial occupancy of the $3d x^2 - y^2$ and z^2 orbitals in $\text{La}_{1-x}\text{Sr}_x\text{MnO}_3$ thin films. Due to the strong correlation between the several degrees of freedom for which manganites, in general, are widely investigated, the resulting orbital and/or charge anisotropy can in turn affect the related physical properties. Indeed, results collected from a spectroscopy study have recently shown that upon the P -reversal, a tuning of the competition between the ferromagnetic and anti-ferromagnetic phases of the half-doped $\text{La}_{0.5}\text{Ca}_{0.5}\text{MnO}_3$ manganite, can be realized [139]. Moreover, a surface x-ray diffraction study of the system $\text{LaAlO}_3/\text{SrTiO}_3$ (LAO/STO) revealed that the presence of a polarity mismatch, at the oxides' interface, induces buckling of the cations [140]. Interestingly, it has been proven that an injection of electrons at the LAO/STO interface, inducing the aforementioned lattice deformations, can be responsible for an orbital reconstruction mainly based on a re-arrangement of the level hierarchy of the partially occupied Ti t_{2g} orbitals [141]. Additionally, recent high resolution TEM measurements on manganite/ferroelectric/manganite heterostructures demonstrated structural distortions of the interfacial MnO_6 octahedra induced by the ferroelectric instability. These structural distortions can be indirectly translated into an inversion of the e_g orbital occupancy [134]. Hence, from crystal field effects, which can be either intrinsic (different lattice symmetries) or extrinsic (strain and/or polar distortions), a fascinating possi-

bility to induce an orbital reconstruction at the interface between two oxides can be derived. Therefore, in suitably engineered devices a clear modulation of the interfacial functional properties can be studied. However, a direct demonstration of an inversion of the transition metal 3d-states, through spectroscopy probes, is still missing. In the attempt to try to fill up the aforementioned gap, XAS spectra at the Mn $L_{2,3}$ -edges and O K -edge were measured for the LSMO/PZT/LSMO/STO FeFED, as a function of the P direction. The belief, that upon the P -reversal the variation of the energy scale of the Mn 3d orbitals may be achieved, was the driving force behind the measurements performed at the Soleil synchrotron radiation facility and presented here.

Differently from the case of the (magneto)transport characterization introduced in the pre-

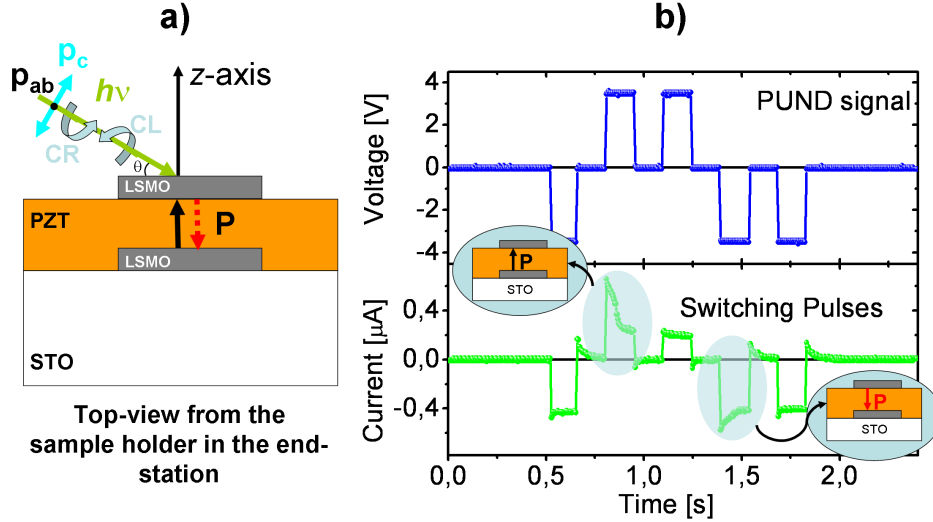


Figure 6.2: (a) Schematic view of the x-ray absorption spectroscopy experiment on the LSMO/PZT/LSMO FeFED. The photon linear polarizations can be set parallel (p_{ab} , vertical polarization) or almost perpendicular to the ab -plane (p_c , horizontal polarization). CR and CL indicate photons circularly right and circularly left polarized, respectively. (b) Ferroelectric switching of the PZT layer during the experiment: (top panel) PUND gate voltage signal applied to the bottom LSMO layer with the top LSMO grounded, and (bottom panel) current vs. time characteristic acquired during the switching process. The ferroelectric polarization directions, related to the PUND polarity, are sketched in the insets (bottom panel).

vious chapter, here the studied heterostructures were suitably patterned through several photolithographic steps. Indeed, in order to study the Mn 3d orbital occupancy as a function of the P direction, the bottom and the top LSMO layers were patterned in two separate steps, realizing a back-gated $200 \times 100 \mu\text{m}^2$ Hall bar (HB) channel. The PZT lying underneath the channel of the HB was switched by applying a suitable voltage pulse between the bottom (gate) and top (HB) LSMO layers. Figure 6.2a shows the schematic view of the FeFED, along with the geometry used for the XLD and XMCD experiments. A typical switching cycle performed on the FeFED tested at the Deimos beamline is shown in Figure 6.2b. More in details, a function generator applies a positive-up negative-down (PUND) signal between bottom gate and the top channel (grounded), while an oscilloscope was used to read the ferroelectric switching pulses [92]. The polarization of the PZT layer was $\sim 80 \mu\text{Ccm}^{-2}$. The insets of Figure 6.2b illustrate the direction of P with respect to the applied voltage pulse. Accordingly for polarization pointing toward (away from) the top LSMO layer the depletion (accumulation) state is realized. The incoming beam, characterized by a vertical \times horizontal size of $80 \times 80 \mu\text{m}^2$, is focused on the upper LSMO layer in grazing incidence conditions (incidence angle of $\sim 30^\circ$ with respect to the device surface). The 60 nm thick PZT layer was characterized by a relatively high value of P and a long retention time. In particular, a

patterned LSMO(6 nm)/PZT/LSMO(12 nm) heterostructure deposited on top of a (001) STO single crystal was investigated. The LSMO/PZT/LSMO/STO heterostructure investigated at

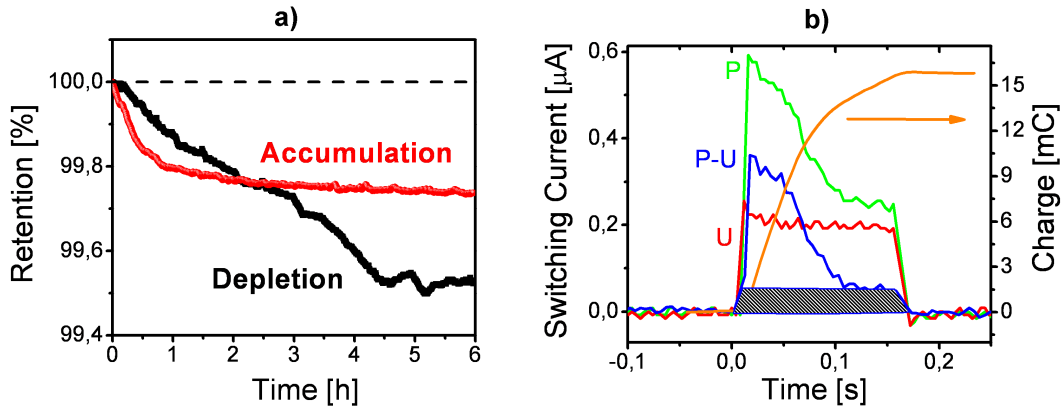


Figure 6.3: (a) Retention measurement for the LSMO/PZT/LSMO/STO FeFED. The resistance of the top LSMO layer was monitored. b) Results related to the polarization calculation for the P-U current pulses displayed in the previous Fig. 6.2b.

the synchrotron radiation facility was made of two separated FeFEDs. After almost 6 hours in average of acquisitions the heterostructure was removed from the ultra high vacuum chamber and the PZT polarization retention tested by sending an appropriate voltage pulse. Unfortunately one of the two FeFEDs was characterized by a bad retention time, since P was found completely reversed and, for this reason, only the results related to the properly working device are shown here. Accordingly, in Figure 6.3a the retention characteristic acquired at 300 K for the properly working FeFED is shown, for both the accumulation and depletion states. Since the top LSMO layer was patterned in a HB geometry it was possible to monitor the resistance value as a function of the P direction. The displayed percentage values are the time dependence of the resistance with respect to the initial values measured just after the P -switching for both the accumulation and depletion states. The following formula has been used to calculate the retention value:

$$Retention = 100 + 100 \cdot [R(t = 0) - R(t)],$$

where $R(t = 0)$ and $R(t)$ represent the measured resistance value just after the P -switching (i.e. at $t = 0$) and at the time t , respectively. After at least 6 hours, the obtained values of the resistance remain practically constant at 300 K, hence, demonstrating the good retention time of the ferroelectric polarization. In Figure 6.3b the P, U and P-U current pulses are shown. The integration over time (see, for example, the orange solid line) of the P-U pulse gives the total amount of charges collected in the parallel plate capacitor-like geometry, i.e. ~ 25 mC that become ~ 16 mC if the shaded area (still accounting for the leakage contribution) is subtracted. Hence, dividing the latter value through the nominal value of the switched area ($\sim 2 \cdot 10^{-4}$ cm²) the relatively high polarization value of ~ 80 μCcm^{-2} is obtained.

Substantial difficulties were faced regarding the alignment of the incoming x-ray beam in correspondence to the channel area of the top LSMO layer patterned in a HB geometry. Accordingly, in order to achieve a reliable alignment, several XAS spectra were acquired scanning along the x, z -direction in resonance and off-resonance modes. Since outside the HB channel no Mn signal was expected, x and z scans were performed at the energies of 641.17 eV (on the Mn L₃ resonance) and 631.17 eV (off resonance). The subtraction of the two scan line profiles for each x, z -direction provided a powerful tool to properly align each FeFED with respect to the incoming x-ray beam. As an example Figure 6.4 shows the result of the aforementioned procedure. The insets of the two graphs reported in Fig. 6.4 show an optical microscope im-

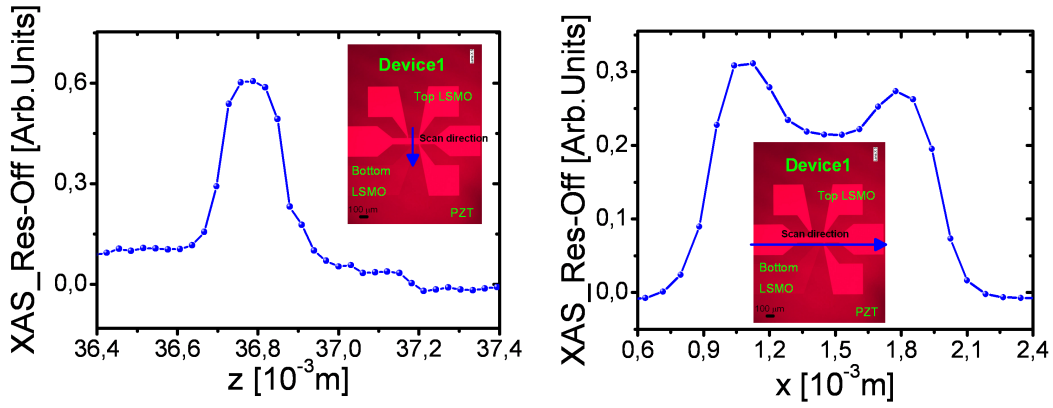


Figure 6.4: Example of the x-ray beam alignment procedure. On the left the result of the z -scan across the HB channel (see blue arrow in the inset) is shown. On the other hand on the right the XAS spectrum obtained from an x -scan along the entire length of the HB geometry is depicted (see blue arrow in the inset). Both insets show the optical microscope image of the LSMO/PZT/LSMO/STO heterostructure with the bottom LSMO shaped as gate and the top LSMO as HB geometry.

age of the studied heterostructure where the (bottom) gate and top HB geometry of LSMO are easily recognizable. Moreover, the blue arrows indicate the two directions used for the x-ray beam alignment. Therefore, in the left graph of Fig. 6.4 the result obtained from a z -scan performed in correspondence to the 100 μm -wide HB channel is reported. On the other hand, in the right graph of Fig. 6.4 the result obtained from the x -scan performed along the entire length of the HB geometry is shown. Correspondingly, only after an adequate alignment of the x-ray beam in correspondence to the channel area of the HB geometry the XAS measurements were suitably performed. In this respect, it is necessary to remember that only in that area it was possible to switch the polarization of the PZT layer due to the chosen geometry of the bottom LSMO layer.

Interestingly, Figure 6.5 shows a clear proof of the particular sensibility of the XAS technique to the electronic configuration of the element under investigation. In Figure 6.5a room tem-

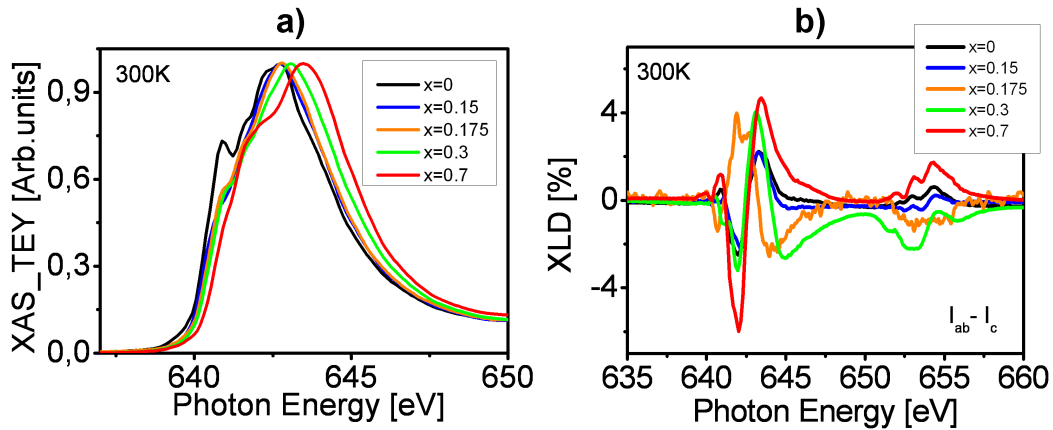


Figure 6.5: a) XAS spectra at the Mn L_3 absorption peak measured at room temperature for several $\text{La}_{1-x}\text{Sr}_x\text{MnO}_3$ thin films characterized by different Sr-contents all grown onto a STO substrate. In b) the related XLD spectra are shown.

perature XAS spectra at the Mn L_3 -edge ($^2P_{3/2}$ multiplet), of several bare $\text{La}_{1-x}\text{Sr}_x\text{MnO}_3$ thin films grown on STO substrates as a function of the doping level x are comparatively shown. It is worth to notice that the absorption peak position shifts to higher energy values when x increases. Indeed, the maximum value of the Mn L_3 peak moves from 642.7 eV in LaMnO_3 to

643.5 eV in $\text{La}_{0.3}\text{Sr}_{0.7}\text{MnO}_3$. The observed shift of the peak is an evidence of a Mn valence state variation, which is linked to the different doping levels and modifications of the MnO_6 symmetry due to unavoidable chemical distortions. In order to have a quantitative information of the energy shift as a function of x , the absorption rising peak which also experiences a shift to higher energy values with the increase of x was considered. By a linear fit of the rising part of the XAS peaks (not shown here for sake of simplicity), the intercept with the photon energy axis E was calculated. At $x=0$, $E = 639.81$ eV and at $x=0.7$ $E = 640.08$ eV. Hence, the relation $\Delta x/\Delta E = 2.6 \text{ eV}^{-1}$ describes qualitatively the effect of the doping level on the shift in energy of the L_3 peak position. As already mentioned before, due to the relevant change of the spectral shape also an alteration of the symmetry related to the ground state of the manganite thin films can be envisaged [142]. Precisely, for the spectrum acquired at $x=0$, an evident complex ${}^2P_{3/2}$ multiplet structure is obtained (see the pre-peak at low energy values in Fig. 6.5a of the black solid line) which is theoretically simulated (not shown here) assuming the stable $3d t_{2g}^3 e_g^1$ electronic configuration for the ground state with a crystal-field splitting of 2 eV. As a result, the electronic ground state of LaMnO_3 is mainly $3d^4$ with $10Dq = 2$ eV. Then, when x is increased, the L_3 peak is much more broadened and a satisfactory agreement with the simulated spectra is found when the crystal-field splitting energy is decreased to a value of 1.2 eV, and also charge transfer effects are considered through the Δ_{CT} parameter. First, the variation of the $10Dq$ value demonstrates, indeed, that the symmetry of the ground state is affected by the variation of the valence state of the Mn ions [143]. Next, the increase of the covalency of the ground state, i.e. the ligand oxygens share electrons with the Mn ions as explained in Ref. [144], justifies the use of charge transfer effects for the simulation. Finally, it can be concluded that the ground state of bare $\text{La}_{1-x}\text{Sr}_x\text{MnO}_3$ thin films grown on top of STO substrates show a clear tendency towards the $3d^4$ electronic configuration for low level of doping and additionally, when x increases, the hypothesis of the hybridization between the Mn and O ions results in a rather complete picture, where the ground state is more close to a mixture of $3d^3$ and $3d^4\bar{L}$, with \bar{L} being a ligand hole. Additionally, Figure 6.5b shows the XLD spectra related

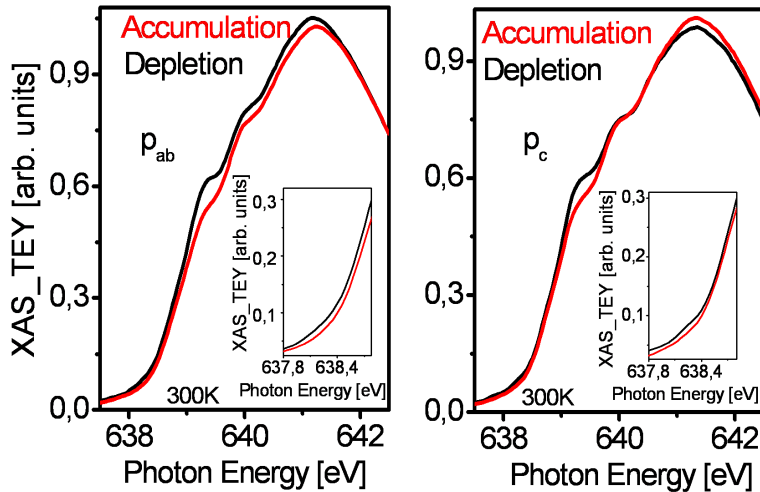


Figure 6.6: Mn L_3 absorption peak measured at room temperature for the FeFED for light polarized in-plane (p_{ab}) and out-of-plane (p_c). The difference of the rising peaks between accumulation and depletion is highlighted in the two insets.

to each of the previously introduced bare $\text{La}_{1-x}\text{Sr}_x\text{MnO}_3$ thin films characterized by different x values. Without entering into details of a realible discussion related to the understanding of the features related to each XLD spectrum, here, the main focus is (barely) on the fact that the variation of x is also capable to affect the XLD spectra. Whether this is due to structural distor-

tions induced by a different level of doping, or due to the intrinsic variation of the valence state of the Mn ions, is so far unknown. In this respect, field effect experiments can be extremely helpful to discriminate between the two aforementioned origins for the differences exhibited by the XLD spectra. Since the ferroelectric field effect, as shown in the previous chapter, can be basically explained as a charge-driven effect, it would be of obvious relevance to reproduce the results shown in Fig. 6.5 (which were obtained by a static variation of the doping level) through the possibility offered by the FeFED, *viz.* with a dynamic variation of the doping level upon the reversal of the P direction.

Along this direction a compelling result is illustrated in Figure 6.6 where the Mn L_3 -edge XAS spectra acquired for both light polarizations, i.e. p_{ab} and p_c , and for both accumulation and depletion states of the investigated FeFED are shown. By a close inspection of the related insets, it is worth to recognize that the Mn L_3 absorption rising peak shifts towards lower energies in depletion, in complete agreement with the aforementioned trend obtained for a static variation of the hole doping level (see Fig. 6.5a). The same result is obtained for both light polarizations. As a result, the doping level of the gated upper LSMO layer can be dynamically tuned upon the P -reversal. By operating, as in the case of Figure 6.5, a linear fitting procedure of the XAS rising peak, a difference in the photon energy, ΔE , of ~ 0.023 eV was found from which an average dynamic modulation of x of ~ 0.06 holes/Mn is calculated. Hence, from the analysis of the XAS measurements acquired in accumulation and depletion, it emerges that the interfacial doping level of the upper LSMO layer is electrostatically modified by switching P . The obtained value for the modulation of x is also consistent with previous reports in literature [70]. Additionally, the relative modulation of the magnitude obtained between p_{ab} and p_c indicates a clear presence of linear dichroism in the system. Hence, relevant information regarding a possible anisotropy of the orbital occupancy can be obtained. Along this direction, it needs to be highlighted that at room temperature and in zero magnetic field, the XLD spectra are mainly related to the orbital anisotropy, and mainly information related to the level hierarchy of the Mn $3d$ t_{2g} and e_g states can be addressed. An important result along this direction is illustrated

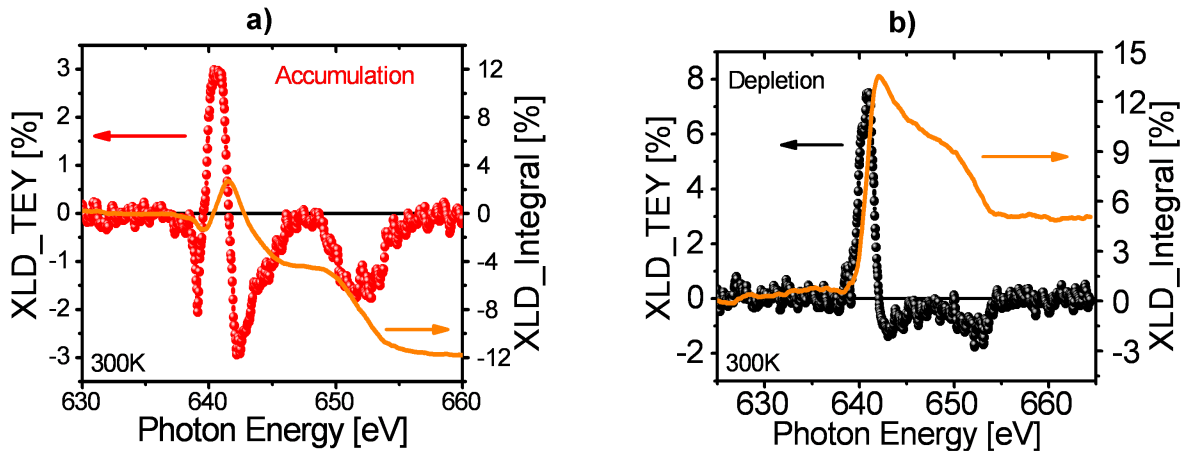


Figure 6.7: a) XLD spectra obtained in the accumulation state of the FeFED. The orange solid line represents the integral of the XLD spectrum calculated over the entire range of photon energy investigated. b) XLD spectrum obtained for the depletion state of the FeFED. Also in this case the solid orange line represents the integral of the XLD spectrum.

in Figure 6.7 where spectroscopic studies performed on the FeFED characterized by a good retention time are shown. The two XLD spectraⁱⁱ were calculated from the Mn $L_{2,3}$ -edges XAS measurements acquired at room temperature and zero magnetic field for the accumulation (see Fig. 6.7a) and the depletion state (see Fig. 6.7b). Interestingly, a peculiar change of the shapes

ⁱⁱBoth XLD spectra were normalized to the value of the Sum XAS spectrum at the L_3 peak value. The Sum XAS spectrum indicates indeed the sum of the two XAS spectra acquired with light parallel and perpendicular to the FeFED plane, respectively.

of the spectra can be easily seen. Specifically, regarding the XLD spectrum calculated in accumulation, the peak centered around the photon energy of ~ 640 eV shows tails that noticeably extend in the negative part of the graph if compared with the one obtained in depletion (see Fig. 6.7b), where substantially those features completely disappear. In an octahedral symmetry of the crystal field interaction, the integrated XLD signal normalized to the total XAS absorption, i.e. D_L as defined by the Eqs. 2.1 and 2.2, offers relevant information about the anisotropy of the orbital occupancy related to the $3d_{x^2-y^2}$ and $3d_{z^2}$ levels. Interestingly, the aforementioned integral (displayed in Fig. 6.7a,b as a solid orange line) exhibits a sign inversion when the polarization direction is reversed. Additionally, a measure of the Mn $3d$ orbital polarization π_{orb} can be obtained as pointed out by the following relation :

$$D_L = \frac{\int_{L_3+L_2} (I_{ab} - I_c) dE}{\int_{L_3+L_2} (2I_{ab} + I_c) dE} \simeq \frac{1}{2} \frac{n_{z^2} - n_{x^2-y^2}}{n_{z^2} + n_{x^2-y^2}} = -\frac{1}{2} \pi_{orb}, \quad (6.1)$$

where $n_{x^2-y^2}$ and n_{z^2} are the electron occupations in the e_g $3d_{x^2-y^2}$ and $3d_{z^2}$ orbitals, respectively, and π_{orb} is the orbital polarization defined as in Ref. [134]. D_L is negative in accumulation (according to Eq. 6.1 an in-plane $3d_{x^2-y^2}$ electron occupancy is favored), and positive in depletion (according to Eq. 6.1 an out-of-plane $3d_{z^2}$ electron occupancy is now favored). These data correspond to a change in the average orbital polarization of the e_g Mn $3d$ states from +1.2 % (accumulation) to -0.5 % (depletion), showing that the orbital hierarchy of the Mn $3d$ -states is controlled by the electric field induced by the PZT layer.

However, it is necessary to highlight here that in Figure 6.1, where the simulated XLD spectra related to two opposite strain states of the octahedron surrounding the Mn ion are shown, an opposite trend of the features related to both L_3 and L_2 peaks is observed when the orbital occupancy is completely reversed. Hence, although D_L reverses sign, the XLD spectra of Figure 6.7 do not exhibit a clear inversion of the L_3 and L_2 peaks. It is clear that this important discrepancy forbids, at first sight, any reliable explanation based on the ligand field approach, and hence, on the validity of the sum rule expressed through Eq. 2.2. On the other hand, even if the obtained change of sign for D_L could be explained in the framework of the aforementioned sum rule, the question of how a genuine charge-driven effect can be responsible of an anisotropy in the orbital occupancy needs to be raised. Indeed, from a pure electrostatic approach and by assuming a simple rigid band picture, the Fermi level of the LSMO can only move up and down across the e_g conduction band as a function of the P direction [81]. In this framework it is clear that a P -dependent anisotropy occupancy of the $3d$ orbitals cannot be explained through simple change of the carrier density. Subsequently, in this particular case, the change of the XLD spectra observed upon the P -reversal might reflect subtle deviations from the octahedral symmetry of the interfacial MnO_6 octahedra. Moreover, since the XAS signals are averaged over the entire thickness of the investigated LSMO layer, the presumed effect of symmetry lowering should, then, propagate in more than interfacial unit cells in order to give measurable effects.

6.2.1 Atomic multiplet calculations

In order to get more detailed information on the changes of the electronic properties of the LSMO layer as a function of the P direction, the XLD spectra were simulated by atomic multiplet calculations. Although the sum rule of Eq. 2.2 does not take into account the splitting of the $3d$ t_{2g} orbitals (see, for example, the lower part of Figure 6.1), the code implemented by the CTM4XAS software gives the possibility to account also for that. Indeed, in principle, the XLD spectra contain also contributions stemming from the anisotropy of the $3d$ t_{2g} states.

The latter are partially related to the orbital splitting, and partially to the different hybridization energy between the Mn 3d orbitals and the 2p orbitals of the neighbouring oxygen ions. For this reason, all the simulated spectra were obtained considering also charge transfer effects, as previously introduced, to properly simulate the XAS spectra related to $\text{La}_{1-x}\text{Sr}_x\text{MnO}_3$ thin films characterized by different x values. Due to the low level of doping of the LSMO layer, i.e. $x=0.175$, the simulations of the XLD spectra were implemented using, as a first assumption, a starting ionic picture with the manganese ions in the Mn^{3+} configuration. Indeed, the contribution to the XLD spectra arising from the presence of the Mn^{4+} ions is minor at that level of doping, and thus completely ignored for the simulations presented below. The values of 1.7 eV and 80 % were used for the crystal field splitting of the t_{2g} and e_g levels (i.e. $10Dq$) and for the standard reduction of the Slater integralsⁱⁱⁱ, respectively. The charge transfer energy Δ_{CT} indicates the energy gap between the $3d^4$ and $3d^5\bar{L}$ electron configuration for a Mn^{3+} ion, \bar{L} being a hole in the O_{2p} band. Hence, Δ_{CT} is strictly related to the hybridization level of the system. Additional parameters used by the theory implemented in the code of the CTM4XAS software were the U_{dd} parameter which is the Hubbard U value, i.e. the Coulomb interaction between the 3d electrons, and the U_{pd} parameter which defines the core-electron potential interaction. Usually for XAS charge transfer multiplet calculations, U_{dd} and U_{pd} separately have no direct influence, and only the energy difference $U_{pd}-U_{dd}$ is important [137]. Finally, the XAS spectra were convoluted with a Lorentzian broadening of 0.35 and 0.7 eV for the L_3 and L_2 peaks, respectively. The bigger value used for the broadening of the L_2 peak is due to the large bandwidth of the Mn 3d states [138].

The XLD spectrum obtained in the accumulation state (i.e. XLD_{acc}) is reasonably reproduced by the solid blue line of Figure 6.8a using as fitting parameters the energy splitting for the t_{2g} and e_g states, i.e. $\Delta t_{2g} = E_{xy} - E_{xz,yz} = -0.15$ eV and $\Delta e_g = E_{x^2-y^2} - E_{z^2} = -0.55$ eV, and a charge transfer Δ_{CT} of 4 eV. The parameter set, i.e. XLD^- , that fits at best the experimental spectrum in accumulation is the result of a simulation batch where the energy splitting parameters, Δt_{2g} and Δe_g together with the Δ_{CT} and the $U_{pd}-U_{dd}$ parameters were appropriately varied. In the CTM4XAS software the D_s and D_t parameters were used to account for the Δe_g and Δt_{2g} energy splittings as indicated by the following relations:

$$\Delta t_{2g} = 4D_s + 5D_t$$

$$\Delta e_g = 3D_s - 5D_t.$$

The negative sign of D_L is recovered as well (see, for example the blue dotted line in Fig. 6.8a), as expected from Figure 6.7a. The XLD^- parameters are displayed in the form of an energy diagram in the bottom panel of Fig. 6.8a. Interestingly, a similar XLD spectrum was also obtained in areas of the upper LSMO layer where it was impossible to switch the PZT outside the channel (no gate electrode). This result confirmed that the as-grown polarization state is characterized by P pointing away from the upper LSMO layer (accumulation). This built-in polarization state of the PZT determines a structural/orbital effect which mainly induced a preferential occupancy of the in-plane $3d_{x^2-y^2}$ orbitals, which is schematically represented in the inset of Figure 6.8a (upper panel). However, only the interfacial unit cells are affected by the P -reversal due to a finite screening length of the LSMO. As a consequence, while the agreement between experimental data and theoretical calculations is quite good in the accumulation state, in depletion it is not possible to get a simulated XLD spectrum which gives at the same time a negative orbital polarization, as required by the sign of D_L (see, for example, the orange solid line in Fig. 6.7b), and a comparable spectral shape. Indeed, in depletion the XLD spectrum

ⁱⁱⁱA standard reduction to 80 % of the Hartree-Fock values is assumed to represent the atomic values, as confirmed by experiment [137]. F_{dd} , F_{pd} and G_{pd} are the symbols used in the CTM4XAS software for the Slater integrals.

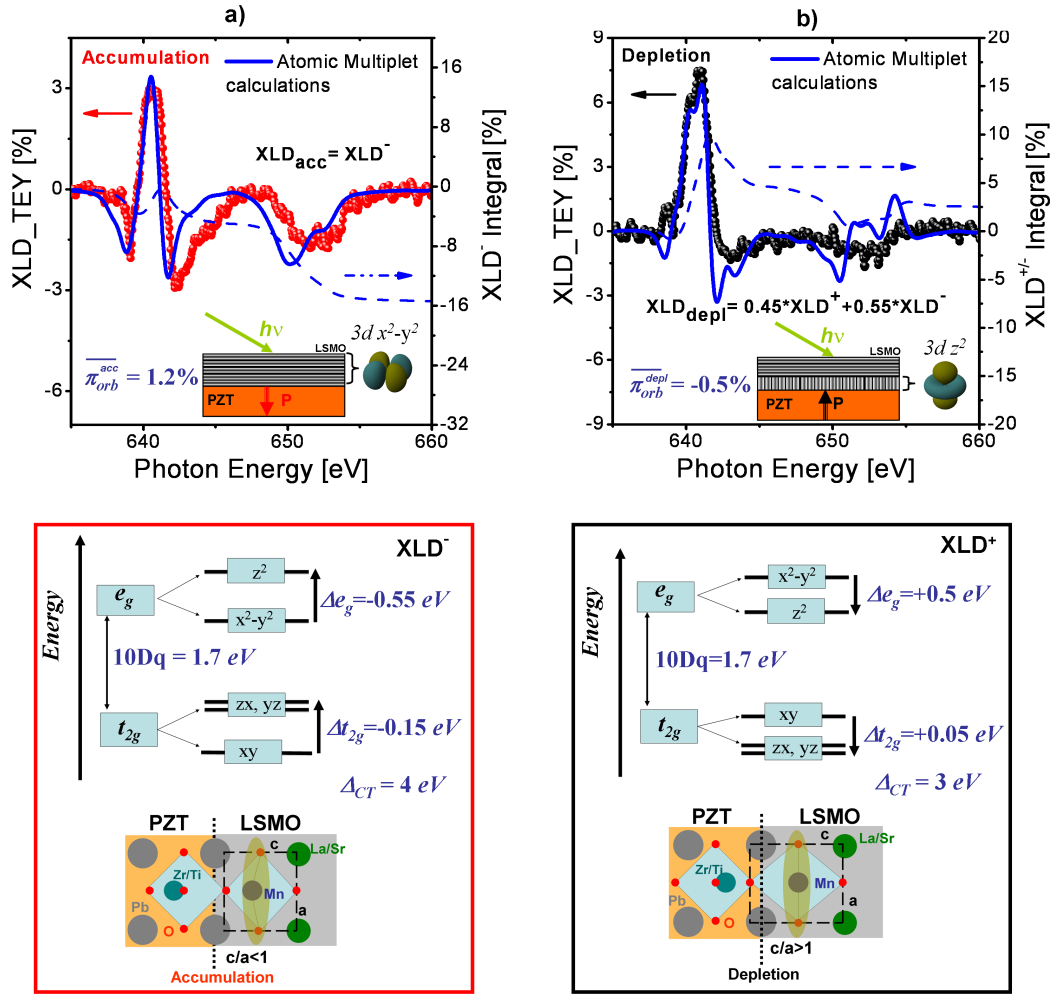


Figure 6.8: Comparison between the atomic multiplet calculations (blue lines) and the experimental XLD spectra described in the text for the (a) accumulation and (b) depletion state, respectively. The blue dotted lines represent the integrals of the simulated XLD spectra that adequately reproduce sign and shape of the integral obtained from the of the measured XLD spectra. In the lower part the energetic diagrams represent the possible modulation of the hierarchy of the Mn 3d levels in accumulation and depletion. The schematic ionic model has been re-adapted from [134].

(i.e. XLD_{depl}), while showing a much reduced negative tail at the L_3 peak (which, basically, determines the negative sign of D_L in accumulation), is still characterized by a positive peak at L_3 and a reduced, but negative, feature at the L_2 peak. A reasonable agreement between the XLD spectra and the calculations, in depletion, is obtained by separating the contributions to the XLD signal of the interfacial unit cells, influenced by the PZT polarization, and of the top-most unit cells of the LSMO which are, on the other hand, not (or at least less) affected by the P -switching. As a result, the LSMO thin film is modelled as constituted by two parts each of them contributing differently to the overall XLD signal, as schematically illustrated in the sketch of Figure 6.8b (upper panel). In this framework the top-most unit cells of the LSMO are characterized by the XLD^- parameters, hence, related to XLD_{acc} . In order to account for the negative value of the orbital polarization a set of parameters related to a preferential out-of-plane occupancy of the Mn 3d orbitals were used as expected from the crystal field theory (see, for example, Fig. 6.1). The best agreement between the experimental XLD_{depl} and its integral (see, for example, the orange solid line in Fig. 6.7b) is obtained if the interfacial unit cells contribute by 45 % to the total XLD_{depl} . As already anticipated, the interfacial unit cells are characterized by positive splitting parameters (denoted as XLD^+): $\Delta t_{2g} = +0.5$ eV and

$\Delta e_g = +0.05$ eV. For the related energy diagram sketch see, for example, the bottom panel of Fig. 6.8b. A simple linear combination (a small energy shift was also considered for the simulated spectrum in accumulation in order to account for the electrostatic doping effect) of the simulated spectra obtained using a set of parameters accounting for a preferential out-of-plane, i.e. XLD^+ , and in-plane, i.e. XLD^- , orbital occupancy rendered a quite satisfactory XLD_{depl} spectrum along with its integral, as shown in Figure 6.8b (upper pannel). Precisely, the simple linear combination $XLD_{depl} = 0.45 \cdot XLD^+ + 0.55 \cdot XLD^-$, was used in order to obtain the best fitting possible. Interestingly, also the calculated integral of the simulated XLD_{depl} spectrum returned the expected positive value, hence, confirming the reliable possibility to induce, upon the P -reversal, a change in the level hierarchy of the Mn $3d$ orbitals. Keeping this in mind and by considering the orbital polarization obtained in accumulation and depletion π_{orb}^{acc} and π_{orb}^{depl} , respectively, the following relations are valid:

$$\begin{aligned}\pi_{orb}^{acc} &= \left(\pi_{orb}^{XLD^-}\right)_{interfacial} = \left(\pi_{orb}^{XLD^-}\right)_{top-most} \\ \pi_{orb}^{depl} &= 0.45 \cdot \left(\pi_{orb}^{XLD^+}\right)_{interfacial} + 0.55 \cdot \left(\pi_{orb}^{XLD^-}\right)_{top-most}.\end{aligned}\tag{6.2}$$

By using the values obtained from the experimental XLD data, i.e. $\pi_{orb}^{acc} = +1.2\%$ and $\pi_{orb}^{depl} = -0.5\%$, the calculated interfacial orbital polarization in depletion (i.e. $(\pi_{orb}^{XLD^+})_{interfacial}$) is $\sim -2.6\%$. Hence, as a result, upon the P -switching which is found to affect 45% of the LSMO thickness, the orbital polarization from the value of +1.2% in accumulation (preferential in-plane occupancy of the orbitals), changes to the value of $\sim -2.6\%$ in depletion (preferential out-of-plane occupancy of the interfacial orbitals). Since in accumulation for the entire thickness value of the LSMO, as the main orbital occupancy the one related to a positive orbital polarization was considered, in depletion the 45% of the total LSMO thickness, i.e. 2.7 nm, needs to be considered as the active interfacial layer where the orbital polarization modulation takes place.

In order to justify the choice done for the depletion state to use a set of parameters i.e. XLD^+ , which provide a preferential out-of-plane orbital occupancy, the examination of a possible P -dependent structural distortion of the interfacial MnO_6 octahedra is necessary. First-principles calculations carried out by Pruneda *et al.* [85] have shown a significant electrostatic sensitivity of manganite thin films to exhibit a surface structural distortion. Precisely, at the film surface, a ferroelastic instability of the Mn-O bond was proposed together with a possible off-centering of the Mn ions from the oxygen cage. As a result, it can be concluded that manganite thin films grown in proximity to a ferroelectric material can exhibit a sensitivity to the ferroelectric distortions, which on the other hand can be "transferred" to the first few unit cells of the adjacent manganite thin film. Hence, a plausible explanation of the XLD simulations can be proposed by enabling the possibility that the PZT ferroelectric distortions (related to the two possible polarization directions) at the interface with the LSMO thin film are substantially capable to alter the Mn-O bond angle/distance as shown in the schematic view of the lower pannel of Figure 6.8a,b (see precisely the shaded area), along with the modification of the c/a ratio related to the interfacial oxygen octahedron of the LSMO unit cells. This model has been derived from the results of an ab-initio calculation, which has been already presented in the previous chapter (work done by H. Chen and co-workers [134]). As a result, the Mn ions undergo a shift induced by the polarization charges of the ferroelectric oxide and, consequentially, a tuning of the orbital anisotropy of the $3d$ Mn states can be achieved. Regarding the depletion state (i.e. interfacial positive polarization charges), the oxygen ions forming the octahedral cage surrounding the Mn ions, having a net negative charge, undergo a displacement toward the

ferroelectric/manganite interface. As a result, the LSMO c/a ratio increases and a preferential occupancy of the Mn $3d$ z^2 orbitals, with respect to the counterpart $3d$ $x^2 - y^2$ orbitals, is favored. On the other side, the opposite situation is realized in the accumulation state. In this case, the interfacial negative polarization charges act as "pushing" away the oxygen ions of the LSMO from the interface, resulting in a decrease of the c/a ratio. Hence, the oxygen octahedra, surrounding the Mn ions, shrink in the c -direction and the occupancy of the $3d$ $x^2 - y^2$ orbitals is now stabilized. The Mn ions move in the respective unit cells in a non-symmetric way, hence, not as expected by a standard JT-effect. Accordingly, the model provides a clear picture of the bending related to the MnO_2 planes (the two sketches shown in the lower pannel of Fig. 6.8a,b for both the accumulation and depletion states highlight, indeed, the bending of the MnO_2 planes). Hence, the model provides circumstances according to which the alteration of the hybridization energy of the LSMO/PZT system can be envisaged as well. In this framework also XAS spectra acquired at the O K -edge were necessary to get important information.

6.2.2 XAS at the O K -edge

In the previous section the simulated XLD spectra obtained to match at best the experimental data provided a clear variation of the Δ_{CT} parameter. The latter decreased from the value of 4 eV in accumulation to 3 eV in depletion. The variation of Δ_{CT} clearly suggests that the P -

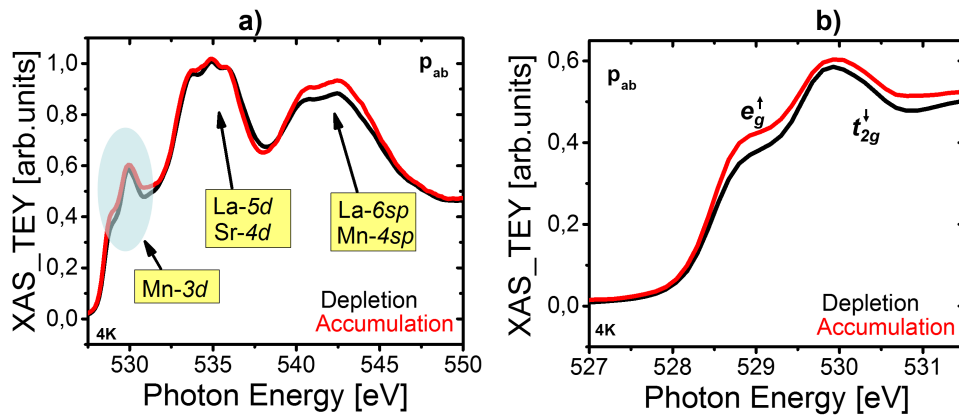


Figure 6.9: a) O K -edge XAS spectra acquired at the temperature of 4 K for light polarized in-plane and for both accumulation and depletion states of the FeFED. Highlighted in azure is the pre-edge structure which stems from the contribution of the Mn $3d$ character band. In b) the latter is suitably magnified in order to better visualize the shift in the absorption edge.

reversal affects the hybridization level between the Mn $3d$ and O $2p$ orbitals. This finding, of course, affects the shape of the XLD spectra as well. In order to be consistent and demonstrate the (partially) covalent nature of the Mn-O bonds, XAS spectra at the O K -edge were measured as well. Practically, in the latter case the transitions from the oxygen core $1s$ to the unoccupied O $2p$ levels are recorded. XAS at the O K -edge are also used to obtain information regarding the empty levels just above the Fermi level which are formed as a result of the hybridization process [145]. Figure 6.9a shows the XAS spectra at the O K -edge for both accumulation and depletion states acquired at the temperature of 4 K for light polarized in-plane (i.e. p_{ab}). The spectra are normalized to the peak height at approximately 533.6 eV after the subtraction of the background signal. The XAS spectra show three main features indicated in Figure 6.9a by arrows. Those features have been described by Abbate and co-workers [144] as stemming from the hybridization process with different empty Mn orbitals. Accordingly, the structure

recorded around the energy values of ~ 535 and ~ 543 eV are attributed to bands of La-5*d*, Sr-4*d* and La-6*sp*, Mn-4*sp* character, respectively. On the other hand, the feature centered at ~ 530 eV and highlighted in Figure 6.9a, is attributed to the overlapping t_{2g} and e_g bands of Mn 3*d* character, from which the important information related to the hybridized O 2*p*-Mn 3*d* states can be accessed. The latter is commonly addressed as "pre-edge structure". The changes observed upon the *P*-reversal regarding the two broad peaks recorded at the energy values of ~ 535 and ~ 543 eV are less important for the main topic addressed in this Thesis and for this reason will not be discussed further. On the other hand, it is of primary importance here to focus on the pre-edge structure of which the observed modulation can be strictly related to the accumulation and depletion states of the FeFED. In this respect Figure 6.9b shows the zoom of the pre-edge structure. The peak centered around the energy value of ~ 530 eV corresponds as already mentioned above, to the orbital overlapping between the Mn 3*d* and the O 2*p* states. Interestingly, the overall magnitude in accumulation is higher than the value obtained in depletion. This finding gave the possibility to have another measure of the Mn 3*d* orbital occupancy. Indeed, the higher magnitude recorded in accumulation reveals a higher number of empty states, hence, a lower occupancy of the Mn 3*d* orbitals. As a result, the value of

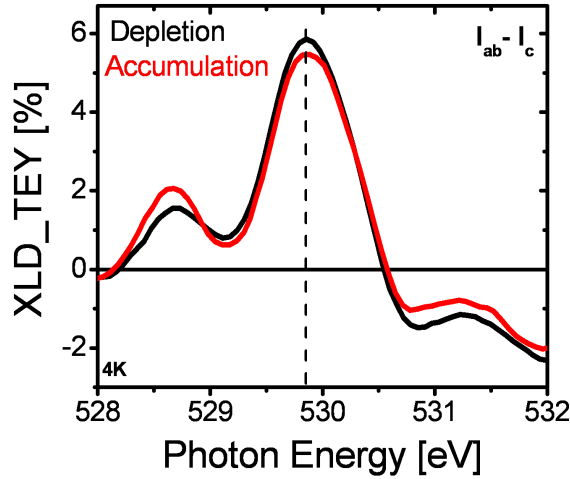


Figure 6.10: XLD spectrum calculated from XAS acquired at the O *K*-edge at the temperature of 4 K for both accumulation and depletion states of the FeFED.

Mn valence increases as, on the other hand, expected in accumulation state. Additionally, by a close inspection of Figure 6.9b, the pre-edge structure can be attributed to a more plausible overlap of two different peaks. XAS spectra acquired at the O *K*-edge of manganites have been already extensively investigated [146] but, up to date, a clear picture of a reliable doublet nature of the pre-edge structure is still missing. However, according to the work of Aruta and co-workers [145], the relevant Mn 3*d* orbitals involved in the pre-edge structure are attributed to the hybridization with the majority spin e_g (i.e. e_g^\uparrow) and to the minority spin t_{2g} (i.e. t_{2g}^\downarrow) as indicated in Figure 6.9b. Besides these considerations, what is important to note here is related to the energy shift towards a low energy region of the absorption edge in the accumulation state. This finding demonstrates that the Fermi level of the system moves toward a lower energy region, and subsequently an increase of the number of holes in the conduction band is obtained, confirming the already reported results related to a static variation of the doping level [144] and the (magneto)transport measurements on different FeFEDs introduced and discussed in the previous chapter. To conclude, it is noteworthy to consider also the presence of dichroism in the O *K*-edge XAS signals which is valuable in determining the local symmetry of the Mn empty states just above E_F . Indeed, it has been shown by Wu and co-workers [147]

that the linear dichroism calculated at the O K -edge at the energy value of ~ 530 eV can give important information regarding the orbital polarization of the unoccupied e_g states just above E_F . Along this direction Aruta and co-workers [145] have reported that a positive peak of the calculated XLD spectra at the O K -edge of a LSMO($x=0.3$) thin film, grown on a LAO substrate, is indicative of an out-of-plane preferential orbital occupancy (i.e. $3d z^2$). On the other hand, a negative peak is found in the case of a LSMO($x=0.3$) thin film grown onto a STO substrate where a preferential in-plane occupancy is achieved (i.e. $3d x^2 - y^2$). In this respect, Figure 6.10 shows the XLD spectrum calculated from the XAS spectra acquired at the O K -edge (i.e. $I_{ab}-I_c$). The remarkable modulation related to the magnitude of the peak centered at ~ 530 eV marks a change in the hybridization level between the out-of-plane and in-plane direction. Relevantly it can be noticed that the amplitude value obtained in depletion is higher than the value obtained in accumulation. From a bare speculation point if the aforementioned findings of Aruta and co-workers can be straightforwardly adopted in the case of the XLD spectra shown in Figure 6.10, a higher preferential out-of-plane occupancy of the Mn e_g orbitals can be concluded for a more positive peak centered around the energy value of ~ 530 eV. Actually, this indirect observation fits completely with the general view of the FeFED in depletion proposed and demonstrated in the previous section of this Thesis. Hence, also from XAS acquired at the O K -edge it can be guessed that the investigated FeFED exhibits upon the reversal of the polarization direction a subtle trend base on which a modulation of the Mn $3d$ orbital occupancy is achieved parallel to a change of the hybridization energy.

6.3 XMCD measurements for the LSMO/PZT/LSMO/STO FeFED

XMCD spectra were also considered in order to get important information regarding the possibility to measure a modulation of the magnetization value upon the polarization switching of the studied FeFED. All the presented spectra were acquired at the temperature of 4 K, and the externally applied magnetic field, when present, was oriented along the in-plane direction. Figure 6.11 shows XMCD spectra acquired for the accumulation and depletion states, respec-

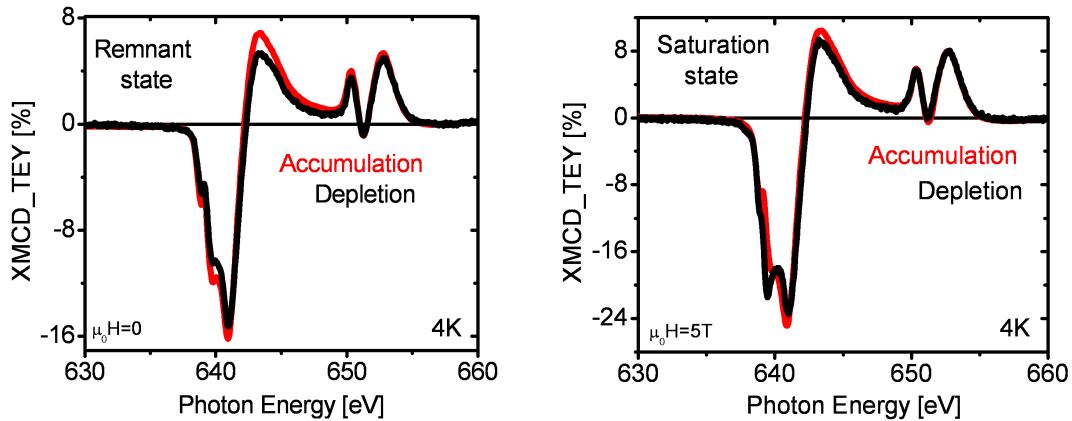


Figure 6.11: XMCD spectra acquired at 4 K for both accumulation and depletion states. In the left (right) the XMCD for $\mu_0H = 0$ ($\mu_0H = 5$ T) is shown.

tively. The two graphs are related to the remnant ($\mu_0H = 0$) and saturation ($\mu_0H = 5$ T) states, respectively. Clearly, a change regarding the amplitude and shape of the spectra as a function of P , can be easily envisaged. In order to obtain quantitative information from the presented spectra, the application of the sum rules (2.3) is necessary. Accordingly, Figures 6.12 and 6.13 depict the results of the analysis carried out for the calculated XMCD spectra in the remnant and saturation states, respectively. In the upper part of the two figures the XAS spectrum is

depicted resulting from the sum of the two x-ray absorption processes performed with *CR* and *CL* polarized light, respectively. Accordingly, the parameter r is also plotted and the value

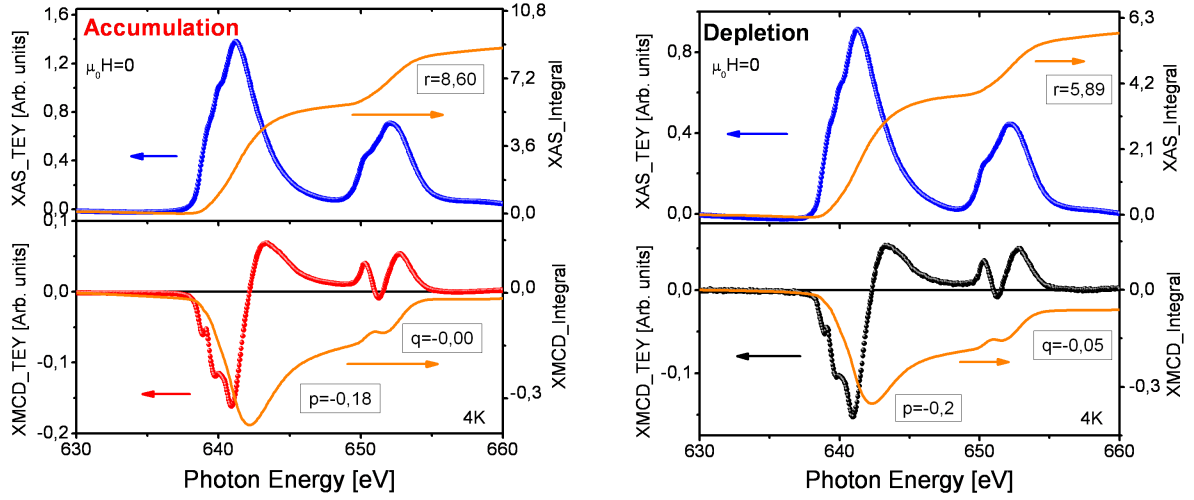


Figure 6.12: Application of the sum rules (see, for example, Eq. 2.3) to the XMCD spectra acquired with $\mu_0 H = 0$ for both the accumulation and depletion states of the FeFED.

at the highest photon energy was used for the sum rule calculation. On the other side, in the lower part of the figures the sum rule is applied directly to the XMCD from which the two parameters, p and q were obtained. Precisely, p was calculated taking the value of the XMCD integral around the separation energy between the two multiplet structures, i.e. around 647 eV, and q going to the highest possible energies. As already highlighted in the section 2.3.2, in order to obtain only the spin moment m_{spin} , from the calculated effective spin moment, i.e. m_{spin}^{eff} , a correction factor is required to take into account the presence of the quadrupole moment (i.e. $\langle T_z \rangle$). Along this direction, a correction factor of 50 %, as tabulated in [148], was

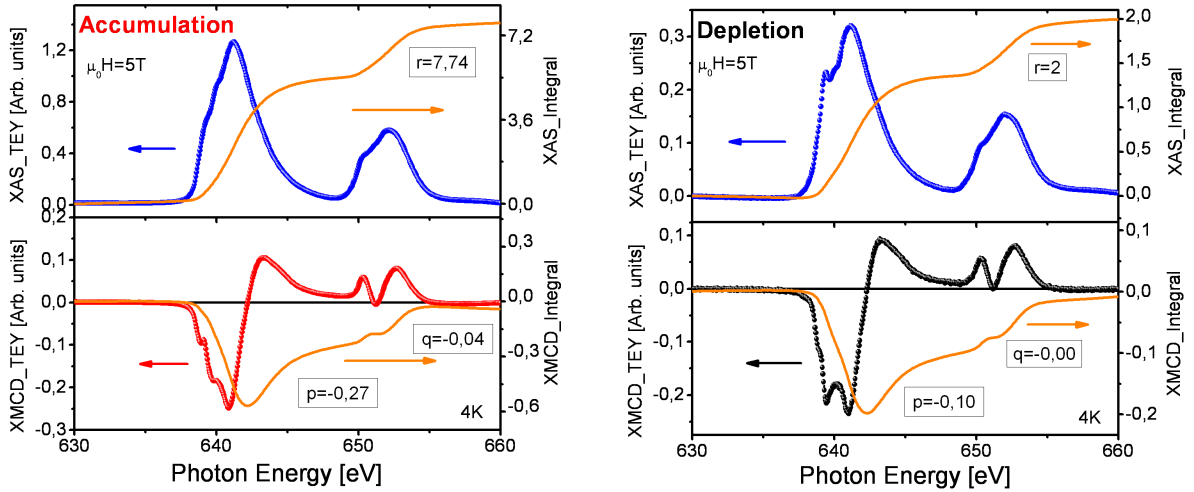


Figure 6.13: Application of the sum rules (2.3) to the XMCD spectra acquired with $H = 5$ T for both the accumulation and depletion states of the FeFED.

used to adjust the calculated effective spin moments. Accordingly, Table 6.1 lists the results obtained from the application of the sum rules for the orbital, effective spin and total spin moment, respectively. At $\mu_0 H = 5$ T, effective spin moments of $1.48 \mu_B/\text{Mn}$ and of $1.8 \mu_B/\text{Mn}$ were obtained from the application of the sum rules to the accumulation and depletion state,

Table 6.1: m_{orb} , m_{spin}^{eff} and m_{spin} values as obtained from the application of the sum rules to the XMCD spectra acquired at 4 K in grazing incidence conditions (H applied parallel to the device plane), for both accumulation and depletion states.

	Depletion $\mu_0 H = 0$	Depletion $\mu_0 H = 5 \text{ T}$	Accumulation $H \mu_0 = 0$	Accumulation $\mu_0 H = 5 \text{ T}$
$m_{orb} [\mu_B/\text{Mn}]$	< 0.005	< 0.005	0.015	0.045
$m_{spin}^{eff} [\mu_B/\text{Mn}]$	1.03	1.8	0.75	1.49
$m_{spin} [\mu_B/\text{Mn}]$	2.06	3.6	1.5	2.98

respectively. Regarding the orbital moments, very small values were obtained, i.e. 0.045 and < 0.005 μ_B/Mn for the accumulation and depletion state, respectively. The latter result, actually, is the one expected due to the quenching of the orbital moment by the crystal field of the perovskite structure. Finally, the effective spin moments, calculated for the remanent state (i.e. with $\mu_0 H = 0$), decrease to the values of 0.75 μ_B/Mn and 1.03 μ_B/Mn for the accumulation and depletion state, respectively.

As a close inspection of the calculated spin moments shows, the values related to the accumulation and depletion states, scale as expected from the *in-situ* magnetometer measurements presented in the previous chapter, see section 5.2. Indeed, according to the formula $M \approx (4-x) \mu_B$, where x is the hole doping of the system (see [80]), a decrease of the doping level (electrostatically achieved in this Thesis), is accompanied always by an increase of the magnetization value at very low temperatures.

6.4 Conclusion

The main result of this chapter is displayed in Figure 6.7, where, the XLD spectra acquired at the Mn $L_{2,3}$ -edges as a function of the P direction are shown. The XAS spectra were obtained in a grazing incidence geometry while keeping the FeFED at 300 K for both the accumulation and depletion states. Along with the XLD spectra also the related integral curves are plotted in Figure 6.7 as well. Besides the clear modulation of the shape of the spectra upon the P -switching, the normalized integral values, i.e. D_L , exhibit a complete reversal of their sign. According to the sum rule of Eq. 2.2 the latter finding indicates that upon the P -switching the electrostatically gated LSMO layer undergoes a variation of the Mn $3d$ orbital occupancy. Additionally, atomic multiplet calculations carried out in order to get more insight clearly confirmed that the aforementioned modulation of the Mn $3d$ orbital polarization as defined in Eq. 6.1 is attributed to the 45 % of the overall LSMO unit cells. Interestingly, the P -reversal seems to influence the orbital polarization of the LSMO in an overall thickness of ~ 2.7 nm well beyond the expected -and normally reported in the literature- value of a few Angstroms (i.e. Thomas-Fermi derivation of the screening length). The parameters obtained from the simulation procedure are summarized in Table 6.2, where also the percentage value used to properly fit both XLD spectra of Figure 6.8 are reported.

Table 6.2: Results of the atomic multiplet calculations undertaken using the CTM4XAS scientific package.

	$\Delta t_{2g} [\text{eV}]$	$\Delta e_g [\text{eV}]$	$\Delta_{CT} [\text{eV}]$	XLD ^{acc}	XLD ^{depl}
XLD ⁻	-0.15	-0.55	4	100%	55%
XLD ⁺	+0.05	+0.5	3	0%	45%

As a result, a noticeable preferential occupancy of the out-of-plane orbitals of the Mn $3d$ levels in depletion can be envisaged as suggested by the electrostatic model proposed by Chen

and co-worker and here re-adopted to ensure a plausible explanation of the XAS data. The modulation of the charge transfer energy parameter, related to a change of the hybridization energy upon the P -switching, was also confirmed through XAS measurements at the O K -edge. Interestingly, as displayed in Figure 6.9b the shift toward lower energy values of the absorption edge confirmed an increase of the Mn valence state in accumulation. Moreover, regarding the XMCD analysis, the expected trend from the magnetization values upon P -reversal is also acceptably reproduced, i.e. in depletion a value of the magnetization higher than the one obtained in accumulation at the temperature of 4 K was calculated (see, for example, the Table 6.1).

*Non sol é degno di onore quell'uno ch'ha meritato il palio:
ma ancor quello e quel altro, ch'ha si ben corso, ch'è giudicato anco degno e sufficiente de l'aver meritato, ben che non
l'abbia vinto.
Opere di Giordano Bruno*

*Not only is worthy of honor who reached the target:
but also who has properly worked, can be considered worthy of honor, although he did't achieve it.
English translation by myself*

Conclusions

The strongly correlated oxide $\text{La}_{1-x}\text{Sr}_x\text{MnO}_3$ exhibits, as a key characteristic, several competing electronic ground states. Accordingly, the strongly correlated system appears to be outstandingly sensitive to external stimuli. Eventually, that sensitivity is remarkably enhanced when the level of doping x , is chosen at the borderline between two different electronic phases. The latter argumentation motivated the choice to grow thin films of $\text{La}_{1-x}\text{Sr}_x\text{MnO}_3$ with $x=0.175$. Indeed, in this case the system is nominally lying at the border between the FM-I and the FM-M electronic phases. Moreover, the relatively high carrier density (of the order of $10^{21} \text{ holes} \cdot \text{cm}^{-3}$) corresponds, according to the Thomas-Fermi model, to an electronic screening length of a few angstroms. As a result, the field effect can only be effective at the interface, and in order to obtain a measurable influence on the functional properties of LSMO, ultrathin films need to be considered. This requirement was challenging, especially in the ferroelectric field effect approach, where an adjacent switchable $\text{PbZr}_{0.2}\text{Ti}_{0.8}\text{O}_3$ layer is necessary in order to obtain, in a reversible and remnant way, the field effect. Along this direction, a suitable AlO_x hard mask, patterned in a Hall bar geometry, was used in order to allow the *in-situ* pulsed laser deposition of the LSMO and PZT oxides, hence, excluding possible post-growth steps of wet and/or dry etching. In this way an atomically smooth interface between the two oxides was successfully ensured as EDX measurements clearly demonstrated. Indeed, in the spatial resolution limit of the TEM used for that characterization, no interdiffusion of any chemical elements was identified at the LSMO/PZT interface. In this work, hence, by using the ferroelectric field effect approach, the modulation of the (magneto)transport and magnetic properties of a 5 nm thin PZT-gated LSMO film was successfully obtained. Different misfit strain states were also studied, choosing STO, LAO and LSAT single crystals as templates for the growth of several FeFEDs, which, indeed, exhibited different (magneto)transport properties. For the FeFED engineered onto a STO substrate, the electric field generated by the polarization charges of the PZT layer induced an interfacial accumulation or depletion of holes in the underneath LSMO film producing a ρ^{depl} to ρ^{acc} ratio of ~ 1.6 at room temperature. Moreover, a shift of ~ 11 K in the T_C value upon the P -reversal was obtained from the temperature dependence of M , acquired by performing several *in-situ* SQUID magnetometer measurements. Additionally, at the temperature of 230 K a modulation of the magnetization value of $\sim 1.5 \mu\text{emu}$ (corresponding to $0.34 \mu_B/\text{Mn}$) was obtained as well.

A key result in this Thesis was achieved thanks to the self-designed out-of-plane AMR measurements. In this case H was allowed to rotate in a plane always perpendicular to J from the out-of-plane towards the in-plane direction (contrarily to what is normally reported in the literature where H rotates in the device plane). The latter was done with the aim to exploit a possible dependence of the well known interfacial orbital anisotropy exhibited by the LSMO layer on the reversal of the polarization direction. Interestingly, the normalized AMR ratio, i.e.

$(\rho_{\perp}^{out} - \rho_{\perp}^{in})/\rho_{H=0}$, exhibited a clear modulation between depletion and accumulation, which in turn was explained in terms of an electrostatic modulation of the surface magnetic anisotropy of the ultrathin LSMO layer. As a result, an electrostatic modulation of the occupancy of the interfacial Mn 3d orbitals was derived by using a model where feasible polar distortions of the interfacial unit cells of the electrostatically gated and/or strained LSMO layer were suggested. In order to get a better insight into the aforementioned orbital reconstructions at the LSMO/PZT interface, XLD measurements at the Mn $L_{2,3}$ -edges and at the O K -edge were performed as a function of the PZT polarization directions as well. In this case, due to the experimental limitations linked to a relatively small probing depth of the XAS measurements (in the soft range ~ 10 nm), the FeFEDs were engineered without hard mask but employing a wet etching procedure for the bottom and top LSMO layers. Most probably due to a deteriorated LSMO/PZT interface quality not all the devices were characterized by a proper retention time. However, in the limit of the polarization direction stability another key result of this Thesis is shown in Figure 6.7. The shape of the XLD spectrum acquired at the Mn $L_{2,3}$ -edges remarkably changes upon the P -reversal of the FeFED. Atomic multiplet simulations of the obtained XLD spectra gave also a quantitative picture of the modulation regarding the interfacial orbital polarization of the electrostatically gated LSMO layer. In accumulation state the best set of Δt_{2g} and Δe_g parameter values was found to be -0.15 and -0.55 eV, respectively. In depletion the simulation rendered the relevant value of 45% regarding the effective interfacial LSMO unit cells that undergo a clear orbital polarization modulation, and in this case the best set of Δt_{2g} and Δe_g parameter values was found to be +0.05 and +0.5 eV, respectively. Moreover, XAS measurements at the O K -edge confirmed the expected modulation of the hybridization energy of the system as well. In the ligand theory picture of the oxygen octahedra surrounding the Mn ions, a remarkable variation in the level hierarchy related to the Mn 3d levels is proposed. As a result, the modulation of the splitting energy parameters were, hence, explained as resulting from polar distortions induced by the P -reversal to the interfacial LSMO unit cells. The latter possibility was introduced by Chen and co-workers [134] who performed *ab-initio* calculations that provided a ionic model which then was successfully re-adapted here. This model was, indeed, a valid playground to explain also the results obtained from the out-of-plane AMR measurements, where in depletion a more "stable" $3d_{z^2}$ orbital occupancy was envisaged. In this context both the (magneto)transport and spectroscopy studies undertaken for the FeFEDs (at least for the one grown onto a STO substrate), revealed the great perspective of the ferroelectric field effect to tailor the orbital occupancy of TMOs such as LSMO. As a further step in the understanding of the aforementioned possibility, a suitable STM study of LSMO/PZT/LSMO heterostructures would be capable to enrich the rather new topic that nowadays is addressed as *orbitronics* [149].

Bibliography

- [1] J. Heber, *Nature* **459**(7243), 28 (2009).
- [2] P. Zubko, S. Gariglio, M. Gabay, P. Ghosez, J.-M. Triscone **2**, 141 (2011).
- [3] P. Yu, Y.-H. Chu, R. Ramesh, *Materials Today* **15**(7-8), 320 (2012).
- [4] H. Y. Hwang, et al., *Nature Materials* **11**(2), 103 (2012).
- [5] C. Mix, S. Finizio, M. Klauui, G. Jakob, *Applied Physics Letters* **104**(26) (2014).
- [6] C. Zhou, D. Newns, J. Misewich, P. Pattnaik, *Applied Physics Letters* **70**(5), 598 (1997).
- [7] J. Coey, M. Viret, S. von Molnar, *Advances in Physics* **48**(2), 167 (1999).
- [8] Y. Tokura, Y. Tomioka, *Journal of Magnetism and Magnetic Materials* **200**(1-3), 1 (1999).
- [9] K. Dörr, *Journal of Physics D* **39**(7), R125 (2006).
- [10] K. Dörr, *Ferromagnetic manganites: spin-polarized conduction and competing interactions*, Habilitationsschrift. Technische Universität Dresden (2006).
- [11] E. Dagotto, T. Hotta, A. Moreo, *Physics Reports* **344**(1-3), 1 (2001).
- [12] K. Chahara, T. Ohno, M. Kasai, Y. Kozono, *Applied Physics Letters* **63**, 1990 (1993).
- [13] M. Egilmez, K. H. Chow, J. A. Jung, *Modern Physics Letters B* **25**(10), 697 (2011).
- [14] E. Dagotto, *Science* **309**(5732), 257 (2005).
- [15] G. H. Jonker, J. H. V. Santen, *Physica* **16**, 337 (1950).
- [16] V. Goldschmidt, *Naturwissenschaften* **14**, 477 (1926).
- [17] J. Rondinelli, S. May, J. Freeland, *MRS Bulletin* **37**(3), 261 (2012).
- [18] Y. Tokura, A. Urushibara, Y. Moritomo, T. Arima, A. Asamitsu, *Journal of the Physical Society of Japan* **63**(11), 3931 (1994).
- [19] A. Urushibara, et al., *Physical Review B* **51**, 14103 (1995).
- [20] A. Asamitsu, Y. Moritomo, Y. Tomioka, T. Arima, Y. Tokura, *Nature* **373**(6513), 407 (1995).

- [21] C. Zener, *Physical Reviews* **82**, 403 (1951).
- [22] H. Jahn, E. Teller, *Proceedings of the Royal Society of London* **161**(A905), 220 (1937).
- [23] A. J. Millis, P. Littlewood, B. Shraiman, *Physical Review Letters* **74**(25), 5144 (1995).
- [24] A. J. Millis, *Nature* **392**(6672), 147 (1998).
- [25] Y. Yamada, O. Hino, S. Nohdo, R. Kanao, T. Inami, *Physical Review Letters* **77**(5), 904 (1996).
- [26] J. Goodenough, *Magnetism and the chemical bond*, Interscience monographs on chemistry: Inorganic chemistry section. Interscience Publishers (1963).
- [27] J. Goodenough, *Physical Review* **100**(2), 564 (1955).
- [28] C. Rao, A. Cheetham, *Science* **276**(5314), 911 (1997).
- [29] G. Grosso, G. P. Parravicini, *Solid-State Physics*. Springer, Berlin (2000).
- [30] P. Anderson, *Physical Review* **79**(2), 350 (1950).
- [31] P. Anderson, H. Hasegawa, *Physical Review* **100**(2), 675 (1955).
- [32] A. Tebano, C. Aruta, P. G. Medaglia, F. Tozzi, G. Balestrino, *Physical Review B* **74**(24) (2006).
- [33] D. Schlom, L.-Q. Chen, C. Fennie, V. Gopalan, D. Muller, *MRS Bulletin* **39**(2), 118 (2014).
- [34] A. Sadoc, et al., *Physical Review Letters* **104**(4), 046804 (2010).
- [35] Y. Konishi, et al., *Journal of the Physical Society of Japan* **68**(12), 3790 (1999).
- [36] A. Tebano, et al., *Physical Review Letters* **100**(13), 137401 (2008).
- [37] P. K. Muduli, S. K. Bose, R. C. Budhani, *Journal of Physics* **19**(22) (2007).
- [38] R. D. Capua, C. A. Perroni, V. Cataudella, F. M. Granozio, P. Perna, *Journal of Physics* **18**(35), 8195 (2006).
- [39] S. Valencia, et al., *Journal of physics* **26**(16), 166001 (2014).
- [40] H. Kawano, R. Kajimoto, M. Kubota, H. Yoshizawa, *Physical Review B* **53**(22), 14709 (1996).
- [41] K. Rabe, C. Ahn, J. Triscone, *Physics of Ferroelectrics: A Modern Perspective*, Topics in Applied Physics. Springer, Berlin (2010).
- [42] C. Lu, et al., *Scientific Reports* **3**, 3374 (2013).
- [43] J. Joseph, T. Vimala, V. Sivasubramanian, V. Murthy, *Journal of Materials Science* **35**(6), 1571 (2000).
- [44] J. Frantti, J. Lappalainen, S. Eriksson, V. Lantto, S. Nishio, *Japanese Journal of Applied Physics* **39**(9B), 5697 (2000).
- [45] C.-L. Jia, et al., *Nature Materials* **7**(1), 57 (2008).
- [46] J. Junquera, P. Ghosez, *Nature* **422**(6931), 506 (2003).

- [47] D. Fong, et al., *Science* **304**(5677), 1650 (2004).
- [48] H. Lee, S. M. Nakhmanson, M. F. Chisholm, H. M. Christen, K. M. Rabe, *Physical Review Letters* **98**(21) (2007).
- [49] I. Vrejoiu, G. L. Rhun, L. Pintilie, D. Hesse, M. Alexe, *Advanced Materials* **18**(13), 1657 (2006).
- [50] J. Kanamori, A. Kotani, *Core-level spectroscopy in condensed systems: proceedings of the Tenth Taniguchi International Symposium, Kashikojima, Japan*, Springer series in solid-state sciences. Springer-Verlag, Berlin (1988).
- [51] M. Abbate, J. Goedkoop, F. D. Groot, M. Grioni, J. Fuggle, *Surface and Interface Analysis* **18**(1), 65 (1992).
- [52] F. de Groot, M. Arrio, P. Sainctavit, C. Cartier, C. Chen, *Solid State Communications* **92**(12), 991 (1994).
- [53] F. Baudelet, *X-ray Magnetic Circular Dichroism*. Springer Netherlands (2006).
- [54] J. Fuggle, J. Inglesfield, *Unoccupied electronic states: fundamentals for XANES, EELS, IPS and BIS*, Topics in Applied Physics. Springer, Berlin (1992).
- [55] H. Y. Hwang, S.-W. Cheong, N. P. Ong, B. Batlogg, *Physical Review Letters* **77**, 2041 (1996).
- [56] A. Tebano, A. Orsini, P. G. Medaglia, D. D. Castro, G. Balestrino, *Physical Review B* **82**(21) (2010).
- [57] D. Pesquera, et al., *Nature Communications* **3**, 1189 (2012).
- [58] J. Stohr, *Journal of Magnetism and Magnetic Materials* **200**(1-3), 470 (1999).
- [59] C. Chen, Y. Idzerda, H. Lin, N. Smith, G. Meigs, *Physical Review Letters* **75**(1), 152 (1995).
- [60] U. Fano, *Physical Review* **178**(1), 131 (1969).
- [61] M. D. Nunez-Regueiro, M. Altarelli, C. T. Chen, *Physical Review B* **51**(1), 629 (1995).
- [62] C. Piamonteze, P. Miedema, *Physical Review B* **80**(18) (2009).
- [63] B. Cullity, C. Graham, *Introduction to Magnetic Materials*. Wiley, New York City (2009).
- [64] L. Nel, *Journal de Physique et le Radium* **15**(12), 255 (1954).
- [65] E. C. Stoner, E. P. Wohlfarth, *IEEE Transactions on Magnetics* **27**(4), 3475 (1991).
- [66] M. Fiebig, *Journal of Physics D* **38**(8), R123 (2005).
- [67] D. Astrov, *Sov. Phys. JETP* **11**, 708 (1960).
- [68] G. Catalan, J. Scott, *Advanced Materials* **21**(24), 2463 (2009).
- [69] G. M. De-Luca, D. Preziosi, F. Chiarella, R. D. Capua, S. Gariglio, *Applied Physics Letters* **103**(6) (2013).
- [70] C. A. F. Vaz, J. Hoffman, C. Ahn, R. Ramesh, *Advanced Materials* **22**(26-27), 2900 (2010).

- [71] K. Sun, Y. Kim, *Journal of Physics D* **44**(18) (2011).
- [72] I. Vrejoiu, D. Preziosi, A. Morelli, E. Pippel, *Applied Physics Letters* **100**(10) (2012).
- [73] S. Stratulat, et al., *Nano Letters* **13**(8), 3884 (2013).
- [74] S. Mathews, R. Ramesh, T. Venkatesan, J. Benedetto, *Science* **276**(5310), 238 (1997).
- [75] N. Ashcroft, N. Mermin, *Solid State Physics*, HRW international editions. Holt, Rinehart and Winston, University of California (1976).
- [76] X. Hong, J. D. Hoffman, C. H. Ahn, Y. Bason, *Physical Review B* **74**(17) (2006).
- [77] C. Ahn, S. Gariglio, P. Paruch, T. Tybell, L. Antognazza, *Science* **284**(5417), 1152 (1999).
- [78] J. Hoffman, et al., *Advanced Materials* **22**(26-27), 2957 (2010).
- [79] C. A. F. Vaz, et al., *Physical Review Letters* **104**(12), 127202 (2010).
- [80] H. J. A. Molegraaf, J. Hoffman, S. Gariglio, *Advanced Materials* **21**(34), 3470 (2009).
- [81] J. D. Burton, E. Y. Tsymbal, *Physical Review B* **80**(17) (2009).
- [82] S. Dong, E. Dagotto, *Physical Review B* **88**(14) (2013).
- [83] S. Dong, X. Zhang, R. Yu, E. Dagotto, *Physical Review B* **84**(15) (2011).
- [84] M. Fechner, et al., *Physical Review B* **78**(21) (2008).
- [85] J. M. Pruneda, et al., *Physical Review Letters* **99**(22), 226101 (2007).
- [86] C.-G. Duan, S. S. Jaswal, E. Y. Tsymbal, *Physical Review Letters* **97**(4), 047201 (2006).
- [87] J. Rondinelli, M. Stengel, N. Spaldin, *Nature Nanotechnology* **3**(1), 46 (2008).
- [88] T. Venkatesan, D. C. Kundaliya, T. Wu, S. B. Ogale, *Philosophical Magazine Letters* **87**(3-4), 279 (2007).
- [89] R. Eason, *Pulsed Laser Deposition of Thin Films: Applications-Led Growth of Functional Materials*. Wiley, New York City (2007).
- [90] B. D. Cullity (1978).
- [91] G. Binnig, C. Quate, C. Gerber, *Physical Review Letters* **56**(9), 930 (1986).
- [92] J. Scott, *Ferroelectric Memories*. Springer, Berlin (2000).
- [93] aixACCT, *TF Analyzer Hysteresis Software Version 2.1* (2000).
- [94] Q. Design, *PPMS User's Manual* (2008).
- [95] P. Ohresser, et al., *Review of Scientific Instruments* **85**(1), 013106 (2014).
- [96] H. Boschker, et al., *Journal of Physics D* **44**(20), 205001 (2011).
- [97] M. Kawasaki, et al., *Science* **266**(5190), 1540 (1994).
- [98] C. de Rango, G. Tsoucaris, C. Zelwer, *Acta Crystallographica* **20**, 590 (1966).
- [99] T. Ohnishi, et al., *Applied Physics Letters* **74**(17), 2531 (1999).

- [100] J. Ngai, et al., *Advanced Materials* **22**(26-27), 2945 (2010).
- [101] S. Majumdar, S. van Dijken, *Journal of Physics D* **47**(3) (2014).
- [102] C. H. Ahn, J. Triscone, J. Mannhart, *Nature* **424**(6952), 1015 (2003).
- [103] D. Pesquera, X. Marti, V. Holy, R. Bachelet, G. Herranz, *Applied Physics Letters* **99**(22) (2011).
- [104] J. van der Pauw, *Philips Research Reports* **13**, 1 (1958).
- [105] J. Dho, N. H. Hur, I. S. Kim, Y. K. Park, *Journal of Applied Physics* **94**(12), 7670 (2003).
- [106] J. Song, T. Susaki, H. Hwang, *Advanced Materials* **20**(13), 2528 (2008).
- [107] T. Higuchi, T. Yajima, L. F. Kourkoutis, Y. Hikita, N. Nakagawa, *Applied Physics Letters* **95**(4) (2009).
- [108] A. Asamitsu, Y. Tokura, *Physical Review B* **58**(1), 47 (1998).
- [109] L. D. Partain, M. R. Lakshminarayana, C. R. Westgate, *Journal of Applied Physics* **48**(6), 2570 (1977).
- [110] C. Hurd, *The Hall Effect in Metals and Alloys*, International cryogenics monograph series. Springer (1972).
- [111] Korenivski, K. Rao, J. Colino, I. Schuller, *Physical Review B* **53**(18), 11938 (1996).
- [112] L. Pintilie, I. Vrejoiu, D. Hesse, M. Alexe, *Journal of Applied Physics* **104**(11) (2008).
- [113] M. Mathews, F. Postma, J. Lodder, R. Jansen, G. Rijnders, *Applied Physics Letters* **87**(24) (2005).
- [114] N. Banerjee, G. Koster, G. Rijnders, *Applied Physics Letters* **102**(14) (2013).
- [115] X. Hong, A. Posadas, C. H. Ahn, *Applied Physics Letters* **86**(14) (2005).
- [116] P. Leufke, R. Kruk, R. Brand, H. Hahn, *Physical Review B* **87**(9) (2013).
- [117] N. Mott, E. Davis, *Electronic Processes in Non-Crystalline Materials*. OUP Oxford (2012).
- [118] N. Bebenin, R. Zainullina, V. Mashkautsan, V. Ustinov, Y. Mukovskii, *Physical Review B* **69**(10) (2004).
- [119] E. Neifel'd, V. Arkhipov, N. Tumalevich, Y. Mukovskii, *JETP Letters* **74**(11), 556 (2001).
- [120] B. I. Shklovskii, A. L. Efros, *Electronic Properties of Doped Semiconductors*. Springer, Berlin (1984).
- [121] N. G. Bebenin, *Journal of Magnetism and Magnetic Materials* **324**(21), 3593 (2012).
- [122] M. Jaime, M. Salamon, M. Rubinstein, R. Treece, J. Horwitz, *Physical Review B* **54**(17), 11914 (1996).
- [123] M. Salamon, M. Jaime, *Reviews of Modern Physics* **73**(3), 583 (2001).
- [124] J. Eckstein, I. Bozovic, J. O'Donnell, M. Onellion, M. Ryzhowski, *Applied Physics Letters* **69**(9), 1312 (1996).

- [125] S. Jin, et al., *Science* **264**(5157), 413 (1994).
- [126] A. Gupta, J. Sun, *Journal of Magnetism and Magnetic Materials* **200**(1-3), 24 (1999).
- [127] W. Thomson, *Proceedings of the Royal Society* (8), 546 (1857).
- [128] E. D. Ranieri, A. W. Rushforth, K. Vyborny, U. Rana, E. Ahmad, *New Journal of Physics* **10** (2008).
- [129] R.-W. Li, H. Wang, X. Wang, X. Z. Yu, Y. Matsui, *Proceedings of the National Academy of Sciences of the United States of America* **106**(34), 14224 (2009).
- [130] J. D. Fuhr, M. Granada, L. B. Steren, B. Alascio, *Journal of Physics* **22**(14), 146001 (2010).
- [131] T. McGuire, R. Potter, *IEEE Transactions on Magnetics* **11**(4), 1018 (1975).
- [132] H. Lu, T. A. George, Y. Wang, I. Ketsman, J. D. Burton, *Applied Physics Letters* **100**(23) (2012).
- [133] K. Kyuno, J. Ha, R. Yamamoto, S. Asano, *Journal of the Physical Society of Japan* **65**(5), 1334 (1996).
- [134] H. Chen, et al., *Nano Letters* **14**(9), 4965 (2014).
- [135] C. Dallera, *Resonant Spectroscopies with Synchrotron Radiation*, Cours du Troisième Cycle. Ecole Polytechnique Fédérale de Lausanne (2003).
- [136] M. Salluzzo, *Electron and X-ray spectroscopy*, PhD course. University of Naples "Federico II" (2010).
- [137] E. Stavitski, F. M. F. de Groot, *Micron* **41**(7), 687 (2010).
- [138] F. de Groot, *Journal of Electron Spectroscopy and Related Phenomena* **62**(1-2), 111 (1993).
- [139] D. Yi, et al., *Physical Review Letters* **111**(12), 127601 (2013).
- [140] S. A. Pauli, et al., *Physical Review Letters* **106**(3), 036101 (2011).
- [141] M. Salluzzo, et al., *Physical Review Letters* **102**(16), 166804 (2009).
- [142] F. de Groot, J. Fuggle, B. Thole, G. Sawatzky, *Physical Review B* **42**(9), 5459 (1990).
- [143] F. de Groot, J. Fuggle, B. Thole, G. Sawatzky, *Physical Review B* **41**(2), 928 (1990).
- [144] M. Abbate, et al., *Physical Review B* **46**, 4511 (1992).
- [145] C. Aruta, G. Ghiringhelli, A. Tebano, N. Boggio, N. Brookes, *Physical Review B* **73**(23) (2006).
- [146] F. M. F. de Groot, et al., *Physical Review B* **40**, 5715 (1989).
- [147] W. Wu, D. Huang, G. Guo, H. Lin, T. Hou, *Journal of Electron Spectroscopy and Related Phenomena* **137**, 641 (2004).
- [148] C. Piamonteze, P. Miedema, F. M. F. de Groot, *Physical Review B* **80**, 184410 (2009).
- [149] Y. Tokura, N. Nagaosa, *Science* **288**(5465), 462 (2000).

Curriculum vitæ et studiorum

CONTACT INFORMATION

First Name Daniele

Last Name Preziosi

Telephone (Office) +49 (345) 5582 621

E-mail preziosi@mpi-halle.de

PERSONAL INFORMATION

Place and Date of Birth Avellino (Italy), 27 August 1983

Citizenship Italian

Sex Male

Marital status Married

EDUCATION

August 2011-To Now PhD position at the Max Planck Institute of Halle (Saale) Germany:
Group of Nanoengineering of functional Oxides. Supervisor: Prof. Dr. Dietrich Hesse.

March 2010 Master Degree in Physics at the University "Federico II" of Naples. Title of the thesis "Growth and characterization of multiferroics thin film of BiMnO₃". Supervisors Prof. R. Vaglio and Dr. M. Salluzzo. Grade 110/110 Cum Laude.

June 2007 Bachelor Degree in Physics at the University "Federico II" of Naples. Title of the thesis "Rilassamento di spin in Quantum Dots". Supervisor A. Tagliacozzo. Grade 110/110.

July 2002 High-School Diploma at the Technical Institute "E.Majorana" of Grottaminarda (AV) as "Electronic and Telecommunication Expert". Grade 100/100.

EMPLOYMENT HISTORY

December 2010-July 2011 Fixed-term contract at the "Nucleco s.p.a." (Roma): Radiological characterization of radioactive waste of low and medium intensity.

April 2010-July 2010 Fixed-term contract at the University of Naples "Federico II": Improvement of thin film deposition for hybrid electronics.

SCHOOLS ATTENDED

02-14 September 2013 International School of Oxide Electronics 2013 (ISOE13) Cargèse, Corsica (France).

29 July-03 August 2012 IFOX Summer School 2012 Hesselberg, Bayern, Germany.

29 January-03 February 2012 European School on Multiferroics 2012 (ESMF2012), ETH Winter School, CSF Monte Verit, Switzerland.

26 September-01 October 2010 European School on Multiferroics 2010 (ESMF2010), University of L'Aquila, Italy.

16-23 May 2009 School on Superconductors and Functional Oxides (NANOXIDE), Lido Paradiso, Marina di Pisciotta, Palinuro Italy.

VISITING STUDENT POSITION

03 September-28 October 2012 ICMAB-Barcelona, Spain, Supervisor Prof. Josep Fontcuberta.

TALKS

21-25 April 2014 Magnetotransport measurements on $\text{La}_{0.825}\text{Sr}_{0.175}\text{MnO}_3/\text{PbZr}_{0.2}\text{Ti}_{0.8}\text{O}_3$ heterostructures. MRS 2014 Spring Meeting, San Francisco, USA.

26-30 May 2013 Field effect in strongly correlated materials induced by ferroelectric polarization. E-MRS 2013, Strasbourg, France.

10-15 March 2013 Charge-mediated magnetoelectric coupling in patterned multiferroic heterostructures. DPG 2013, Regensburg, Germany.

PUBLICATIONS

1. I. Vrejoiu, **D. Preziosi**, A. Morelli and E. Pippel, "Multiferroic $\text{PbZr}_x\text{Ti}_{1-x}\text{O}_3/\text{Fe}_3\text{O}_4$ epitaxial sub-micron sized structures", Applied Physics Letters 100(10) (2012).
2. A. G. Boni, I. Pintilie, L. Pintilie, **D. Preziosi**, H. Deniz and M. Alexe, "Electronic transport in (La,Sr)MnO₃-ferroelectric-(La,Sr)MnO₃ epitaxial structures", Journal of Applied Physics 113(22) (2013).

3. G. M. De Luca, **D. Preziosi**, F. Chiarella, R. D. Capua, S. Gariglio, S. Lettieri and M. Salluzzo, "Ferromagnetism and ferroelectricity in epitaxial BiMnO₃ ultra-thin films", *Applied Physics Letters* 103(6) (2013).
4. C. Lu, A. Quindeau, H. Deniz, **D. Preziosi**, D. Hesse and M. Alexe, "Crossover of conduction mechanism in Sr₂IrO₄ epitaxial thin films", *Applied Physics Letter* 105, 082407 (2014).
5. **D. Preziosi**, X. Marti, I. Fina, F. Bern, M. Ziese, E. Pippel, D. Hesse and M. Alexe, "Tailoring the interfacial magnetic anisotropy in multiferroic field effect devices", *Physical Review B* 90, 125155 (2014).
6. I. P. Krug, H. Doganay, F. Nickel, D. Gottlob, C.M. Schneider, A. Morelli, **D. Preziosi**, I. Vrejoiu, R. Laskowski and N. Barrett, "Interface-mediated ferroelectric internal bias and valence states in nano-structured PbTiO₃/La_{0.7}Sr_{0.3}MnO₃". In Press for *Journal of Applied Physics*.
7. C. Lu, S. Dong, A. Quindeau, **D. Preziosi**, N. Hu and M. Alexe, "Dual gate-control of bulk transport and magnetism in the spin-orbit insulator Sr₂IrO₄". Under review for *Physical Review X* (October 2014).
8. **D. Preziosi**, M. Alexe, D. Hesse and M. Salluzzo, "Electric-field control of the orbital occupancy and magnetic moment of a transition metal oxide". Submitted to *Physical Review Letters* (November 2014).
9. H. Deniz, **D. Preziosi**, C. Eisenschmidt, G. Schmidt, D. Hesse and M. Alexe, "Chemistry of parasitic phases in Sr₂FeMoO₆ thin films grown on SrTiO₃ substrates under non-optimized Argon pressure". Under preparation

Acknowledgement

The first thanks go to my academic supervisors Prof. Dietrich Hesse and Prof. Marin Alexe who gave me the possibility to continue my PhD at the Max Planck Institute of Halle when my stay here became uncertain. They kindly received me and helped me with all my request. Especially I appreciate the careful and the constant guidance that Prof. Hesse gave me along the entire PhD period. I will never forget the eclectic conversations that occasionally I had with him at our coffee/tea table. Marin is a smart researcher who, in attempting to answer my several questions, basically introduced me to the world of ferroelectric materials. He taught me that (material) science is done principally in the lab where the only driving force is represented by a focused curiosity.

I would like also to express my special thanks to Prof. Josep Fontcuberta who introduced me to the world of AMR measurements. I really appreciated the friendly atmosphere experienced at the ICMAB during my stay in Barcelona with all the people working in the community of oxide materials.

I'm really thankful to Prof. Michael Ziese and Francis Bern for the interest they put on my research topic and especially for the successful *in-situ* SQUID measurements.

I want also to thank some of the persons that I met in occasion of the IFOX meetings: Dr. Daniele Pullini and Prof. Lucian Pintilie; I will always remember with pleasure the several discussions that we had drinking a good wine or whisky.

A special thank to Dr. Marco Salluzzo who in an extraordinary way helped me to carry out the XAS measurements at the Soleil synchrotron facility. He taught me everything I know about that kind of physical characterizations. Basically without his help the last chapter of this Thesis would have never been written.

Thanks are due, of course, also to my colleagues of MPI with whom I shared many and different experiences. They have been positively contributing to my new life in Halle. Hence, thanks to Akash, Hakan, Simon, Ignasi&Xavi (the Cooper pair), Flora, Geanina, Dr. Lu(1), Dr. Lu(2), Andy, Florian, Daniel, Ayan, Dr. Kim, Alessio and Stratulat. How can I not mention Norbert? With his brilliant ability he repaired everything in the PLD lab and my thanks also go to Sven Holger who always treated my parcel professionally and kindly brought them in my office.

While I'm writing my thoughts go also to other people, for example my football friends like Roman, Jim, Augusto, Roland, Alex, Haider, Christoff, Vasyl, and many many others whom I really enjoyed to play football with. I thank Maria, who practically helped me to find an apartment. My thanks also to David, Federica and Florian, Antonio, Makarenko, Alberto, Marco, Maria, Dabrowski, Matthias, Sujit, Thiago, Tamene, Jan, Alexander, Sven, Attila, Arkady, Mareike, Mariusz, Andrey, Roy, Roozbeh, Martin with whom I spent my free time and alto-

gether they made a real difference in my life here in Halle far from Italy.

In this respect also my family played an important role. Indeed I would like to thank my whole family not only for the moral support but especially for sending me the products of my land that I love. In fact my Sunday's lunch here in Halle has always had an Italian fingerprint.

Finally, I would like to thank Cecilia who became my wife during my PhD period, and from whom I received a special support. She decided to leave with me for Halle, and this decision made me, actually still makes me, a happy man.

D.

Eidesstattliche Erklärung

Hiermit erkläre ich eidesstattlich, dass ich meine Dissertation selbständig und ohne fremde Hilfe verfasst und keine anderen als die von mir angegebenen Quellen und Hilfsmittel zur Erstellung meiner Dissertation verwendet habe. Die wörtlich und inhaltlich entnommenen Stellen habe ich als solche gekennzeichnet und den entnommenen Werken zugeordnet. Die Arbeit ist in vorliegender oder ähnlicher Form bei keiner anderen Prüfungsbehörde zur Erlangung eines Doktorgrades eingereicht worden.

Halle an der Saale, November 2014